Bow Thruster Currents at Open Quay Constructions on Piles

MSc thesis

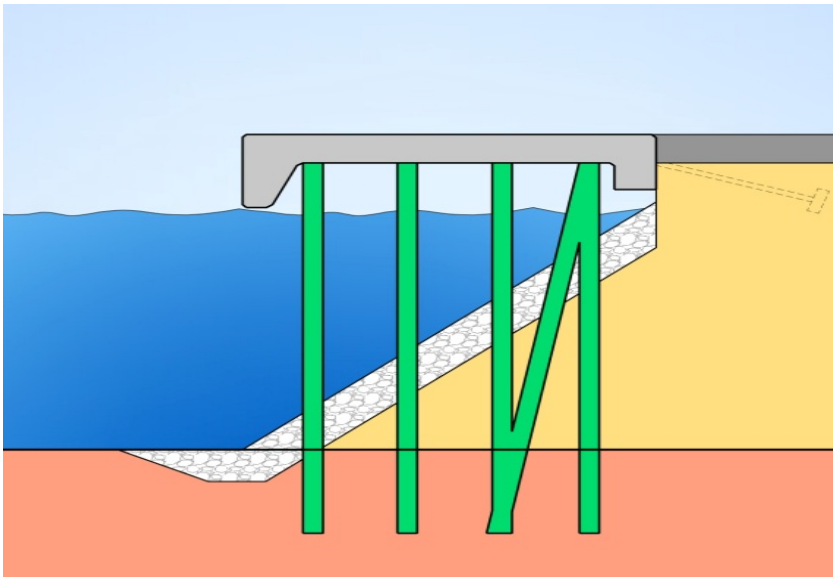

Rory van Doorn

March 2012

TU Delft Delft University of Technology

Challenge the future

Bow Thruster Currents at Open Quay Constructions on Piles

MSc thesis

Rory van Doorn

March 2012

Graduation Committee:

prof. ir. T. Vellinga [a]

prof. dr. ir. W.S.J. Uijttewaal [a]

ir. H.J. Verheij [a]

ir. H.J. Verhagen [a]

ir. T. Blokland [b]

[a)] Delft University of Technology, Delft, The Netherlands
[b)] Rotterdam Public Works, Rotterdam, The Netherlands

Executive summary

This research focuses on the hydraulic loads from a bow thruster on an inclining slope with piles. Methods to determine hydraulic loads from propeller jets and bow thrusters are provided in the literature. Bow thrusters at open quay constructions on piles have not been investigated yet, and available engineering guidelines are based on free non-ducted propeller jets without piles on a slope. Scale model tests were performed to provide details about the hydraulic loads in such situations and as result, recommendations are provided for engineering purpose.
Open quay constructions on an inclining slope with pile foundation penetrating the slope are commonly used in ports, besides vertical quay walls. Propeller jets from mooring vessels may induce scouring of bed material. Estimation of scour holes and the design of bed protection require details about the hydraulic loads due to propeller jets. This research focuses on the hydraulic loads due to bow thrusters. Bow thrusters are mounted near the bow of vessels and enhance manoeuvring by inducing a transversal thrust force. Bow thrusters are mainly used for mooring manoeuvres in ports and the resulting jet flow commonly reaches up to quay constructions. Main propellers and stern thrusters are not explicitly included in this research.
Concluding from the literature review, commonly the 'Dutch' and 'German' engineering guidelines are used to predict hydraulic loads from propeller jets. PIANC [1997] contains engineering guidelines for propeller jets and currently a new PIANC guideline on this subject is being written, called PIANC [2012].

Ten scenarios were tested using scale model tests. Starting point was a 7000 TEU container vessel, with a 2.75 metre bow thruster diameter. This vessel and an open quay construction on piles were scaled using a length scale factor 25. In the Delft University's Laboratory of Fluid Mechanics, a basin of 10 by 2 metres was used to test the ten different scenarios. Each scenario was different by changing one of the following parameters: slope angle, rough or smooth slope, bow thruster distance to the slope, with or without piles and in case of piles a displacement parallel to the slope.
Furthermore, mean velocities and fluctuations were measured in each scenario using an Acoustic Doppler Velocimeter (ADV) in order to determine the hydraulic loads on the (non erodible) bed. Thruster outflow velocity measurements were done, whereas the main part consisted of velocity measurements near the bed. Using an ADV with a sample frequency of 25 Hz, turbulent velocity fluctuations were measured, which are part of the hydraulic bed loads.
The measurements resulted in a large dataset, which covered more than 2200 measurement locations, each consisting of a few thousand samples that were acquired using the ADV. The hydraulic loads in the scale model tests consisted only of the load by the bow thruster, whereas waves and other bed loads were not included.
Results are presented for each scenario, containing mean velocities and turbulence intensities. Analysis of each scenario resulted in several aspects that were not taken in consideration in former research. Conclusions to incorporate in current engineering guidelines are provided, with in addition, recommendations for further research. All original data and calculation scripts were saved and attached to this thesis to ensure the reproducibility of the performed tests.

The nowadays 'Dutch' engineering guideline is analysed and compared to the measurements. First, the outflow velocity is slightly overestimated using the current design method. Calculation of momentum flux shows a 1.52 m/s outflow velocity in scale model tests, whereas 1.60 m/s was estimated. This difference could be due to measuring errors or an overestimation of the propeller thrust coefficient. It seems that the thrust coefficient was overestimated; however, further research could provide a definite answer.

Secondly, the axial velocities are overestimated using the current 'Dutch' and 'German' design methods, where the 'Dutch' method is in best agreement with the measurements.
Third, the resulting hydraulic loads on the bed are discussed. A distinction is made between flow velocities, turbulence intensities, flow direction and location of maximum bed load. Using current design methods, the mean flow velocities that are used as an input are underestimated, whereas in this research, the main hydraulic load is a combination of mean flow velocity and turbulence intensity.

The maximum hydraulic bed load is located where the jet edge bumps up against the inclining slope and measurements show this angle to be dependent on slope conditions. In case of a slope with obstructions (piles), the angle is large, causing the maximum hydraulic load to occur low on the inclining slope. Near-bed flow is not straight up to the slope but slightly under an angle, which has a negative effect on, for example, stability of armour stones. In addition, the flow direction is swaying around a mean value and not constant, causing extra instability of armour stones.

Concluding, the current design method underestimates the hydraulic loads as measured. This does not imply direct failure of existing bed protections, however, unexpected damage may occur. Further research with erodible bed protection is recommended to verify the conclusions in this thesis. Recommendations for further research and new coefficients to use in current engineering guidelines are provided in this thesis.

Keywords:
Bow thruster, propeller jet, inclining slope, piles, open quay construction, bed protection, hydraulic loads

Acknowledgements

This thesis is the final report of a research into bow thruster induced loads. Research is focused on the hydraulic loads on an inclining slope with piles. The performed research would not be achieved without the assistance of many people who I would like to thank. The research was mainly conducted at the office of Rotterdam Public Works and the Laboratory of Fluid Mechanics at the Technical University in Delft.

First of all I would like to thank my graduation committee prof. ir. T. Vellinga, prof. dr. ir. W.S.J. Uijttewaal, ir. H.J. Verheij, ir. H.J. Verhagen and ir. T. Blokland for their guidance and feedback in this project.

Secondly I would like to thank all staff members from the Laboratory of Fluid Mechanics for their help and support. Special thanks to Sander de Vree, Arie den Toom and Jaap van Duin for the good cooperation.

Furthermore, I thank my colleagues at Rotterdam Public Works for my pleasant time at the office and support to my graduation project. Especially thanks to the Harbour Engineering Division, where I was stationed.

Finally, I want to thank my family, friends and especially my girlfriend Geertrui for their support.

Rotterdam, March 2012
Rory van Doorn

Abbreviations

ADV	Acoustic Doppler Velocimeter
EMS	Electromagnetic velocity sensor
IGWR	Ingenieursbureau Gemeentewerken Rotterdam, Rotterdam Public Works
LDA	Laser Doppler Anemometry
MSc	Master of Science
S1	Scenario 1 (S1, S2, S3, ...)
TU	Technical University

Contents

1 Introduction

Several types of quay constructions can be found in ports. Closed vertical quay walls are commonly used, as well as quay construction types as displayed in Figure 1.1. This open type of quay construction has a deck on piles, combined with an inclining slope. The pile foundation penetrates the inclining slope, which can be protected against hydraulic loads, such as propeller jets from vessels. Yet no validated method is available to calculate the hydraulic load from propeller jets in such a situation.

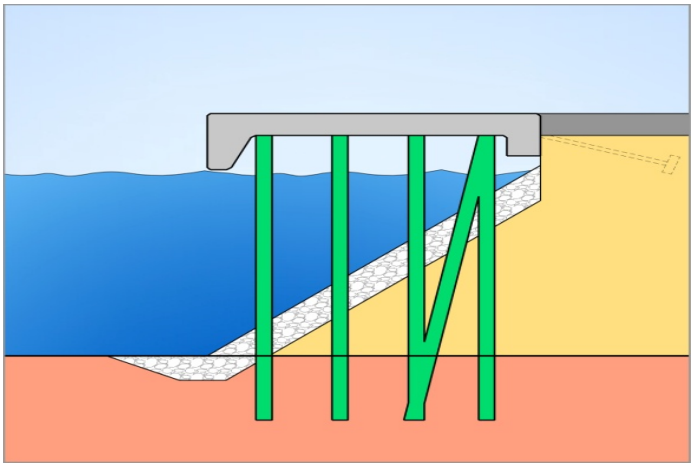

Figure 1.1: Schematic view of open quay construction

The long-term objective is to gain a validated calculation method for this problem. Within this Master thesis, only a part of this problem is dealt with, considering the amount of work.

Hydraulic loads can be seen as a combination of factors that load the slope, possibly leading to erosion of bed material. Examples of hydraulic loads are flow velocity, turbulence intensity and pressures.

1.1 Problem definition

The common way to protect the slope at an open quay construction is to apply a bed protection that prevents erosion of bed material. Another option, which could result in lower costs, is an unprotected bed or less heavy bed protection, resulting in scour holes. When scouring is taken into account in the design of the foundation and bank stability, this does not have to be a problem.
The problem in this case is that the acting hydraulic loads on the bed are not fully understood. The main question for this thesis is what the occurring hydraulic loads are from bow thrusters.

Bow thrusters are commonly used in inland- and sea-going vessels, increasing the navigability of a vessel by inducing a transverse force near the bow of a vessel. Especially in ports and near quay constructions, bow thrusters are used extensively in order to facilitate easy and safe mooring of vessels.
Figure 1.2 shows a transversal thruster which is commonly applied in sea-going vessels. An engine drives the propeller by a bevel gearbox.

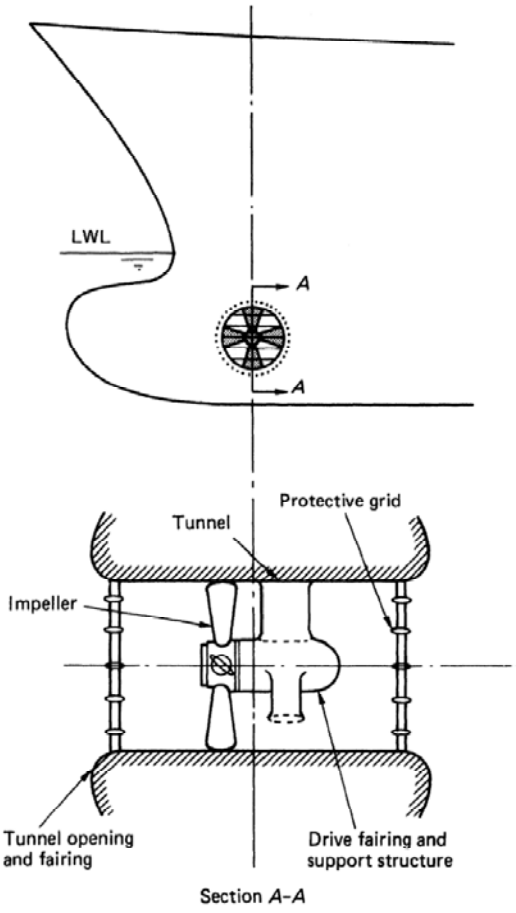

Figure 1.2: Transverse propulsion unit by CARLTON [2007]

1.2 Objective

The objective of this Master thesis is to:
"Develop a method to predict the hydraulic loads from a bow thruster on a non erodible slope."

A non erodible slope is selected because the focus within this project is on the loads. Erosion of bed material can be included in future research following this thesis.

The objective will be achieved with the help of a main and several sub questions. The main question for this thesis is: *how large is the hydraulic load from a bow thruster on a slope with piles?*
In order to answer the main question, the following sub questions have been posed: *What is the expected hydraulic load on a slope without piles? What is the expected hydraulic load on a slope with piles? Are the measured hydraulic loads in agreement with the expected hydraulic loads?*

1.3 Outline

This project can be globally divided into three main parts: a literature review, scale model tests and results, ending with an analysis of the results and recommendations. In chapter 2, a short overview of existing literature is provided. The complete literature review is included in several appendices, as referred to in the main report. The remaining part of this report consists of an explanation of the scale model tests in chapter 3, results of these tests in chapter 4, and an analysis of the results in chapter 5. Discussion follows in chapter 6, resulting in conclusions and recommendations in chapter 7.

Furthermore, lists of references, used symbols, figures and tables are included after chapter 7. Detailed literature review and all results are included in appendices.

2 Literature

The results of the literature review can be divided into several parts as shown below.

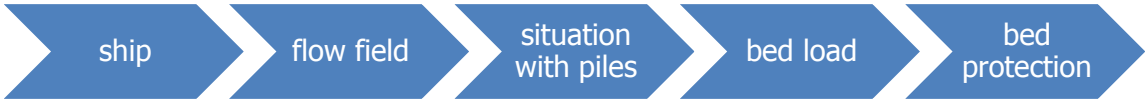

First, some global knowledge about the ships, propellers and bow thrusters is discussed, followed by a concise overview of methods to determine the flow field from a propeller and from bow thrusters. Hereafter this is extended for a situation with piles, resulting in a certain load at the bed, ending with ways to design proper bed protection.

2.1 Ships and their thrusters

This paragraph gives a brief overview with respect to the ships that are included in this research. These ships have propulsion with propellers, which may create a high load on bed layers at, for example, quay constructions. Some aspects about main propellers are discussed as well as bow thrusters. This thesis focuses on bow thrusters. Figure 2.1 shows a typical example of a large sea-going container vessel as a starting point for the performed scale model tests.

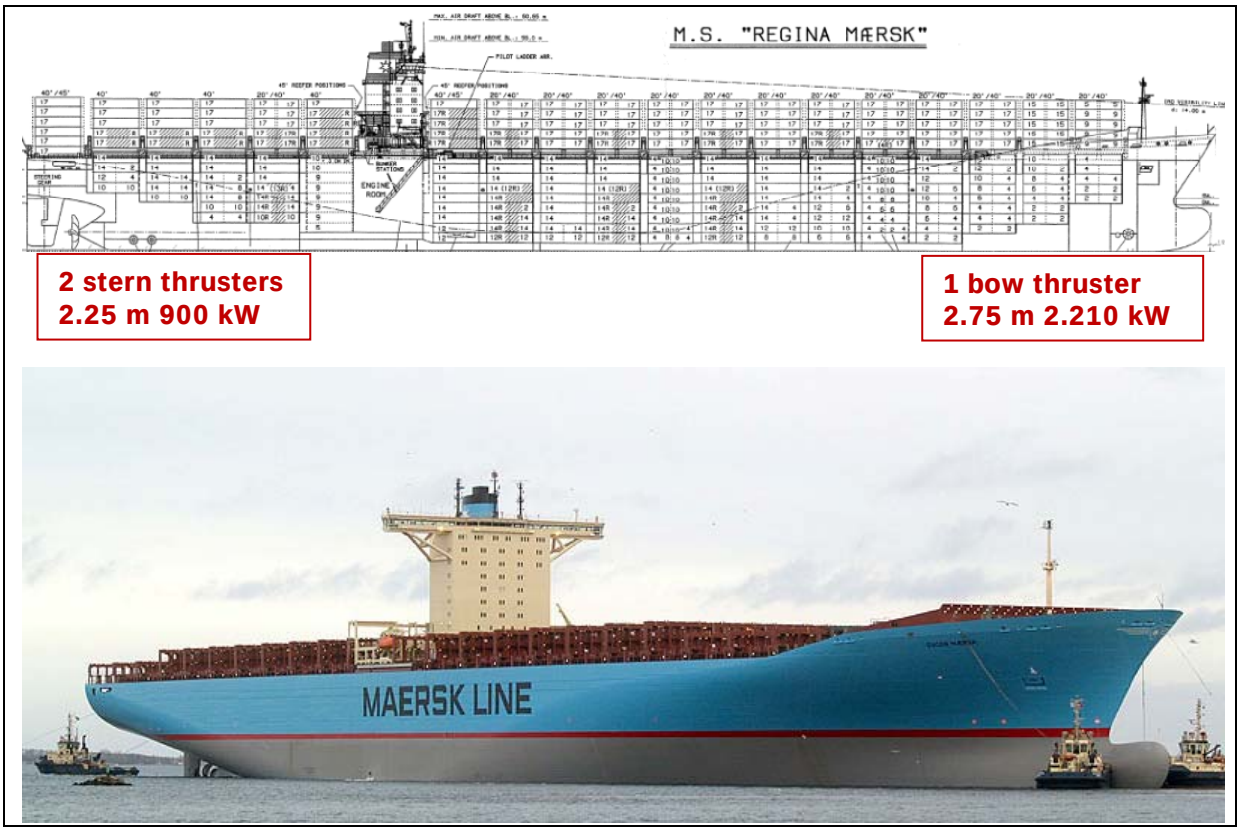

Figure 2.1: Regina Maersk (347 x 43 x 14 m) from IGWR [2010]

Remark: In case of ship propellers one can speak about free propeller jets or (non-)ducted propeller jets (and of course 'free (non-)ducted propeller jets'). A free jet means that the jet is not bounded by bed, water level or other obstacles. A ducted jet means that the propeller is mounted in a tunnel, which is in case of a bow thruster.

2.1.1 Propellers and thrusters

For specific details about propellers and bow thrusters, the reader is referred to Appendix A, which gives a detailed view on the operation of propellers, different propeller types, bow thrusters and installed engine powers. The following paragraph contains details about propellers and thrusters, to understand considerations that have been made.

For sea-going container vessels, one specific type of bow thruster is used. This is a transversal thruster with mainly a controllable pitch propeller and Kaplan-shaped blades, as shown in Figure 1.2. The Kaplan shape increases the thrust force (outflow velocity) for the same propeller diameter compared to conventional blade types. In the scale model tests, a comparable Kaplan type propeller is used in order to create a good comparison with prototype thrusters. The Kaplan shape is characterized by the cut-off blades as shown in Figure 2.2, blade number 4.

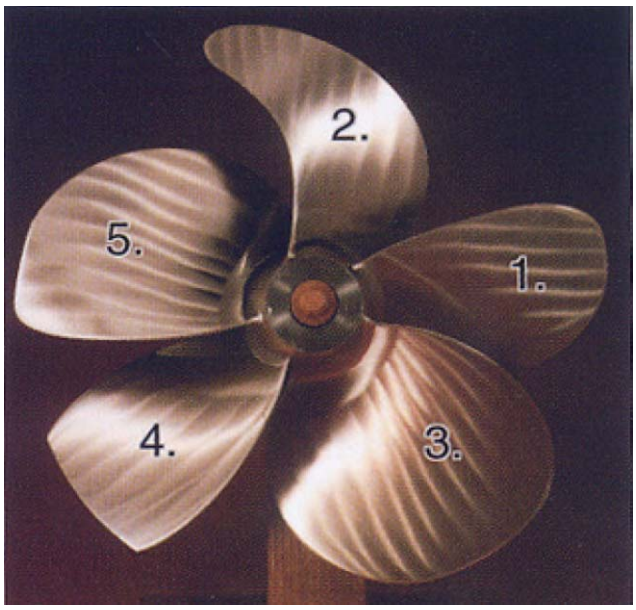

Figure 2.2: Different types of blades attached to a hub

In the past, some research has been done for bow thruster induced flow. VAN VELDHOVEN [2002] and SCHOKKING [2002] performed tests for bow thruster loads and used a propeller type Raboesch, as shown in Figure 2.3. The disadvantage of this propeller was the conventional blade type, which could result in deviating flow velocities. However, no further research has been done to investigate this possible deviation.

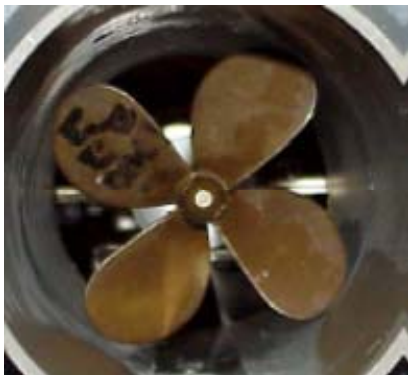

Figure 2.3: Raboesch propeller 176-31 R, 100 mm

Remark: not all vocabulary and symbols for geometry of propellers are according to NEN [2004], because of conflicting symbols.

2.2 Flow distribution for a propeller or thruster

Quite a lot of research has been done to determine flow velocities just behind ship propellers and the resulting flow velocities over a horizontal bed. Furthermore for situations with an inclining slope, there has been some research, but the amount of literature is declining fast as one goes more into detail.

2.2.1 Design methods

Almost all current design methods for bow thruster induced flow are using the same theory. PIANC [2012] prescribes two calculation methods. The so-called Dutch and German method are two separate ways of calculating the required flow velocities and should not be mixed. Because of different reasoning for both methods, mixing of those two may result in inaccuracies. The methods employ similar principles, but other empirical constants. A short view at these methods is presented here:

Both methods are based on the axial momentum theory presented by Froude in the 19th century. ALBERTSON *et al.* [1948] did research based on an ordinary water jet, which formed the foundation for subsequent derived equations for propeller jets. Appendix B.2.1 gives details about this theory and those derived equations for the efflux velocity.

2.2.2 Efflux velocity

The efflux velocity is regarded as the outflow velocity just behind a propeller.
In the Dutch and German method, the efflux velocity is estimated by using equation (2.1) from BLAAUW and VAN DE KAA [1978].

$$U_0 = 1.60 \cdot n_p \cdot D_p \cdot \sqrt{K_T} \qquad (2.1)$$

Not always the thrust coefficient is known. For that case, another equation is derived by BLAAUW and VAN DE KAA [1978] and is presented in VERHEIJ [1985] as:

$$U_0 = 1.15 \cdot \left(\frac{P}{\rho_w D_0^2} \right)^{1/3} \qquad (2.2)$$

Where:

n_p	rotational speed of the propeller	[s^{-1}]
D_p	propeller diameter	[m]
K_T	propeller thrust coefficient	[-]
P	engine power	[W]
ρ_w	density of water	[kg/m^3]
D_0	diameter of the jet just behind the propeller, located at the point of maximal contraction $D_0 = D/\sqrt{2} \approx 0.71 \cdot D_p$ at thrusters without tunnel $D_0 = 0.85 \cdot D_p$ propeller-jet combinations in a tunnel $D_0 = 1.00 \cdot D_p$ at ducted thrusters	[m]

Several other equations are derived to determine the efflux velocity for propellers and bow thrusters. However, in practice equation (2.1) and (2.2) provide good results. In this investigation, equation (2.2) is used to determine the efflux velocity. Other methods as described in appendix B.2.1 could be investigated in future research.

2.2.2.1 Limitations of the axial momentum theory, regarding propeller jets

Investigations of the velocities in a ship's propeller jet started with a water jet and the axial momentum theory. There are some important limitations for the axial momentum theory: the axial momentum theory only considers axial flow directions while in a propeller jet tangential and radial velocity components occur additionally. Therefore, the assumption in the axial momentum theory that energy is supplied without any rotational effects is invalid.

In the axial momentum theory, the disk consists of an infinite number of rotating blades, rotating at an infinite speed. A propeller rotates at a few hundred revolutions per minute, designed in combination with the number of blades, usually three to six. Furthermore, the thickness in the axial direction of the propeller is not negligible as blades have a certain pitch ratio and thickness. Pitch is the travel distance of a point in the longitudinal direction of the jet in one propeller rotation. Hereby, the assumption is incorrect that on each side of the disk (propeller) the velocity is approximately equal.

Due to the presence of the propeller hub, a low velocity core occurs just behind the propeller in the zone of flow establishment. The assumption in the axial momentum theory that the maximum axial velocity occurs at any lateral section at the rotation axis is hereby not true.

The distributions of flow velocities in a propeller jet all depend on the efflux velocity. These velocities are not investigated well for bow thrusters, which results in errors in the prediction of the flow field.

2.2.2.2 Zone of flow establishment and established flow

In the literature with respect to propeller jets, two zones are commonly discussed. The zone of flow establishment follows directly behind the propeller and at a certain distance; one considers transition to the zone of established flow. For propeller jets, this transition is commonly at a distance of around three times the propeller diameter behind the propeller. For the Dutch method discussed below, this transition is, for example, at 2.8 times the propeller diameter.

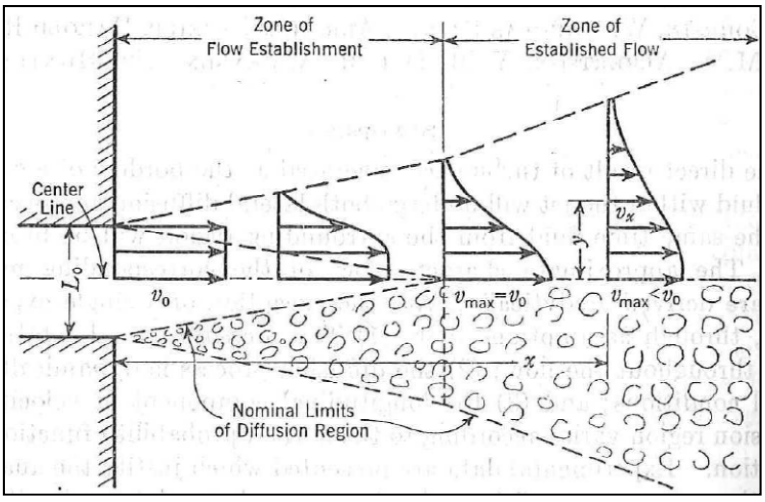

Figure 2.4: Schematic representation of jet diffusion, according to ALBERTSON *et al.* [1948]

ALBERTSON *et al.* [1948] discussed these zones for a free water jet from a pipe. An equal approach is applied to propeller jets.

2.2.3 Dutch method

BLAAUW and VAN DE KAA [1978] and VERHEIJ [1983] discussed the following equations, which are discussed in detail in appendix B.2.

$$U_0 = 1.60 \cdot n_p \cdot D_p \cdot \sqrt{K_T} \tag{2.1}$$

$$U_{x,axis} = 2.8 \cdot U_0 \cdot \left(\frac{D_p}{x} \right) \tag{2.3}$$

$$U_{x,r} = U_{s,axis} \cdot \exp\left[-15.4 \cdot \left(\frac{r}{x} \right)^2 \right] \tag{2.4}$$

The maximum flow velocities at the bed occur for r/x = 0.18.
Tests by VERHEIJ [1983] showed values of 0.1 - 0.25.

This results in:

$$U_{b,\max} = 0.3 \cdot U_0 \cdot \frac{D_0}{h_{pb}} \tag{2.5}$$

Where:

U_0	flow directly behind a propeller, located at the point of maximal contraction of the jet	[m/s]
$U_{x,axis}$	flow velocity along jet axis	[m/s]
x	distance in the axial direction	[m]
$U_{x,r}$	flow velocity distribution	[m/s]
r	radial distance to the propeller axis	[m]
$U_{b,\max}$	maximum flow velocity along horizontal bed	[m/s]
h_{pb}	distance between the propeller axis and the bed	[m]

2.2.3.1 Limitations to the Dutch and German method

Differences between the Dutch and German method are observed in the calculated velocities. The German method results in a larger near-bed velocity, compared to the Dutch method. However, this effect is compensated using a smaller stone stability coefficient in the German method, which eventually results in comparable stone diameters.

A mayor limitation to the Dutch and German method is that both methods are valid for a non-ducted propeller jet. Coefficients are presented for the German method to include restrictions by walls, bed and water level. The German method used in the Hamburg harbour resulted in heavier bed protection, compared to the Dutch method in the Rotterdam harbour. Although in the Rotterdam harbour occurs no extensive damage level to bed protection. Hereby the Dutch method is considered leading.

2.2.4 German method

According to PIANC [2012], the German method is based on Fuehrer, Römisch and Engelke (1981).

$$U_0 = 1.60 \cdot n_p \cdot D_p \cdot \sqrt{K_T} \tag{2.6}$$

$$U_{x,axis} = A \cdot U_0 \cdot \left(\frac{D_p}{x}\right)^a \tag{2.7}$$

$$U_{x,r} = U_{x,axis} \cdot \exp\left[-22.2 \cdot \left(\frac{r}{x}\right)^2\right] \tag{2.8}$$

With

$$U_{x,\max} = U_0 \cdot A \cdot \left(\frac{x}{D_p}\right)^{-C_4} \tag{2.9}$$

Where A and C_4 are constants:

$A = 1.88 \cdot \exp\left(-0.092\left(h_{pb}/D_p\right)\right)$ Without rudder, for $0.9 \le h_{pb}/D_p \le 9$

$A = 1.88 \cdot \exp\left(-0.161\left(h_{pb}/D_p\right)\right)$ With central rudder, for $0.9 \le h_{pb}/D_p \le 8$

A = 2.6 for unobstructed jets
C_4 = 0.25 for two propellers
C_4 = 0.30 with a restriction at a transverse wall
C_4 = 1.62 for a jet reflected at a quay wall
C_4 = 0.60 in case of a restriction from bed and water level

And a simplified approach for the maximum velocity at the bed:

$$U_{b,\max} = E \cdot U_0 \cdot \left(\frac{h_{pb}}{D_p}\right)^{-1.0} \tag{2.10}$$

With:
E = 0.71 for sea going vessels with a rudder
E = 0.42 for sea going vessels without a rudder
E = 0.25 for inland vessels with a tunnel stern and a twin rudder configuration

As included in appendix B.2.2.9, RÖMISCH [2006] presents the following updated equation for a bow thruster in the zone of established flow (after x/Dp = 6):

$$U_{x,\max} = U_0 \cdot 2.3 \cdot \left(\frac{x}{D_p}\right)^{-0.825} \tag{2.11}$$

2.3 Flow around piles

At open quay structures, piles form obstacles for the flow. This results in a contraction of the flow between the piles and horseshoe vortices around the piles.
This jet scour consists of two basic mechanisms. The pile obstruction is dominated by the down flow and the horseshoe vortex. The jet diffusion is controlled by bed shear stress.
The scour process by the pile obstruction is initiated due to local flow acceleration and the formation of a down flow and horseshoe vortex around the pile.
The erosion process by the diffusion mechanism is caused by the action of the shear stress and turbulence

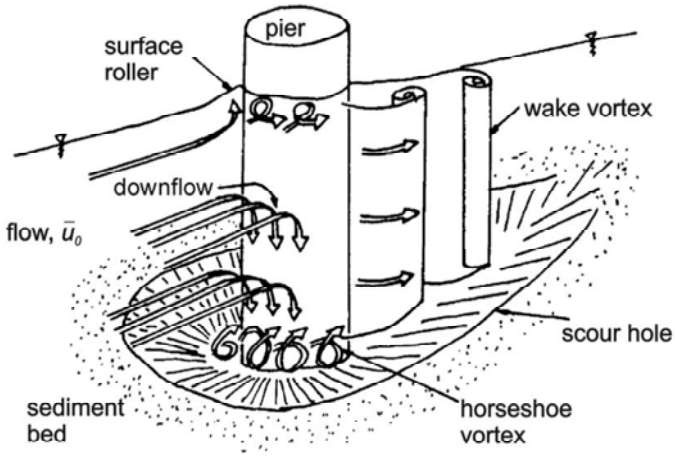

Figure 2.5: Scour around a cylinder, figure from SCHIERECK [2004], by BREUSERS and RAUDVIKI (1991)

In case of a much smaller pile diameter than the water depth, which is the case for these kind of constructions HOFFMANS and VERHEIJ [1997] presented an equation to estimate the final scour depth:

$$S = 2.0 \cdot D \qquad (2.12)$$

Where:

S	final scour depth	[m]
D	pile diameter	[m]

When the spacing between the piles is larger than 5 D, the scour holes of the individual piles do not influence each other. For open quay constructions regularly have a spacing of about 10 D.
In case of a smaller distance between the piles than 5 D, the different effects should be included:

$$S = 2.0 \cdot K_i \cdot D \qquad (2.13)$$

In the Scour Manual by HOFFMANS and VERHEIJ [1997] the case of a single cylindrical pier has been used as a reference and deviations to this case are expressed in K-factors:

$$K_i = K_s \cdot K_\omega \cdot K_g \cdot K_{gr} \qquad (2.14)$$

Where:

K_g	factor for the influence of gradation of bed material	[-]
K_{gr}	factor for the influence of a group of piers	[-]
K_i	correction factor	[-]
K_s	pier shape factor	[-]
K_ω	factor for orientation of the pier to the flow	[-]

Since this investigation is focused on piers of quay constructions, only cylindrical and square piles will be included.
For rectangular piles, the shape factor K_s is 1.1. The factor K_ω is 1 for a single pile, because of the symmetrical shape of the piles.

This thesis includes the effect of piles on a slope. Literature with respect to flow around piles can be divided into the flow around large structures as bridge piers and small structures as piles. Due to the relatively large difference in main dimensions for these structures, this creates different properties for flow around these structures. Foundation piles of open quay constructions can be classified as slender piles, which are commonly square when made of concrete and cylindrical when made of steel.

Literature review as presented in Appendix C did not provide sufficient details about differences between hydraulic loads for slender piles or bridge piers. For propeller jets with relatively high turbulence intensities, one should focus on methods which include certain turbulence intensity.

2.3.1 Increase in local flow velocity

By a strong simplified view at the flow velocity between piles, an increase in flow velocity occurs between the piles. Because of a decreased flow area because of obstruction by the piles, the flow velocity increases when the flow rate is assumed constant.

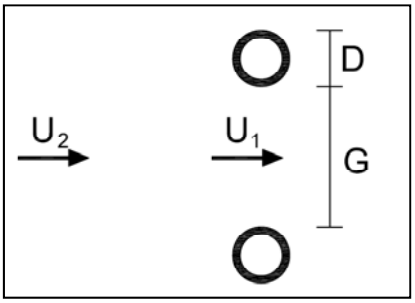

$$U_1 = \left(\frac{G + \alpha_P \cdot D}{G} \right) \cdot U_2 \qquad (2.15)$$

Where:

U_2	undisturbed mean flow velocity	[m/s]
U_1	disturbed mean flow velocity	[m/s]
α_P	coefficient	[-]
G	spacing between piles	[m]
D	pile diameter	[m]

Recently, VAN VELZEN [2012] published a MSc thesis that clearly describes the local flow pattern around cylindrical piles, which is based on existing literature about flow around piles. Results from that thesis are not included in this research, because that thesis was published about one month before finishing this research and thesis. Future research into propeller jets around piles could also use results from that thesis.

2.4 Bed load and protection

Commonly scour on an inclining slope is prevented using armour stone bed protection. Hydraulic loads and bed protection in this thesis is mainly focused on armour stone, whereas for example also concrete mats are applied as bed protection. This paragraph contains a summary of Appendix D in order to ensure readability of this main report.

When a stone is exposed to flow, several hydrodynamic forces may be considered as (for example) described in HOAN [2008], these forces can be considered as in Figure 2.6.

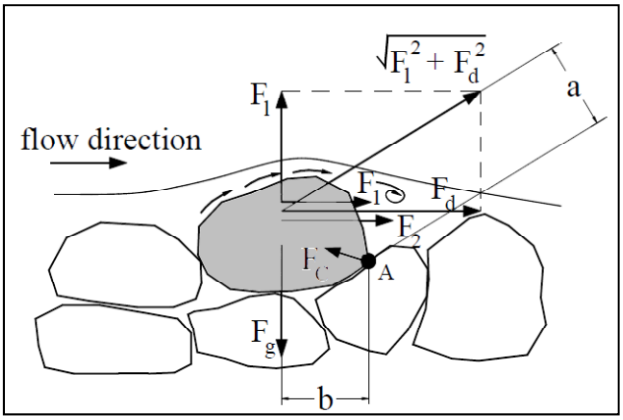

Figure 2.6: Forces acting on particles resting on a bed surface by HOAN [2008]

HOAN [2008] considers a frictional force F_1 on the rough surface of the stone. Surface friction is the main force acting on a stone in case the particle Reynolds number is less than 3.5. In case that this Reynolds number is larger than 3.5, "separation of streamlines in the form of a small wake occurs behind the top of the particles and vortexes form there. This causes a pressure difference between the front and the back surface of the particle, forming the resistance F_2." As a resultant of F_1 and F_2 the drag force F_D remains. The frictional force F_1 can be neglected in case that the Reynolds number is larger than around 500.
Hydraulic loads by propeller jets are commonly approached using an Izbash type equation, taking into account mean flow velocities combined with a factor to count for turbulence intensities. Equation (2.16) is commonly applied in case of propeller jets to determine required stone diameters according VERHEIJ [1985].

$$D_{50} \geq \beta_{Iz,cr} \cdot m_h \cdot \frac{U_{b,\max}^2}{2 \cdot g \cdot \Delta} \qquad (2.16)$$

Where:

$\beta_{Is,cr}$	critical stability coefficient (commonly 2.5 – 3.0)	[-]
m_h	slope coefficient to account for stone stability on an inclining slope	[-]
$U_{b,\max}$	maximum flow velocity along the bed	[m/s]

In (2.16) maximum mean flow velocities are included and the critical stability coefficient accounts for a certain turbulence intensity. Mean flow velocities are squared because of the relation with forces on a stone. Hereby the hydraulic bed load is depending on the flow velocity to the power two.

2.4.1 Stability around piles

VAN VELZEN [2012] provides equations for granular filters around piles. Equations by BONASOUNDAS and BREUSERS do not include a certain turbulence factor, while equations by RICHARDSON and HOFFMANS do this. As the stone diameter is equivalent to a certain hydraulic bed load, required stone diameters can be compared to situations without piles.

$$D_{50} = 0.692 \cdot \frac{\left(K_s \cdot U\right)^2}{2 \cdot g \cdot \Delta} \quad \text{(Richardson)} \tag{2.17}$$

$$D_{50} = 0.7 \cdot \frac{\left(r_0 \cdot U_{0,u}\right)^2}{\psi_c \cdot g \cdot \Delta} \quad \text{(Hoffmans)} \tag{2.18}$$

Where:

D_{50}	median stone diameter	[m]
K_s	correction factor for the pile shape, see 0	[-]
U	local flow velocity near piles	[m/s]
$U_{0,u}$	undisturbed flow velocity	[m/s]
g	acceleration due to gravity	[m/s^2]
Δ	relative density of rock	[-]
r_0	depth-averaged relative turbulence intensity	[-]
ψ_c	critical Shields parameter	[-]

The HOFFMANS approach is applicable for uniform flow; however it is not further used, because it has not been validated yet.

RICHARDSON's equation is based on the Izbash equation and assumes the maximum velocity near the pile is twice the undisturbed mean flow velocity and, in addition, a correction factor for the pile shape. However, turbulence intensities in propeller jets are assumed higher compared to the situation of bridge piers in the RICHARDSON equation. Thereby the use of RICHARDSON's equation could provide inaccurate results.

3 Set-up of model tests

In this chapter, a description is given about the preparation and execution of the model tests. Some remarks are made about the configuration of the quay construction and model-ship dimensions. In addition, the measured variables and measuring instruments are described.

3.1 General

The model tests are focused on sea-going vessels because the examined type of berthing hardly exists in inland navigation.
In the scale model tests both average flow velocities and turbulence are included. Turbulence plays an important role in the stability of bed protections. For a non-ducted propeller jet, turbulence intensities are relatively high, compared to a free (normal) jet from a pipe. Bow thruster tunnels in sea going vessels have a relatively short length, with expected turbulence intensities in-between non-ducted propeller jets and a (normal) water jet.
In the scale model, a standard type bow thruster is used, to match prototype situations.

For the scale model tests, some considerations about deviations from reality have to be made. These have been explained hereafter. In addition, the measuring equipment is explained and some specific details about the propeller used in the scale model are discussed.

3.1.1 Basis for model dimensions

As a basis for the scale model tests one specific type of open quay construction is used. The construction in Figure 3.1 (PIANC [1997]) is a real-world example of the type of quay construction under investigation. It consists of a flat bed in front of the quay construction, a deck on piles with a certain centre-to-centre distance and an underwater slope below the deck on piles.

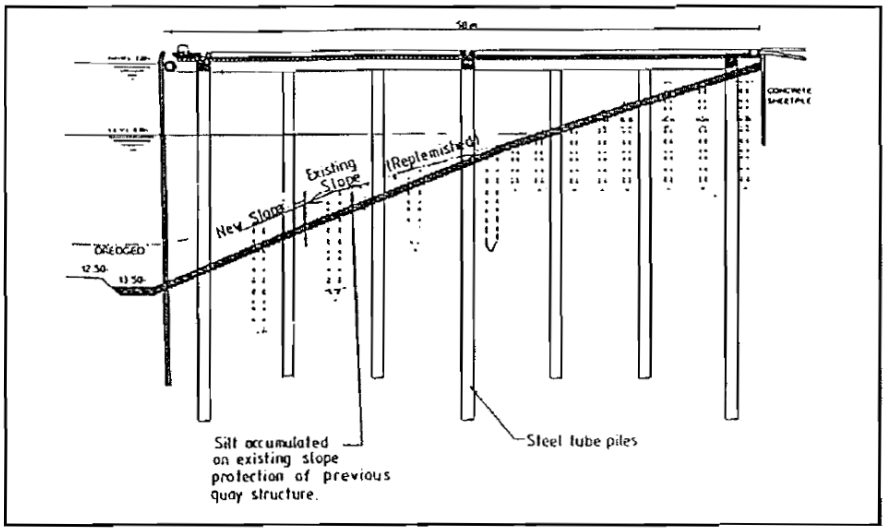

Figure 3.1: Examined quay construction, Beira, Mozambique from PIANC [1997]

From Figure 3.1 some characteristic dimensions can be derived for this specific open quay construction. In Table 3.1, the relevant quay construction dimensions are listed, followed by ship dimensions in Table 3.2.

3.1.2 Derived dimensions

In this paragraph the derived dimensions for the considered quay constructions and vessels are discussed.

Quay dimensions		
Distance between piles in x-direction	6	[m]
Distance between piles in y-direction	6	[m]
Assumed pile diameter	0.75	[m]
Adjusted water depth	15	[m]
Slope angle	1.2	[1:...]
Top armour layer	100-200	kg
Thickness armour layer	2 x D_{50}	[m]

Table 3.1: Characteristic quay dimensions from Figure 3.1

According to IGWR's ship database, two specific ships have dimensions that approach the suitable dimensions for the quay construction in Figure 3.1. In addition, the database contains detailed information about the ship dimensions and bow thrusters. These detailed bow thruster specifications are needed in order to model the bow thruster accurately in the scale model. Coincidentally, these detailed specifications are both based on Maersk vessels.

Ship dimensions	Sovereign Maersk	Regina Maersk	
Length Over All (LOA)	347	318	[m]
Width	42.8	42.8	[m]
Maximum draught	14.5	14.0	[m]
Capacity	7,500	6,400	[TEU]
Dead weight tonnage	104,700	82,135	[T]
Gross register tonnage	91,560	81,488	[T]
Power of main engine	54,840	54,840	[kW]
Main propeller diameter	9,0	9,0	[m]
Power of bow thruster	2,210	2,210	[kW]
Diameter thruster tunnel	2.75	2.75	[m]
Length of tunnel	5.8	5.8	[m]
Height of tunnel-axis above keel	4.6	4.6	[m]
Distance tunnel-axis to bow	23.6	-	[m]
Bow thruster outflow velocity	8	8	[m/s]

Table 3.2: Derived ship dimensions

3.2 Scaling

Criteria need to be taken into account in order to simulate prototype situation in a proper way in the scale model. Hence the scale factor for this is indicated by 'n' and a factor 10 means that the physical dimensions in the model are 10 times smaller than in prototype. This scale factor is thereby defined as:

$$n_L = \frac{L_p}{L_{sm}} \tag{3.1}$$

In scale models, it is impossible to achieve dynamic and geometrical similarity. This means that it is impossible to scale length dimensions as well as achieve proper scaling of all dynamic forces. For fluid motions in combination with a flow around structures the Froude number and Reynolds number are defined as main criteria in SCHIERECK [2007].

3.2.1 Geometrical and dynamic similarity

The geometrical similarity means that each geometrical dimension is modelled on the same scale. Geometrical similarity for example applies to length, height and width of the object to be tested.
The requirement of dynamic similarity refers to the similarity of the movements of objects or bodies of water. Dynamic similarity is accomplished by using the Froude criterion and minimizing viscous scale effects. This required using a high enough Reynolds number. Figure 3.2 shows the definition of the Froude number and Reynolds number.

$$Fr = \frac{u^2}{g \cdot h} \text{ (ratio inertia - gravity)}$$

$$\mathrm{Re} = \frac{u \cdot L}{\upsilon} \text{ (ratio inertia - viscosity)}$$

Figure 3.2: Important dimensionless numbers from SCHIERECK [2007]

Since acceleration by gravity is the same in prototype and model:

Using the Froude number: $n_u = \sqrt{n_L}$

In addition, for the Reynolds number: $n_u = n_L^2$

Where:

n_L	scale factor for length	[-]
n_u	scale factor for flow velocity	[-]
L_p	length in prototype	[m]
L_{sm}	length in scale model	[m]

These two criteria show conflicting requirements. When the fluid motion is dominated by gravity and not by viscosity, the Froude criterion has to be applied.

In VERHEIJ [1985], GUTSCHE (1966) and PEARCE (1966) suggested that the scaling effects due to viscosity were negligible if the Reynolds number of the propeller and of the jet-flow were greater than respectively 7×10^4 and 3×10^3. Using the two equations:

$$\mathrm{Re}_{prop} = \frac{n_p \cdot D_p \cdot L_{smb}}{\upsilon} \tag{3.2}$$

$$\mathrm{Re}_{jet-flow} = \frac{U_0 \cdot D_p}{\upsilon} \tag{3.3}$$

Within near-bed flow possible scale effects may occur, according to the Reynolds criterion:

$$\mathrm{Re}_* = \frac{u_* \cdot D_{50}}{\nu} \qquad (3.4)$$

Near the bed, flow conditions are influenced by the size of the bed material compared to the thickness of the viscous sub layer. When the Reynolds number is smaller than approximately 5, the bed is called hydraulically smooth. The resistance of a grain is in that case completely determined by viscous forces.
From $\mathrm{Re}_* > 70$ the bottom is called hydraulic rough because the grains are large against the laminar sub layer. When $\mathrm{Re}_* > 600$ $(D_{50} \geq 5\,\mathrm{mm})$, the influence of the viscous sub layer on the turbulent pressure forces is fully negligible.

Where:

U_0	outflow velocity of propeller jet	[m/s]
D_p	propeller diameter	[m]
υ	kinematic viscosity (water of $15° = 1.141 \cdot 10^{-6}$)	[m^2/s]
n_p	rotational speed of the propeller	[s^{-1}]
L_{smb}	length term dependent on the blade area ratio β $L_{smb} = \beta \cdot D_p \cdot \pi \cdot \left(2 \cdot N\left(1 - \frac{D_h}{D_p}\right)\right)^{-1}$	[-]
N	number of blades	[-]
D_h	diameter of hub	[m]
U_*	velocity near the bed	[m/s]
D_{50}	sieve diameter, diameter of stone that exceeds the 50% value of sieve curve	[m]

BLAAUW and VAN DE KAA [1978] and VERHEIJ [1983] proposed that scale effects by differences in Reynolds number due to flow in a propeller are insignificant. The Reynolds number for the jet should be greater than 3000, satisfying the Froude criterion for scaling.

According to VAN DER SCHRIEK [2011], the filter velocity between deposited stones is a possible problem. The flow in the prototype is turbulent because of the large pores. Therefore, the flow through the pores in the model must be turbulent as well, which means that they should not be too small. VAN DER SCHRIEK [2011] sets the requirement that in the model the stone diameter should not be smaller than approximately 10 mm.

3.3 Scale factor

Based on data from those two vessels the normative vessel has a length of 332 m, a width of 42.8 m and a draught of 14.25 m. At several quay constructions worldwide, pile distances range mainly from five to eight metres. For this experiment, a prototype centre-to-centre pile distance of five metre and a diameter of 0.75 metre are used.

Due to the basin-restrictions with a maximum width of 2.0 m, the scale factor should be large in order to accommodate as much of the prototype situation in the model. On the other hand, scale effects may occur especially for a large scale-factor. Besides these two considerations, the available sizes of bow thrusters to include in the scale model are limited.

As described in paragraph 3.1.1, the required stone size is larger than 10 mm. The first suitable stone class is 11-16 mm with a D_{50} of 13.2 mm. This small stone class would result in the largest scale factor and it would be possible to include the largest part of the prototype situation in the model.

The selected bow thruster is manufactured by Vetus. The smallest available one has a tunnel diameter of 110 mm, which is therefore an extra boundary condition for the model dimensions. With a prototype propeller diameter of 2.75 m, a tunnel diameter of 0.11 m results in a scale factor 25. Table 3.3 presents the resulting scale model dimensions, based on Table 3.2. Some dimensions were not scaled using a factor 25, for example because of scale model limitations. In that case, annotations are added below Table 3.3.

Derived model dimensions	prototype	scale model	
Ship length over all (LOA)	332	2.50 (1)	[m]
Ship width	42.8	0.30 (2)	[m]
Ship draught	14.25	0.57	[m]
Water depth	15.75	0.63	[m]
Keel clearance	1.5	0.06	[m]
Diameter thruster tunnel	2.75	0.11	[m]
Length of tunnel	5.8	0.30 (3)	[m]
Height of tunnel-axis above keel	4.6	0.184	[m]
Height of tunnel-axis above bed	6.1	0.244	[m]
Distance tunnel-axis to bow	23.6	0.60 (4)	[m]
Thruster outflow velocity	8	1.6 (5)	[m/s]
Pile diameter	0.75	0.03	[m]
Pile distance	5.0	0.20	[m]

Table 3.3: Scale model dimensions

(1) The ship length is smaller than 1:25, because of restricted basin dimensions. Increased circulation effect of water in the basin is assumed negligible with a length of 2.50 m.
(2) A basin width of 2.0 m, required a small ship width. Minimal flow velocities under the vessel are assumed, resulting in negligible influence of this width restriction.
(3) In a vessel width of 0.3 m, a tunnel length of 0.3 m was easy to use, compared to the 0.23 m following from a scale factor 25.
(4) Because of the block-shape scale model bow, a reduction for this distance is used, compared to the bulb-shape bow in prototype.
(5) Velocities are scaled using the square root of 25, according to paragraph 3.2.1.

In the scale model, a slope of 1:1.5 is used even though this is a usual upper limit for slopes with an armour stone top layer. In practice, slopes vary between the steep 1:1.2 as in Figure 3.1 and a mild 1:4. The reason for a slope of 1:1.5 was used because of restrictions from the available basin dimensions. Within the relatively short preparation period for the model tests, only a basin with a length of 10 meter and a width of 2.0 meter was available.

3.3.1 Circulation in basin

The basin that was available for the scale model tests had a width of 10 meter and a length of 2 meter. In prototype situations, the flow at quay constructions is not limited by four walls close to the vessel. Hereby one could expect a certain circulation throughout the basin.

In earlier research VAN VELDHOVEN [2002] used a basin with an inclining slope of nearly 2 by 2 metres. This research shows that the basin width should be larger in order to decrease the slightly hindering circulation flow as pointed out in Figure 3.3.

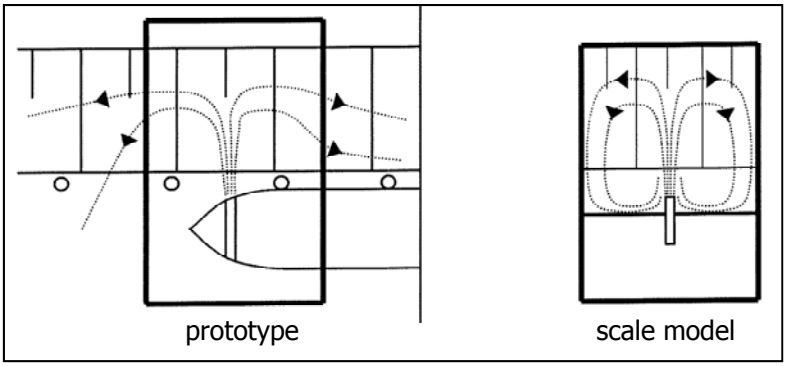

Figure 3.3: Circulation by width restriction from VAN VELDHOVEN [2002]

Based on experience we know that water jets and propeller jets have a diffusing character, which occurs with a slope of respectively 1:10 and 1:5 (approximately). For a basin of 2 metres wide, a propeller jet with a diameter of 0.1 metre would thereby reach a maximum width of 0.9 metre. At the slope this flow is expected to move sideways as indicated in the left part of Figure 3.3. Based on the water laboratory staff's experiences it was advised to use a basin width of 10 meter. This should be large enough to have negligible circulation effects in the measurement area.

3.4 Equipment

Based on experience in the past with measuring equipment in the water lab of the TU Delft, an Acoustic Doppler Velocimeter (ADV) was used. For an ADV, the main disadvantage is the need of non-water particles for a measurement, the so-called seeding. This seeding results in decreased visibility through the water. In a discharge flume, a constant inflow of seeding material would be needed, but in the closed basin for this scale model, the seeding material is circulating through the basin. Therefore, seeding material only needs to be stirred up before a series of tests starts and further on this is stirred up by the flow from the thruster. In the past, similar measurements were performed by using an (Electromagnetic Velocity Sensor) EMS, but this type of equipment has some disadvantages. Disadvantages of the EMS are discussed below. In addition, Laser Doppler equipment is used in experiments to perform similar tasks, but for safety considerations (shield off light), this is not used.

An electromagnetic velocity sensor (EMS) can be used to measure flow velocities. A disadvantage of this equipment is the large measuring probe (diameter around 3 cm). The measuring volume has a characteristic length of approximately 1 cm. This causes deviations, especially in case of measuring velocity fluctuations.

3.4.1 Acoustic Doppler Velocimeter (ADV)

The Acoustic Doppler Velocimeter (ADV) is a high-resolution acoustic instrument used to measure 3D water velocity. In the TU Delft's laboratory two ADV instruments are available from manufacturer Nortek. The used type ADV from this manufacturer is the 'Vectrino'. The probe emits an acoustic signal emitted and at a certain distance from the probe a sample volume is examined. The scattered and Doppler shifted signal is transformed into velocities in x-, y- and z-direction. This sample volume is a cylinder with a diameter of 6 mm and a selectable height of 3 to 15 mm.
The probe consists of a sound emitter at 10 MHz and four receiver beams, tilted 30º from the vertical in order to minimize the part near the surface that could not be measured. VERMAAS *et al.* [2011] did experiments in a flume with measurements varying from 0.045 m beneath the surface to 0.01 m above the bottom. According to VERMAAS *et al.* [2011], the error in time mean velocity and turbulent shear stress as measured by an ADV is very small (< 1%). VERMAAS *et al.* [2011] stated, that depth averaged flow velocities in the order of 0.3 m/s were present. In combination with other sources this gives confidence about performing measurements for flow velocities of this order of magnitude.

Figure 3.4: Detail of the ADV probe

Velocity data are recorded at 25 Hz. In research by VAN BLAADEREN [2006] and VERMAAS *et al.* [2011] measurements were done for respectively 6 and 3 minutes. VERMAAS *et al.* [2011] showed that the sampling error at this interval with 4500 samples is negligibly small. Hereby a recording time of at least 3 minutes at every position is used.

3.4.1.1 Doppler theory

The ADV uses the Doppler Effect to measure current velocities. The Doppler Effect is the change in pitch a listener hears when either the source or receiver of a sound is in motion. For example when one hears a siren, the pitch is higher when the vehicle is moving towards the listener and lowers when going away from the listener. This change in pitch tells the listener how fast the vehicle is moving.

The ADV transmits short pairs of sound pulses. The ADV listens to their echoes and measures the change in pitch of frequency of the returned sound.

The sound reflects from particles in the water. These particles are typically suspended sediment or seeding particles, which move with the same speed as the water. In this experiment, Chinese clay is used as seeding material. This material has a particle size of 2 to 3 microns. In Appendix F a detailed specification of this seeding material is included.

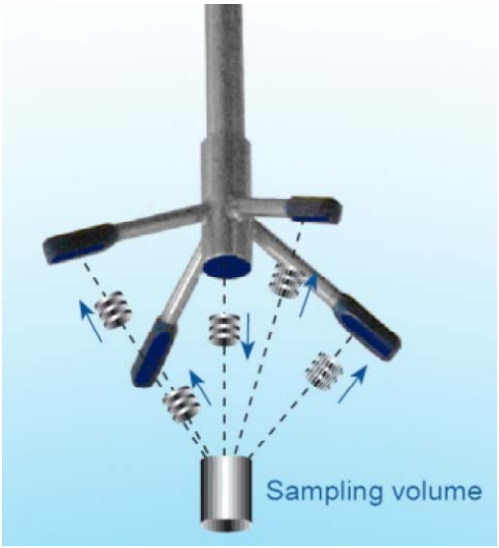

Figure 3.5: The ADV operating principle

3.4.1.2 Settings

For the measurements, the ADV can be adjusted to the velocity range that has to be measured. The nominal velocity can be varied between 0.03 m/s and 4.0 m/s. In Table 3.4 the velocity ranges are given for every configuration. As input, the nominal velocity is set:

Nominal velocity [m/s]	Maximum velocity [m/s]	
	x- and y- direction	z-direction
0.03	0.26	0.08
0.1	0.44	0.13
0.3	0.94	0.27
1.0	1.88	0.54
2.5	3.28	0.94
4.0	5.25	1.50

Table 3.4: ADV velocity ranges

In addition, the measurement volume of the instrument can be configured. The instrument has a measurement volume with a fixed diameter of 6 mm and an adjustable height. Of course, with a smaller measurement volume, the instrument needs more seeding and with a large measurement volume more details are averaged out. In practice, the settings have to be altered until acceptable signal strength is reached. In Table 3.5 the possible settings for the sampling volume are given.

Transmit length [mm]	Sampling volume height [mm]				
0.3	1.0	2.5	4.0	5.5	7.0
0.6	1.3	2.8	4.3	5.8	7.3
1.2	1.9	3.4	4.9	6.4	7.9
1.8	2.5	4.0	5.5	7.0	8.5
2.4	3.1	4.6	6.1	7.6	9.1

Table 3.5: ADV sampling volumes

During the tests, a transmit length of 1.2 mm with a sampling volume height of 3.4 mm turned out to provide the best results. In other words, this resulted in the lowest noise level for the measurements. For the nominal velocity, 4.0 m/s resulted in the lowest noise level. This combination of ADV settings is mainly used for the tests.

3.4.2 Processing data

Flow velocities and velocity fluctuations are needed in order to predict scouring. From some recent approaches to design bed protections it follows that velocity fluctuations are important as well. For example research by VAN VELDHOVEN [2002] and NIELSEN [2005] showed that it is required to measure the fluctuations in flow velocity accurately. The flow velocities were measured in x-, y-, and z-direction in order to reproduce the complete velocity field.

From the measured values, flow characteristics can be determined. The average flow velocity, standard deviation of the velocity, Reynolds stresses and kinetic turbulent energy can be determined as characteristics.

The average velocity is calculated using:

$$U_{m,i} = \overline{U_i} \qquad (3.5)$$

Where:

U_i	measured velocities in the i-direction	[m/s]
$U_{m,i}$	mean velocity in the i-direction	[m/s]

Standard deviation of the velocity (turbulence intensity) is determined by:

$$\sigma_{u,i} = \sqrt{\left(U_i - \overline{U_i}\right)^2} \tag{3.6}$$

From the measured velocities, Reynolds stresses can be determined as well. The Reynolds stresses give a value for the momentum exchange:

$$\tau_{ij} = -\rho_w \cdot \overline{U'_i \cdot U'_j} \tag{3.7}$$

Where:

τ_{ij}	turbulent shear stress in the ij-plane	[N/m^2]
ρ_w	density of the fluid	[kg/m^3]

Another turbulence characteristic is the kinetic turbulent energy, which is used in comparison with computational turbulence models. By calculating the contribution for every stress direction, the kinetic turbulent energy can be determined. As an alternative, used in combination with viscous turbulence models, a total value of the turbulent kinetic energy can be calculated regardless of the direction.

$$k_{ij} = \frac{1}{2} \cdot \overline{U'_i \cdot U'_j} \tag{3.8}$$

$$k_t = \frac{1}{2} \cdot \overline{U'^2_t} \tag{3.9}$$

Where:

k_{ij}	turbulent kinetic energy	[J/kg] = [m^2/s^2]
k_t	total turbulent kinetic energy	[J/kg] = [m^2/s^2]
U'_t	$= \sqrt{U'^2_i + U'^2_j + U'^2_k}$	[m/s]

3.5 Model bow thruster

A complete bow thruster tail piece is used for the model tests. It is manufactured by Vetus for pleasure crafts with a tunnel tube diameter of 110 mm, made by Vetus. Figure 3.6 shows this bow thruster. In the scale model the 12 Volt engine was replaced by another controllable electric motor. The standard type 12V motor cannot run for more than a few minutes due to the risk of burning out of the electrical circuit.

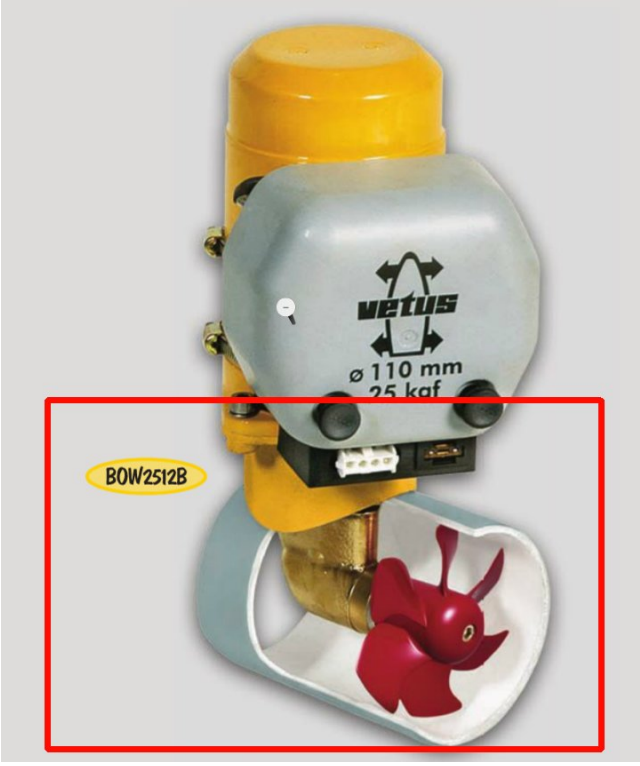

Figure 3.6: Vetus bow thruster type 2512B

This type of thruster has geometry comparable to the bow thrusters in sea-going vessels. It is a six-bladed Kaplan type propeller, unlike prototype thrusters that commonly have four blades. Propeller details such as the type and number of blades are discussed in Appendix A–1.

In the scale model, the thruster is controlled by the use of an engine with adjustable RPM. Based on contact with the thrusters' manufacturer, a thrust coefficient of 0.28 is used to calculate the efflux velocity. In prototype thrusters, efflux velocities of 8 m/s are present, which can be translated to 1.6 m/s for the scale model. According to equation (2.1), this results in a required rotation rate of 1021 rotations per minute. The used electrical engine (1.5 kW) has a maximum RPM of 1400 per minute at 50 Hz and thereby the frequency regulator is set to 36.46 Hz to decrease the RPM to the required 1021 rotations per minute.

$$1.60 \cdot 1021 / 60 \cdot 0.11 \cdot \sqrt{0.28} = 1.60 \text{ m/s}$$

3.6 Set-up of measurements

This paragraph contains the set-up for the scale model tests and considerations that have been made. The measuring program consists of ten scenarios. In these scenarios, several parameters are varied:
- Slope angle;
- Water depth;
- Slope or rough slope;
- Distance between thruster and slope;
- Slope with or without piles;
- Location of thruster axis parallel to the slope.

In the original plan before the measurements started, the *horizontal angle of the thruster axis with the slope* was defined as well as a parameter to vary. Because of the limited available time to perform the measurements this parameter (considered as less important than others) has been omitted.

Changing one parameter per scenario results in ten relevant scenarios. In Table 3.6 an overview of the ten scenarios is given, with an example plotted in Figure 3.7, where dimensions are provided in mm.

Figure 4.2 offers a visual plot of all scenarios.

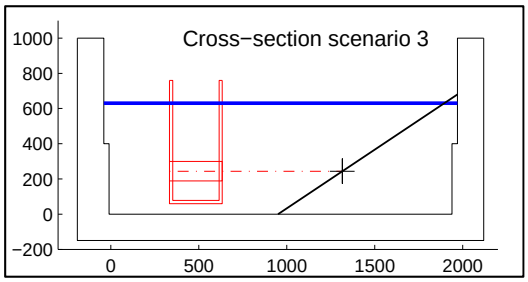

Figure 3.7: Example of model dimensions

Scenario	Slope	Depth	x/D_0	Cover	Pile alignment
S1	1:2.5	0.42 m	6.2	smooth	
S2	1:1.5	0.42 m	6.2	smooth	
S3	1:1.5	0.63 m	6.2	smooth	
S4	1:1.5	0.63 m	6.2	rough	
S5	1:1.5	0.63 m	4	rough	
S6	1:1.5	0.63 m	6.2	smooth	axis at piles
S7	1:1.5	0.63 m	6.2	smooth	axis mid between piles
S8	1:1.5	0.63 m	6.2	rough	axis mid between piles
S9	1:1.5	0.63 m	6.2	rough	axis quart between piles
S10	1:1.5	0.63 m	6.2	rough	axis at piles

Table 3.6: Scenario settings

3.6.1 Measuring points

Tests by VERMAAS *et al.* [2011] show that velocity measurements with the ADV are possible from 0.045 m beneath the surface to 0.01 m above the bed level. This range is taken as a boundary condition for the measurements.

The measurements consisted of:
- Location and value of efflux velocity;
- Decay of efflux velocity;
- Representing locations just above the bed.

Locations of the measurements are presented in chapter 4 with the results of the measurements. Beforehand important locations to measure were determined. During the tests insight was gained into distribution of flow velocities and measuring locations were optimised.

3.6.2 Properties of rough bed

Seven out of ten scenarios were performed with a rough bed protection of stones, which simulates a prototype bed protection of armour stone. In prototype, these stones can be placed as individual stones at the bed. Another commonly applied solution is a penetrated bed layer with asphalt to increase the strength of the armour layer.
In the scale model, a bed protection layer is simulated without this penetration. In order to measure the flow velocities above the bed and not measure damage to bed, the stones in the scale model were glued together. This forms a layer with comparable properties to an Elastocoast protection layer as applied on dikes. The difference is that instead of Elastocoast polyurethane a 2-component epoxy (paint) coating is used to glue the stones together. In a cement mixer, the stones are mixed together with a small amount of epoxy coating. In that way, a thin layer of coating is formed around all stones. When the stones are spread out on a wooden plate, within 24 hours all the stones are glued together at their contact surfaces. Hereby a bed protection is created with the properties of a loose bed protection, which cannot be easily damaged by the propeller jet in the scale model.

Figure 3.8: Impression of applied rough bed layer (thickness ≈ 5 cm)

Two students doing a minor project at the TU Delft did a research project with respect to the porosity and permeability of Elastocoast plates. In that project, similar tests of the bed protection with the Epoxy coating were performed. The results may be used in future research in order to give insight in the boundary conditions of this bow thruster current research.

A sample was tested with the following properties:
- Sample dimensions: 26 * 26 * 3.5 cm;
- Porosity: 0.548 (54.8 % pore volume);
- Permeability (K-factor) = 0.079.

This permeability K-factor is explained in paragraph 5.2 of SCHIERECK [2004].

3.6.3 Resulting scale model

Figure 3.9 gives an impression of the resulting scale model dimensions. A concrete basin of 2 metres by 10 metres is used. In this basin the model vessel has a keel clearance of 0.06 m and is positioned with the bow thruster in the centre of the basin (5 metres from both walls). In this particular scenario a slope of 1:1.5 is used with a rough bed protection. Furthermore piles are situated in the determining area for the propeller jet. Here a water depth of 0.63 metres is used. The outflow opening of the bow thruster is at a distance of 6.2 * D_0 from the slope.
More visual impressions with respect to the scale model are included in Appendix E to ensure the reproducibility of the performed tests.

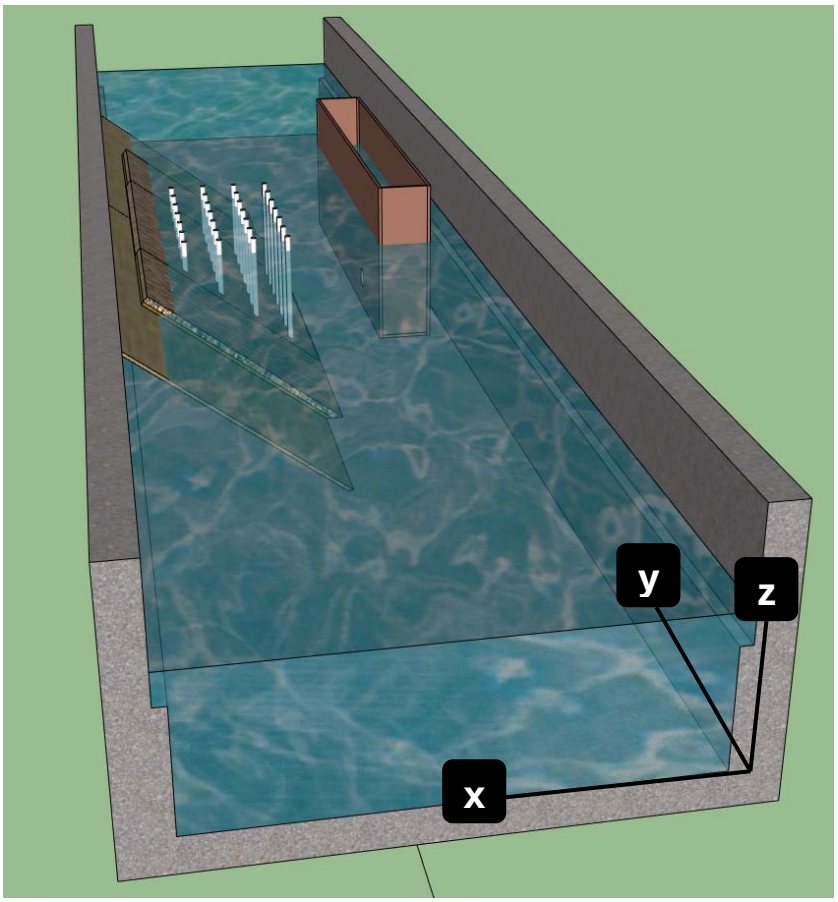

Figure 3.9: Impression of scenario 10, with a rough bed and piles

Five scenarios include a rough bed layer with a certain thickness. In these scenarios the thruster is positioned at equal distance to the slope, compared to smooth scenarios. This movement causes that the pile distance with respect to the outflow opening is different for smooth and rough scenarios with piles.

3.7 Sources of errors

In the scale model tests, errors may be included. Some errors can be caused by the layout of the scale model and errors are included in the measurements. Here some sources of errors are discussed in combination with the measures that have been taken to minimize possible errors.

3.7.1 Scale model layout

In paragraph 3.3.1 certain circulation flow in the basin is discussed. By using a basin with dimensions sufficiently large to exclude main circulation from the measurement area, errors are minimised. Furthermore, the scale model vessel has a simplified layout compared to prototype vessels. The keel clearance and thruster distance from the bow are considered to have significant influence on the measurements. Based on literature reviews, the length of the total vessel, hull shape and width are assumed to have a negligible influence on the required measurements.

The bow thruster in the scale model has dimensions similar to prototype bow thrusters. In combination with the preferred propeller type, this is considered to have only a small error. A possible error source could be the shape of the tunnel openings. Prototype vessels commonly have sharp edges removed. In the scale model the thruster tunnel had sharp edges.

In addition to the considerations above, the inclining slope with rough bed protection is not perfectly. A certain roughness and permeability is introduced by using stones glued together. The use of this epoxy coating results in stones with a smooth layer of coating and smaller pore volumes. No mayor influence is expected, due to the relatively small volume of coating that is added. The permeability is also discussed in paragraph 3.6.2.
The length of the inclining slope (5 m) is not equal to the length of the basin (10 m). Based on the laboratory staff's experience, a slope length of 5 metre was considered enough. Hereby disturbances resulting from the slope length are assumed to be negligible.

3.7.2 Measurements

Measurements will always include errors; the question is how large they are. Hereby possible error sources are defined.
Misalignment of the ADV results in an error in the registration of locations. This error is considered to be around 1 or 2 mm. In addition, the ADV has limited accuracy for velocity measurements. As mentioned in paragraph 3.4.1, this error is expected to be smaller than 1 %.

Appendix G.5 contains an ADV checklist, based on experience from the performed scale model tests. Using this checklist in future tests, should give results that are more accurate and less time needed to gain experience in working with an ADV.

Appendix J.2.1 provides insight in the assessment of measurement signal and data.

4 Results of model tests

From the scale model tests a lot of data were retrieved. In ten different scenarios over 2200 points were measured at a sampling frequency of 25 Hz by the ADV and with a sample time of a few minutes per point, which results in a dataset with approximately 10 million samples.

All original data files are saved and Matlab scripts to analyze the data can be found with the data. Appendix J describes the details on this.

The results of the measurements can be divided into four groups:

- Flow velocities and turbulence intensities just behind the thruster;
- Vertical distribution of flow velocity;
- Average flow velocities just above the bed material on the inclining slope;
- Turbulence intensities just above the bed material on the inclining slope.

How to read the figures

The figures in this chapter show various plots from the measurements.

- Blue vectors represent time averaged flow velocities;
- Red vectors represent turbulence intensities;
- A continuous green line gives the velocity profile according to the 'Dutch method' in the subplots below and right from the main vector plot;
- Dashed lines indicated with A' and B' present the locations of the values in the subplots;
- Green continuous lines in the main vector plot give the locations of the (maximum) flow velocities according to the 'Dutch method', as plotted in the subplots;
- Within the subplots, average flow velocities are plotted with a bullet (•) and turbulence intensities are represented by a plus (+) sign;
- In the main vector plot, the location of the bow thruster is indicated and called 'thrust', with the exact locations of the thruster in the left corner;
- In the right sub corner of the total figures the three largest vectors are indicated by their value and location in x- and y-direction.

Figure 4.1 shows the used coordinate system, where x is thereby the direction of the outflow from the bow thruster. In Figure 3.9 the coordinate system is plotted within the scale model impression.

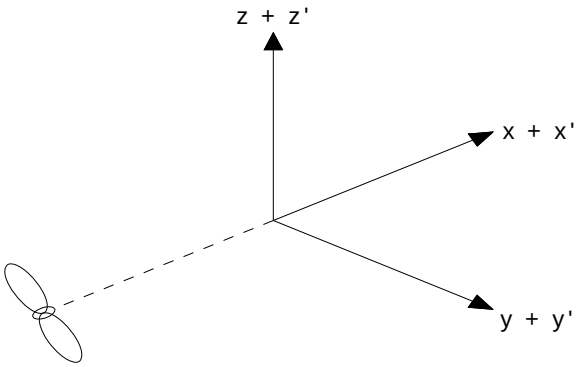

Figure 4.1: Used coordinate system, see also Figure 3.9

In the figures below, cross-sections of the ten different scenarios are schematically plotted. Variables are respectively the slope angle, water level, smooth or rough slope, distance to the slope and with or without piles. Scenario 6 and 7 have equal cross-sections, but here the ship is shifted in the lateral direction. In addition, scenario 8, 9 and 10 have equal cross-sections for the same reason. A shift in the lateral direction means a shift parallel to the slope.

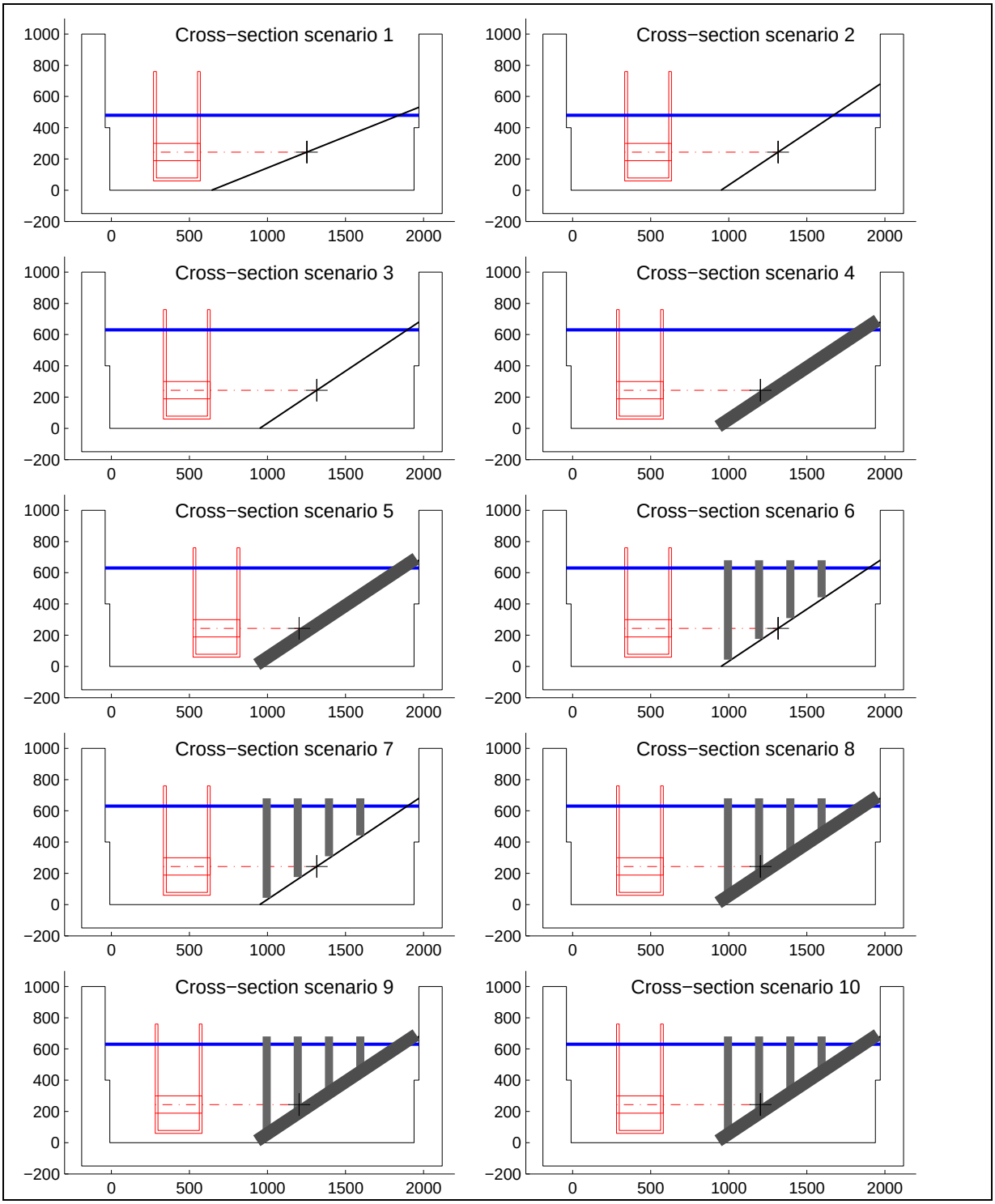

Figure 4.2: Schematic scenario cross-sections

- Distance between outflow opening and toe = [72 316 316 316 74 316 316 316 316 316] mm;
- X-coordinate of axis intersection with slope = [1242 1306 1306 1210 1210 1306 1306 1210 1210 1210] mm;
- In case of a rough slope, piles are located at larger distance from the toe;

4.1 Outflow velocity

In Figure 4.3 (left) the measured flow velocities behind the propeller are projected. These velocities are measured in a horizontal plane behind the outflow opening. At a distance of 1, 2, 3 and 4 times the propeller diameter the velocity profile is measured. As expected this figure shows the largest flow velocities at a short distance behind the thruster, decreasing at a larger distance. The profile changes from an asymmetric profile with two peaks into a symmetric profile with one centred peak velocity.

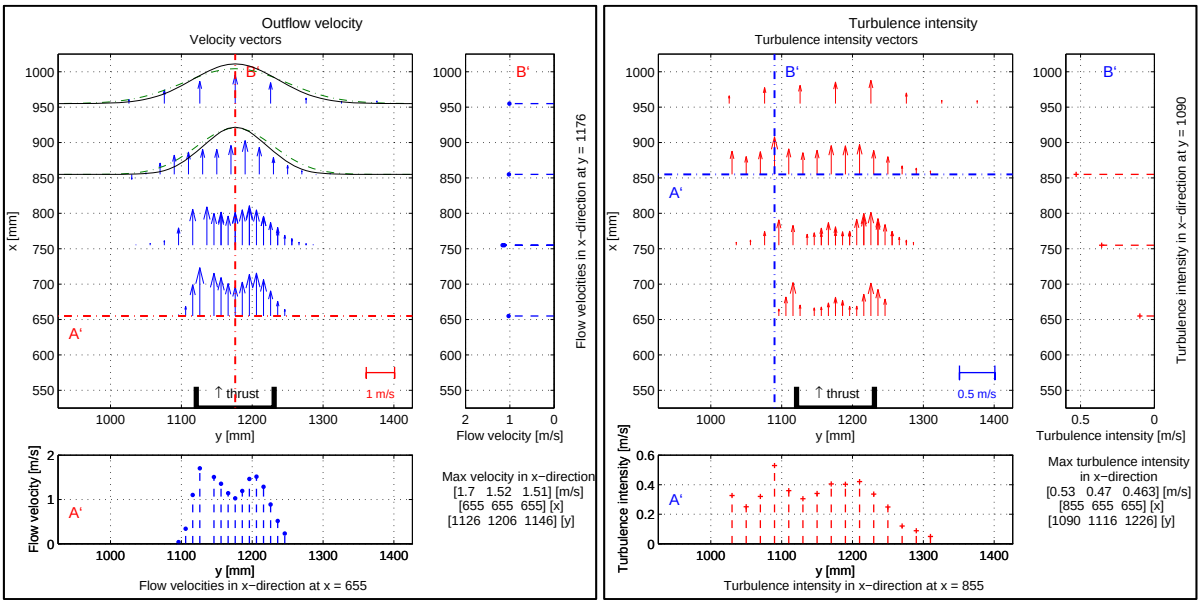

Figure 4.3: Measured flow velocities and turbulence intensity in horizontal plane behind propeller

Full-size printed figures can be found in Appendix G, Figure G-1 and Figure G-2.

The outflow velocity profile is not perfectly symmetrical. At x = 655 mm this profile has a larger peak at y = 1126 mm compared to the second peak at y = 1206 mm. This asymmetric profile is assumed to be caused by the propeller gearbox, which is mounted in the thruster tunnel. This can be seen in Figure 3.6 where the propeller gearbox is a bevel gear between the engine axis and the propeller axis.

In addition to the mean velocities, turbulence intensities are plotted. Figure 4.3 (right) shows the calculated turbulence intensities from the measurements. Turbulence intensities are in the order of 0.4 m/s within the jet. Just behind the outflow opening (at x = 655 mm, which is 100 mm behind the outflow opening) a high turbulence intensity can be observed at the edges of the jet. Furthermore, higher turbulence intensity occurs at the jet axis, caused by the propeller shaft.

4.2 Vertical distribution of flow velocity

Figure 4.4 shows the measured flow velocities in x-direction (propeller axis direction). This reaches from 10 mm above the bottom, up to 50 mm below the surface. This vertical distribution of the flow velocities is measured in scenario 3 at x = 1300 mm and y = 2300 mm. This location also covers the jet axis, which is located at y = 2300 mm. Over the lower 30 mm, the average flow velocities are more or less equal. This also holds for the measured turbulence intensities.

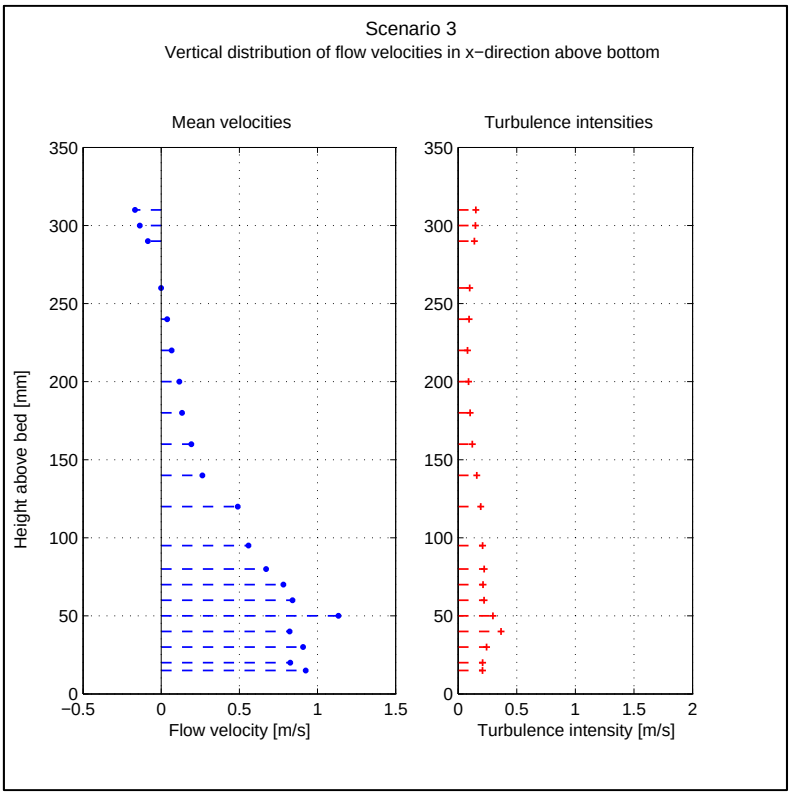

Figure 4.4: Vertical distribution of flow velocities

For a full-size view the reader is referred to Appendix G, Figure G-3.

Used data in Figure 4.4 were measured in scenario 3, at the location indicated by the green line.

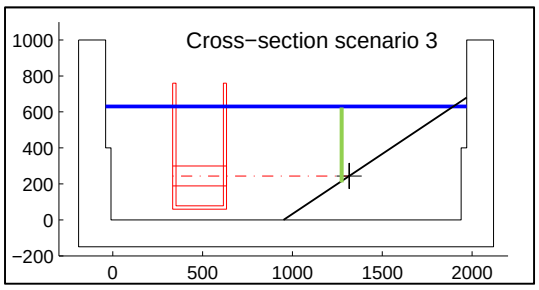

4.3 Near-bed flow velocity and turbulence intensity

In this paragraph, the measured near-bed velocities are included. In all ten scenarios, the near-bed velocities are measured, but the number of measuring points varies. In addition, the locations of the measuring points are not the same for the ten different scenarios. During the two months of measurements, insight was gained into the flow distribution over the bed. Therefore in the first scenario relatively more 'useless' points are measured compared to scenario 10. Of course, the results of the first scenarios are not useless, only a less dense grid is measured at normative locations at the bed.
Flow velocities in this paragraph are plotted in direction parallel to the slope. Coordinates in x- and y-direction are given according to Figure 3.9.

4.3.1 Scenario 1

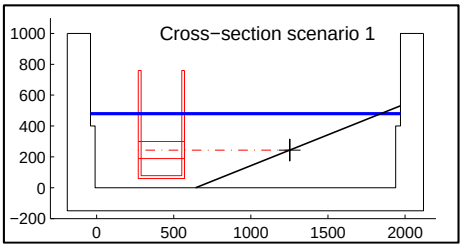

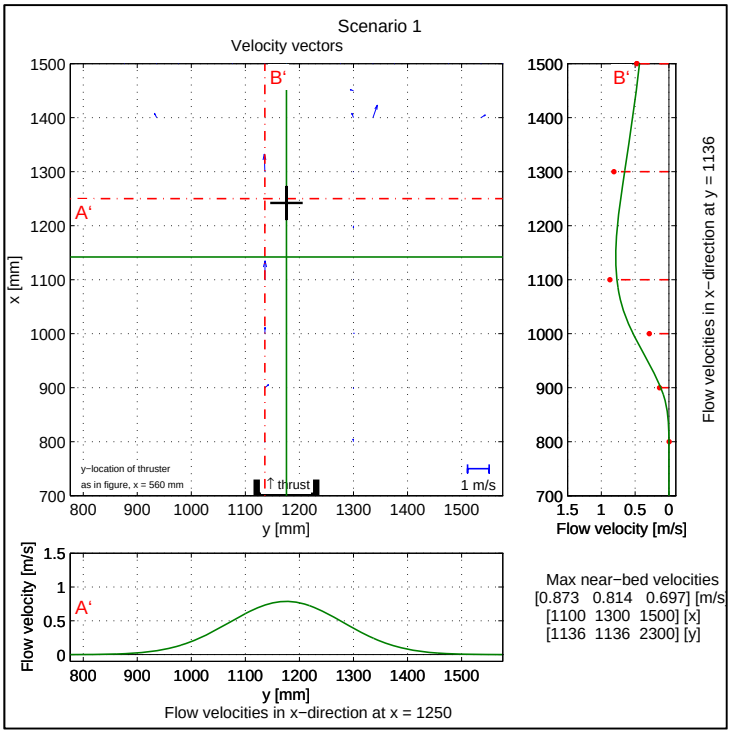

Figure 4.5: Near-bed flow velocity, scenario 1

Within scenario 1, the flow velocities are not measured exactly at the bed in line with the propeller axis. Measurements were done at y = 1136 instead of the jet axis at y = 1176. This misalignment was discovered after measurements in scenario 1 were completed and the scale model was prepared for scenario 3. Since the acquired results were satisfactory for comparison with existing theories and executed research, no extra measurements were done for scenario 1. The measurements show a small underestimation by the existing method to determine the flow velocities near the bed. Furthermore, the velocity profile according to the 'Dutch method' estimates the maximum flow velocities to occur at a larger x-distance compared to the measurements. Measured maximum flow velocities for scenario 1 are around 0.87 m/s, which can be observed in Figure 4.5.

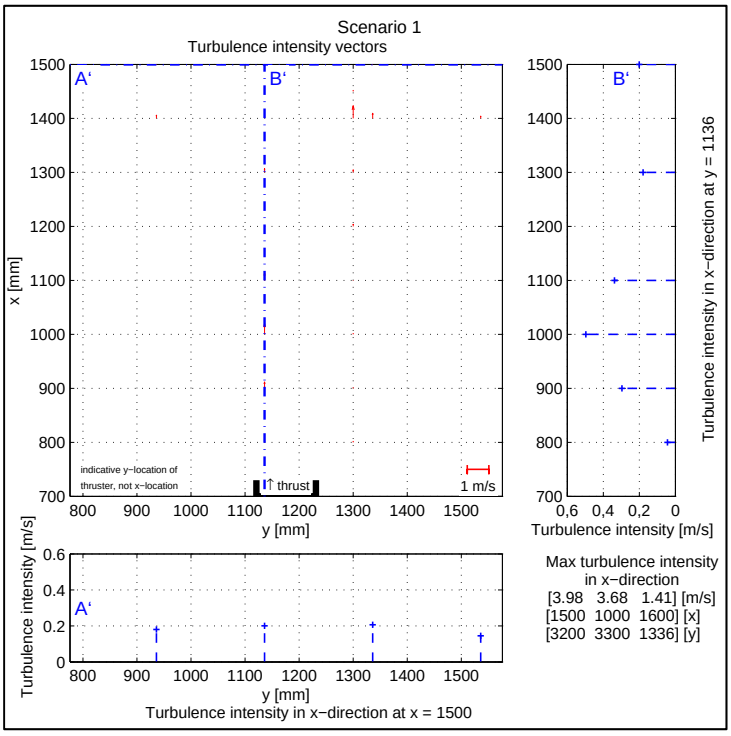

Figure 4.6: Near-bed turbulence intensity, scenario 1

Turbulence intensities near the bed are plotted beside this text, in Figure 4.6. Some large values in the order of 1 m/s can be observed, which are measuring inaccuracies. Turbulence intensities are around 0.4 or 0.45 m/s at the location x = 1000 mm, where the jet boundary 'hits' the slope. Besides this location, overall turbulence intensities are all around 0.2 m/s.

Full-size figures are included in Appendix G, respectively Figure G-4 and Figure G-14.

4.3.2 Scenario 2

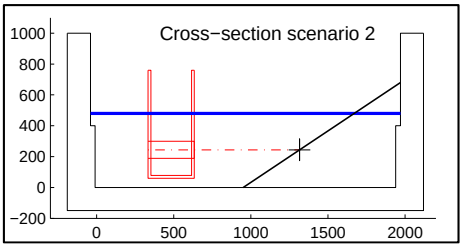

In scenario 1, the slope angle was 1:2.5, which changes to 1:1.5 for scenario 2 until 10. The distance between the outflow opening and the intersection of the jet axis with the slope is kept equal to scenario 1 and the water level is equal to scenario 1. As a result, the average flow velocities are smaller. The maximum observed flow velocity is 0.8 m/s for scenario 2, which was 0.87 for scenario 1.

For scenario 2, more measuring points are used, in order to improve the flow pattern. Measurements for the locations with an x-value smaller than 1300 could unfortunately not be used, because of the large amount of noise in these measurements. Maximum flow velocities seem to be underestimated by the existing calculation method, as visible for scenario 1. Later on we will see this recurring for all scenarios.

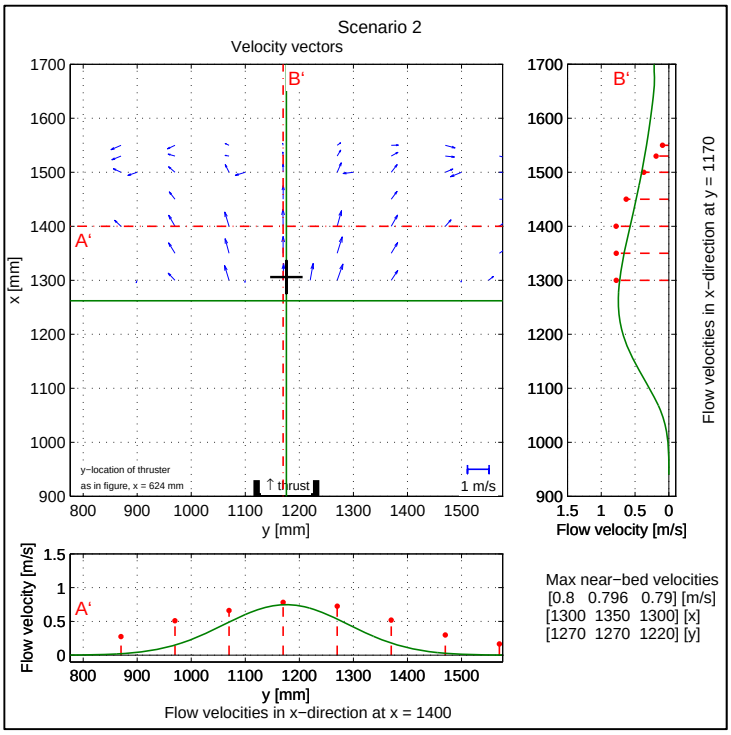

Figure 4.7: Near-bed flow velocity, scenario 2

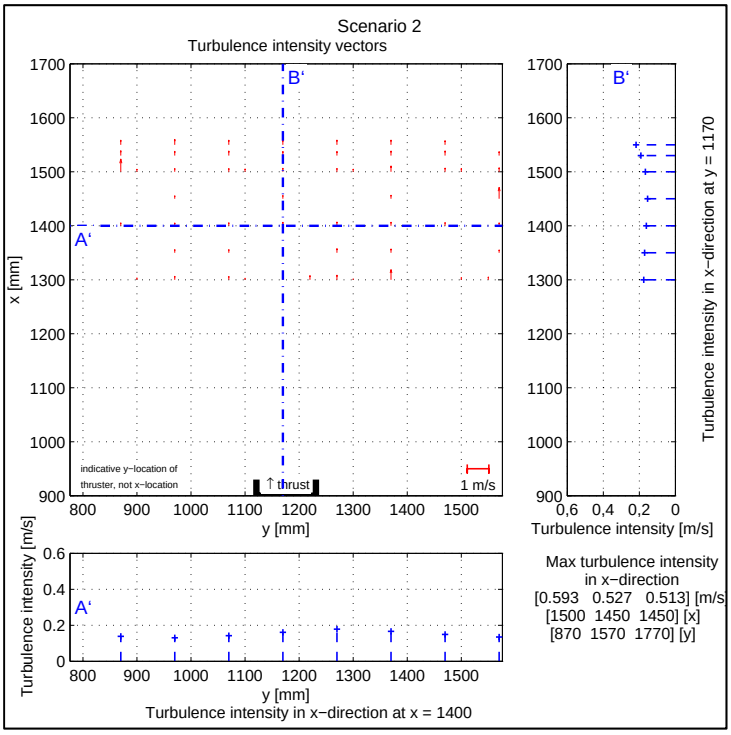

Figure 4.8: Near-bed turbulence intensity, scenario 2

For scenario 2 the turbulence intensities are in the order of 0.2 m/s. This corresponds to the observed 0.2 m/s for scenario 1. A closer view shows the turbulence intensities to be a factor 0.9 smaller in scenario 2, compared to scenario 1.

Full-size figures are respectively included in Appendix G, Figure G-5 and Figure G-15.

4.3.3 Scenario 3

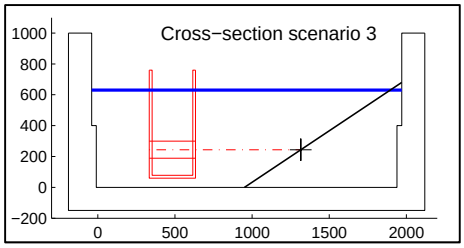

After a change in the slope angle, in scenario 3 the water level is increased from 0.48 m to 0.63 m.
As a result, the maximum flow velocities are 0.89 m/s in and around the jet axis.
For scenario 3, measuring points at locations closer to the thruster outflow opening are used. These measurements show that the theoretical velocity profile predicts the maximum flow velocities to occur at a larger distance from the outflow opening than measured. This was stated earlier at the results for scenario 1. The shift in x-direction of the theoretical profile compared to the measurements seems to be larger for scenario 3 than for scenario 1. This could be caused by the change in slope angle, water level or a combination of these two.

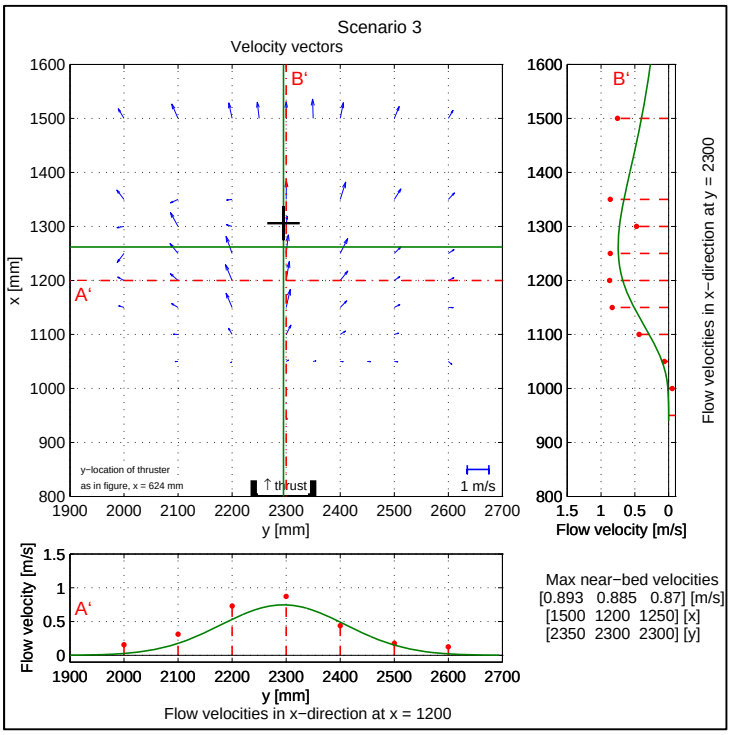

Figure 4.9: Near-bed flow velocity, scenario 3

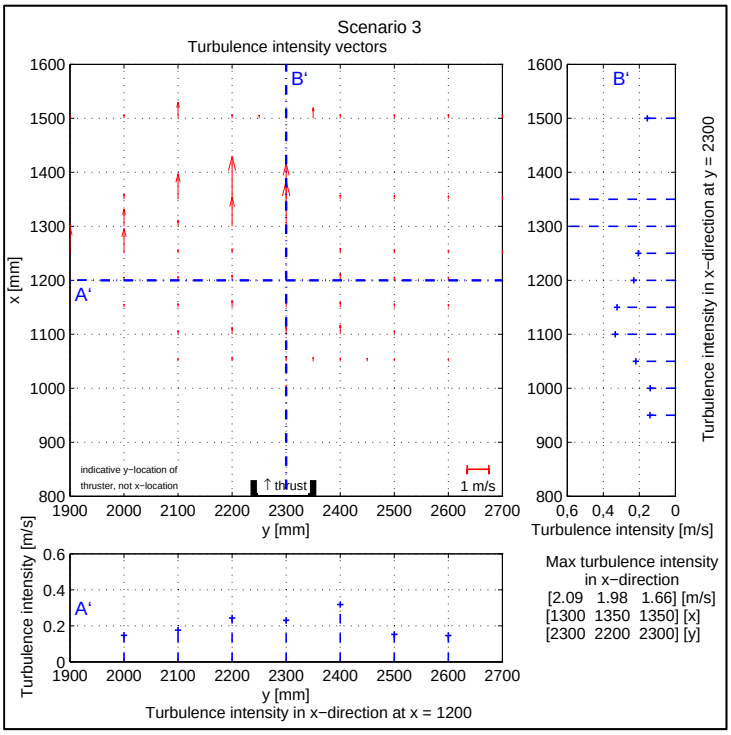

Figure 4.10: Near-bed turbulence intensity, scenario 3

Observed turbulence intensities are around 0.2 m/s, with a peak to 0.37 m/s in line with the jet axis.

Full-size figures are included in Appendix G, respectively Figure G-6 and Figure G-16.

4.3.4 Scenario 4

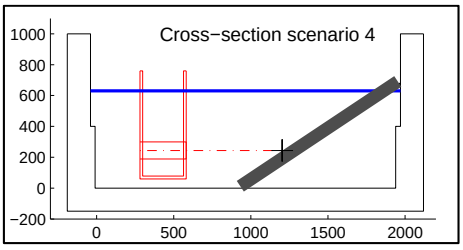

A rough slope is added for scenario 4, with properties as described in chapter 3. Maximum flow velocities of 0.94 m/s are the result. The highest three flow velocities are situated within the jet axis, between x = 1050 mm and x = 1150 mm.
Subplot B' in Figure 4.11 shows a fast increase in the measured flow velocities in the jet axis from x = 900 to x = 1000.

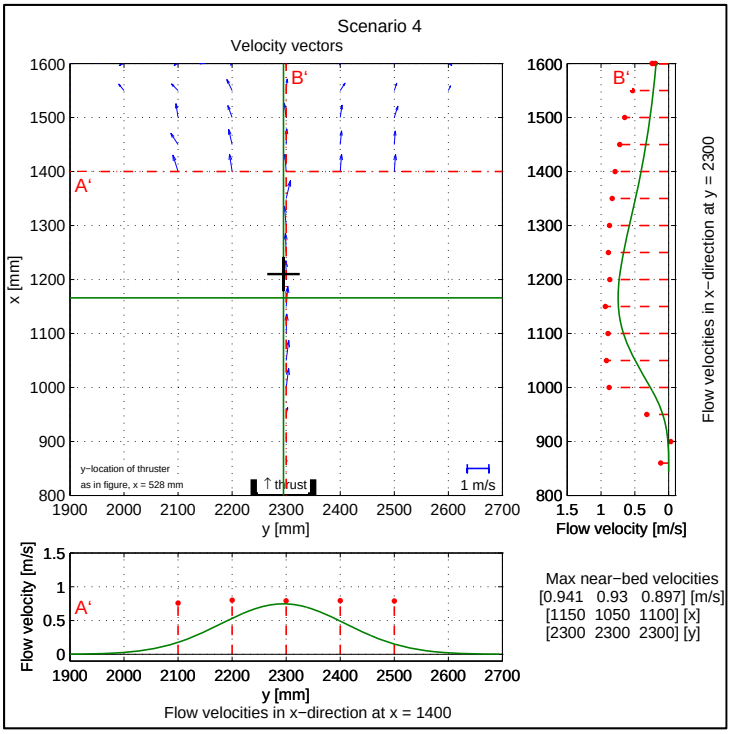

Figure 4.11: Near-bed flow velocity, scenario 4

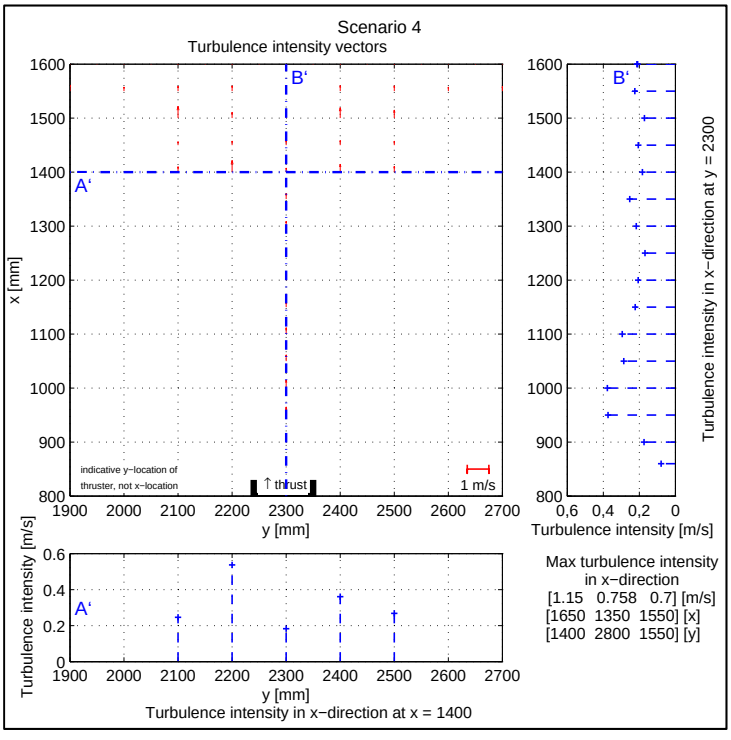

Figure 4.12: Near-bed turbulence intensity, scenario 4

Turbulence intensities show within the jet axis a fast increase from x = 850 mm to x = 950 mm. This is approximately 50 mm closer to the thruster outflow. In general, turbulence intensities seem to be larger than the 0.2 m/s as measured in scenario 1 to 3. Influence by the rough bed could cause these higher turbulence intensities.

The observed spike in turbulence intensity at y = 2200 mm can be explained due to the relatively high noise level in this single measurement. In the analysis of the plots, this extreme value is excluded.

Full-size figures are included in Appendix G, respectively Figure G-7 and Figure G-17.

4.3.5 Scenario 5

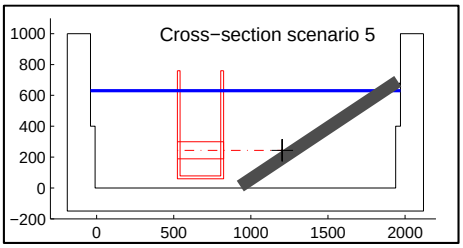

Scenario 5 shows the result of a smaller distance of the outflow opening to the slope. The outflow opening is positioned at a distance of 440 mm to the slope-intersection instead of the 'standard' 682 mm for the other scenarios.
Maximum flow velocities of 1.35 m/s occur. The velocity profile A' in y-direction is narrow compared to scenario 4. This is caused by the short length for the jet to expand in y- and z-direction.

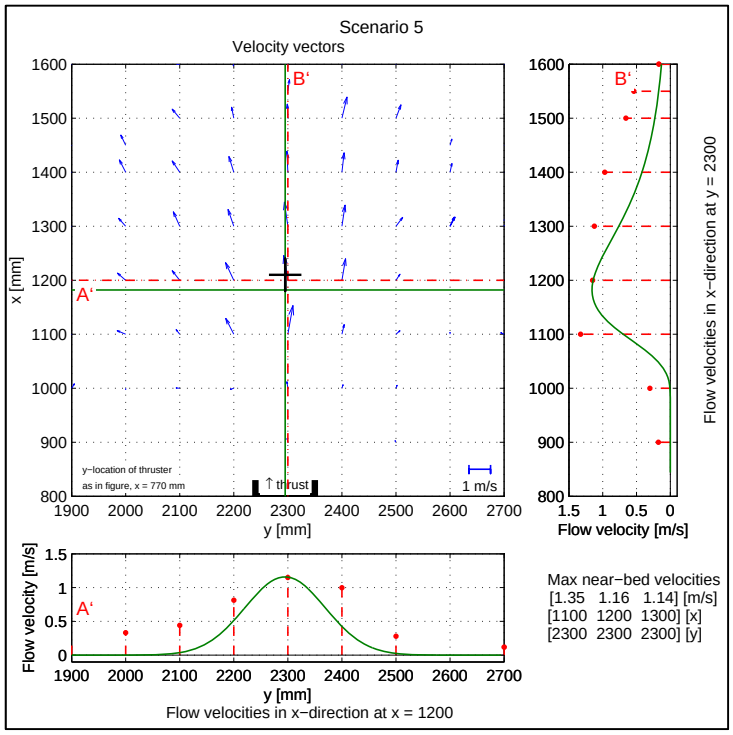

Figure 4.13: Near-bed flow velocity, scenario 5

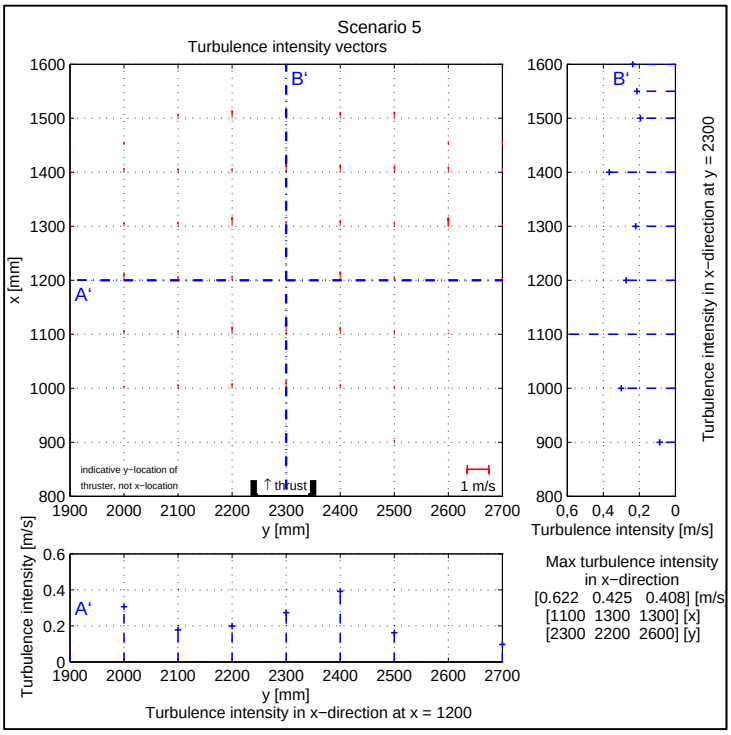

Figure 4.14: Near-bed turbulence intensity, scenario 5

Turbulence intensities for scenario 5 show a peak of 0.62 at x = 1100 mm. This peak is where the edge of the jet intersects with the slope. Because of the short distance between outflow opening and slope, turbulence intensities and flow velocities are higher compared to scenario 4.

Full-size figures are included in Appendix G, respectively Figure G-8 and Figure G-18.

4.3.6 Scenario 6

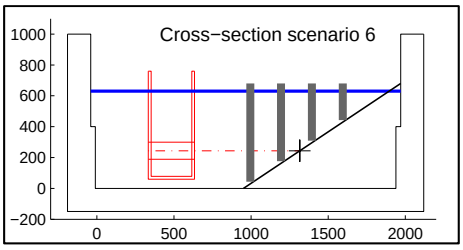

Scenario 6 is the first scenario with piles mounted on the inclining slope. Other model dimensions are equal to scenario 3, with a smooth bed. As Figure 4.15 shows, flow velocities are low around piles and show their maximum values between two rows of piles. Peaks of 1.05 m/s are measured at x = 1255 mm at locations (y = 2250 and 2340 mm) just around the middle row of piles.

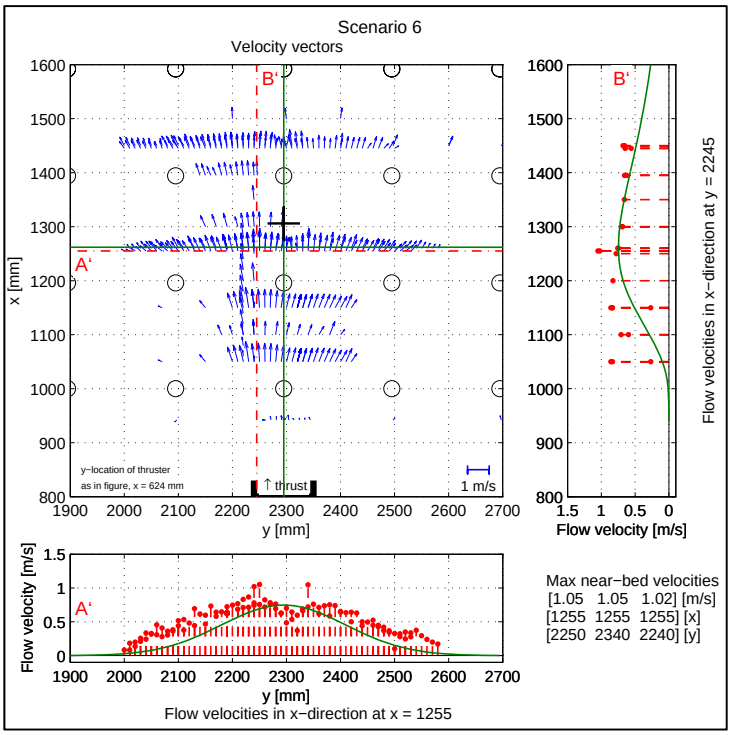

Figure 4.15: Near-bed flow velocity, scenario 6

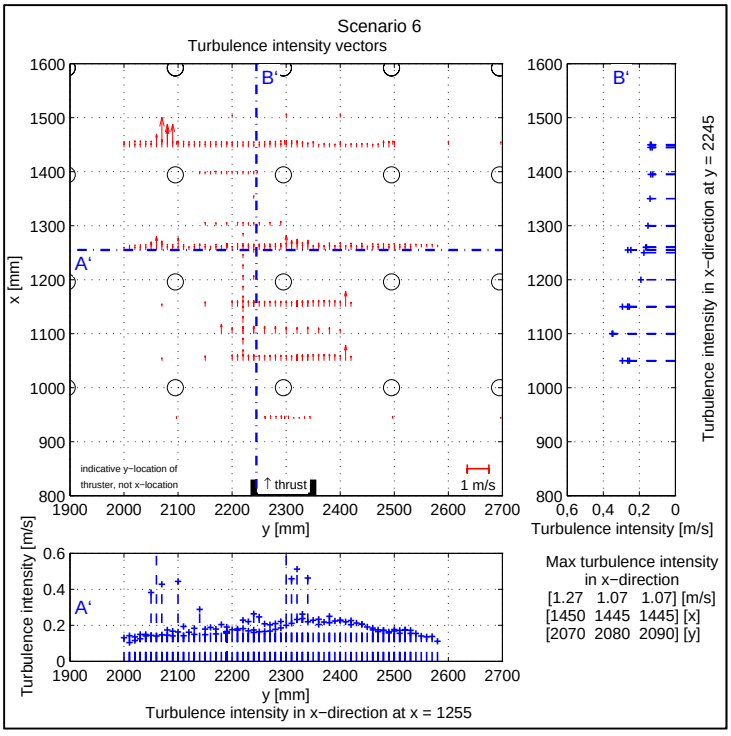

Figure 4.16: Near-bed turbulence intensity, scenario 6

Turbulence intensities show peaks at locations near piles. Globally the vector field shows values around 0.2 m/s.

Full-size figures are included in Appendix G, respectively Figure G-9 and Figure G-19.

4.3.7 Scenario 7

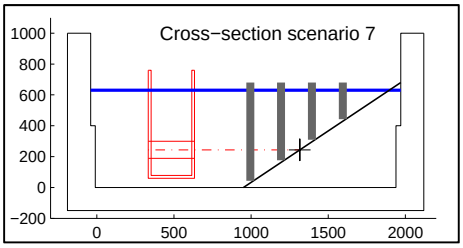

At scenario 7 the vessel and thereby the outflow opening is shifted 100 mm in negative y-direction. As a result, the jet flow is centred between two rows of piles. In scenario 6 the jet was directed right at one row of piles. As a result, the measured flow velocities are shown in the lower plot of Figure 4.17. Compared to scenario 6 the flow velocities exceed the theoretical line less, with maximum values of 0.96 m/s at this location. The flow field looks more as in scenario 3 (without piles).

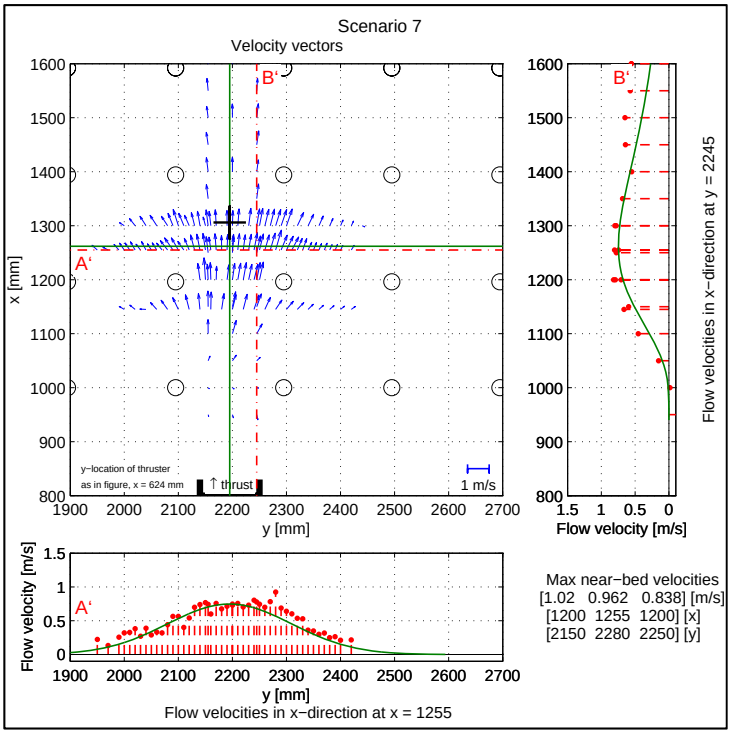

Figure 4.17: Near-bed flow velocity, scenario 7

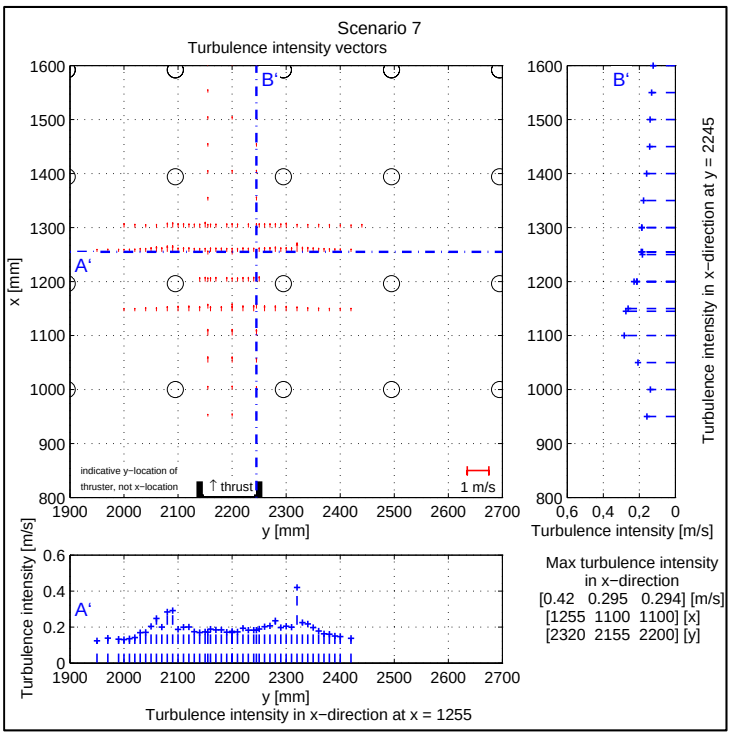

Figure 4.18: Near-bed turbulence intensity, scenario 7

A peak for the turbulence intensities can be found around x = 1100 mm. Except for this peak other peaks are found around pile locations. For other locations, turbulence intensities are in the order of 0.2 m/s.

Full-size figures are included in Appendix G, respectively Figure G-10 and Figure G-20.

4.3.8 Scenario 8

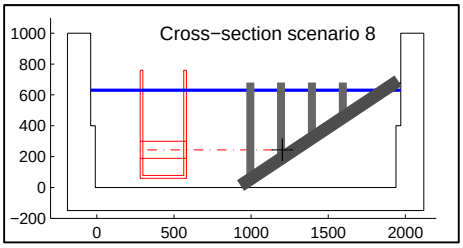

A rough slope is added in scenario 8. Thereby this scenario can be compared to scenario 4 (rough slope without piles) and scenario 7 (smooth slope with piles). In fact scenario 8 is a combination of scenario 4 and 7. Maximum flow velocities at x = 1255 mm are around 1.0 m/s and higher than for scenario 7. A peak of 1.22 m/s is observed in the line x = 1200. This combination of scenario 4 and 7 shows higher flow velocities than for the separate scenarios 4 or 7.

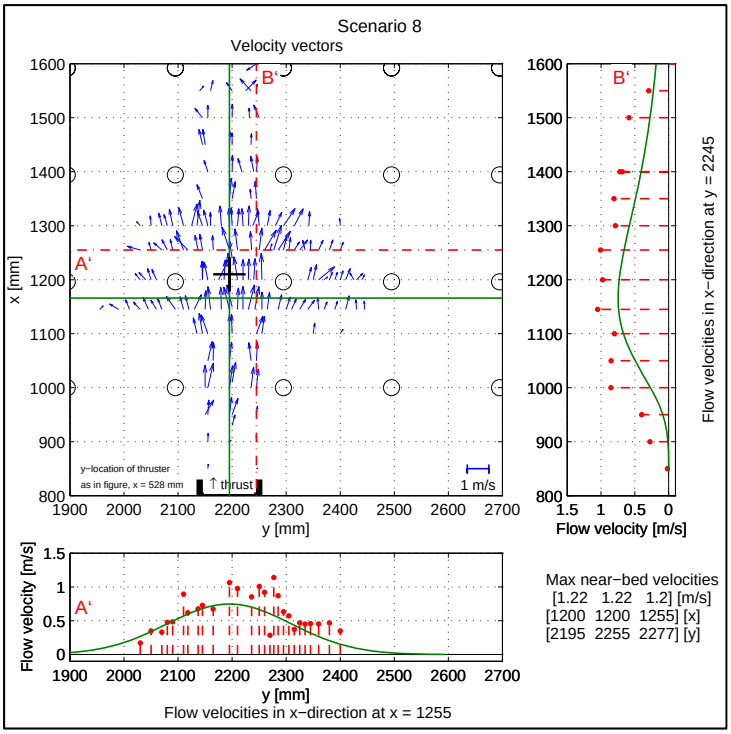

Figure 4.19: Near-bed flow velocity, scenario 8

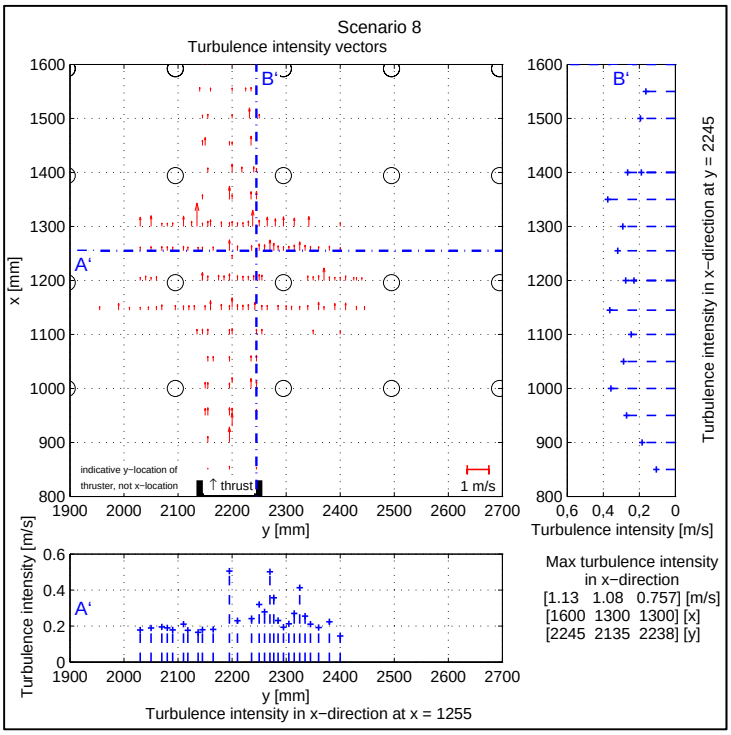

Figure 4.20: Near-bed turbulence intensity, scenario 8

For scenario 8, turbulence intensities higher than 0.2 m/s occur regularly. As an example, the right plot in Figure 4.20 shows quite a lot of variation in the measured turbulence intensities. In this subplot, values vary from 0.2 m/s to 0.4 m/s.

In this single scenario a relatively small amount of seeding material was used, causing an increased noise level in the measurements. This explains the larger variations in turbulence intensities, compared to other scenarios.

Full-size figures are included in Appendix G, respectively Figure G-11 and Figure G-21.

4.3.9 Scenario 9

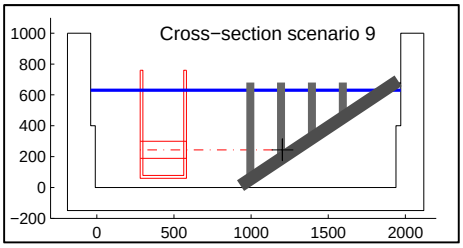

Comparable to scenario 6 and 7, in scenario 9 and 10, the vessel is shifted in y-direction. Scenario 9 shows an outflow opening shifted +50 mm compared to scenario 8.

Measurements show the flow field to be changed, with maximum flow velocities measured at x = 1000 mm. The right subplot in Figure 4.21 shows an interesting change, compared to the same subplot for scenario 8.

Flow velocities for the lower subplot show to be a little bit lower compared to scenario 8.

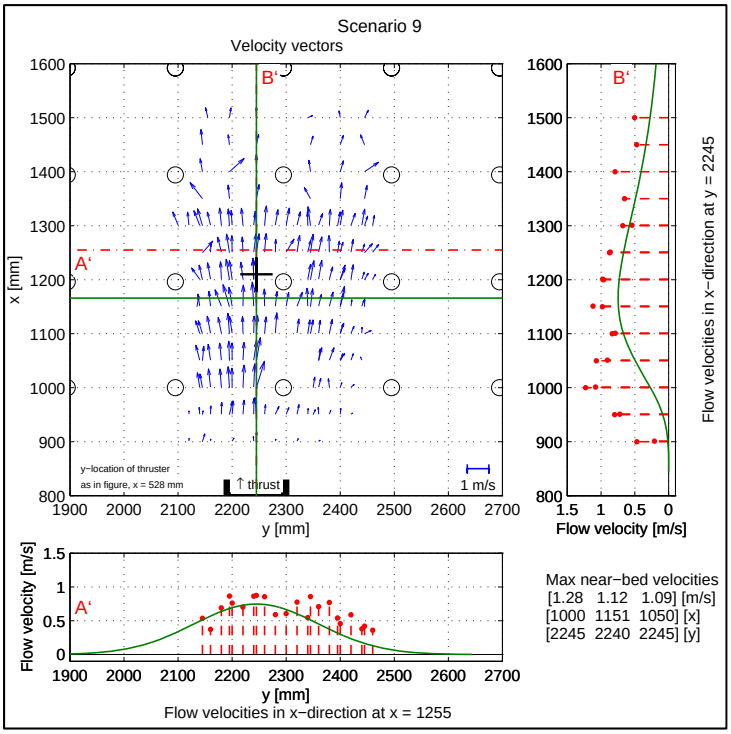

Figure 4.21: Near-bed flow velocity, scenario 9

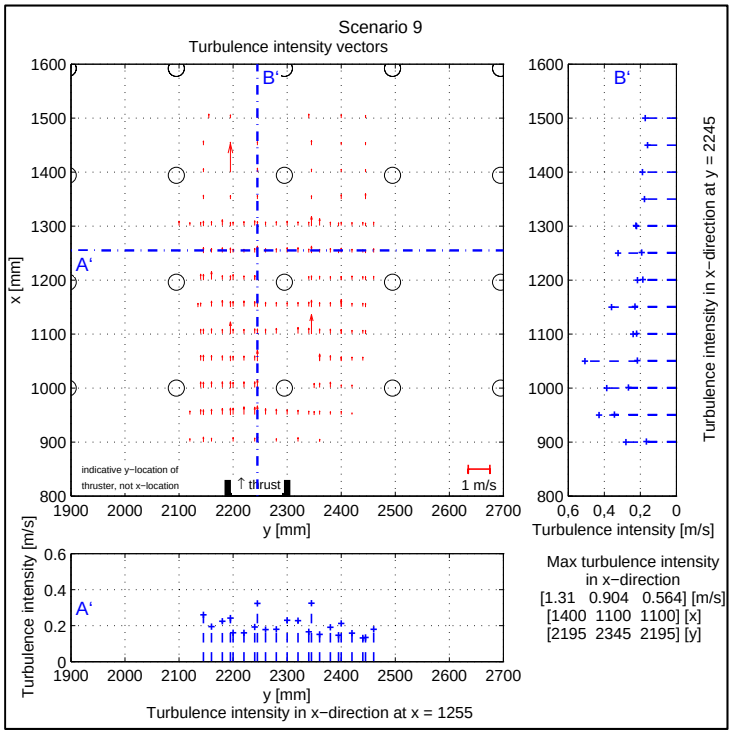

Figure 4.22: Near-bed turbulence intensity, scenario 9

For scenario 9 high turbulence intensities are in the zone of x = 900 to 1255 mm. Here values of 0.4 m/s occur, with a peak of 0.46 m/s.

Full-size figures are included in Appendix G, respectively Figure G-12 and Figure G-22.

4.3.10 Scenario 10

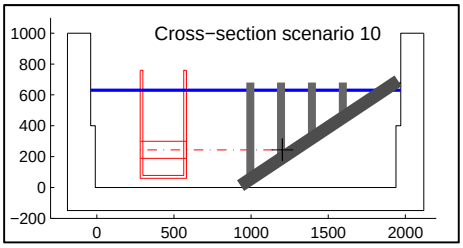

Average flow velocities for scenario 10 show a comparable flow field as for scenario 9. At scenario 10, the vessel is shifted another 50 mm in y-direction compared to scenario 9, which means 100 mm compared to scenario 8.
Flow velocities drop down at locations near piles and show their peak values for locations plus and minus 50 mm from the pile centre.

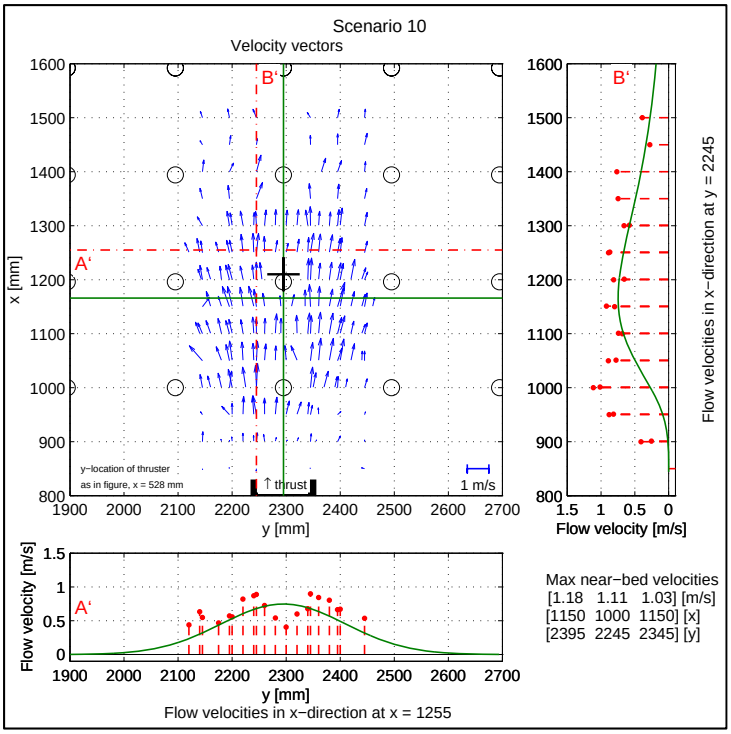

Figure 4.23: Near-bed flow velocity, scenario 10

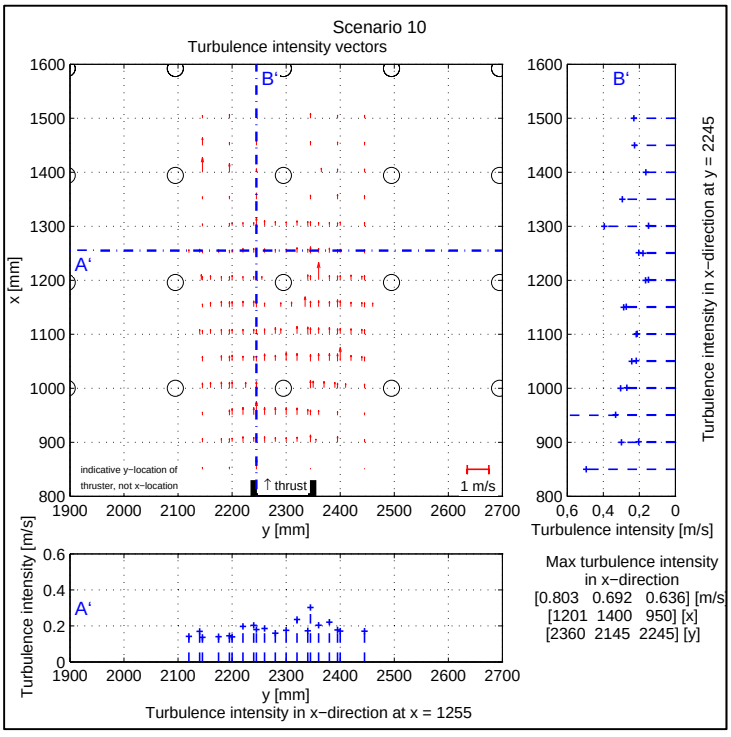

Figure 4.24: Near-bed turbulence intensity, scenario 10

The measured turbulence intensities have maximum values close to the outflow opening and some peaks around piles. Beside these locations, turbulence intensities are around 0.2 m/s.

Full-size figures are included in Appendix G, respectively Figure G-13 and Figure G-23.

5 Analysis

The results from chapter 4 are analysed in several parts. First, the measured outflow velocities are analysed followed by the near bed flow velocities and turbulence intensities. Then the results are compared to existing design methods to draw conclusions for the design of bed protections.

5.1 Outflow velocity

Equation (2.1) resulted in a theoretical outflow velocity of 1.60 m/s in the scale model tests. Results from the scale model tests show a deviation to this value.
Figure 5.1 gives an overview of the outflow velocity as discussed in paragraph 4.1. The outflow opening is located at x = 555 mm and the nearest measurements are located at x = 655 mm, because of the size of the measurement equipment.

In literature the outflow velocity from a water jet is analogous to the momentum flux as discussed in ALBERTSON *et al.* [1948]. However, equation (2.1) for propeller jets is based on propeller theories and not on water jets.
ALBERTSON *et al.* [1948] provides:

$$\frac{M}{M_0} = \frac{\int_0^\infty U_{x,r}^2 \, dA}{U_0^2 \cdot A_0} = 1 \qquad (5.1)$$

Which results at x = 655 mm in:

$$U_0 = \sqrt{\frac{\sum U_{x,r}^2 \cdot 2\pi \cdot r \cdot \Delta r}{1/4 \cdot \pi \cdot D_0^2}} \qquad (5.2)$$

$$U_0 = 1.52 \text{ m/s}$$

Remark: (5.1) only includes axial velocities and no tangential or radial velocities. Answer (5.2) shows that equation (5.1) provides comparable results as equation (2.1) and is thereby useful in propeller jets.

If an average value for the outflow velocity is determined as described in BLAAUW and VAN DE KAA [1978], this results in 1.33 m/s based on measurements. This average 'block profile' with 1.33 m/s is drawn as a constant line in the subplot of Figure 5.1.

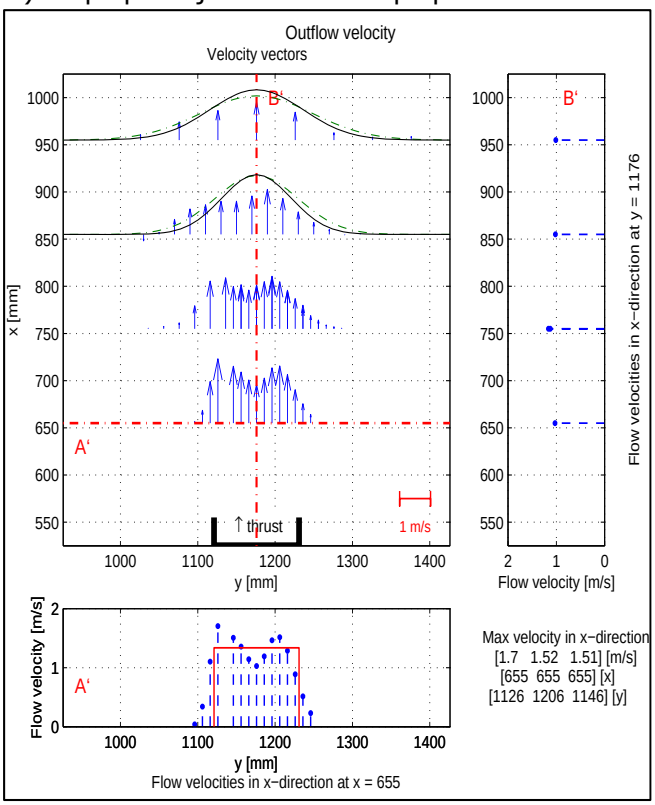

Figure 5.1: Validation of outflow velocity

If the outflow velocity according to equation (5.2) is used, this results in a reduced thrust coefficient of 0.26 instead of the assumed 0.28 for the scale model thruster, using equation (2.1):

$$1.60 \cdot 1021 / 60 \cdot 0.11 \cdot \sqrt{0.26} = 1.52 \text{ m/s}$$

This difference in thrust coefficient could be due to a rotational speed of 1021 RPM, instead of 3000 RPM for which the thrust coefficient 0.28 is provided by the manufacturer. However, the thrust coefficient of 0.26 only holds if (5.1) is valid for propeller jets. Future research could provide an improved method to validate the outflow velocity, instead of equation (5.1).
The green-dotted and black-continuous lines in the main plot of Figure 5.1 represent respectively the 'Dutch' and 'German' guidelines, using 1.52 m/s as input. Even with 1.52 m/s as an input, measurements deviate compared to the guidelines. In further analysis the outflow velocity according engineering guidelines (1.60 m/s) is used as reference to compare measurements with the existing guidelines.

5.1.1 Outflow velocity profile

The measured outflow velocities just behind the bow thruster are presented in paragraph 4.1. These measurements are in good agreement with existing guidelines. SCHOKKING [2002] performed tests with a non-ducted and a ducted propeller. Unfortunately SCHOKKING [2002] did not publish a plot with data for the ducted propeller, therefore, the non-ducted results are provided below.

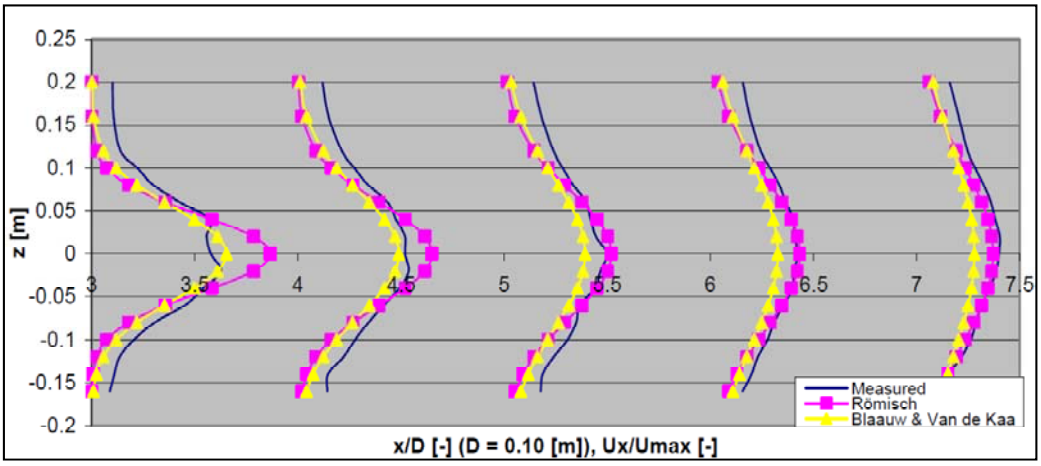

Figure 5.2: Axial velocity distribution for the non-ducted propeller jet by SCHOKKING [2002]

The results from the present scale model tests are comparable to the velocity profiles SCHOKKING [2002] measured for a non-ducted propeller jet. For both situations (see Figure 4.3), the influence of the propeller shaft has dissipated at a distance of 4 times the propeller diameter behind the outflow. Figure 5.1 shows values from measurements with a bow thruster. Figure 5.2, however, has measured values for a non-ducted jet as used by SCHOKKING [2002]. The measured velocity distribution at a distance of 3 to 4 times the propeller diameter in Figure 5.1 shows a better correlation with the method of BLAAUW and VAN DE KAA [1978] (green, dotted line) compared to RÖMISCH and HERING [2002] (black, continue line). Compared to HAMILL *et al.* [1996b], for example Figure B-14 is in agreement with the measurements. As the 'Dutch' method provides is in best agreement with the measurements, this method is further used in the analysis.

5.2 Oblique wall effect

Appendix B.3.1 provides a method to determine flow velocities near vertical quay walls, or walls under a small angle. According to equation (5.3), C_α is 19% for a slope 1:1.5, if we assume this equation to be valid for all slope angles. Measurements, however, are not in agreement with this value. Possibly equation (5.3) is strictly valid for slope angles up to 40 degrees (1:1.16) as provided in RÖMISCH [2001] and no slope angles smaller than 40 degrees, as suggested valid according to PIANC [2012].

$$C_\alpha = \frac{Q_{bottom,\alpha}}{Q_{bottom,\alpha=0°}} = \frac{1}{0.5} \cdot \left[\frac{90° - \alpha}{180°} - \frac{\sin 2(90° - \alpha)}{2 \cdot \pi} \right] \quad (5.3)$$

With:

C_α	jet-wall coefficient	[-]
$Q_{bottom,\alpha}$	discharge at inclining wall	[m^3/s]
$Q_{bottom,\alpha}$	discharge with vertical wall	[m^3/s]
α	slope angle	[°]

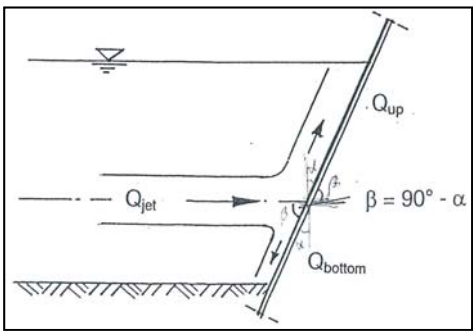

Figure 5.3: Jet impinging on a wall according to RÖMISCH [2001]

Based on the results in chapter 4 one would conclude that for a slope angle 1:2.5 and 1:1.5 the amount of flow directed to the bottom is negligible. Instead of a flow directed to the bottom, all scenarios result in a flow direction upward the slope. Based on these measurements, equation (5.3) is not valid for slopes 1:1.5 and 1:2.5.

5.3 Potentially oscillating vectors

The results as described in chapter 4 are discussed with time-averaged vectors. In reality, the flow direction at one single location is not constant. In the design method for a bed protection, the influence of the slope angle and angle of internal friction for stones are included.
According to CIRIA *et al.* [2007], the influence of the slope angle is calculated by:

$$m_h = \frac{\tan(\varphi_s)}{\cos(\theta_u)\cdot\sin(\alpha)+\sqrt{\cos^2(\alpha)\cdot\tan^2(\varphi_s)-\sin^2(\theta_u)\cdot\sin^2(\alpha)}} \qquad (5.4)$$

Where:

m_h	slope coefficient	[-]
θ_u	angle of the velocity component (0 = upwards the slope)	[°]
α	slope angle	[°]
φ_s	angle of repose (for armour stone 40° - 42°)	[°]

This angle of the velocity component can be calculated from the measurements. Because of a certain turbulence intensity one would expect an oscillating angle of the flow direction. This can be visualized by plotting the samples of one measurement in a rose.

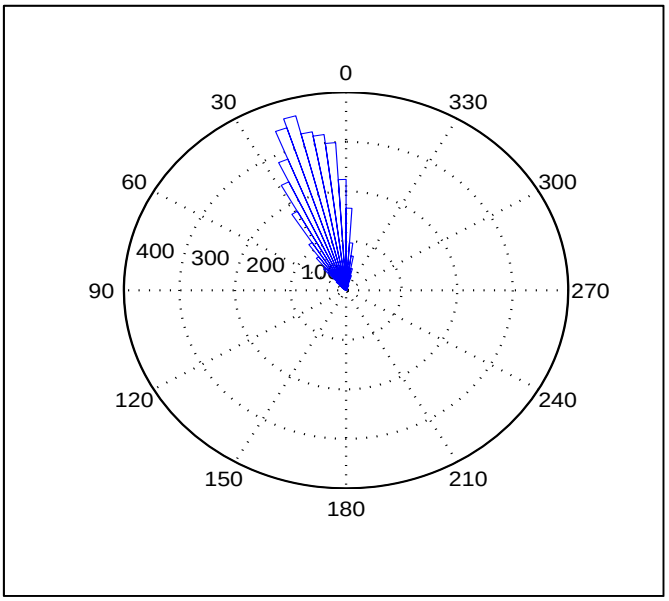

Figure 5.4: Oscillating flow direction for scenario 10 at (x,y) = (1250,2195)

Figure 5.4 shows an example plot based on 3340 samples (for one single measurement location), acquired at a frequency of 25 Hz by the ADV. The average angle is 15 degrees, which is the angle for the average velocity vector as in chapter 4.
The average angle of 15 degrees would result in a slope coefficient of 0.688 instead of 0.670 for flow straight up the slope. However, for an angle of 30 degrees (small probability according to Figure 5.4) this would result in a slope coefficient of 0.747. Due to the linear relation with the stone diameter, this has a significant effect on the required stone diameter.
In Appendix H several situations are investigated. For example, a smooth bed is compared to one with a rough bed.

The flow direction can be considered as an average angle with a certain standard deviation. Figure 5.5 shows a Normal distribution fitted to samples of Figure 5.4.

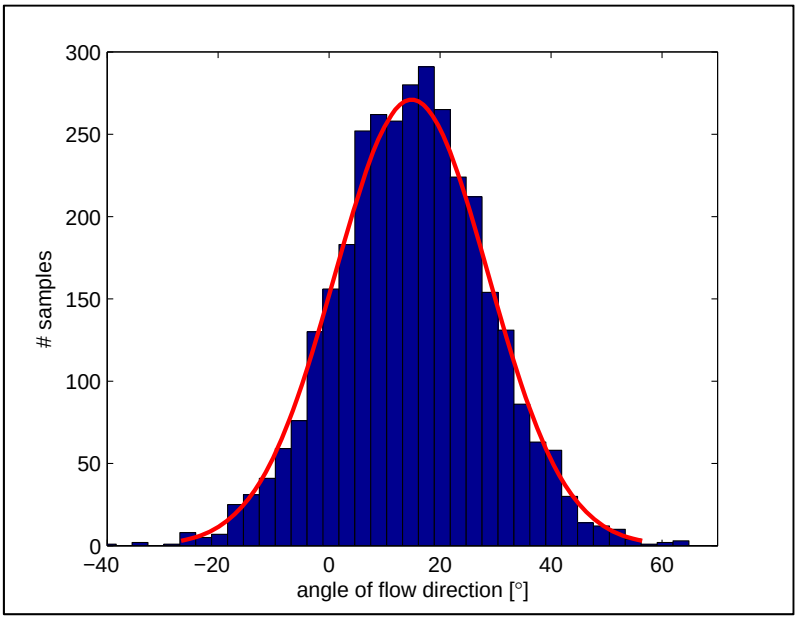

Figure 5.5: Normal distribution fitted to the angle of flow direction

The standard deviation for this specific location is 14 degrees. Hereby the average of 15 degrees, plus one standard deviation is 29 degrees, which showed to have a significant influence on the slope coefficient. Consequently a large probability for this angle of (for example) 29 degrees follows.

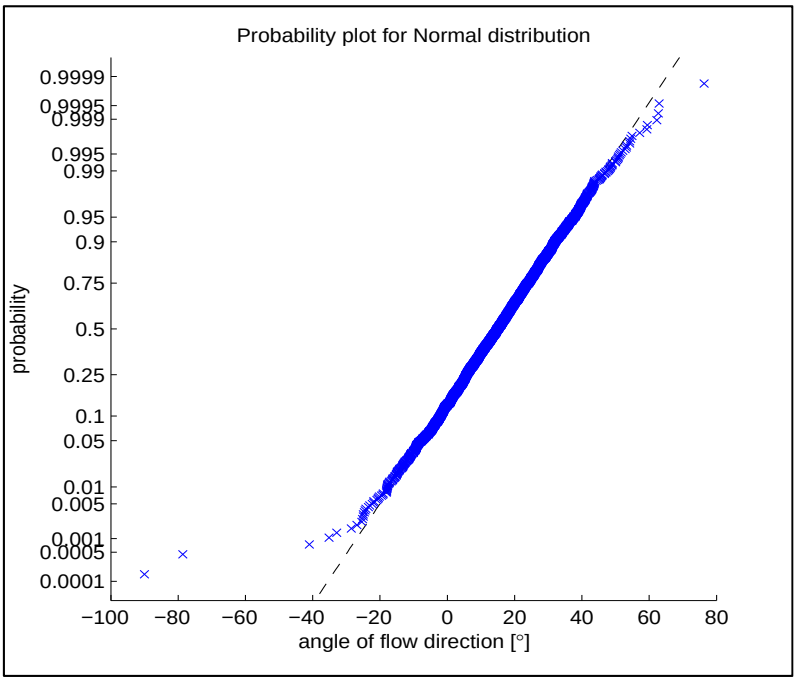

Figure 5.6: Fit of measurements to Normal distribution

Figure 5.6 shows the fit of the measurements to the Normal distribution, which can be considered as a good fit by the Normal distribution.
Because of the available time for this thesis, no extensive analysis of oscillating vectors had been executed. It is recommended to do further research in this subject, because of significant consequences for bed protection.

5.4 Location of maximum bed load

The results as discussed in chapter 4 reveal locations of maximum bed load: a combination of average flow velocities and turbulence intensities. Analysis of these locations shows some remarkable results. First, the location of maximum turbulence intensity for all scenarios is located at a certain x-coordinate. Furthermore, the maximum flow velocity increases fast in the area around that certain x-coordinate. This is expected because the jet edge of the bow thruster jet contains relatively high turbulence intensities.

In Figure 5.7 a plot is given for scenario S6 to S10.
Locations with a maximum bed load are analysed by count up p-times (here p = 3) the turbulence intensity, to the mean velocity. This combination of mean velocity and turbulence intensity is proportional to a certain bed load. One could, for example, use three times the turbulence intensity, depending on the requirements.

Plotting the bed load compared to the dimensionless distance from the outflow opening, results in a zone of maximum bed load, as pointed out in the subplot.

Since the location of maximum bed load is known, one can calculate the angle from the axis of the bow thruster tunnel to the location of maximum bed load. These angles are indicated with green dotted lines in Figure 5.7. All ten scenarios have been analysed, resulting in Table 5.1.

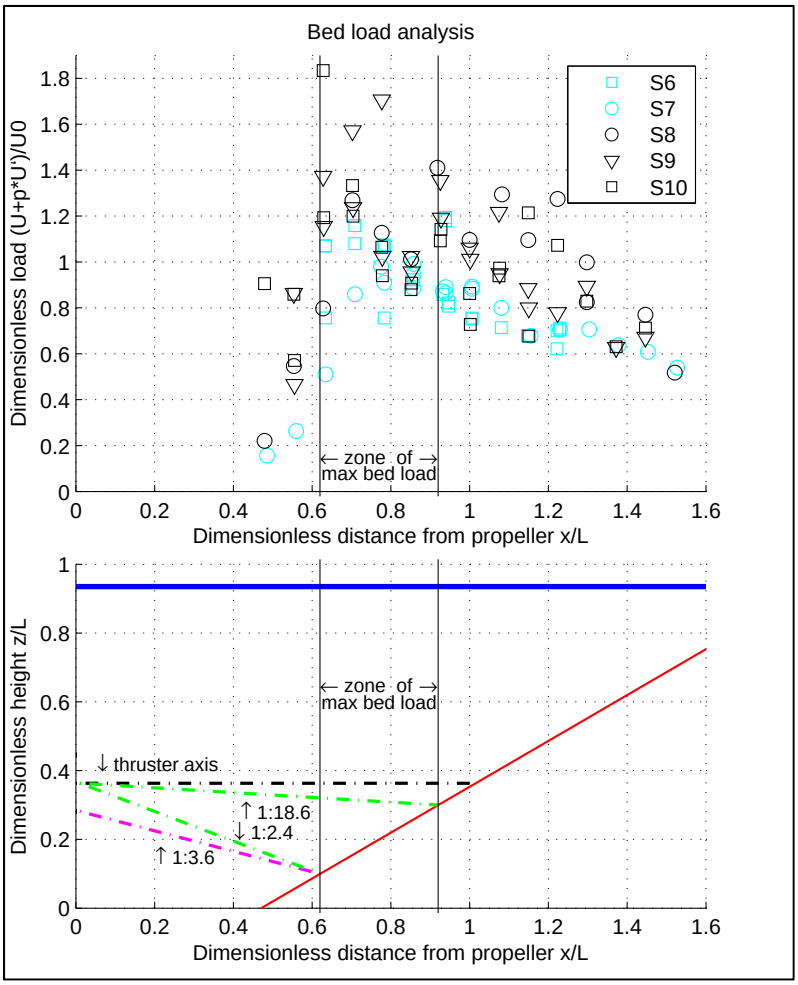

Figure 5.7: Dimensionless plot of measured velocity profiles

Table 5.1 shows obstructions to have an effect on the location of maximum bed load and angles are larger for a steeper slope. For S2 no angle is included, because of insufficient measurement data at the required locations.

Scenario	Angle	Comments
S1	1:9.5	Slope 1:2.5
S3	1:5.1	Slope 1:1.5 and increased water depth
S4	1:3.4	Rough slope
S5	1:4.5	Bow thruster close to slope
S6	1:18.6	Piles in front of thruster
S7	1:8.2	Jet axis mid between piles
S8	1:14.2	Rough, compared to S7
S9	1:4.9	Obstructing pile close to front of thruster
S10	1:2.4	Obstructing pile in front of thruster

Table 5.1: Spreading of the bow thruster jet

Concluding: rough slopes seem to obstruct the flow, resulting in a larger angle. In case of piles, piles in front of the propeller jet form most obstruction, resulting in a larger angle compared to situations with the jet axis between the piles. However, this is not valid for S6, possibly because of local turbulence intensity peaks around piles.

5.5 Consequence for armour layer design

The design of a bed protection against propeller jets mainly consists of formulas validated in experiments with propellers. Commonly used methods are based on the Izbash relation, due to its relation with the flow velocities near the bed. For situations with an open quay construction on piles, no research has been done until now. Current engineering guidelines are based on an equation for free non-ducted propeller jets above a horizontal bed. This method provides acceptable values for bow thruster jets on a slope. An important parameter that is missing in the current approach is the turbulence intensity. One assumed certain relative turbulence intensity, which is included in the 'black-box' parameter β .

In this paragraph, first the current design method is compared to the performed scale model tests. Secondly, the flow velocity measurements are translated into a required stone diameter. Third, the turbulence intensity as a result of the measurements is included.

5.5.1 Current design approach

For the ten scenarios, time averaged flow velocities and turbulence intensities are provided. In the current design method by IGWR the flow velocities, and thereby the maximum flow velocities, are calculated based on the method according to BLAAUW and VAN DE KAA [1978]. These values are input for the method described according to BLOKLAND [1997] to determine the required stone dimensions. This results in a D_{50} at the location of the maximum average flow velocities according to the current engineering guidelines.

For all ten scenarios, the required bed protection based on the current Dutch design method is presented in the first column of Table 5.2. This is based on equation (2.3) and (2.4) in combination with a slope correction as described in appendix B.3.2. The maximum required D_{50} is calculated using equation (5.5).

$$D_{50} \geq 3.0 \cdot m_h \cdot \frac{U_{b,\max}^2}{2 \cdot g \cdot \Delta} \tag{5.5}$$

5.5.2 Measured velocity as input

Time averaged flow velocities are a result of the scale model tests. When the measured flow velocities are used as an input in equation (5.5), this should result in an improved approximation for the required bed protection, compared to the use of flow velocities according to the current guidelines.
Using equation (5.5) according to BLOKLAND [1997], results in the required D_{50}. The second column of Table 5.2 presents the calculated maximum D_{50}, using the mean velocities from the measurements.

5.5.3 Measured velocity and turbulence intensity as input

By using the turbulence intensity as an input in the Izbash equation, the adopted $\beta = 3.0$ is no longer necessary. This β coefficient is used as a safety factor to include the unknown turbulence intensity. From the scale model tests the turbulence intensity is known as well. With this as an input, follows:

$$\Delta \cdot g \cdot D_{50} = m_h \cdot \frac{\beta_{Iz}}{2} \cdot \left(\overline{u} + p \cdot \sqrt{\overline{u'^2}} \right)^2 \tag{5.6}$$

The applied Normal distribution for turbulence intensity is valid according to SCHOKKING [2002], who refers to HINZE [1975].

Commonly (SCHIERECK [2004], ROUBOS [2006]) a factor p = 3 is applied. Consequently a 0.13 % probability of exceeding follows by the Normal distribution.

Figure 5.8 provides an adapted plot of the vertical distribution of flow velocities as presented in paragraph 4.2. Relative turbulence intensities were calculated, which 'explode' when the mean velocity approaches zero. In addition, β values are calculated using equation (5.7):

$$\beta = \beta_{Iz,0,p} \cdot \left(\overline{u} + p \cdot \sqrt{\overline{u'^2}} \right)^2 \Big/ \overline{u}^2 \qquad (5.7)$$

with

$$\beta = \left(1 + p \cdot r\right)^2 \cdot \beta_{Iz,0,p}$$

$$0.7 = \left(1 + 3 \cdot 0.1\right)^2 \cdot 0.41 \;\Rightarrow\; \beta_{Iz,0,p} = 0.41$$

Average relative turbulence intensities near the bed are around 0.3, which is conform existing literature. Relative turbulence intensities near the bed show a peak up to 0.5, according to Figure 5.8, which is in agreement with observed maximum relative turbulence intensities in VERHEIJ [1985].

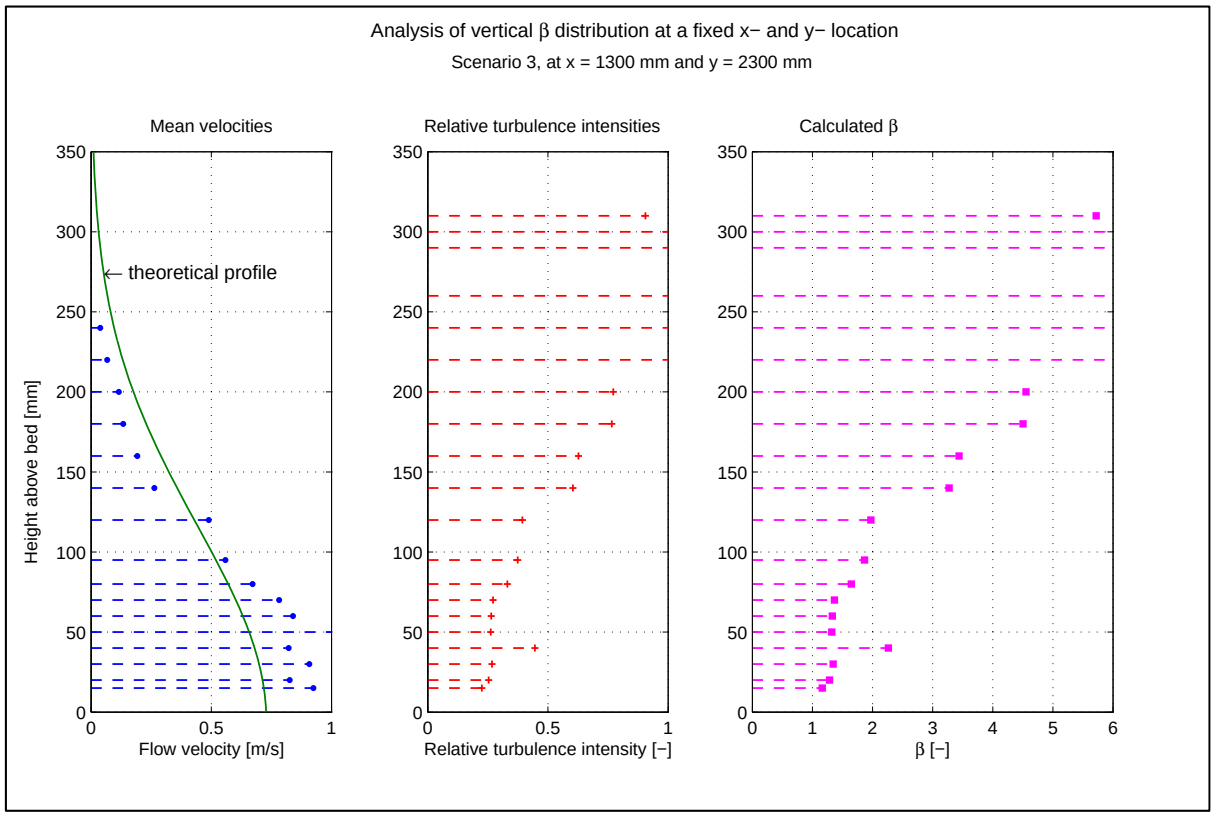

Figure 5.8: Analysis of vertical β distribution

From Figure 5.8 follows that one should take into account the vertical flow distribution for measurements near the bed. Measurements in this research are performed in the zone of 10-30 mm above the bed, however measurements at 50 mm above the bed would provide a 150 % higher bed load.

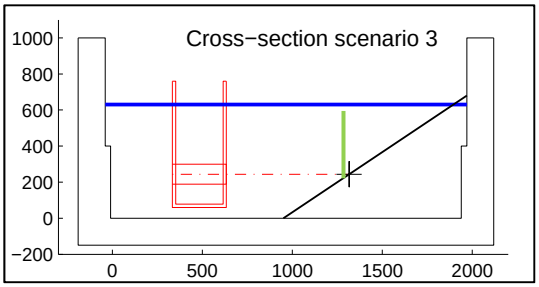

Used data in Figure 5.8 were measured in scenario 3, at the location indicated by the green line.

In Table 5.2 calculated stone diameters are presented, using a relative stone density of 1.65.
First, current engineering guideline (the 'Dutch method') is used to predict maximum flow velocities and calculate required stone diameters using equation (5.5). Second, measured mean flow velocities are used to calculated the required stone diameter using equation (5.5). Third, measured mean flow velocities and turbulence intensities are used to determine the required stone diameters, using equation (5.6). The second and third method are different, because the second method does not include measured turbulence intensities. Thereby, the locations of maximum required stone diameters are different, which results in different 'u' and 'u'' values for the second and third method.

Stone diameters are calculated for all measuring points; hereafter maximum stone diameters are extracted and included in Table 5.2.

These methods do not include the improved slope coefficient from paragraph 5.3. In addition, the third method uses $\beta_{lz,0}$ = 0.41 as determined in equation (5.7), with p = 3.

	Engineering guideline		Measurements Normative location using u				Measurements Normative location using u and u'				
	$\overline{u}$ [m/s]	D_{50} [m]	$\overline{u}$ [m/s]	$\sqrt{u'^2}$ m/s]	r_T [-]	D_{50} [m]	$\overline{u}$ [m/s]	$\sqrt{u'^2}$ [m/s]	r_T [-]	D_{50} [m]	β [-]
S1	0.79	0.044	0.87	0.34	0.39	0.054	0.70	0.53	0.76	0.051	4.45
S2	0.75	0.036	0.80	0.21	0.27	0.041	0.39	0.59	1.53	0.073	12.94
S3	0.75	0.036	0.89	0.49	0.55	0.051	0.89	0.49	0.55	0.050	2.91
S4	0.75	0.036	0.94	0.22	0.24	0.057	0.81	0.54	0.66	0.053	3.70
S5	1.16	0.087	1.35	0.62	0.46	0.118	1.35	0.62	0.46	0.093	2.35
S6	0.75	0.036	1.05	0.25	0.23	0.072	0.70	0.67	0.96	0.066	6.25
S7	0.75	0.036	1.02	0.21	0.20	0.067	0.58	0.42	0.72	0.032	4.14
S8	0.75	0.036	1.22	0.31	0.25	0.097	0.95	0.61	0.65	0.070	3.59
S9	0.75	0.036	1.28	0.39	0.30	0.106	0.95	0.56	0.59	0.062	3.21
S10	0.75	0.036	1.18	0.35	0.30	0.090	0.99	0.61	0.62	0.073	3.38

Table 5.2: Maximum bed load expressed in stone diameter

Remark: as provided with the results in chapter 4, possibly the maximum bed loads in S2 are not measured due to unusable measurements close to the propeller.

With:

$\overline{u}$	mean flow velocity	[m/s]
$\sqrt{u'^2}$	turbulence intensity	[m/s]
r_T	relative turbulence intensity	[-]
D_{50}	diameter of stone that exceeds the 50% value of sieve curve	[m]
β	critical stability coefficient	[-]

Table 5.2 shows the maximum required stone diameters, to compare the different scenarios. In order to present opportunities for the measurement data, Figure 5.9 is computed and provides an impression of the hydraulic bed load distribution. This figure shows the required stone diameters for the third method as used in Table 5.2. In this way one may examine the hydraulic bed load for each scenario and compare the measurements to a future computer model that predicts the hydraulic bed load.

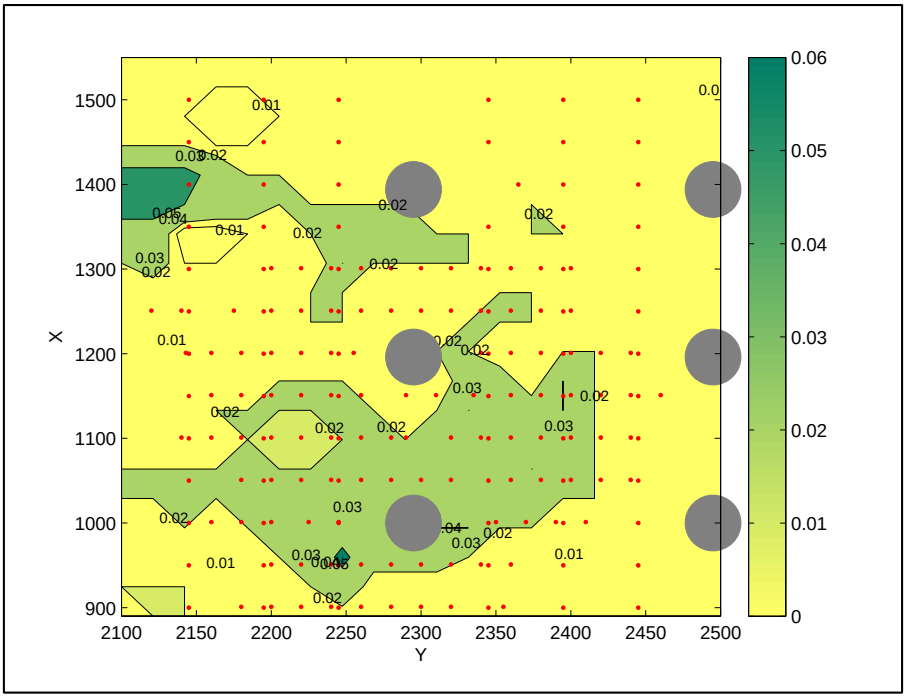

Figure 5.9: Required stone diameters for S10 according to (5.6) with p = 3

Furthermore, an equal plot is shown in Figure 5.10, containing the critical stability coefficient β for each location according to equation (5.7). Red dots represent the measured locations and cubic interpolation is used in between. Grey circles represent the piles.

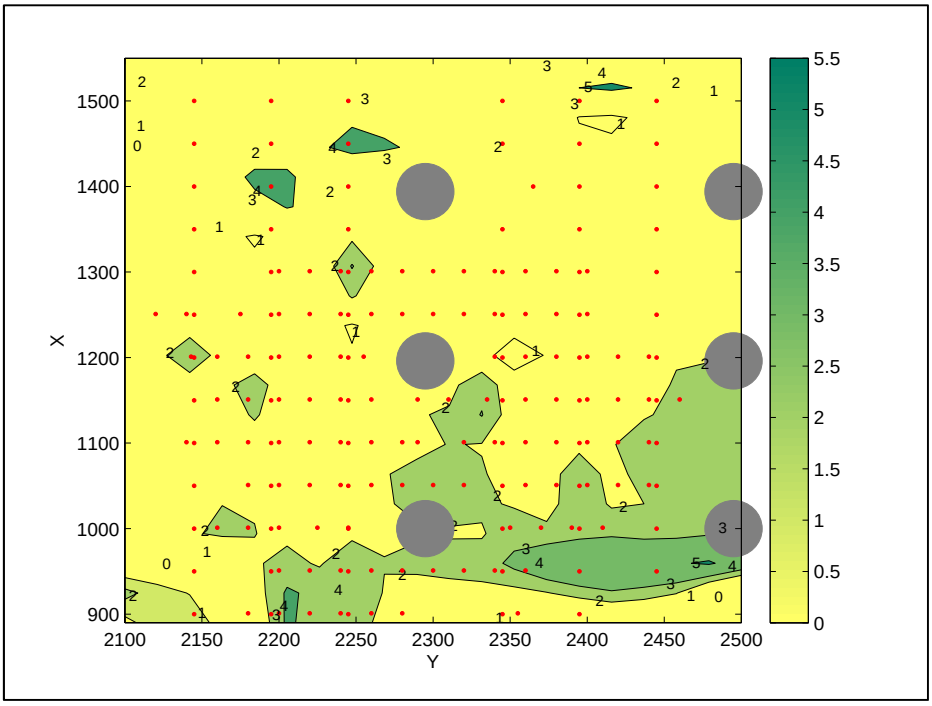

Figure 5.10: β coefficient for S10 with p = 3

Figure 5.11 provides β coefficients in case of p = 1.64, compared to p = 3 in Figure 5.10. Turbulence intensities become less important in case of a decreasing p, whereas mean velocities become more important in that case. Hereby the largest β coefficients are now shifted more to locations with high mean flow velocities, instead of locations with high turbulence intensities. Figure 5.9 - Figure 5.11 provide details for scenario ten; however, this method could be used for all measurements to provide an overview of the hydraulic bed load distribution.

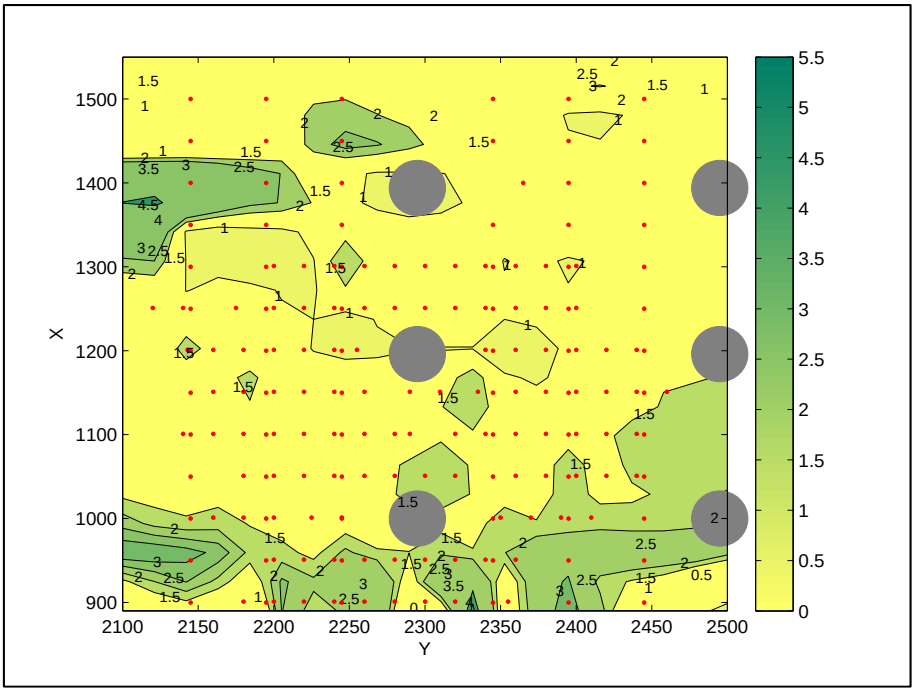

Figure 5.11: β coefficient for S10 with p = 1.64

5.5.4 Difference between engineering guidelines and measurements

Table 5.3 contains the factor difference between the engineering guidelines (the 'Dutch method') and results from the measurements for all used parameters. For example, a factor 1.15 means that a certain parameter is 1.15 times larger in the measurements, compared to the engineering guidelines. Remark: as provided with the results in chapter 4, possibly the maximum bed loads in S2 are not measured due to unusable measurements close to the propeller.

Parameter	Value	Scen	Mean velocity	D_{50} using u	D_{50} using u & u'
Slope angle	1:2.5	S1	1.11	1.23	1.17
	1:1.5	S2	1.07	1.14	2.02
Water depth	0.42	S2	1.07	1.14	2.02
	0.63	S3	1.19	1.43	1.39
x/D_0	6.2	S4	1.26	1.58	1.47
	4.0	S5	1.16	1.36	1.07
Roughness, no piles	smooth	S3	1.19	1.43	1.39
	rough	S4	1.26	1.58	1.47
Roughness, piles frontal	smooth	S6	1.41	1.98	1.83
	rough	S10	1.58	2.49	2.02
Roughness, piles mid	smooth	S7	1.36	1.86	0.89
	rough	S8	1.63	2.69	1.94
Piles, smooth	no piles	S3	1.19	1.43	1.39
	with piles front	S6	1.41	1.98	1.83
	with piles mid	S7	1.36	1.86	0.89
Piles, rough	no piles	S4	1.26	1.58	1.47
	with piles front	S10	1.58	2.49	2.02
	with piles mid	S8	1.64	2.68	1.94
	with piles quart	S9	1.72	2.95	1.72

Table 5.3: Factor difference between engineering guidelines and measurements

5.6 Effects due to variations in parameters

In addition to Table 5.3, the effect of each parameter is provided in Table 5.4. Here the factor difference between two scenarios is calculated for the mean velocities and two methods regarding the stone diameter. The factor difference for 'D_{50} using u' is equal to the squared 'mean velocity' factor, because the mean velocity is used as an input for this D_{50}.

Parameter	Value	Scen	Mean velocity	D_{50} using u	D_{50} using u & u'
Slope angle	1:1.5 / 1:2.5	S2 / S1	0.97	0.93	1.73
Water depth	0.63 / 0.42	S3 / S2	1.12	1.25	0.68
Slope angle & water depth		S3 / S1	1.08	1.16	1.18
x/D_0	4.0 / 6.2	S5 / S4	0.93	0.86	0.73
Roughness, without piles	rough / smooth	S4 / S3	1.05	1.11	1.06
Roughness, piles frontal	rough / smooth	S10 / S6	1.12	1.25	1.11
Roughness, piles mid	rough / smooth	S8 / S7	1.20	1.44	2.19
Piles, smooth	piles front / without piles	S6 / S3	1.18	1.39	1.32
	piles mid / without piles	S7 / S3	1.14	1.30	0.64
Piles, rough	piles front / without piles	S10 / S4	1.25	1.57	1.38
	piles mid / without piles	S8 / S4	1.30	1.69	1.32
	piles quart / without piles	S9 / S4	1.36	1.86	1.17

Table 5.4: Effects due to parameter variations

Each parameter is discussed below, in equal order to Table 5.4.

5.6.1 Variation in slope angle

According to Table 5.3 the mean flow velocities in S1 are underestimated by a factor 1.11 compared to the measurements. In S2, the mean flow velocities are underestimated by a factor 1.07. Goal is to investigate these under- or overestimation factors for variations in parameters such as the slope angle. Table 5.4 provides a factor difference of 0.97 for the mean flow velocity, due to a variation in slope angle. This means that for a slope angle 1:1.5 the mean flow velocities are a factor 0.97 smaller compared to an angle of 1:2.5. Translated into a required stone diameter, the mean flow velocity is used with a power two, which results in a factor difference of 0.93. However, if turbulence intensities from the measurements are included, the required stone diameter is a factor 1.73 in S2, compared to S1. Concluding, mean flow velocities are underestimated using current engineering guidelines, however, the underestimation is almost equal (0.97) for a slope 1:2.5 and 1:1.5. This confirms the validity of the used slope 1:1.5 in the scale model tests.

Comparing the D_{50} using the mean flow velocities and the D_{50} using mean flow velocities in combination with turbulence intensities, a large difference (0.93 versus 1.73) is observed. Flow velocities and turbulence intensities for S2 are not measured at all locations. Hereby information about the location with maximum flow velocities and turbulence intensities is excluded, which could explain the large difference.

5.6.2 Changed water depth

According to the guidelines, S3 requires a stone diameter equal to S2. The water level is raised from 0.42 to 0.63 metre and measurements show an increase in the maximum bed load. A reason for this could be the increased branch off by the jet towards the bed. This phenomena is described in WL

[1988]. Consequently the jet 'hits' the inclining slope at a smaller distance from the outflow opening, which explains the increased bed load. Branch off by the jet for S3 compared to S2 cannot be visualised with measurements, because in S2 no measurement results are available at the location where the jet 'hits' the slope.

In addition, because of less measurement results in S2, variation in slope angle and water depth are compared together. This shows a difference of 1.08 for mean flow velocities and 1.16 - 1.18 for both calculated stone diameters, which is a relatively small difference, showing the relevance of the performed scale model tests.

5.6.3 Distance to slope

With the outflow opening at a smaller distance to the slope, measurements show results fitting better to the engineering guidelines. This holds for mean flow velocities as well as turbulence intensities.
In addition to the change in water depth, the shorter distance of the outflow opening to the slope could result in less branching off by the jet, because of less distance to encounter branching off.
If branching off by the jet is underestimated using the current engineering guidelines, this would explain the factor 0.93 for the mean flow velocity. Due to the fact that the jet is branching off less, the distance between propeller and the location where the jet hits the slope is larger, where a larger distance results in a larger decrease in mean flow velocities.

5.6.4 Roughness

For scale model tests with a rough bed, all results show a larger factor difference compared to tests with smooth slopes. Without piles the factor difference is 1.05 for mean flow velocities, whereas with piles frontal placed, this increases to 1.12. Largest difference (1.20) is observed for situations with the jet axis pointed mid between two rows of piles.
These results clearly show that a rough-bed has a large influence on results from the scale model tests. Thereby, a rough bed should be used in scale model tests regarding rough prototype situations. No variations in stone diameters (variations in roughness) have been tested in this research, although this is recommended to include in further research, because a rougher bed layer could result in different flow distributions and hydraulic loads compared to this research.

5.6.5 Piles

In case of a situation with piles compared to a situation without piles, all difference factors are larger than one, which means that these measurements provide larger hydraulic loads compared to situations without piles. One value is clearly different; 0.64 for S7 compared to S3. Turbulence intensities show less peaks compared to all other scenarios, causing this low value. Measurements closer to piles could result in higher turbulence intensities, compared to current measurements. These additional measurements can be done in future research, to verify the results for S6 and S7. Thereby, the effect of piles can be shown best, using only the rough-bed scenarios.
Current engineering guidelines are equal for situations with and without piles (no guidelines for piles), resulting in a relatively large underestimation for situations with piles using current guidelines.

5.6.6 Pile location

Within the scenarios for situations with piles the vessel and thereby the bow thruster is shifted in the longitudinal direction, parallel to the slope. Hereby the outflow opening was tested frontal to a row of piles, as well as mid between two rows of piles. The determining situation for maximum bed load follows from the measurements. Maximum bed load, including turbulence intensity, occurs when the bow thruster axis is in line with a row of piles.

Mean velocities for rough bed scenarios, however, are smaller with piles in front, compared to piles at mid- and quart-position. In contradiction, smooth bed scenarios show larger mean velocities with piles in front, compared to piles at mid-position. Further research is recommended to explain this contradiction.

5.7 Bed load with(out) piles

This thesis focuses on the hydraulic bed load for a situation with piles. From the scale model tests follows that the current design method however, underestimates the mean flow velocities for an inclining slope (without piles). Hereby some further details for an inclining slope without piles are determined, which is the basis for an inclining slope with piles.

As determined in paragraph 5.4, the location of maximum flow velocities is different compared to the current design method. Concerning the fact that the current design method is based on the flow distribution for a free non-ducted propeller jet, one would expect possible differences.
The maximum bed load follows when diffusion of the bow thruster jet is assumed under an angle of 1:2.4 to 1:18.6 (Table 5.1). This location is for all ten scale model scenarios located at the inclining slope. With the bow thruster at a larger distance from the inclining slope, also the toe of the bed protection could be the location of maximum bed loads. As the distance of the bow thruster to the inclining slope increases, this moves over to the horizontal bed in front of the inclining slope. Here the current design method can be applied, as it is derived for.

5.7.1 Bed load without piles

Maximum mean flow velocities are underestimated in all scenarios, using the current engineering method. In all situations without piles, mean flow velocities are underestimated with a factor 1.07 to 1.26 (Table 5.3). Translated into the hydraulic bed load, with the velocity to the power two, this is a factor 1.14 to 1.58.
Analysis of measurements taking into account the turbulence intensities, results in a hydraulic bed load that is underestimated by a factor 1.07 to 2.02 for situations without piles, which reduces to 1.07 to 1.47 for rough situations.

5.7.2 Bed load with piles

An important aspect of this thesis is the mean flow velocity near the bed. In combination with the turbulence intensities this is determining, in the current design methods, for bed protections.
Compared to situations without piles, piles result in larger mean flow velocities and larger hydraulic bed loads. Mean flow velocities for situations with piles are underestimated by a factor 1.36 to 1.72, using the current engineering method. Translated into the hydraulic bed load, this is a factor 1.86 to 2.95 for the required D_{50}.
Including turbulence intensities from the measurements and p = 3, this results in a factor 0.89 to 2.02. Taking only rough scenarios into account provides a factor 1.72 to 2.02, from Table 5.3.

In chapter 2 a rough approximation for the mean flow velocities around piles is provided:

$$U_1 = \left(\frac{G + \alpha_P \cdot D}{G} \right) \cdot U_2 \qquad (2.15)$$

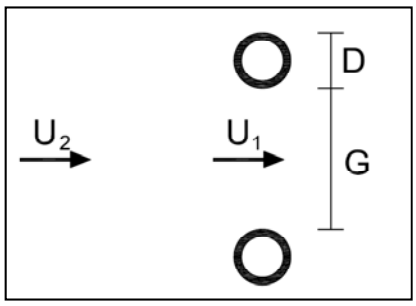

Where:

U_2	undisturbed mean flow velocity	[m/s]
U_1	disturbed mean flow velocity	[m/s]
α_P	coefficient	[-]
G	spacing between piles	[m]
D	pile diameter	[m]

Piles in the scale model have a diameter of 0.03 m and a centre-to-centre distance of 0.20 m. For a situation with piles, the available 'flow area' thereby reduces to 75 % of the original area. If this approach would be valid, the flow velocity for the situation with piles would be 133 % of the original flow velocity without piles. This approach seems to be a good approximation, with Table 5.4 containing difference factors of 1.14 to 1.36 in case of comparing situations with piles to situations without piles.

5.8 Extension of the flow field

In addition, the flow field in all ten scenarios has been measured up to a large distance from the propeller axis. However, results in chapter 4 show only results in the area close to the outflow opening. Sideways flow is considered inferior compared to the bed load as discussed in chapter 4.

Sideways flow is thus considered not as a main research objective for this thesis, although this information is available in the measurement data. A short example is discussed here.
As an example, data acquired in scenario 10 are used. Table 5.5 shows measured flow in y-direction at the largest distance from the bow thruster (x = 1600 mm). These velocities are indicated with red dotted arrows in Figure 5.12.

y-location relative to propeller axis [m]	Mean velocity in y-direction [m/s]
-1.20	0.23
-1.10	0.25
-1.00	0.21
-0.90	0.19
-0.80	0.22
0.80	-0.26
0.90	-0.26
1.00	-0.26
1.10	-0.26

Table 5.5: Extended flow field S10

In this thesis not all scenarios are analysed in this way. The data could be used in future research.

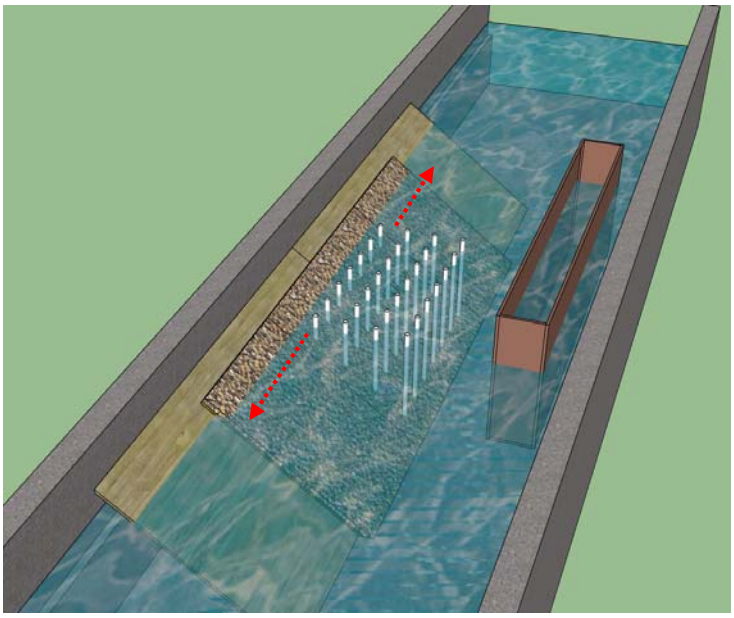

Figure 5.12: Indication of velocities in y-direction

6 Discussion

This chapter includes findings and the contribution to existing research. Focus is on propeller-jet characteristics, flow velocity distribution, turbulence intensities and the resulting total hydraulic load at the bed.

6.1 Propeller-jet characteristics

Concluding from the analysis of measured outflow velocities, the current design method overestimates the outflow velocity slightly. Although equation (5.1) is meant for water jets, the validation of predicted outflow velocities provides reasonable results using equation (5.1).

Furthermore, the propeller thrust coefficient in scale model tests showed a deviation compared to the expected value. This relatively low thrust coefficient could be due to the used propeller rotational speed. The Vetus bow thruster is designed to operate at 3000 rpm, whereas 1021 rpm is used in the scale model tests. For the Vetus bow thruster the thrust force is optimised for 3000 rpm, which means that propeller blades could perform less at different rpm.

Measured relative turbulence intensities near the bed are up to 0.55 at locations of maximum mean flow velocity, compared to 0.3 mentioned in literature. BLAAUW and VAN DE KAA [1978] provided relative turbulence intensities up to 0.3 in the jet axis and up to 0.6 at larger radial distances. It should be mentioned that current engineering guidelines mainly use 0.3 (SCHIERECK [2004]) as value for the relative turbulence intensity, while measurements show relative turbulence intensities up to 0.55 at critical locations.

6.2 Propeller jet diffusion

According to VERHEIJ [1985], OEBIUS and SCHUSTER (1975) report diffusion of the jet under an angle of 18.8 and 20.8 degrees, which is 1:2.94 and 1:2.63 for respectively undisturbed extension of the jet or a restriction by water level and bed. In paragraph 5.4 angles up to 1:2.4 are reported in a situation with piles, which introduce extra flow obstruction.
Design methods for open quay constructions on piles need to be updated with this larger diffusion angle, which effects the location of maximum bed load. Sideways diffusion is considered less important and therefore not discussed in this thesis. However, analysis of a sideways diffusion could be performed using the available data from this research.

Bed loads for a bow thruster at larger distances from the inclining slope are not incorporated in this thesis. Maximum bed load could occur close to the toe or even in front of the toe of the inclining slope, if the bow thruster is located at a larger distance. Further research into this effect is required.

6.3 Flow direction

In an oral conversation, BLOKLAND (2012) states that a certain angle of flow direction is sometimes used in the current design method incorporated in the slope coefficient. A larger angle is sometimes used when a larger safety margin is preferred. Commonly engineering consultants mostly calculate the slope coefficient by assuming the flow direction straight upward the slope.

At locations with maximum bed load under mean velocities and turbulence intensities, the flow directions deviate slightly from straight upwards the slope. Based on the results from measurements one should take into account a mean angle of 15 degrees for these locations. This holds for smooth and rough situations, as well as situations with and without piles.
A remark should be made, that in the performed scale model tests no measurements were done at locations very close to piles (< 0.5 times the pile diameter). Determining loads for bed protection could occur in this region. In addition, flow directions close to piles could deviate more than the proposed 15 degrees.

An angle of 15 degrees, results in a 2.7 % larger slope coefficient, compared to a flow straight upwards a slope. For an angle of 30 degrees, this difference is 11.5 %. As recommendation, one should include a deviating angle of flow direction in the calculation of the bed protection. When a probabilistic approach is used, a mean value of 15 degrees should be used. As a standard deviation, 30 degrees should be used for a rough slope. This standard deviation is relatively large and further research is recommended. In Appendix H details are discussed.
For a deterministic approach, a safe value of 15 + 30 = 45 degrees is recommended at this moment. In current design methods this is not included, resulting in a less safe design.

6.4 Velocity distribution

From the results in chapter 4 follows that the velocity distribution at the inclining slope deviates from the engineering guidelines. However, besides the maximum flow velocities and location of maximum bed load, the distribution according to equation (2.4) from BLAAUW and VAN DE KAA [1978] is in good agreement with the measurements. Sideways diffusion by the propeller jet shows a good match with the guidelines, as well as for situations with piles.
No extensive research for inclining slopes with or without piles is known from literature and thereby presented maximum flow velocities and turbulence intensities in this thesis are an extension of what can be found in literature.

6.5 Hydraulic load

Hydraulic bed loads for situations with piles are not four times larger compared to situations without piles, whereas in paragraph 2.4 this assumption was made using equation (2.17). As analysed in paragraph 5.7.2 the hydraulic load for a situation with piles is up to 2.02 times larger. However, this is only valid for this specific combination of scale model dimensions. Possibly smaller or larger hydraulic loads may occur with different pile diameters or centre-to-centre distances.
Remark: no measurements of hydraulic loads were performed close to the piles, within 0.5 pile-diameter distance from piles. Maximum hydraulic loads may occur in this region.

Concluding, hydraulic loads at inclining slopes and inclining slopes with piles are underestimated using existing design methods. Taking into account the presented subjects in this chapter, results in a more accurate design for the investigated types of quay constructions. In addition, hydraulic loads as presented in this thesis should be further investigated using a non-fixed bed protection. Recently research is done by HOAN [2008], which clearly describes potential damage to a bed protection and presents a method to determine bed transport.
Besides hydraulic loads at bed protection using armour stone, further research is recommended with other types of bed protection such as concrete mattresses.

In order to provide sufficient bed protection, a new β factor should be used in the current design method, in combination with larger mean flow velocities. Future research with erodible bed protection is needed to investigate damage levels and required bed protection.

7 Conclusions and recommendations

As stated in the introduction, the objective of this research is to:
"Develop a method to predict the hydraulic loads by a bow thruster on a non erodible slope."

In this chapter the concluding remarks are provided in paragraph 7.1. The objective of this research is achieved by presenting answers to the research questions. Paragraph 7.2 contains several recommendations following on the performed research.

7.1 Concluding remarks

First a concluding list of remarks is presented, followed by the main conclusion that can be drawn. Details regarding these remarks are discussed in chapter 5 and 6.

- Axial velocity distribution is different compared to the common design method. Axial velocities are overestimated using the 'Dutch method' (2.3) and even more overestimated with the 'German method' (2.7);
- Using the Dutch design method, the location of maximum bed load is estimated higher on an inclining slope compared to the measurements. Depending on the slope angle, roughness and piles, the location of the maximum load from a bow thruster is at an angle between 1:18.6 and 1:2.4 from the propeller jet axis;
- The location of the maximum bed load furthermore seems to strongly depend on obstacles such as piles on a slope. Piles in front of the propeller jet result in a larger angle;
- The slope stability coefficient depends on flow direction, which has negative effects for armour stone stability. Thereby, flow direction needs further research and should be included in engineering guidelines.
- Measured hydraulic bed loads, including turbulence intensities with p = 3, for a rough bed without piles are underestimated by a factor 1.07 to 1.47, using current engineering method.
- Measured hydraulic bed loads, including turbulence intensities with p = 3, for a rough bed with piles are underestimated by a factor 1.72 to 2.02, using current engineering method.
- Measured hydraulic bed loads for rough beds are up to 1.38 times larger in a situation with piles, compared to situations without piles.

7.1.1 Conclusion

Considering the above stated remarks, the following main conclusions are drawn:
Measurements provide that hydraulic loads for rough beds are up to 1.38 times larger in case of a situation with piles, compared to a situation without piles. The current design method underestimates the average flow velocities for an inclining slope as well as an inclining slope with piles.
Hydraulic loads including turbulence intensity seem to be larger than the current engineering method with Izbash (β = 3) provides.

7.2 Recommendations

In this paragraph several recommendations for further research are presented. Situations with piles require detailed investigation as well as situations considering an inclining slope without piles. To start, some recommendations regarding propeller jets induced by bow thrusters are included.

7.2.1 Bow thrusters

More research is needed to estimate propeller thrust coefficients and outflow velocities accurately, due to the significant influence to bed protection. The current research shows that the thrust coefficient and outflow velocity have certain uncertainty.
In the current scale model a six-bladed propeller was tested, whereas four-bladed propeller types are commonly used in prototype thrusters. Influence of this deviating number of blades on propeller jets is unknown from this research.

7.2.2 Slope angle

Slope roughness influences the flow velocity distribution near the bed. Influence by different roughness should be investigated, whereas in the scale model tests a relatively moderate stone diameter was used in the bed layer.
Slope angles have been tested being 1:2.5 and 1:1.5. It is recommended to do similar tests as done for this thesis, investigating the effect of other slope angles to test current conclusions, because these smaller slope angles occur more frequently at quay constructions compared to the steep 1:1.5.

7.2.3 Piles

As mentioned before, measurements close to piles are missing because of the ADV size. Further research is recommended close to piles and research into damage of bed protection is needed. Furthermore, the influence of variation in pile diameter, centre-to-centre distance and shape (square) should be tested.

7.2.4 Other

It is advised to perform similar scale model tests with an erodible bed to investigate damage levels to bed protection. In addition the method described in HOAN [2008] could possibly be used to analyse damage to bed protection.
Analysis of Reynolds stresses would give more insight into the hydraulic load and processes.
Current research focuses on the hydraulic load close to the propeller axis and circulation in the basin is assumed to be negligible. However, for measurements far from the propeller jet circulation becomes more important to investigate.
In addition, research into the oscillating angles of flow velocity is required, which is described in Appendix H. More knowledge is needed to design the distance along the bank over which a protection is needed, which requires research into sideward flow.

References

ALBERTSON, M.L., DAI, Y.B., JENSEN, R.A. and ROUSE, H. [1948] Diffusion of submerged jets. *ASCE Transactions* paper No. 2409: 639-644.

BAW [2011] Grundlagen zur bemessung von böschungs- und sohlensicherungen an binnenwasserstraßen. *BAW, Karlsruhe, Germany*.

BLAAUW, H.B. and VAN DE KAA, E.J. [1978] Erosion of bottom and sloping banks caused by the screw-race of maneuvering ships, publication 202, *Delft, The Netherlands*.

BLOKLAND, T. [1997] Bodembescherming belast door schroefstralen - huidige ontwerpmethode. *Ingenieursbureau Gemeentewerken Rotterdam*

CARLTON, J.S. [2007] Marine propellers and propulsion. *Elsevier, Hythe, Kent*.

CHIN, C.O., CHIEW, Y.M. and LIM, S.Y., LIM, F.H. [1996] Jet scour around vertical pile. *Journal of Waterway, Port, Coastal and Ocean Engineering* 122(2): 59-67.

CIRIA, CUR and CETMEF [2007] The rock manual. C683 the use of rock in hydraulic engineering. *CIRIA, London*.

DE JONG, M. [2003] Schade veroorzaakt door boegschroeven van manoeuvrerende schepen bij verticale kademuren, *Delft University, Delft, The Netherlands*.

FUEHRER, M. and RÖMISCH, K. [1977] Effects of modern ship traffic on islands and ocean waterways and their structures. *Proceedings 24th PIANC Congress, Leningrad, Russia*, pp. 187-198.

FWHA [2001] Evaluating scour at bridges. *FWHA, Washington DC, USA*.

HAMILL, G.A., JOHNSTON, H.T. and STEWART, D.P.J. [1996a] Estimating the velocities in a ship's propellor wash. *PIANC Bulletin No.* 89: 46-54.

HAMILL, G.A., QURRAIN, R.M.M. and JOHNSTON, H.T. [1996b] The influence of a revetment on diffusion of a propellor wash. *PIANC Bulletin No.* 91: 39-43.

HINZE, J.O. [1975] Turbulence. Mcgraw-hill series in mechanical engineering. *McGraw-Hill, New York*, 790 blz. pp.

HOAN, N.T. [2008] Stone stability under non-uniform flow, *Delft University, Delft, The Netherlands*.

HOFFMANS, G.J.C.M. and VERHEIJ, H.J. [1997] Scour manual. *Balkema Publishers, Rotterdam, The Netherlands*.

IGWR [2010] Bed and bank protection, Intern presentation by IGWR. *IGWR, Rotterdam, The Netherlands*.

LAM, W., HAMILL, G.A., ROBINSON, D.J. and RAGHUNATHAN, S. [2010] Observations of the initial 3d flow from a ship's propeller. *Ocean Engineering* 37(14-15): 1380-1388.

LAM, W., HAMILL, G.A., SONG, Y.C., ROBINSON, D.J. and RAGHUNATHAN, S. [2011] Experimental investigation of the decay from a ship's propeller. *China Ocean Engineering* 25(2): 265-284.

MARIN [2011] New initiatives and probe thruster interaction effects (r99 p10-12). *MARIN, Wageningen, The Netherlands*.

MASSEY, B. [2006] Mechanics of fluids. *Taylor and Francis*.

NEN [2004] Nen-en-iso 3715-1. *Netherlands Standardization Institute, Delft, The Netherlands*.

NIELSEN, B.C. [2005] Bowthruster-induced damage - a physical model study on bowthruster-induced flow, *Delft University, Delft, The Netherlands*.

PIANC [1997] Guidelines for the design of armoured slopes under open piled quay walls. *PIANC, Brussels, Belgium*.

PIANC [2012] Guidelines for berthing structures related to thrusters. *PIANC, Brussels, Belgium*.

RAES, L., ELSKENS, F., RÖMISCH, K. and SAS, M. [1996] The effects of ship propellors on bottom velocities and on scour near berths and protection methods using thin flexible revetments. *Proceedings 11th Int. Harbour Congress, Antwerp, Belgium*, pp. 433-443.

RÖMISCH, K. [2001] Scouring in front of quay walls caused by bow thrusters and new measures for its reduction. *Proceedings 5th Int. Seminar on Renovation and Improvements to existing Quay Structures, Gdansk, Poland*, pp. 1-11.

RÖMISCH, K. [2006] Erosion potential of bow thrusters on canal banks (in german). *Binnenschifffahrt – ZfB* 11.

RÖMISCH, K. and HERING, W. [2002] Input data of propeller induced velocities for dimensioning of bed protection near quay walls – a comment on existing recommendations. *PIANC Bulleting* 109(january 2002).

ROUBOS, A.A. [2006] Omgaan met onzekerheden bij het ontwerpen van bodembescherming nabij kademuren, *Delft University, Delft, The Netherlands*.

SCHIERECK, G.J. [2004] Introduction to bed, bank and shore protection, engineering the interface soil and water. *Delft University Press, Delft, The Netherlands*.

SCHIERECK, G.J. [2007] Concise overview of scale rules in coastal engineering, *Hanoi, Vietnam*.

SCHOKKING, L.A. [2002] Bowthruster-induced damage, *Delft University*, *Delft, The Netherlands*.

SCHOKKING, L.A., JANSSEN, P.C. and VERHAGEN, H.J. [2003] Bowthruster-induced damage. *PIANC Bulletin No.* 114: 53-63.

STEWART, D.P.J., HAMILL, G.A. and JOHNSTON, H.T. [1991] Velocities in a ship's propellor wash. *Environmental Hydraulics*: 651-657.

VAN BLAADEREN, E.A. [2006] Modelling bowthruster induced flow near a quay-wall, *Delft University*, *Delft, The Netherlands*.

VAN DER LAAN, T. [2005] Het ontwikkelen van een model voor boegschroefstralen bij verticale kademuren, *Delft University*, *Delft, The Netherlands*.

VAN DER SCHRIEK, G.L.M. [2011] Dredging technology. Guest lecture notes. *TU Delft, Delft, The Netherlands*.

VAN DOKKUM, K. [2003] Ship knowledge. A modern encyclopedia. *Dokmar, Enkhuizen, The Netherlands*.

VAN VELDHOVEN, V.J.C.G.L. [2002] Vooronderzoek schroefstraal op een talud met breuksteen, *Delft University*, *Delft, The Netherlands*.

VAN VELZEN, G. [2012] Flexible scour protection around cylindrical piles, *Delft University*, *Delft, The Netherlands*.

VERHAGEN, H.J. [2001] Bowthrusters and the stability of a riprap revetment. *Proceedings 22nd Int. Conference on Hydronamics and Aerodynamics in Maritime Engineering, Varna, Bulgaria*, pp.

VERHEIJ, H.J. [1983] The stability of bottom and banks subjected to the velocities in the propeller jet behind ships. *Proceedings 8th Int. Harbour Congress, Antwerp, Belgium*, pp. 1-11.

VERHEIJ, H.J. [1985] Aantasting van dwarsprofielen in vaarwegen, schroefstralen en de stabiliteit van bodem en oevers onder invloed van de stroomsnelheden in de schroefstraal. *WL | Delft Hydraulics*, *M1115-VII & Xa*, *Delft, The Netherlands*.

VERHEIJ, H.J. [2010] Inland waterways - lecture 3, TU Delft lecture CT4330*, Delft, The Netherlands*.

VERMAAS, D.A., UIJTTEWAAL, W.S.J. and HOITINK, A.J.F. [2011] Lateral transfer of streamwise momentum caused by a roughness transition across a shallow channel. *Water Resources Research* 47.

WL [1988] Aantasting van dwarsprofielen in vaarwegen, technische aanbevelingen voor oeververdedigingen van losgestorte en gezette steen. *WL | Delft Hydraulics*, *M1115-VII & Xa*, *Delft, The Netherlands*.

List of symbols

A_R	coefficient by Römisch	[-]
A	coefficient by HAMILL *et al.* [1996a]	[-]
A'	coefficient by HAMILL *et al.* [1996b]	[-]
A_0	circular jet outflow area	[m^2]
A_{jet}	water jet outflow factor, 1.17 as upper limit	[m^2]
a	coefficient = 2.8	[-]
B	coefficient by HAMILL *et al.* [1996a]	[-]
B'	coefficient by HAMILL *et al.* [1996b]	[-]
B_s	beam of the ship	[m]
b	coefficient = 15.4	[-]
C_1	coefficient for the principal propeller characteristics 1.59 by VERHEIJ [1985] from FUEHRER and RÖMISCH [1977] 1.60 by BLAAUW and VAN DE KAA [1978] and VERHEIJ [1983]	[-]
C_2	coefficient: 0.081 for a free jet by ALBERTSON *et al.* [1948] 0.19 for a free non-ducted propeller by BLAAUW and VAN DE KAA [1978] 0.17 for a free ducted propeller by BLAAUW and VAN DE KAA [1978] 0.18 for a free propeller jet by BLAAUW and VAN DE KAA [1978]	[-]
C_3	coefficient: 1.17 for ducted propellers 1.48 for non-ducted propellers 1.23 for non-ducted propellers by Hamill and Johnston (1993) 1.06-1.10 for-ducted propellers by Maynord (1999) 1.29-1.34 for non-ducted propellers by Maynord (1999)	[-]
C_4	coefficient: C_4 = 0.25 for two propellers C_4 = 0.30 with a restriction by a transverse wall C_4 = 0.57 when the jet is divided by a rudder C_4 = 0.60 in case of a restriction by bed and water level	[-]
C_5	coefficient for spreading of jet: 0.3 (or 0.306), as a result of m, n, a, and b by BLAAUW and VAN DE KAA [1978]	[-]
C_6	merit coefficient: 1.80 for ducted propellers 2.90 for non-ducted propellers	[-]
C_S	shear coefficient	[-]
C_α	jet-wall coefficient	[-]
D	pile diameter	[m]
D_0	diameter of the jet just behind the propeller, located at the point of maximal contraction $D_0 = D/\sqrt{2} \approx 0.71 \cdot D_p$ at thrusters without tunnel $D_0 = 0.85 \cdot D_p$ propeller-jet combinations in a tunnel $D_0 = 1.00 \cdot D_p$ at ducted thrusters	[m]
D_{50}	diameter of stone that exceeds the 50% value of sieve curve	[m]
D_h	propeller hub diameter	[m]
D_{n50}	median nominal diameter	[m]
D_p	propeller diameter	[m]
F_0	densimetric Froude number	[-]

Fr	Froude number	[-]
f_p	percentage of installed power that is used	[-]
G	spacing between piles	[m]
g	acceleration due to gravity	[m/s^2]
h_{pb}	distance between the propeller axis and the bed	[m]
J	advance coefficient	[-]
K_g	factor for the influence of gradation of bed material	[-]
K_{gr}	factor for the influence of a group of piers	[-]
K_i	correction factor	[-]
K_S	pile shape coefficient	[-]
K_T	propeller thrust coefficient	[-]
K_Q	propeller shaft torque coefficient	[-]
K_ω	factor for orientation of the pier to the flow	[-]
k	kinetic turbulent energy	[m^2/s^2]
k_{ij}	kinetic turbulent energy through ij-plane	[m^2/s^2]
k_s	coefficient for spreading of the jet	[-]
k_t	total kinetic turbulent energy	[m^2/s^2]
L	axial distance between slope and propeller-plane	[m]
L_m	Bakmetev mixing length	[m]
L_p	length in prototype	[m]
L_s	length of the ship	[m]
L_{sm}	length in scale model	[m]
m	coefficient = γ = 1	[-]
m_h	slope coefficient	[-]
N	number of blades	[-]
n	coefficient for the number of propellers: $\sqrt{2}$ for two propellers	[-]
n_L	scale factor for length	[-]
n_p	rotational speed of the propeller	[s^{-1}]
n_u	scale factor for flow velocity	[-]
P	engine power	[W]
P'	propeller pitch ratio	[-]
P_{bow}	bow thruster power	[kW]
P_{max}	used engine power per propeller	[kW]
p	exceeding factor for Normal distribution	[-]
Q	torque of propeller	[Nm]
$Q_{bottom,\alpha}$	discharge at inclining wall	[m^3/s]
$Q_{bottom,\alpha}$	discharge with vertical wall	[m^3/s]
Q_0	circular jet discharge, at the point of maximum contraction	[m^3/s]
Re	Reynolds number	[-]
R_h	propeller hub radius	[m]
R_{m0}	radial distance to the location of the maximum velocity on the propeller face, the efflux velocity	[m]

R_p	propeller radius	[m]
r	radial distance from the propeller axis	[m]
r_T	relative turbulence	[-]
T	thrust force	[N]
T_{dps}	actuator disk thrust force	[N]
T_p	propeller thrust force	[N]
T_s	draught of the ship	[m]
t	duration	[s]
U	flow velocity	[m/s]
U_0	flow directly behind a propeller, located at the point of maximal contraction of the jet	[m/s]
U_1	disturbed mean flow velocity	[m/s]
U_2	undisturbed mean flow velocity	[m/s]
U_A	axial inflow velocity = 0 for a stationary ship	[m/s]
U_i	measured velocities in the i-direction	[m/s]
$U_{m,i}$	mean velocity in the i-direction	[m/s]
$U_{x,axis}$	flow velocity along jet axis	[m/s]
$U_{x,r}$	flow velocity distribution	[m/s]
$U_{x,\max}$	maximum flow velocity	[m/s]
$U_{b,\max}$	maximum flow velocity along the bed	[m/s]
$\overline{u}$	mean flow velocity	[m/s]
u'	turbulent velocity fluctuation	[m/s]
u_*	shear velocity	[m/s]
u,v,w	local velocities, usually defined in x, y, z directions	[m/s]
w	typical width of the jet used by Rajaratnam, where $U = U_{x,axis}/2$	[m]
w_A	width of a jet, $w_A = x \cdot k^{-\frac{1}{2}}$	[m]
x	distance in axial direction	[m]
x_0	length of zone of establishing flow	[m]
x_R	horizontal distance between the propeller face and the point of intersection of the wash centreline with the slope	[m]
z	vertical distance of the bed from the jet-axis	[m]
z_b	distance from bed	[m]

See next page for Greek symbols.

α	slope angle	[°]
α_m	cotangent of the slope angle	[1:…]
α_P	coefficient	[-]
α_T	turbulence coefficient	[-]
β	critical stability coefficient	[-]
β_p	propeller blade area ratio	[-]
$\beta_{Is,cr}$	critical stability coefficient from BLOKLAND [1997]	[-]
β_{Iz}	original stability coefficient for Izbash equation	[-]
$\beta_{Iz,0,p}$	stability coefficient for a certain p	[-]
β_s	critical stability coefficient from WL [1988]	[-]
γ	= m = 1	[-]
Δ	relative density of rock	[-]
ε_0	turbulent shear stress coefficient	[-]
κ	Von Kármán constant (≈0.38)	[-]
ψ	Shields number	[-]
ϕ'	contraction of slipstream	[-]
φ_s	angle of repose (for armour stone around 40°)	[°]
ρ	density	[kg/m^3]
ρ_s	density of stones	[kg/m^3]
ρ_w	density of water	[kg/m^3]
θ	propeller rake angle	[°]
θ_u	angle of velocity component, where 0 = upwards slope	[°]
σ	standard deviation	[-]
$\sigma_{u,i}$	standard deviation of the measured flow velocities in i-direction	[m/s]
τ	turbulent shear stress	[N/m^2]
υ	kinematic viscosity (water of $15° = 1.141 \cdot 10^{-6}$, $20° = 1.004 \cdot 10^{-6}$)	[m^2/s]

List of figures

List of tables

Appendix A Propulsion systems and thrusters

A.1 Main propulsion systems

The propulsion systems of ships vary largely by vessel type. Here first the basic propulsion systems are discussed in order to form an overview of the used systems in vessels. After the basic propulsion systems, the focus will go to bow thruster systems. The used figures are mainly from VAN DOKKUM [2003].

A.1.1 General aspects

The efficiency of a propeller takes an important place in the design process of the propulsion of a ship, because its efficiency has a direct relation with the fuel consumption.
The efficiency depends on the flow field of the propeller, which depends on:
- The shape of the ship's body;
- The torque delivered to the propeller;
- The number of blades;
- Rotations per minute (RPM);
- The propeller diameter;
- The blade surface and smoothness of the blade;
- The pitch and blade shape.

For a given torque delivered to the propeller, if the diameter increases, the rotations per minute decrease. This generally increases the efficiency of a propeller.
The choice for high efficiency with a large diameter propeller and low number of revolutions per minute is however usually difficult to arrange. The propeller diameter has a direct effect on the dimensions of the propeller casing or tunnel.

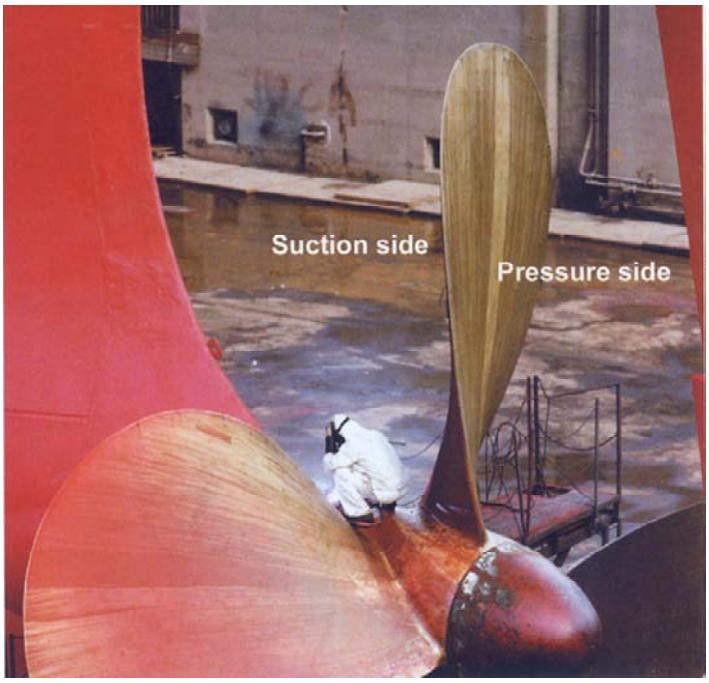

Figure A-1: Fixed right-handed propeller on a tanker. Propeller being polished to reduce roughness, for less rotation friction and less fuel consumption.

RPM and the number of blades have influence on vibrations on board and the resonance frequency of a ship. Most small single-screw ships use a 4-bladed propeller, while 5-bladed propellers are more common on bigger ships, where a large power is necessary. However nowadays more and more ships use the 5-bladed propeller, to reduce vibrations.
3-Bladed propellers are used on twin-screw vessels and on ships with a high number of revolutions per minute and a low power (700 rpm, 600 kW).

Here some basic propeller concepts are schematized:

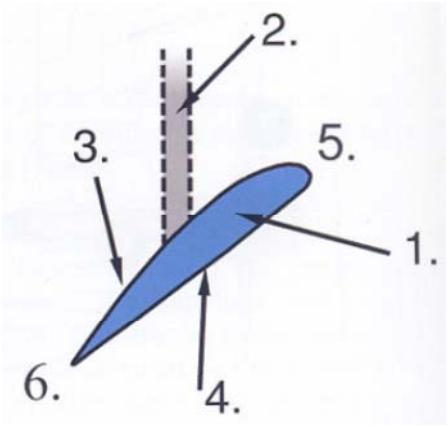

With:
1. Cross-section of propeller blade;
2. Propeller shaft;
3. Suction side;
4. Pressure side;
5. Leading edge;
6. Trailing edge.

Figure A-2: A drawing of the upper fixed propeller blade of a right-handed propeller, top-view

A.1.1.1 Shape

There is a large variety in shapes of propeller blades. The following remarks for each shape of blade apply to the fixed and the controllable pitch propellers.

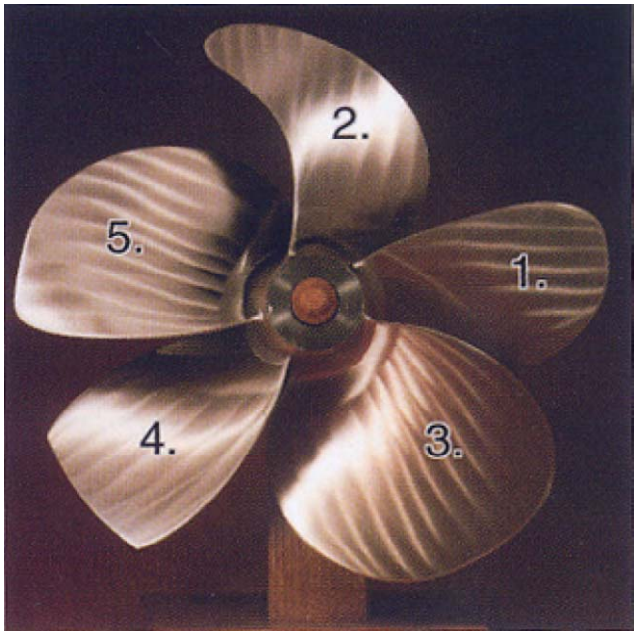

Figure A-3: Different types of blades attached to a hub

1. Is hardly used anymore;
2. Used when there are strict demands regarding noise and vibrations on board;
3. Used when the rpm is high and, consequently, the diameter is small. A large blade surface reduces the efficiency, but is very favourable for the ability to stop the ship and for the reverse propulsion force;
4. Used in nozzles, Kaplan propeller;
5. Used in nozzles if the noise and vibration levels have to be limited to a minimum.

A.1.1.2 Cavitation

The pressure of a rotating propeller is both the result of the water-pressure on the pressure side and the under-pressure on the other side of the propeller. Propellers that rotate rapidly can create an under-pressure that is so low that water-vapour bubbles are being formed on the suction side of the propeller. These gas-bubbles implode again when the pressure rises and this may cause damage when this is located on the blade surface. Severe cavitation results in wear of the blades, an increase if blade roughness and vibrations.

Figure A-4: Cavitation damage due to missing plug

A.1.1.3 Wheel-effect

The propeller's turning direction has influence on the ship's manoeuvring. Propellers can be divided into right- and left-handed propellers. Ships with a fixed-pitch propeller usually have a right-handed propeller. A right-handed propeller means a propeller can be seen as a propeller that is pushing a ship forward when turning clockwise.
A propeller creates a force that is called the 'wheel-effect', the effect that a propeller is pulling towards its turning direction. A propeller will pull to the starboard side of a ship when turning clockwise. When the propeller is turning counter clockwise, this results in a force to port. Even when the rudder is in mid-ships position, this effect occurs.

Propellers with adjustable blades (controllable-pitch propellers, abbreviated CPP) are often left-handed. When the propeller is in the astern mode, the effect of the propeller is the same as in a right-handed propeller going astern, both turning counter clockwise. Going ahead, they have the same effect as a left-handed propeller. This is done in order not to confuse pilot.
When going astern, the efficiency of the propeller can drop below 50% of the ahead going efficiency, depending on the type of blade and the type of propeller.

A.1.1.4 Alternative propeller designs

Apart from the blade form and the number of blades, many alternative designs have been tried and rested. Propellers with tip plates have been invented in order to reduce the energy loss. Tip plates are attached to the blade tips. These prevent the water from flowing too fast from the pressure areas to the suction areas, resulting in vortices. The improved hydro-dynamics caused by the tip-plates contribute to the reduction of vibrations and noise of the propeller.

Figure A-5: Propeller with tip plates

Another development is the contra-rotating propeller. This system consists of two propellers placed one behind the other, with opposite directions of rotation.
In addition, other types of thrusters are available, as Voith Schneider propellers.

A.1.2 Fixed pitch propellers

Propeller blades of a fixed pitch propeller have a fixed position. Consequently the direction of rotation of the propeller has to change if the ship stops or must go astern. This is realized with a reversing gearbox or a reversible engine. A reversible gearbox and therefore the fixed pitch propeller, is approximately economical in ships up to 1250 kW.

There are advantages of a fixed propeller compared to a controllable-pitch propeller:
- Less vulnerable to damage;
- The propeller does not revolve when berthing, so it imposes less danger to mooring boats and there is less risk of ropes being entangled in the propeller.

On the other hand disadvantages of the fixed propeller over a CPP can be named:
- In adverse weather, the propeller may turn with too many rpm. This can hamper propulsion.
- Fixed propellers also have a limited range of rpm for manoeuvring, and so with their power range.

A.1.3 Controllable-pitch propellers (CPP)

This type of propellers has turn able blades, around the blade-axis, thereby changing the propeller pitch. CPP are internally complicated propellers because of the mechanism that adjusts the pitch. The most important feature of this propeller is that it rotates only in one direction. This makes the reversing gearbox or engine unnecessary. In addition, the propulsive forces can be easily controlled by changing the positions of the blades.

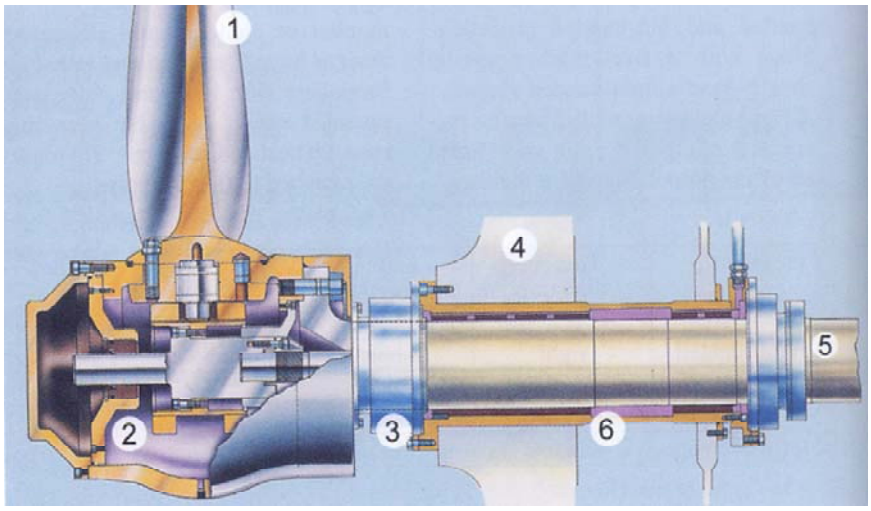

Figure A-6: Mechanism in a CPP

Advantages of a CPP:
- It can propel the ship at all speeds, even at very low speed without stopping the engine;
- It can change quickly from ahead to astern and vice versa;
- Improved efficiency on ships with changing power demands as fishing craft and tugs;
- It can stop a ship with maximum power;
- Sometimes changing a blade is possible afloat, in case of propeller damage.

Disadvantages of a CPP:
- CPP systems are vulnerable due to the hydraulic components and many sealing rings. A damaged ring can result in oil pollution.

A.1.4 Contra rotating propellers (CRP)

The contra-rotating propeller consists of two propellers placed one after each other. These are driven by concentric shafts (an inner and an outer shaft) with opposite turning directions. The number of blades and the diameter of the two propellers are different. This second (aft) propeller reduces the losses of energy by making use of the rotative energy from the first propeller.

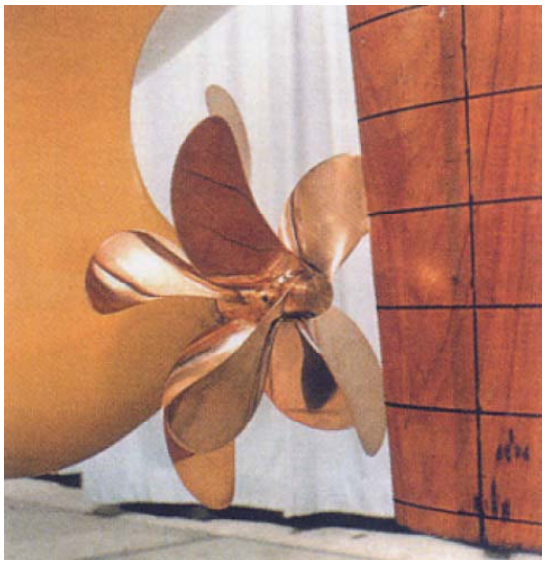

Figure A-7: Model test of a contra-rotating propeller

A.1.5 Nozzles and Azimuthal thrusters

The purpose of a tunnel is to increase the propulsive force. The increase results from the fact that the propeller forces water to flow through the tunnel. This water-flow has a higher velocity in the tunnel than the water outside and the resulting pressure gradient creates the additional propulsive force. Of course, if the friction losses by the tunnel become larger than the additional propulsive force, the tunnel is not effective anymore. Another purpose following from this is a decrease in draught by the use of a tunnel, compared to a 'normal' propeller with the same thrust force.

Figure A-8: Controllable pitch propeller in a fixed nozzle

Besides this type of a controllable pitch propeller in a fixed tunnel, other types of tunnel-constructions are applied. For example, a fixed propeller in a tunnel-rudder, or a rudder-propeller in a tunnel with 360 degrees rotation is possible.

A.1.6 Water-jet propulsion

Water-jet propulsion is based on the reaction force of a high-velocity water-jet at the stern of a ship. An impeller (propeller) draws in water through an inlet and the same impeller boosts the water pressure for the water flow. The water is pushed out of a nozzle and the nozzle converts the water pressure into a high-speed jet that generates a thrust force.
For sailing astern, the water-flow exiting from the nozzle can be reversed in the forward direction with reversing plates.

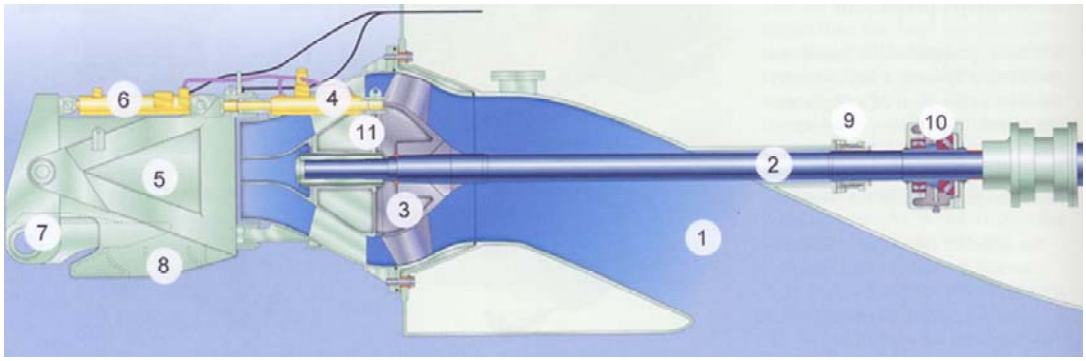

Figure A-9: Cross-section of water-jet (Wärtsilä Propulsion Jets)

1. Inlet; 2. Driving shaft; 3. Impeller; 4. Hydraulic steering cylinder; 5. Jetavator, steering part;	6. Hydraulic cylinder that alters the direction of the propulsion; 7. Reversing plate, can be moved by the cylinder; 8. Reverse section; 9. Sealing box to prevent water from entering the ship; 10. Combined guide and thrust; 11. Nozzle.

Some advantages of water-jets are: no rotating parts under water, this makes it safe to manoeuvre in shallow waters; Less resistance, especially at high speeds; Excellent manouevring capabilities; Less sensitive to cavitation than propellers on fast ships; High propulsion efficiencies, of up to 72%.

A.2 Bow thrusters

In this chapter the types of bow thrusters are discussed. Trends of installed power for bow thrusters are included.

A.2.1 Types of bow thrusters

Several types of bow thrusters are used. Varying from propellers mounted in tunnels to externally mounted azimuth propellers. For sea going cargo vessels, the standard type of bow thruster is a thruster tunnel. In inland vessels several other systems are well represented current days.

In bow thrusters, mostly a Kaplan type propeller is applied. These propellers vary in diameters up to several metres (around 3 m) in current bow thrusters. The main advantage of a Kaplan type propeller is the increased thrust by 'cutting off' the end of the propeller blades. Kaplan propellers originate from water turbines, where a high efficiency is aspired.
Also for models ships Kaplan propellers are available. Figure A-10 shows the Kaplan propeller type.

Figure A-10: Raboesch 149, from 30 to 110 mm

First the tunnel thruster is shown in Figure A-11. This is the 'standard' type of bow thruster for sea going vessels. Several options are available for this type of thruster, such as a roster in front of the outflow opening to prevent obstruction. Furthermore controllable pitch propellers and several blade shapes are possible.

Figure A-11: Thruster tunnel

Besides this standard tunnel thruster, several other systems have been designed. Figure A-12 shows a pump jet which is mostly applied for inland vessels. This type of thruster increases navigability by its ability of thrust in 360 degrees.

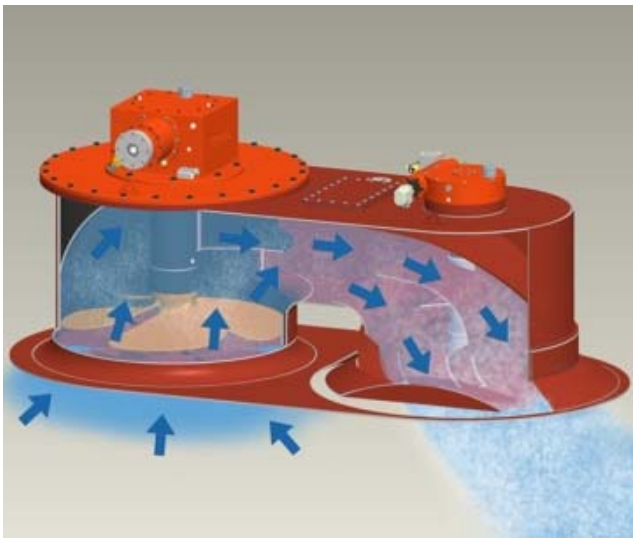

Figure A-12: Veth pump jet for inland vessels (source: Veth website)

Another system is the channel thruster as in Figure A-13. Here a system of two, three or four channels increases manoeuvrability. This thruster is controlled by opening a valve for one of the channels and only applied in inland vessels.

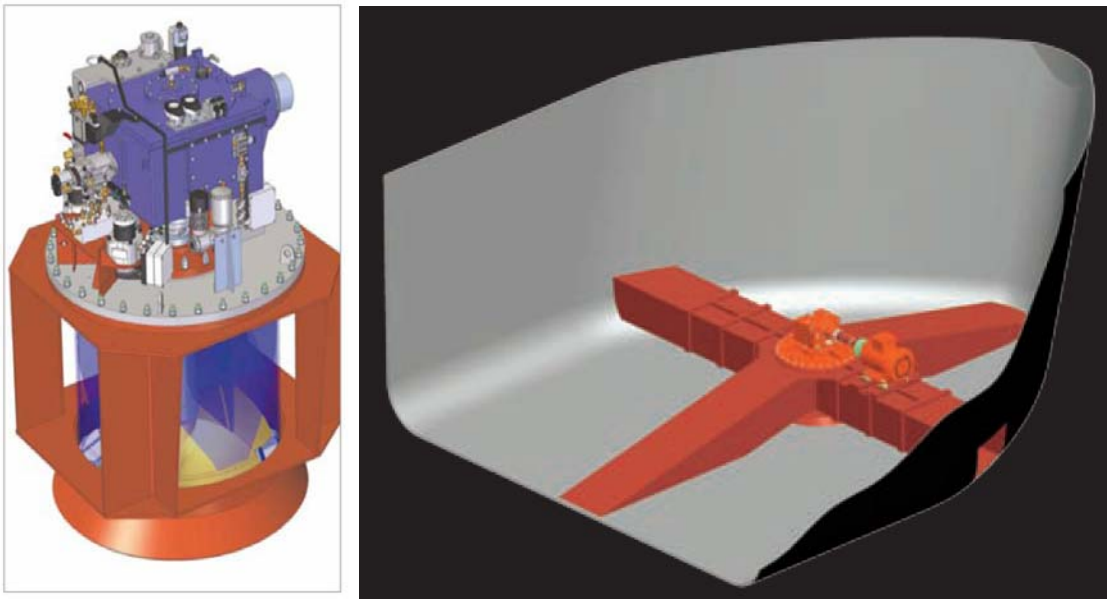

Figure A-13: Veth channel thruster for inland vessels

A.3 Installed power

By VERHEIJ [2010] the following graph is made and equations for the propeller diameters are derived.

$$D_p = 0.1636 \cdot P^{0.3656} \quad \text{(with P in kW)} \qquad \text{(A-1)}$$

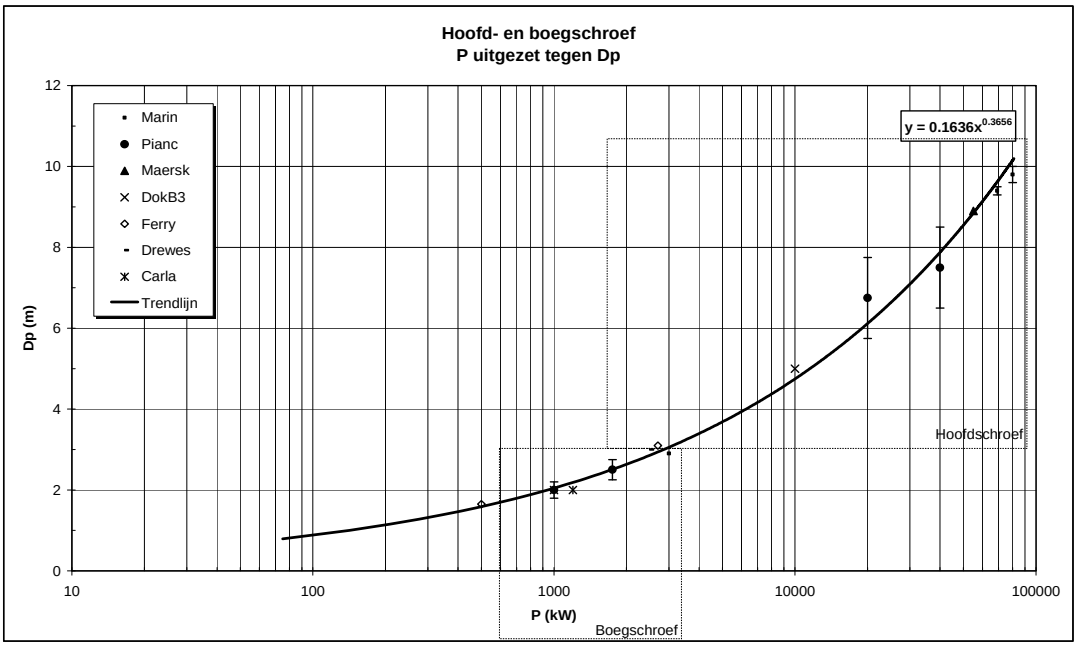

Figure A-14: Installed power for main and bow thrusters by VERHEIJ [2010]

A.3.1 Sea going container vessels

ROUBOS [2006] found a relationship between the width of a container vessel and the installed power of the bow thruster. His relation is based on a limited number of ship data, but no more accurate data is available as known by the writer.

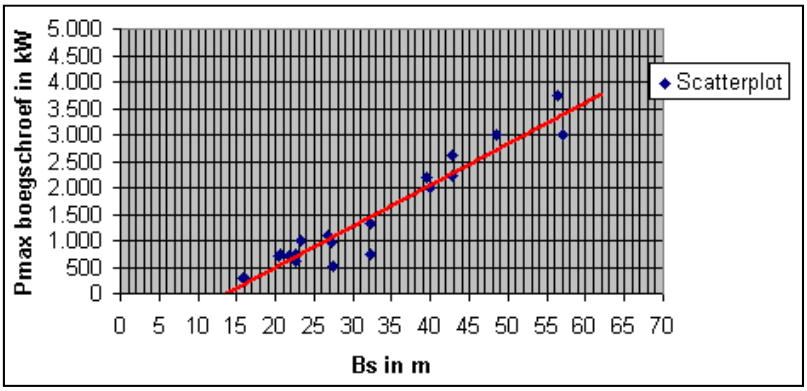

Figure A-15: Relation between width and installed bow thruster power by ROUBOS [2006]

With the relation:

$$P_{max} = 78.2 \cdot B_s - 1068 \qquad \text{(A-2)}$$

Where:

P_{max}	used engine power per propeller	[kW]
B_s	beam of the ship	[m]
D_p	diameter of the propeller	[m]

And a correlation and variance:

$\rho(B_s, P_{max})[-]$	0.916
$\sigma_{P\,max}\,[kW]$	284.7

In addition, Roubos derived a relation between the diameter of the bow thruster and width of the container vessel:

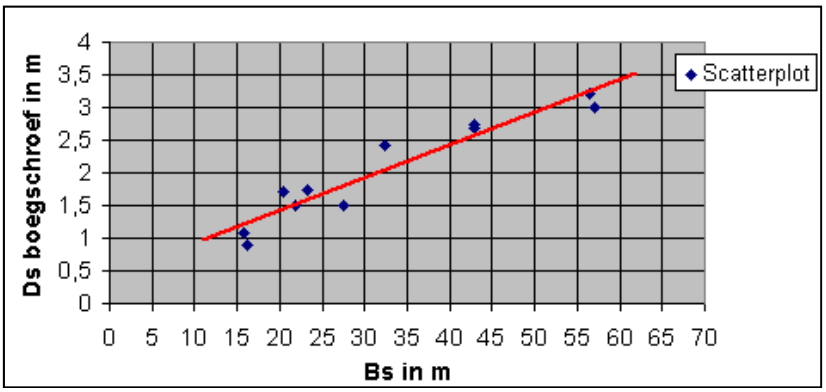

Figure A-16: Relation between width and bow thruster propeller diameter by ROUBOS [2006]

With:

$$D_p = 0.05 \cdot B_s + 0.464 \qquad \text{(A-3)}$$

And:

$\rho(B_s, D_s)[-]$	0.867
$\sigma_{Ds}\,[kW]$	0.227

The distance of bow thrusters to a quay wall is of main importance. Roubos found for sea going container vessels the following relation for the distance of the outflow to the quay:

$$x = 0.5 \cdot B_s \qquad \text{(A-4)}$$

A.3.2 Inland shipping

For bow thrusters at inland shipping VERHEIJ [2010] shows:
- Container vessels: $P_{bow} = 2.0\ L_s * T_s - 250$
- General cargo vessels: $P_{bow} = 1.75\ L_s * T_s - 150$
- Tankers: $P_{bow} = 0.8\ L_s * T_s + 100$
- Cruise vessels: $P_{bow} = 275$ kW
- 90%: $P_{bow} + 175$ kW

Where:

B_s	beam of the ship	[m]
L_s	length of the ship	[m]
T_s	draught of the ship	[m]

For main engines at inland shipping this is: $P_{main} = 0.66 * L_s * (2\ T_s + B_s)$

Appendix B Thrusters and flow velocities

B.1 Some remarks from previous graduation research

Early research to propeller jets was carried out with real propellers: After SCHOKKING [2002] and DE JONG [2003] established from their research that a propeller jet cannot be modelled as a water jet, VAN DER LAAN [2005] started his graduation thesis. From this investigation, the rotation has been found an important factor. In addition, a ducted propeller cannot be easily compared to a non-ducted propeller jet. This results in a doubtful validity of the free non-ducted jet theory for bow thrusters.

Core flow velocities

VAN BLAADEREN [2006] measured the velocity field close to the bow thruster and concluded that the propeller jet from a bow thruster has a core which has stagnant core, which stays stagnant up to the quay wall in that particular case.

Extra research has to be performed in order to determine the velocity distribution, because a stagnant core of the propeller jet is doubtful. This is shown in the following images of MARIN.

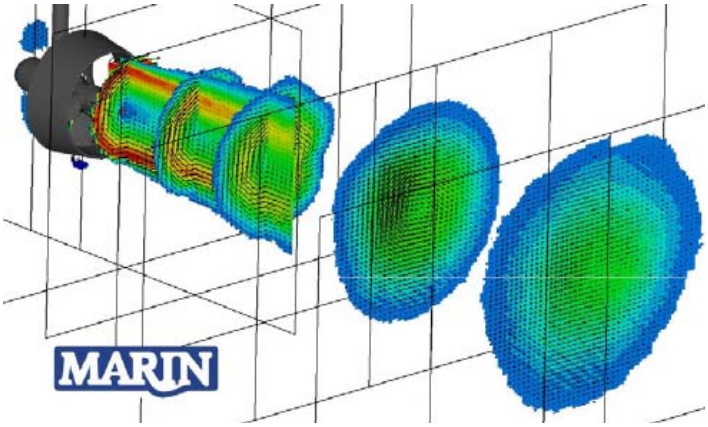

Figure B-1: Flow behind a thruster, by MARIN [2011]

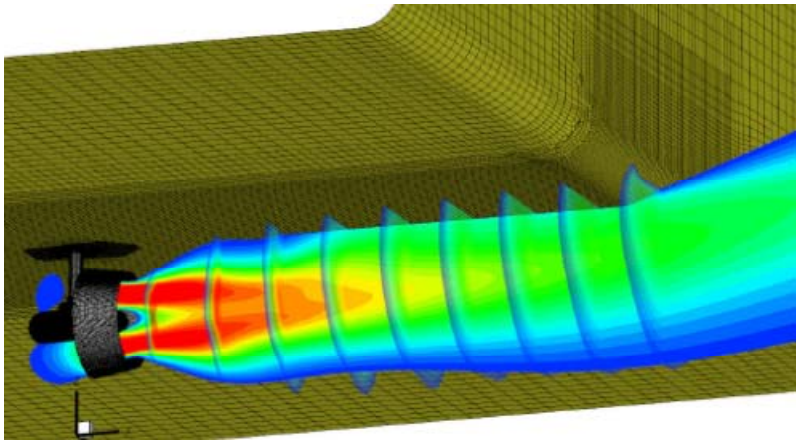

Figure B-2: Flow behind a thruster, by MARIN [2011]

B.2 Velocities behind propeller

For the velocity distribution behind a propeller, several theories have been established in the past. A propeller jet can be characterized by several quantities such as the efflux velocity and decay of the maximum axial velocity. Most of these theories are focused on the average velocities and not on turbulent fluctuations.

B.2.1 Efflux velocity

The maximum axial velocity at the initial plane of a propeller is named efflux velocity. The prediction of the efflux velocity is based on the axial momentum theory and has been refined through several experimental investigations.

B.2.1.1 Axial momentum theory

ALBERTSON *et al.* [1948] investigated an ordinary water jet. This investigation was based on the axial momentum theory, which Froude presented in the 19th century. The research by ALBERTSON *et al.* [1948] can be considered as the basis for the later on derived equations for propeller jets.

BLAAUW and VAN DE KAA [1978] mention that several assumptions are made for the axial momentum theory:
- The propeller is presented by an ideal actuator disk;
- The propeller has an infinite number of blades, rotating at an infinite speed;
- There is negligible thickness of the disk in axial direction;
- The disk is submerged in an ideal fluid (invicid fluid) without disturbances;
- All elements of fluid passing through the disc undergo an equal increase of pressure;
- The energy supplied to the disk is, in a turn, supplied to the fluid without any rotational effects being induced.

Figure B-3 shows the propeller represented as an ideal actuator disk. In this presentation a simplified view is given. In reality, the velocity and pressure at the edge of the slipstream reduce due to mixing with the surrounding fluid.

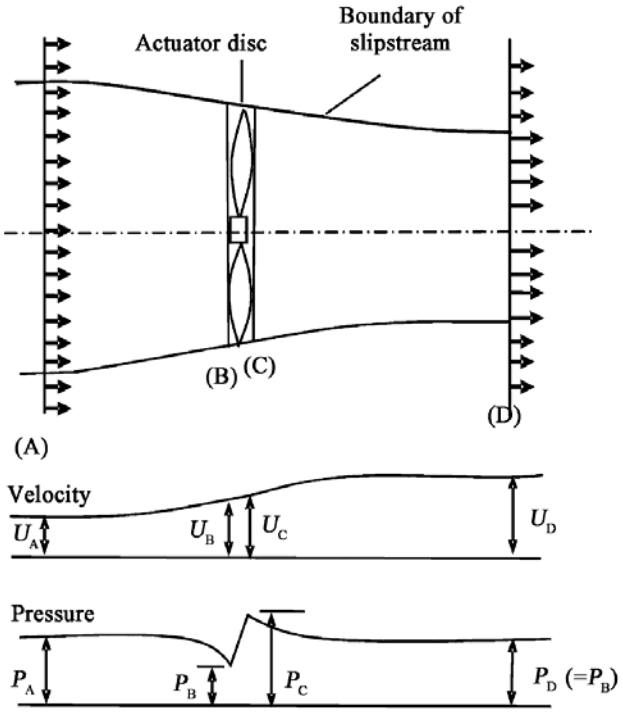

LAM *et al.* [2011] describes this view as: Upstream the pressure and the velocity are given by P_A and U_A, respectively. As the flow approaches the propeller disc at section B, acceleration due to the reduced pressure P_B of the upstream side of the disc occurs. Owing to the negligible thickness of the disc, the velocities at sections B (U_B) and C (U_C) are equal. While passing through the disc, the pressure at section C increases to P_C, which further accelerates the flow. At section D, the velocity reaches U_D and pressure P_D is that of the surrounding undisturbed fluid. In Figure B-3, the slipstream at downstream reduces with the increase of velocity in order to maintain the continuity principle. The energy is supplied to the system as the fluid passes through the disc, and as a result, Bernoulli's equation is not applied between regions B and C. However, Bernoulli's equation may be applied between sections A and B and between sections C and D.

Figure B-3: Propeller as an ideal actuator disk from MASSEY [2006]

The change of the momentum due to the energy supplied to the system through the presence of the actuator disc results in a net thrust on the fluid. This thrust can be related to Bernoulli's equation in order to develop an equation for the efflux velocity as follows by BLAAUW and VAN DE KAA [1978]:

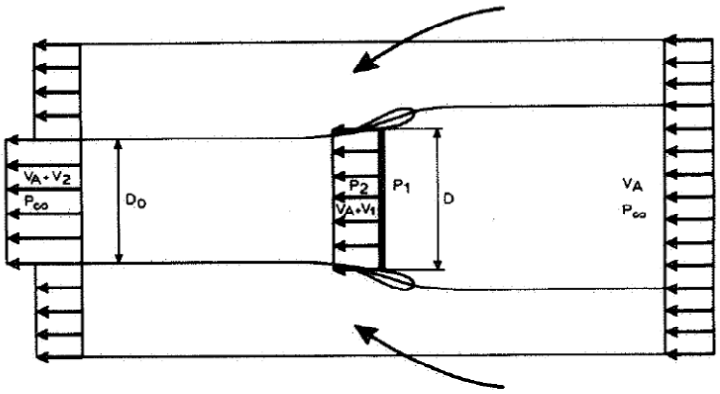

Figure B-4: Control volume for momentum considerations by BLAAUW and VAN DE KAA [1978]

The thrust of a ducted actuator disk can be written as:

$$T_{dps} = \rho_w \cdot \left(U_A + U_1\right) \cdot U_2 \cdot \frac{1}{4} \cdot \pi \cdot D_p^2 \qquad \text{(B-1)}$$

The thrust of the propeller without the influence of the duct can be calculated by applying Bernoulli's theorem fore and aft of the disk, which results in:

$$T_p = \rho_w \cdot \left(U_A + \frac{U_2}{2}\right) \cdot U_2 \cdot \frac{1}{4} \cdot \pi \cdot D_p^2 \qquad \text{(B-2)}$$

With the condition of conservation of mass:

$$\frac{1}{4} \cdot \pi \cdot D_p^2 \cdot \rho_w \cdot \left(U_A + U_1\right) = \frac{1}{4} \cdot \pi \cdot D_0^{\,2} \cdot \rho_w \cdot \left(U_A + U_2\right) \qquad \text{(B-3)}$$

The contraction is defined as:

$$\phi' = \frac{D_0^2}{D_p^2} = \frac{U_A + U_1}{U_A + U_2} \qquad \text{(B-4)}$$

Often it is more advantageous to use the thrust coefficient as determined for the systematic screw series as a function of the advance coefficient:

$$J = \frac{U_A}{n_p \cdot D_p} \qquad \text{(B-5)}$$

$$K_T = \frac{T_p}{\rho_w \cdot n_p^{\,2} \cdot D_p^4} \qquad \text{(B-6)}$$

$$K_T = \frac{\rho \cdot \left(U_A + \frac{U_2}{2}\right) \cdot U_2 \cdot \frac{1}{4} \cdot \pi \cdot D_p^2}{\rho_w \cdot n_p^{\,2} \cdot D_p^4} \qquad \text{(B-7)}$$

For bollard pull condition (U_A = 0) it follows that:

$$U_0 = 1.60 \cdot n_p \cdot D_p \cdot \sqrt{K_T} \qquad \text{(B-8)}$$

In other literature, 1.59 is used beside 1.60. This can be explained by rounding off errors.

$$\sqrt{8/\pi} = 1.5958 \qquad \text{(B-9)}$$

But not always all the required data are available (especially K_T). By using the following equations the value of K_T can be calculated by BLAAUW and VAN DE KAA [1978]:

$$T_P = 205.72 \cdot D_p^2 \cdot C_6 \cdot \left(\frac{1.36 \cdot P}{0.25 \cdot \pi \cdot D_p^2} \right) \quad \text{(B-10)}$$

The value for the merit coefficient C_6 can be taken as:
- 1.80 for propellers in ducts;
- 2.90 for propellers without a duct.

Moreover, since $D_p = \sqrt{2} \cdot D_0$ for a non-ducted propeller, this results in:

$$U_0 = C_3 \cdot \left(\frac{f_p \cdot P}{\rho_w D_p^2} \right)^{1/3} \quad \text{(B-11)}$$

With C_3 for ducted and free propellers:
- 1.17 for ducted propellers;
- 1.48 for non-ducted propellers.

$$C_3 = \sqrt{\frac{4}{\pi} \frac{K_T}{K_Q^{2/3} \cdot (2\pi)^{2/3}}} \quad \text{(B-12)}$$

Where:

C_3	1.17 for ducted propellers 1.48 for non-ducted propellers	[-]
C_6	merit coefficient in bollard pull condition: 1.80 for propellers in ducts 2.90 for propellers without a duct	[-]
D_p	propeller diameter	[m]
f_p	percentage of installed power that is used, 100% for a bow thruster	[-]
J	advance coefficient	[-]
K_T	propeller thrust coefficient	[-]
K_Q	propeller shaft torque coefficient	[-]
n_p	rotational speed of the propeller	[s^{-1}]
P	engine power	[W]
T_{dps}	actuator disk thrust force	[N]
T_p	propeller thrust force	[N]
U_A	axial inflow velocity = 0 for a stationary ship	[m/s]
ϕ'	contraction	[-]
ρ_w	density of water	[kg/m^3]

By VERHEIJ [1985] the coefficient C_3 has a value of 1.15 and D_0 is used instead of D_p to include the propeller diameter:

$$U_0 = 1.15 \cdot \left(\frac{P}{\rho_w D_0^2} \right)^{1/3} \quad \text{(B-13)}$$

By VERHEIJ [1985], Blaauw and Van de Kaa (1979) presented for propellers in tunnels:

$$D_0 \approx 0.85 \cdot D_p$$
$$D_p \approx 1.15 \cdot D_0 \quad \text{(B-14)}$$

By ROUBOS [2006] values for C_3 have been analyzed for several pitch-diameter combinations of propellers. Here propeller type B4-70 of the Wageningen series propellers is applied. Here should be kept in mind that the B4-70 type propeller is a non-ducted propeller, not a propeller in a tunnel.

Pitch/ diameter	0.4	0.5	0.6	0.7	0.8	0.9	1.0	1.1	1.2	1.3	1.4
Pitch-angle	7.3°	9.0°	10.8°	12.6°	14.3°	16.0°	17.6°	19.3°	20.9°	22.5°	24.0°
K_Q	0.013	0.018	0.025	0.034	0.043	0.055	0.068	0.088	0.106	0.122	0.141
K_T	0.15	0.20	0.25	0.30	0.35	0.40	0.45	0.50	0.55	0.60	0.65
C_3	1.007	1.043	1.046	1.034	1.033	1.017	1.005	0.972	0.958	0.955	0.947

Table B-1: C3 for a varying pitch-diameter ratio ROUBOS [2006]

Where:

K_T	propeller thrust coefficient	[-]
K_Q	propeller shaft torque coefficient	[-]
C_3	coefficient, 1.48 for non-ducted propellers	[-]

B.2.1.2 Refined efflux velocity by experiments

In several experiments, the factor C_1 is investigated and refined.

$$U_0 = C_1 \cdot n_p \cdot D_p \cdot \sqrt{K_T} \qquad \text{(B-15)}$$

By HAMILL *et al.* [1996a], Hamill (1987) adjusted the factor C_1 to 1.33 which results in:

$$U_0 = 1.33 \cdot n_p \cdot D_p \cdot \sqrt{K_T} \qquad \text{(B-16)}$$

By experiments, STEWART *et al.* [1991] found a large influence of some principal propeller characteristics:

$$C_1 = D_p^{-0.0686} \cdot P'^{1.519} \cdot \beta^{-0.323} \qquad \text{(B-17)}$$

By HAMILL *et al.* [1996a], Hashmi (1993) found the factor C_1 varying for different propellers. This introduced another factor for the principal propeller characteristics:

$$C_1 = \left[\frac{D_p}{D_h}\right]^{-0.323} \cdot \left[K_T\right]^{-1.459} \cdot P'^{0.44} \cdot \beta^{0.513} \qquad \text{(B-18)}$$

The pitch ratio P' was excluded because large errors could not be introduced by applying the equation to propellers with a pitch ratio outside the proposed limited range:

$$C_1 = \left[\frac{D_p}{D_h}\right]^{-0.403} \cdot \left[K_T\right]^{-0.179} \cdot \left[\beta\right]^{0.744} \qquad \text{(B-19)}$$

Where:

β	propeller blade area ratio	[-]
C_1	constant for the principal propeller characteristics	[-]
D_p	propeller diameter	[m]
D_h	propeller hub diameter	[m]
K_T	propeller thrust coefficient	[-]
n_p	rotational speed of the propeller	[s^{-1}]
P'	propeller pitch ratio	[-]

Additional: the propeller pitch ratio is the ratio of pitch to propeller diameter. Due to the complex dimensions of modern propellers a nominal pitch is given, usually a radius of 70% of the total is used.

B.2.1.3 Other systems

For high and low powered jets, different flow field formulas are present. The outflow velocity is calculated using equation (B-20) according to VERHEIJ [2010].

$$U_0 = 0.9 \cdot \left(\frac{f_p \cdot P}{\rho_w \cdot A_{jet}} \right)^{1/3} \quad \text{(B-20)}$$

B.2.2 Decay of maximum axial velocity

Once the efflux velocity is known, certain decay in maximum velocity occurs as the distance from the propeller plane increases. For the decay in maximum velocity, commonly a separation is made between the so-called zone of flow establishment and the zone of established flow.

B.2.2.1 Albertson et al.

ALBERTSON *ET AL.* [1948] suggested for a pipe jet no maximum velocity decay within the zone of flow establishment. The maximum axial flow velocity is assumed constant within the entire zone of flow establishment.

For the zone of established flow, the velocities in the centre line are given by:

$$U_{x,\max} = U_0 \cdot \frac{1}{2 \cdot C_2} \cdot \frac{D_0}{x} \quad \text{(B-21)}$$

Research by FUEHRER and RÖMISCH [1977] and BLAAUW and VAN DE KAA [1978] resulted also in this assumption, but with a shorter zone of flow establishment. Research by ALBERTSON *ET AL.* [1948] resulted in a zone of flow establishment of $x/D_0 = 6.2$ for a free jet. FUEHRER and RÖMISCH [1977] reported a length for this zone of $x/D_p = 2.6$ and BLAAUW and VAN DE KAA [1978] a length of $x/D_p = 2.8$ for a non-ducted propeller jet.
LAM *et al.* [2011] presented that in research by Berger et al. (1981), Verheij (1983) and Hamill (1987) was assumed that no velocity decay occurs up to respectively $x/D_p = 1.0$, $x/D_p = 1.5$, and $x/D_p = 0.35$. Above these distances, the velocity decreases. Here no equations are presented for the zone of established flow.

B.2.2.2 Fuehrer and Römisch

The maximum axial velocity is assumed constant for the entire zone of flow establishment (for $x/D_p > 2.6$). For the zone of established flow($x/D_p > 2.6$), tests by FUEHRER and RÖMISCH [1977] resulted in:

$$U_{x,\max} = 2.6 \cdot U_0 \cdot \left(\frac{x}{D_p} \right)^{-1.0} \quad \text{(B-22)}$$

B.2.2.3 Blaauw and Van de Kaa

Experiments by BLAAUW and VAN DE KAA [1978] showed C_2 to be 0.18. The maximum axial velocity is assumed constant for the entire zone of flow establishment. Hereby the equations by ALBERTSON *ET AL.* [1948] result for $x/D_p > 2.8$ in:

$$U_{x,\max} = 2.78 \cdot U_0 \cdot \left(\frac{x}{D_p}\right)^{-1.0} \quad \text{(B-23)}$$

B.2.2.4 Berger et al.

In this research by Berger et al. (1981) the maximum axial velocity is constant close to the propeller, but not for the entire zone of flow establishment. For $x/D_p > 1.0$:

$$U_{x,\max} = 1.025 \cdot U_0 \cdot \left(\frac{x}{D_p}\right)^{-0.6} \quad \text{(B-24)}$$

B.2.2.5 Verheij

The maximum velocity is assumed to be constant close to the propeller until $x/D_p > 1.5$ by VERHEIJ [1983]. In addition, for the axial velocity:

$$U_{x,\max} = 1.275 \cdot U_0 \cdot \left(\frac{x}{D_p}\right)^{-0.7} \quad \text{(B-25)}$$

B.2.2.6 Hamill

By LAM *et al.* [2011] Hamill (1987) the zone of flow establishment is constant between $x/D_p = 0$ and $x/D_p = 0.35$. Within this zone the maximum axial velocity is assumed to be equal to U_0.
For the zone of flow establishment between $x/D_p = 0.35$ and $x/D_p = 2$, the velocity can be predicted by an equation:

$$U_{x,\max} = U_0 \cdot 0.87 \cdot \left(\frac{x}{D_p}\right)^{-\beta/4} \quad \text{(B-26)}$$

In addition, within the zone of established flow:

$$U_{x,\max} = U_0 \cdot A' \cdot \left(\frac{x}{D_p}\right)^{B'} \quad \text{(B-27)}$$

With:

$$A' = -11.4 \cdot K_T + 6.65 \cdot \beta + 2.16 \cdot (P') \quad \text{(B-28)}$$

$$B' = -(1.0 \cdot K_T)^{-0.216} \cdot \beta^{1.024} \cdot (P')^{-1.0} \quad \text{(B-29)}$$

B.2.2.7 Stewart

By STEWART *et al.* [1991] follows for the zone of flow establishment between $x/D_p = 0$ and $x/D_p = 2.8$:

$$U_{\max} = U_0 \cdot \left[1.023 - 0.192\left(\frac{x}{D_p}\right)\right] \quad \text{(B-30)}$$

For the zone of established flow Stewart presented:

$$U_{x,\max} = U_0 \cdot \left[0.548 - 0.031 \cdot \left(\frac{x}{D_p}\right)\right] \quad \text{(B-31)}$$

After STEWART *et al.* [1991] new experiments showed small deviations of the above equations. By LAM *et al.* [2011] Stewart (1992) refined these equations by respectively:

$$U_{x,\max} = U_0 \cdot \left[1.0172 - 0.1835 \left(\frac{x}{D_p} \right) \right] \quad \text{(B-32)}$$

$$U_{x,\max} = U_0 \cdot \left[0.543 - 0.0281 \cdot \left(\frac{x}{D_p} \right) \right] \quad \text{(B-33)}$$

Here the extends of the zone of flow establishment were set from $x/D_p = 0$ to $x/D_p = 3.25$. These equations are not valid at the efflux plane, since $1.023*U_0$ and $1.0172*U_0$ cannot occur at the efflux plane.

B.2.2.8 Hashmi

Hashmi (1993) proposed for the zone of established flow an equation to predict the velocity decay up to $x/D_p = 16$. This was based on the work of Stewart (1992) and for the zone of established zone from $x/D_p = 3.25$:

$$U_{\max} = U_0 \cdot \left[0.638 \cdot \exp\left(-0.097 \cdot \left(\frac{x}{D_p} \right) \right) \right] \quad \text{(B-34)}$$

B.2.2.9 Römisch

By VAN VELDHOVEN [2002], Römisch uses a method taking into account surfaces that restrict the extension of the jet by applying a number of constants. In Römisch (1993) these constants are only used for the influence of boundaries that are present parallel to the jet axis. In RAES *et al.* [1996] is not evaluated if these constants are valid for boundaries that are not parallel to the jet axis. Römisch takes into account the following three zones for the flow velocity:

1. Zone with constant velocity, core:

$U_{x,\max} = U_0$

The length of the zone of establishing flow is $x_0 = 2.6 \cdot D_0$.

Here Römisch always uses $D_0 = D_p$.

2. Zone of undisturbed extension:

$$U_{x,\max} = U_0 \cdot A_R \cdot \left(\frac{x}{D_p} \right)^{-1.0} \quad \text{(B-35)}$$

3. Zone of restricted extension by bed, water level, wall or slope:

$$U_{x,\max} = U_0 \cdot A_R \cdot \left(\frac{x}{D_p} \right)^{-C_4} \quad \text{(B-36)}$$

Where A and C_4 are constants:

$A_R = 1.88 \cdot \exp\left(-0.092 \left(h_{pb}/D_p\right)\right)$ without rudder, for $0.9 \le h_{pb}/D_p \le 9$

$A_R = 1.88 \cdot \exp\left(-0.161 \left(h_{pb}/D_p\right)\right)$ with central rudder, for $0.9 \le h_{pb}/D_p \le 8$

$C_4 = 0.25$ for two propellers
$C_4 = 0.30$ with a restriction by a transverse wall
$C_4 = 0.57$ when the jet is divided by a rudder
$C_4 = 0.60$ in case of a restriction by bed and water level
$C_4 = 1.0$ in case of no restriction

RÖMISCH [2006] presents the following updated equation for a bow thruster. For $x/D_p > 1.0$, the zone of flow establishment:

$$U_{x,\max} = U_0 \cdot 1.9 \cdot \left(\frac{x}{D_p}\right)^{-C_4} \quad \text{(B-37)}$$

With for the zone of established flow (after $x/D_p = 6$):

$$U_{x,\max} = U_0 \cdot 2.3 \cdot \left(\frac{x}{D_p}\right)^{-0.825} \quad \text{(B-38)}$$

B.2.2.10 Hamill et al

HAMILL *et al.* [1996a] used in his publications another way for the decrease of the maximum flow velocity. A distinction is made between the establishing zone and the established zone.
For the establishing zone:

$$U_{x,\max} = U_0 \cdot \left(1.107 - 0.1835 \cdot \left(\frac{x}{D_p}\right)\right) \quad \text{(B-39)}$$

For the established zone from $x/D_p = 3$:

$$U_{x,\max} = U_0 \cdot \left(0.543 - 0.0281 \cdot \left(\frac{x}{D_p}\right)\right) \quad \text{(B-40)}$$

B.2.2.11 Schmidt

According to NIELSEN [2005], Schmidt (1998) derived a solution which is valid for bow thrusters:

$$U_{x,\max} = U_0 \cdot 2.0 \cdot \left(\frac{x}{D_p}\right)^{-1.0} \quad \text{(B-41)}$$

This is valid for the zone of established flow and for the zone of flow establishment until $x/D_p = 2.0$ is assumed that: $U_{x,\max} = U_0$

B.2.2.12 Lam

LAM *et al.* [2011] proposed a linear relationship to enhance Stewart's (1992) equation to predict the velocity from the efflux plane. This equation is valid until $x/D_p = 3.68$:

$$U_{x,\max} = U_0 \cdot \left[1 - 0.1592\left(\frac{x}{D_p}\right)\right] \quad \text{(B-42)}$$

B.2.2.13 Bundesanstalt für Wasserbau

By BAW [2011] an equation is given for bow thrusters of (inland) vessels in the situation with an inclining slope, based on Römisch (2006):

$$U_0 \approx 1.1 \cdot \left(\frac{P}{\rho_w \cdot D_p^2}\right)^{1/3} \quad \text{(B-43)}$$

$$\text{For } x/D \le 1.0 : U_{x,\max} = U_0 \quad \text{(B-44)}$$

$$\text{For } x/D > 1.0 : U_{x,\max} = U_0 \cdot \left(\frac{x}{D_p}\right)^{-1/3} \quad \text{(B-45)}$$

B.2.3 Position of maximum axial velocity from the rotation axis

VERHEIJ [1985] assumes the maximum axial velocities to occur at 0.5 times the propeller radius, based on OEBIUS AND SCHUSTER (1979). LAM *et al.* [2010] presents a comparison between the his LDA measurements and previous works for estimating the efflux velocity distribution:

Source	Equation	Position (mm)	Variation (%)
Berger et al. (1981)	$R_{m0} = 0.67\left(R_p - R_h\right)$ $R_p = 38\ mm$ $R_h = 7.46\ mm$	20.46	-
Prosser (1986)	$R_{m0} = 0.6\left(R_p - R_h\right)$	18.32	10
Hamill (1987)	$R_{m0} = 0.7\left(R_p - R_h\right)$	21.38	4
Stewart (1992)	Agree with Berger et al. (1981) eq.		2-5
McGarvey (1996)	Agree with Berger et al. (1981) eq.		30
Lam's measurements		22.5	10

Table B-2: Comparison of efflux velocity by LAM *et al.* [2010]

Where:

R_{m0}	radial distance to the point of maximum velocity in the propeller plane, which is called the efflux velocity	[m]
R_p	propeller radius	[m]
R_h	propeller hub radius	[m]

LAM *et al.* [2010] found a maximum tangential component of the velocity being 82% of the maximum axial velocity, in contradiction with the 30% approximation by Prosser (1986).
LAM *et al.* [2010] reported the tangential velocity profile to have two peaks in between the rotation axis and the jet boundary, at the efflux plane.

From LAM *et al.* [2010] the following conclusions are of interest:
The contraction at the efflux plane is insignificant and the 0.707 D_p contraction derived from a water jet is less than 0.707 D_p for a ship's propeller jet.
Propeller geometry gives significant influence to the axial, tangential and radial components of velocity.

By LAM *et al.* [2011] the position of the maximum velocity within the zone of flow establishment remains a constant location of $r/R_p = 0.53$ from the rotation axis. For the zone of established flow the position of the maximum velocity remains at the rotation axis ($r/R_p = 0$). In Figure B-5 the position of these maximum axial velocities is presented.

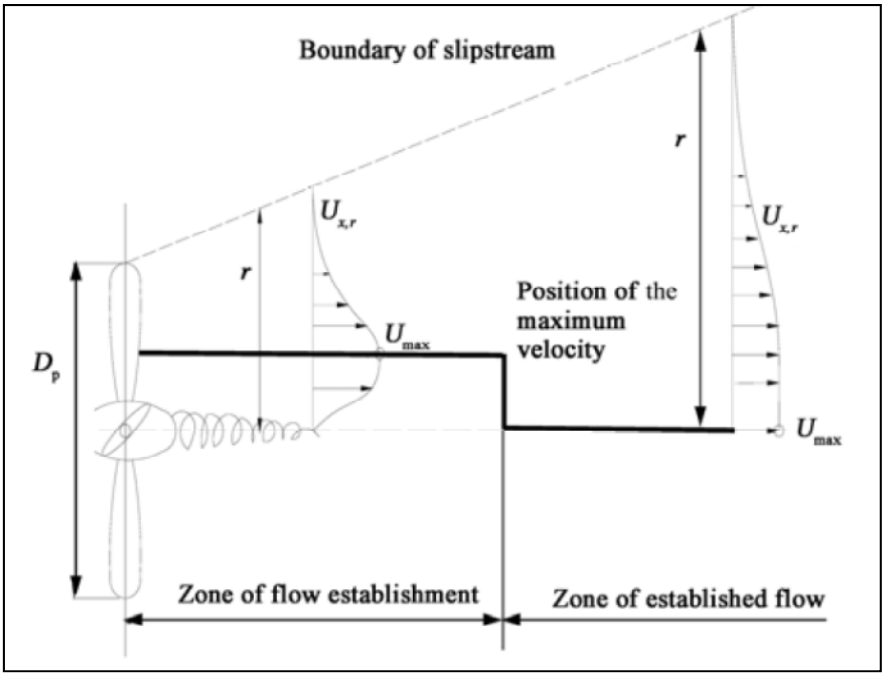

Figure B-5: Schematic representation of the max. axial velocity by LAM *et al.* [2011]

B.2.4 Axial distribution of velocity

B.2.4.1 Zone of flow establishment

By ALBERTSON *et al.* [1948] the velocity distribution for a pipe jet in the zone of flow establishment can be written as a function of x and r (radius from the axis):

$$U_{x,r} = U_{x,\max} \cdot \exp\left[-\frac{r^2}{2 \cdot \sigma^2}\right] \tag{B-46}$$

This results in:

$$U_{x,r} = U_0 \cdot \exp\left[-\frac{\left(r + C_2 \cdot x - \frac{D_0}{2}\right)^2}{2 \cdot \left(C_2 \cdot x\right)^2}\right] \tag{B-47}$$

By the assumption "diffusion process is dynamically similar under all conditions" from ALBERTSON *et al.* [1948] here is a constant ratio C of the standard deviation σ and axial distance x from the initial efflux plane. By experiments ALBERTSON *et al.* [1948] determined the value for C_2, which was C_2 = 0.081. This means that the zone of flow establishment for a pipe jet has a length of:

$$x_0 = \left(2 \cdot C_2\right)^{-1} = 6.2 \cdot D_0 \tag{B-48}$$

VERHEIJ [1985] provides a refined equation based on ALBERTSON *et al.* [1948] and suggested 2 equations to estimate the lateral distributions at cross sections in the zone of flow establishment. The refined equation is:

$$U_{x,r} = U_0 \cdot \exp\left[\frac{-\left(r - R_{m0}\right)^2}{2 \cdot \left(\sigma\right)^2}\right] \tag{B-49}$$

Where r-R_{mo} takes into account the peak velocities on either side of the jet centreline, where R_{m0} is the radial distance to the location of the maximum velocity on the propeller face.
Hamill proposed up to 0.5 D_p:

$$\sigma = \frac{1}{2} \cdot R_{m0} \tag{B-50}$$

And beyond 0.5 D_p:

$$\sigma = \frac{1}{2} \cdot R_{m0} + 0.075\left(x - \frac{D_p}{2} \right) \tag{B-51}$$

Within the zone of flow establishment, applicable to distances up to 0.5 D_p downwards of the propeller:

$$U_{x,r} = U_{\max} \cdot \exp\left[\frac{-\left(r - R_{m0}\right)^2}{2 \cdot \left(R_{m0} / 2\right)^2} \right] \tag{B-52}$$

For the remainder, beyond 0.5 D_p:

$$U_{x,r} = U_{\max} \cdot \exp\left[\frac{-\left(r - R_{m0}\right)^2}{2 \cdot \left(\left(R_{m0} / 2\right) + 0.075\left(x - R\right)\right)^2} \right] \tag{B-53}$$

Stewart (1992) confirmed the validity of these two equations, by measurements of the velocity distribution in the zone of flow establishment.

B.2.4.2 Zone of established flow

And the velocity distribution for a pipe jet in the zone of established zone is given by Albertson et al. [1948]:

$$U_{x,r} = U_0 \cdot \frac{1}{2 \cdot C_2} \cdot \frac{D_0}{x} \cdot \exp\left[-\frac{1}{2 \cdot C_2^2} \frac{r^2}{x^2} \right] \tag{B-54}$$

With:

$$U_{x,\max} = U_0 \cdot \frac{1}{2 \cdot C_2} \cdot \frac{D_0}{x} \tag{B-55}$$

Results in:

$$U_{x,r} = U_{x,\max} \cdot \exp\left[-\frac{1}{2 \cdot C_2^2} \frac{r^2}{x^2} \right] \tag{B-56}$$

With C_2 = 0.15 by FUEHRER and RÖMISCH [1977] and this results in:

$$U_{x,r} = U_{x,\max} \cdot \exp\left[-22.2 \cdot \left(\frac{r}{x} \right)^2 \right] \tag{B-57}$$

By BLAAUW and VAN DE KAA [1978], with C_2 = 0.18 for a propeller jet this results in:

$$U_{x,r} = U_{x,\max} \cdot \exp\left[-15.43 \cdot \left(\frac{r}{x} \right)^2 \right] \tag{B-58}$$

BLOKLAND [1997] uses the method from VERHEIJ [1985] but with a factor n for the number of propellers:

$$\mathrm{U}_{x,r} = n \cdot 2.8 \cdot U_0 \cdot \left(\frac{D_0}{x} \right) \cdot \exp\left(-15.4 \cdot \left(\frac{r}{x} \right)^2 \right) \quad \text{for } x > 2.8 \cdot D_0 \tag{B-59}$$

$$U_{x,r} = U_{x,axis} \cdot \exp\left[-15.4 \left(\frac{r}{x} \right)^2 \right] \tag{B-60}$$

Here 15.4 is applied instead of 15.43 by rounding off.

Where:

n	coefficient for the number of propellers: $\sqrt{2}$ for two propellers	[-]

According to SCHIERECK [2004] the distribution of the velocity for a free non-ducted jet is described as a Gaussian curve with two parameters, $u_{x,axis}$ in the centre of the jet and w as a typical width, usually where $U = U_{x,axis}/2$.

$$\left.\begin{aligned} U_{x,axis} &= 2.8 \cdot U_0 \cdot \frac{D_0}{x} \\ w &= 0.21 \cdot x \\ U_{x,w} &= U_{x,axis} \cdot \exp\left(-0.69\left(\frac{r}{w}\right)^2\right) \end{aligned}\right\} U_{x,r} = 2.8 \cdot U_0 \cdot \frac{D_0}{x} \cdot \exp\left[-15.7\left(\frac{r}{x}\right)^2\right] \quad \text{(B-61)}$$

B.2.4.3 Flow velocity for a free water jet

For a circular, free water jet C_2 is 0.081 by ALBERTSON *et al.* [1948], which results in:

$$U_{x,r} = 6.2 \cdot \left(\frac{D_0}{x}\right)^{1.0} \cdot U_0 \cdot \exp\left(-69 \cdot \left(\frac{r}{x}\right)^2\right) \quad \text{(B-62)}$$

B.2.4.4 Flow velocity due to water jet

For high and low powered water jets different flow field formulas are presented in VERHEIJ [2010]. With for the velocity field for high-powered jets:

$$U_{x,r} = 12.4 \cdot \left(\frac{1}{x}\right)^{1.17} \cdot U_0 \cdot \exp\left(-92.8 \cdot \left(\frac{r}{x}\right)^2\right) \quad \text{(B-63)}$$

And for low powered jets:

$$U_{x,r} = 2.8 \cdot \frac{D_0}{(x)^{0.85}} \cdot U_0 \cdot \exp\left(-25 \cdot \left(\frac{r}{x}\right)^2\right) \quad \text{(B-64)}$$

Where:

A_{jet}	water jet outflow factor, 1.17 as upper limit	[m^2]

In Figure B-6 and Figure B-7 flow velocities by respectively a high- and low-powered water jet are presented.

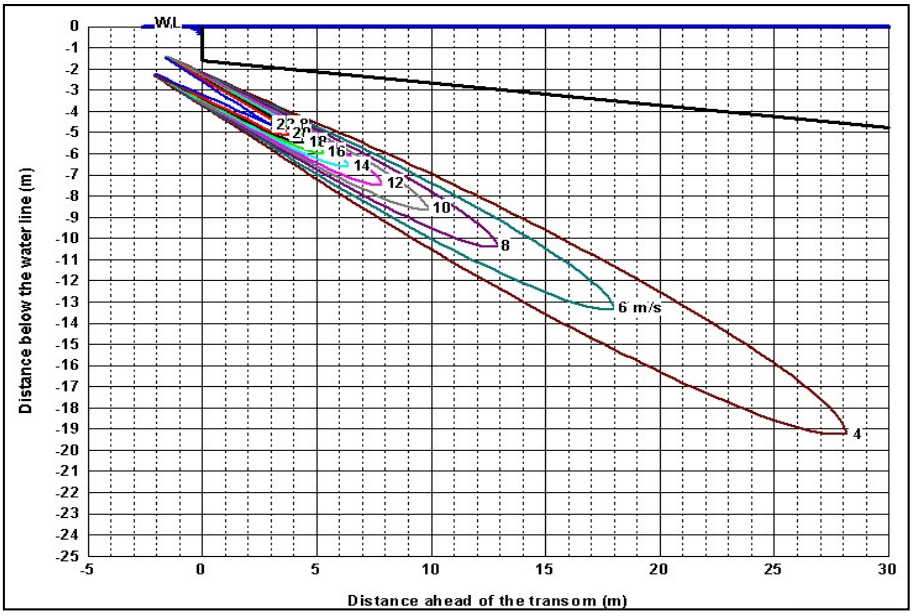

Figure B-6: flow velocities in a high powered jet according to VERHEIJ [2010]

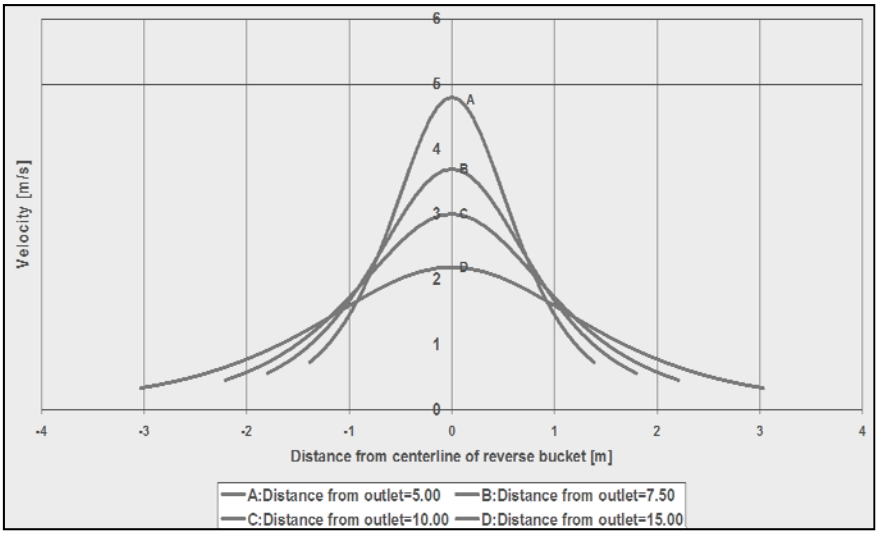

Figure B-7: flow velocities in a low powered jet according to VERHEIJ [2010]

B.2.5 Maximum bed velocity behind thruster

For design considerations of a bed protection, it is desired to have insight into the acting maximum bed velocities. In Figure B-8 a schematic view is given for this situation.

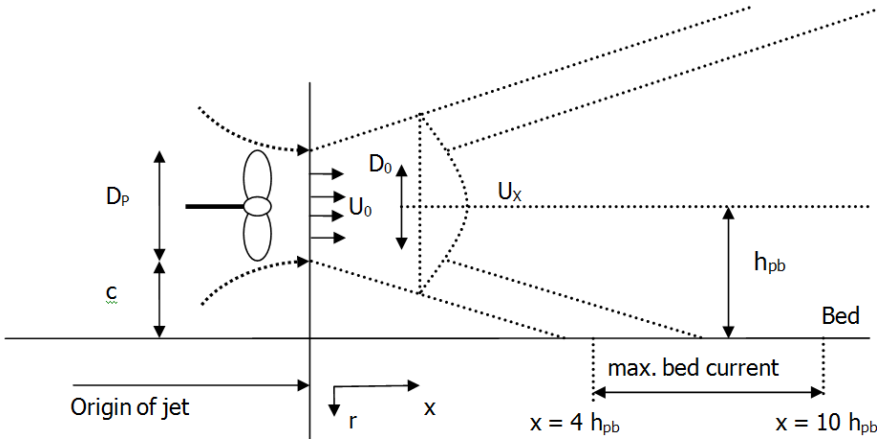

Figure B-8: Water movements due to main propeller

According to VERHEIJ [1985] the derivation of the maximum flow velocity above a horizontal bottom is presented for the method developed by BLAAUW and VAN DE KAA [1978]:

$$U_{x,r} = n \cdot 2.8 \cdot U_0 \cdot \left(\frac{x}{D_0}\right)^{-1.0} \cdot \exp\left(-15.4 \cdot \left(\frac{r}{x}\right)^2\right) \quad \text{for } x > 2.8 \cdot D_0$$

$$U_{x,r} = n \cdot a \cdot U_0 \cdot \left(\frac{D_0}{x}\right)^{m} \cdot \exp\left(-b \cdot \left(\frac{r}{x}\right)^2\right) \quad \text{for } x > 2.8 \cdot D_0$$

$$\left.\frac{\partial U}{\partial x}\right|_{r=h_{pb}} = 0 \quad \Rightarrow \quad -m \cdot \left(\frac{D_0}{x}\right)^{m} \cdot \frac{1}{x} \cdot \exp\left(-b \cdot \left(\frac{h_{pb}}{x}\right)^2\right) - \left(\frac{D_0}{x}\right)^{m} \exp\left(-b \cdot \left(\frac{h_{pb}}{x}\right)^2\right) \cdot (-2) \cdot (-b) \cdot \left(\frac{h_{pb}}{x}\right)^2 \cdot \frac{1}{x} = 0$$

$$\Rightarrow \quad 2b \cdot \left(\frac{h_{pb}}{x}\right)^2 = m \quad \Rightarrow \quad x = \sqrt{\frac{2b}{m}} \cdot h_{pb}$$

$$\frac{U_{b,\max}}{U_0} = n \cdot \underbrace{a \cdot \left(\frac{1}{\sqrt{2b/m}}\right)^{m} \cdot \exp\left(\frac{-m}{2}\right)}_{=C_2} \cdot \left(\frac{D_0}{h_{pb}}\right)^{m}$$

$$C_5 = a \cdot \left(\frac{m}{2 \cdot e \cdot b}\right)^{m/2} \approx a \cdot \left(\frac{m}{5.43 \cdot b}\right)^{m/2}$$

If: m=1 ; b=15.4 , then x = 5.55 $\cdot$ h_{pb}

and a = 2.8 , then C_5 = 0.306

This leads to the following equation by BLAAUW and VAN DE KAA [1978]:

$$U_{b,\max} = n \cdot f_p \cdot C_5 \cdot \frac{U_0 \cdot D_0}{h_{pb}} \qquad \text{(B-65)}$$

Where:

C_5	Factor for maximum flow by propeller (= 0.306 in derivation) 0.3 by BLAAUW and VAN DE KAA [1978]	[-]
f_p	percentage of installed power that is used	[-]
h_{pb}	distance between the propeller axis and the bed	[m]
n	coefficient for the number of propellers: $\sqrt{2}$ for two propellers	[-]
$U_{b,\max}$	maximum flow velocity along horizontal bed	[m/s]

In CIRIA *et al.* [2007] the next equation is presented. Here the coefficients for the number of propellers and percentage of used power are omitted:

$$U_{b,\max} = C_5 \cdot U_0 \cdot \left(\frac{D_0}{h_{pb}} \right)^{\gamma} \qquad \text{(B-66)}$$

with $C_5 = 0.3$

B.3 Propeller jet on slope

For a propeller jet on a slope, several methods have been developed to calculate the flow velocities at the bed. From the view of vertical and slightly inclining quay walls a method as displayed in Figure B-9 is known. This method considers the flow rate that is directed at the wall. This is separated into a discharge upward and a discharge downward directed.
Secondly BLOKLAND (T. Blokland, IGWR, personal communication, October 2011) uses the equation by BLAAUW and VAN DE KAA [1978] for a free non-ducted propeller jet to calculate flow velocities at an inclining slope. Also measurements by SCHOKKING [2002] and HAMILL *et al.* [1996b] are discussed.

B.3.1 Effect of an oblique quay wall on a jet

RÖMISCH [2001] defined the method as shown below, which splits the incoming discharge into an upward and downward directed flow.

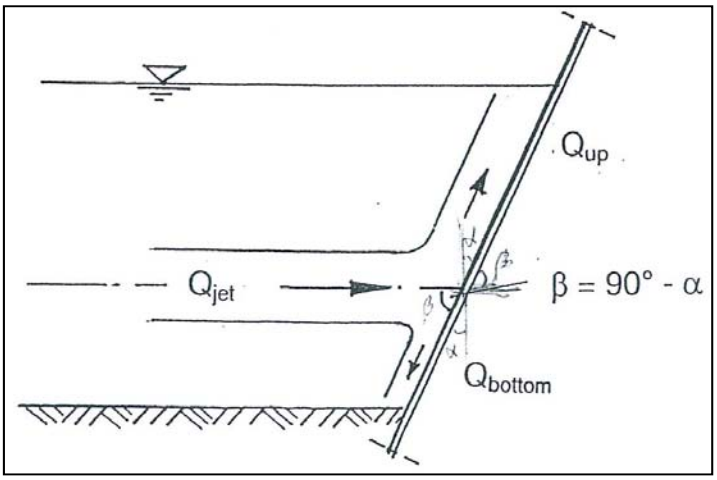

Figure B-9: Jet impinging on a wall by RÖMISCH [2001]

By RÖMISCH [2001] for the part of the jet directed towards the bottom:

$$C_\alpha = \frac{Q_{bottom,\alpha}}{Q_{bottom,\alpha=0°}} = \frac{1}{0.5} \cdot \left[\frac{90° - \alpha}{180°} - \frac{\sin 2(90° - \alpha)}{2 \cdot \pi} \right] \qquad \text{(B-67)}$$

Here c_a is the coefficient that gives the distribution of the flow downward directed. In Figure B-10 the distribution of c_a is plotted against the inclination angle of the (quay) wall. The graph gives the percentage of the flow that is downward directed with respect to the downward discharge at a vertical wall at an angle of zero degrees. The zone from 40 to 90 degrees is added using a value at 68 degrees from SCHOKKING [2002].

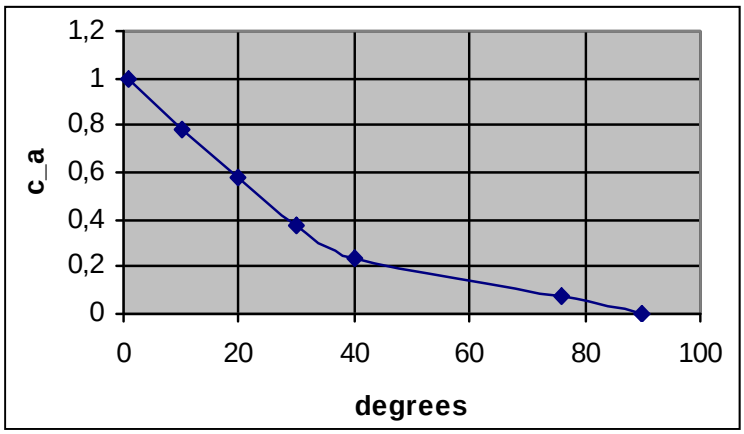

Figure B-10: Ca depending on slope angle, by PIANC [2012]

B.3.2 Blokland

BLOKLAND (T. Blokland, IGWR, personal communication, October 2011) presents a derivation for the maximum flow velocity near the bottom. In this derivation, the location and angle of the inclining slope are included. This derivation is based on the method by BLAAUW and VAN DE KAA [1978] for a horizontal bed. In Figure B-11 the schematization used by Blokland is shown.

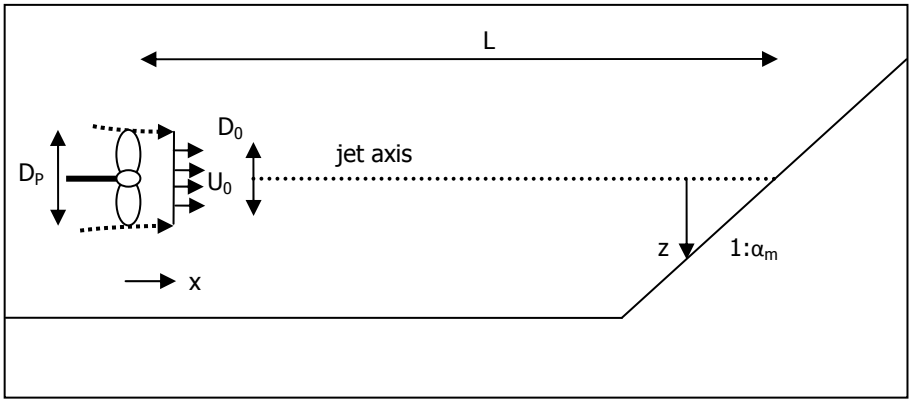

Figure B-11: Schematization for derivation by BLOKLAND

Below the derivation for the maximum bed velocity by BLOKLAND (T. Blokland, IGWR, personal communication, October 2011) is inserted with some values as an example.

$$z = \frac{1}{\alpha_m}(L - x) = \frac{L}{\alpha_m}\left(1 - \frac{x}{L}\right)$$

$$\Rightarrow \quad \frac{z}{L} = \frac{1}{\alpha_m} \cdot \left(1 - \frac{x}{L}\right)$$

$$\text{and} \quad \frac{z}{x} = \frac{1}{\alpha_m} \cdot \left(\frac{L}{x} - 1\right)$$

$$U_{x,z} = n \cdot a \cdot U_0 \cdot \left(\frac{D_0}{L} \cdot \frac{L}{x}\right)^m \cdot \exp\left(-\frac{b}{\alpha_m^{\,2}} \cdot \left(\frac{L}{x} - 1\right)^2\right)$$

$$\left.\frac{\partial U}{\partial x}\right|_{r=z} = 0 \quad \Rightarrow \quad -m \cdot x^{-m-1} + x^{-m} \cdot (-2) \cdot \frac{b}{\alpha_m^{\,2}} \cdot \left(\frac{L}{x} - 1\right) \cdot \frac{-L}{x^2} = 0$$

$$\Rightarrow \quad +2 \cdot \frac{b}{\alpha_m^{\,2}} \cdot (L - x) \cdot \frac{L}{x^2} = m \quad \Leftrightarrow \quad \frac{1}{2} \cdot \frac{m \cdot \alpha_m^{\,2}}{b} \cdot \left(\frac{x}{L}\right)^2 = 1 - \frac{x}{L} \qquad \text{(B-68)}$$

$$\Rightarrow \quad \frac{x_{\max}}{L} = K \cdot \left(\sqrt{1 + 2/k} - 1\right) \quad \text{with} \quad K = \frac{b}{m \cdot \alpha_m^{\,2}}$$

If: b = 15.4 ; m = 1 ; α_m = 1.5 ; K = 6.844 ; $\frac{x_{\max}}{L} = 0.936$;

$\frac{z}{L} = 0.0427$; $\frac{z}{x_{\max}} = 0.0456$; a = 2.8

Then: $U_{b,\max} = a \cdot \frac{U_0 \cdot D_0}{L} \cdot \frac{0.9685}{0.9360} = 1.035 \cdot a \cdot \frac{U_0 D_0}{L}$

$U_{b,\max} = 2.897 \cdot \frac{U_0 \cdot D_0}{L}$ if a = 2.8

Where:

a	coefficient = 2.8	[-]
m	coefficient = γ = 1	[-]
b	coefficient = 15.4	[-]
n	factor for the number of propellers: $\sqrt{2}$ for two propellers	[-]
U_0	flow directly behind a propeller, located at the point of maximal contraction of the jet	[m/s]
$U_{x,r}$	flow velocity distribution	[m/s]
$U_{b,\max}$	maximum flow velocity along the bed (= slope)	[m/s]
L	axial distance between slope and propeller-plane	[m]
z	vertical distance of the bed from the jet-axis	[m]
x	distance in axial direction from propeller	[m]
$x_{\max}$	distance in axial direction where the maximum flow velocity occurs	[m]
h_{pb}	distance between the propeller axis and the bed	[m]
α_m	cotangent of slope angle	[1:…]

B.3.3 Schokking

SCHOKKING [2002] performed measurements of the flow velocity, caused by a propeller jet on an inclining slope. A figure of the measured flow velocities is included in Figure B-12.

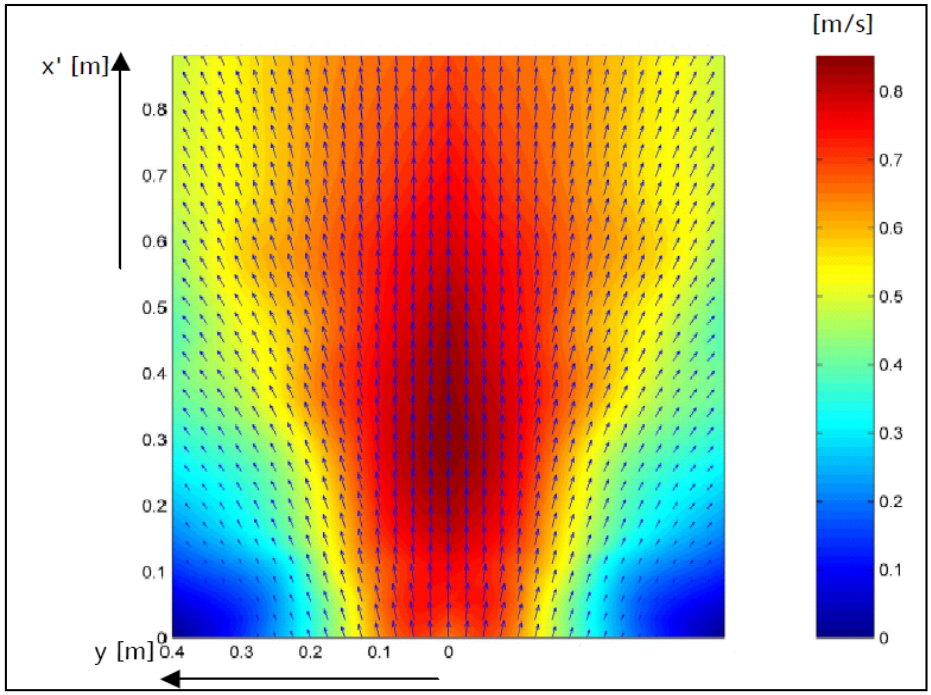

Figure B-12: Measured flow caused by a propeller on an inclined slope by SCHOKKING [2002]

SCHOKKING concluded that a bow thruster should be modelled using a propeller in a duct and not without a duct. In addition, he provided that the initiation of movement was caused by a combination of shear force and pressure force. Both forces were related to the peak velocities, with the pressure force being dominant on the lower part of the slope.
Comparison with measurements in the Amsterdam-Rijnkanaal provided that bow thruster induced scour is of the same order of magnitude as main thruster induced scour.

B.3.4 Hamill

HAMILL *et al.* [1996b] investigated the influence of a revetment on diffusion of a propeller wash. For a jet confined by a revetment at an angle of 15 degrees (1:3.73) the following lines (Figure B-13) are found. These represent different revetment positions from the propeller face, namely 2-, 5- and $9 \cdot D_p$. This figure shows that the presence of a slope has an influence on the maximum axial velocity. Unclear in this figure is which distance is used, because with a revetment on a distance of 2 * D_p it should be impossible to measure flow velocities at a distance of 10 * D_p from the propeller face.

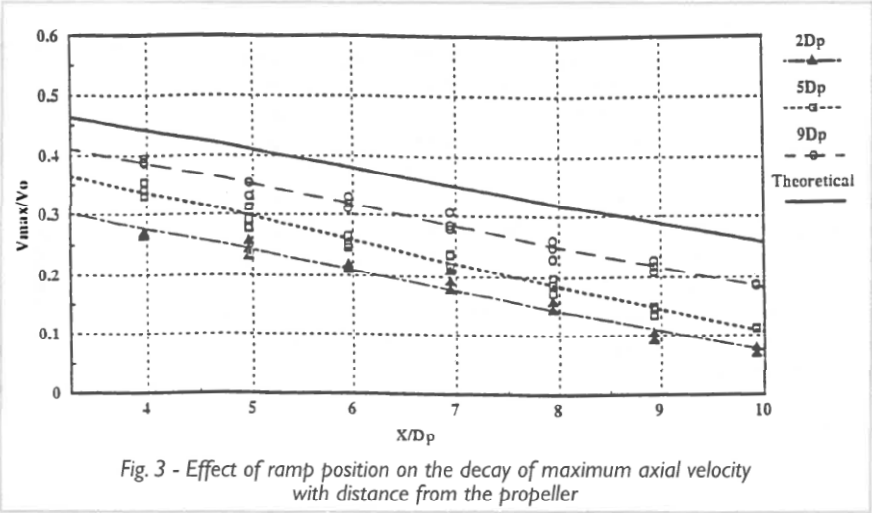

Fig. 3 - Effect of ramp position on the decay of maximum axial velocity with distance from the propeller

Figure B-13: Effect of slope position on decay of max. axial velocity by HAMILL *et al.* [1996b]

Where:

α =	slope angle of the revetment	[°]
x_R =	horizontal distance between the propeller face and the point of intersection of the wash centreline with the slope	[m]

HAMILL *et al.* [1996b] proposed an equation to predict the maximum axial flow velocities:

$$U_{x,\max} = U_0 \cdot \left(A - B \cdot \left(\frac{x}{D_p} \right) \right) \qquad \text{(B-69)}$$

Hamill found that A (= 1.107) remained unchanged regardless of the slope values or location, while the values of B were related to the blockage coefficient by the slope. It was found for the zone of establishing flow that:

$$B = 0.1835 \cdot (1 + \tan\alpha)^{-1.03} \cdot \left(1 + \frac{D_p}{x_R} \right)^{-4.865} \qquad \text{(B-70)}$$

If the slope angle is zero, and the horizontal distance goes to infinity, then the equation reduces to:
$B = 0.1835$
For the zone of established flow a regression analysis provided the following equations:

$$A = 0.543(1 + \tan\alpha)^{1.968} \cdot \left(1 + \frac{D_p}{x_R} \right)^{-9.13} \qquad \text{(B-71)}$$

$$B = 0.0281(1 + \tan\alpha)^{2.725} \cdot \left(1 + \frac{D_p}{x_R} \right)^{-6.3} \qquad \text{(B-72)}$$

From where the equations for a free non-ducted propeller jet in the established zone follow:

$$U_{x,\max} = U_0 \cdot \left(0.543 - 0.0281 \cdot \left(\frac{x}{D_p} \right) \right) \qquad \text{(B-73)}$$

In Figure B-14 and Figure B-15 it can be seen that the velocity distributions in a horizontal plane are over estimated by the existing equations after HAMILL *et al.* [1996a]. Figure B-16 and Figure B-17 show the theoretical and experimental velocity distributions in the vertical plane, which are also being overestimated by the equations after HAMILL *et al.* [1996a].
The figures Figure B-18 and Figure B-19 show the vertical velocity distributions within the wash, with a re-calculation of the theoretical curves by using equations as mentioned above. These results show a good correlation between the measured and calculated values.

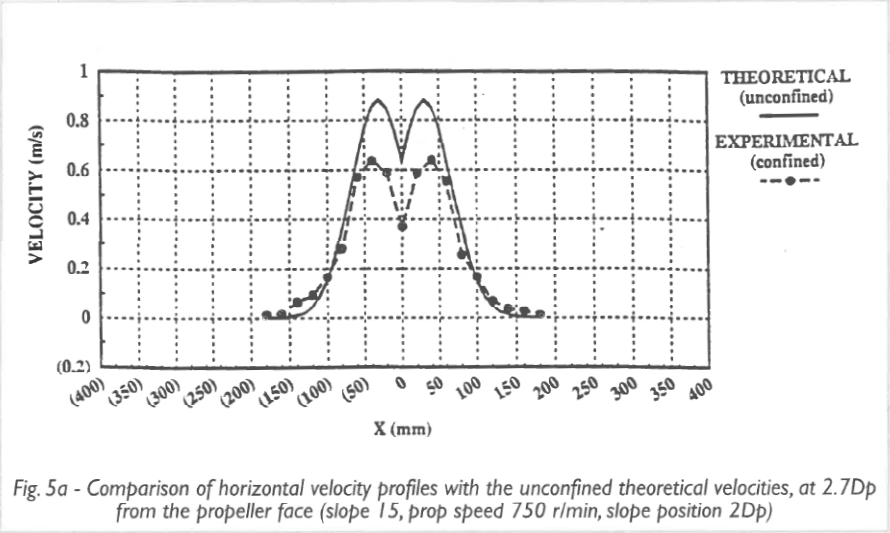

Fig. 5a - Comparison of horizontal velocity profiles with the unconfined theoretical velocities, at 2.7Dp from the propeller face (slope 15, prop speed 750 r/min, slope position 2Dp)

Figure B-14: HAMILL *et al.* [1996b]

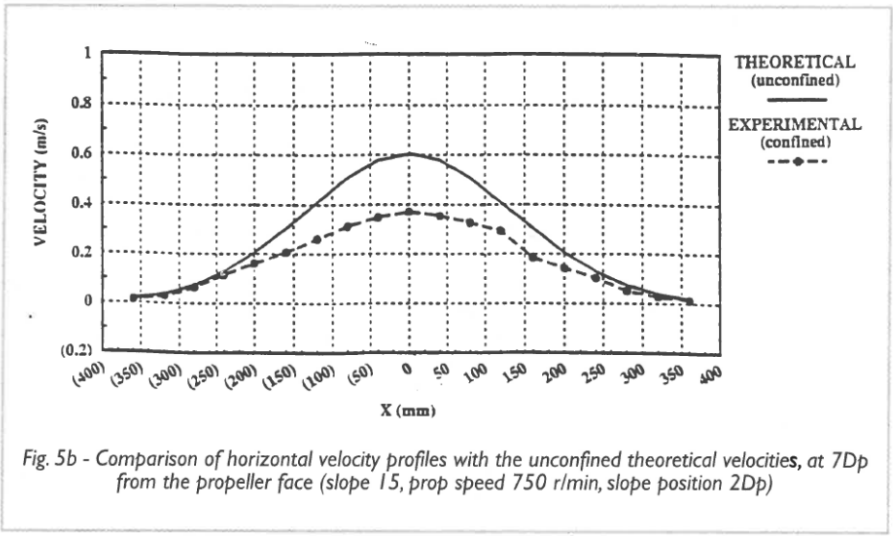

Fig. 5b - Comparison of horizontal velocity profiles with the unconfined theoretical velocities, at 7Dp from the propeller face (slope 15, prop speed 750 r/min, slope position 2Dp)

Figure B-15: HAMILL *et al.* [1996b]

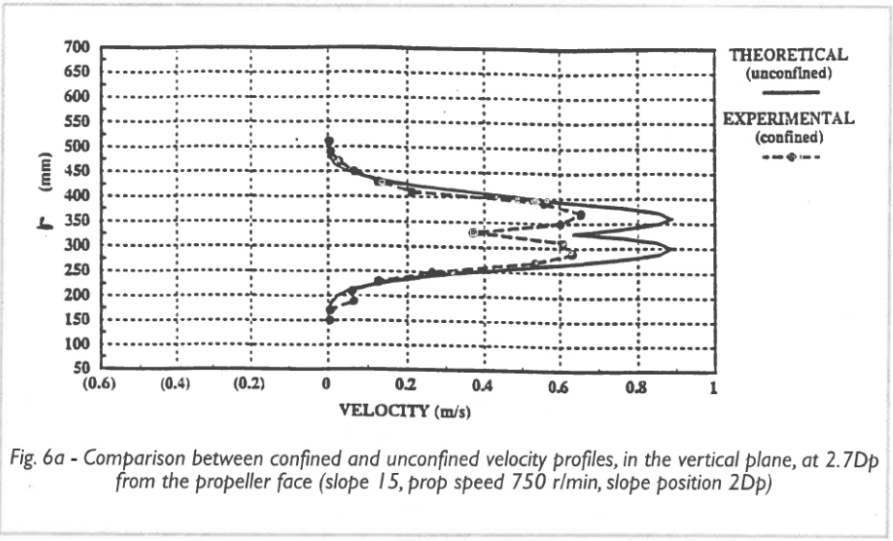

Fig. 6a - Comparison between confined and unconfined velocity profiles, in the vertical plane, at 2.7Dp from the propeller face (slope 15, prop speed 750 r/min, slope position 2Dp)

Figure B-16: HAMILL *et al.* [1996b]

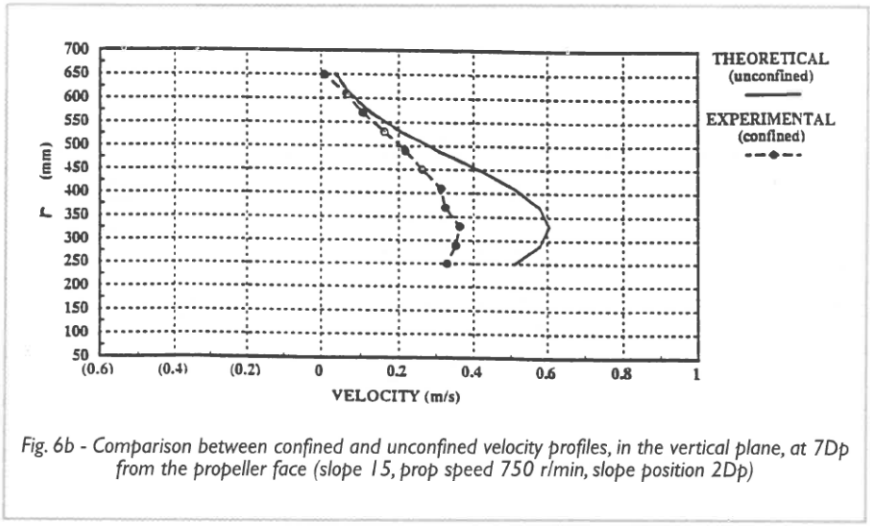

Fig. 6b - Comparison between confined and unconfined velocity profiles, in the vertical plane, at 7Dp from the propeller face (slope 15, prop speed 750 r/min, slope position 2Dp)

Figure B-17: HAMILL *et al.* [1996b]

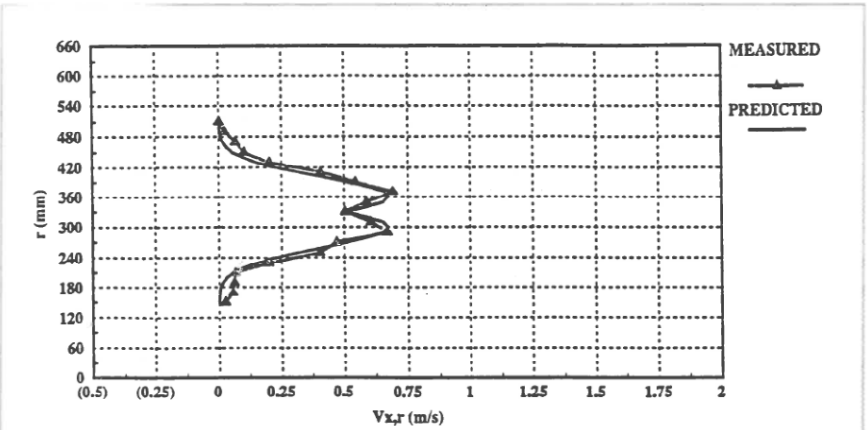

Fig. 7a - Checking the velocity distribution in the vertical plane in zone one at 3.05Dp from the propeller (slope 15, prop speed 750 r/min, slope position 5Dp)

Figure B-18: HAMILL *et al.* [1996b]

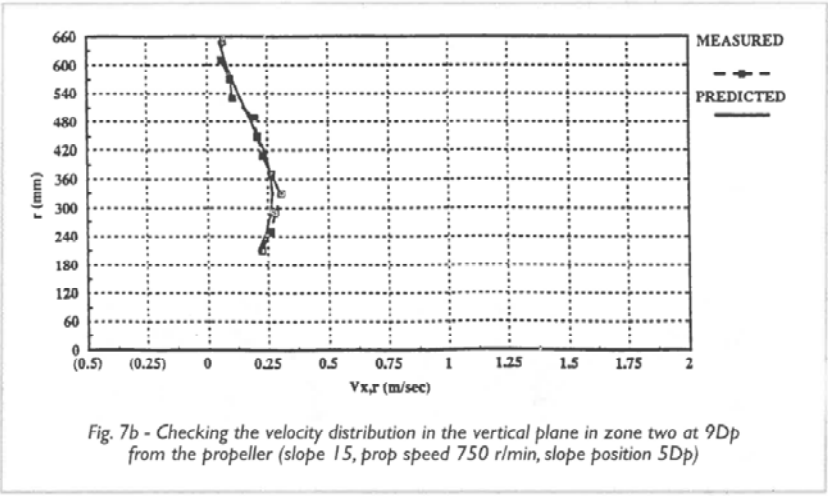

Fig. 7b - Checking the velocity distribution in the vertical plane in zone two at 9Dp from the propeller (slope 15, prop speed 750 r/min, slope position 5Dp)

Figure B-19: HAMILL *et al.* [1996b]

B.3.5 Turbulent fluctuations

Velocities can be written as an average velocity component and a fluctuation:

$$U = \overline{u} + u' \qquad \text{(B-74)}$$

Where:

U	total velocity component	[m/s]
$\overline{u}$	average value of U	[m/s]
u'	turbulent velocity fluctuation	[m/s]

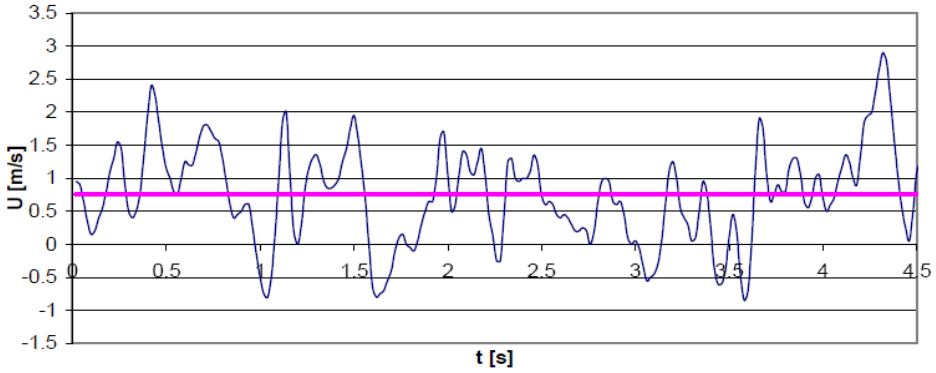

Figure B-20: Turbulence in a propeller jet by SCHOKKING *et al.* [2003]

Turbulence can be expressed in several forms such as:

$$k_t = \frac{1}{2} \cdot \left(\overline{u'^2} + \overline{v'^2} + \overline{w'^2} \right) \qquad \text{(B-75)}$$

Where:

k_t total kinetic energy in a turbulent flow [J/m^3]

A term to express turbulence is by the 'turbulence intensity':

$$\sqrt{\overline{u'^2}} \tag{B-76}$$

Another term is the so called 'relative turbulence'.

$$r_u = \frac{\sqrt{\overline{u'^2}}}{\overline{u}} \tag{B-77}$$

According to VERHEIJ [1985] the turbulence in a propeller jet is explained with low-frequent energy and high-frequent energy. At a jet from a circular opening turbulence occurs that is generated by the jet (low-frequent energy). For a propeller jet flow turbulence occurs caused by the jet (low-frequent energy) and by eddy flow (high-frequent energy).
The high-frequent energy is damping out first, which results for some distance behind the propeller a flow pattern where the low-frequent energy is dominating. For short distances behind the propeller plane $\left(x/D_0 < 20\right)$ eddies occur which are being formed at the tip of the propeller blades and just behind the propeller hub. Also eddies are present due to helicoidally eddies formed by the rotating propeller. One may assume that the hereby-induced turbulence in this area dominates the turbulence induced by a normal jet. These assumptions suggest that within short distance behind the propeller plane the spreading of the jet is larger than for a normal jet. After some distance, the spreading will be comparable to the spreading of a normal jet.

VERHEIJ [1985] presented the following equation by Abraham:

$$\tau = \rho \cdot \varepsilon_0 \cdot \overline{u} \cdot b \cdot \frac{\partial u}{\partial z} \tag{B-78}$$

Where:

ε_0	turbulent shear stress coefficient	[-]
w_A	width of a jet, $w = x \cdot k_s^{-\frac{1}{2}}$	[m]
ρ	density	[kg/m^3]
τ	turbulent shear stress	[N/m^2]

With $\partial u/\partial z \approx \overline{u}/w_A$ follows:

$$\tau :: \rho \cdot k_s^{-\frac{1}{2}} \cdot \overline{U}^2 \tag{B-79}$$

And:

$$\tau = \rho \cdot \left(u'\right)^2 \tag{B-80}$$

This results in:

$$u'/\overline{u} :: k_s^{-\frac{1}{4}} \tag{B-81}$$

Hereby the parameter k_s follows for the spreading of the jet:

$$k_s = \frac{1}{2 \cdot c_2^2} \tag{B-82}$$

VERHEIJ [1985] found with C_2 = 0.081 for a circular jet and C_2 = 0.18 for a propeller jet, a ratio of 1.5 for the difference in U' between a circular jet and a propeller jet.

BLAAUW and VAN DE KAA [1978] find a maximum relative turbulence intensity of 0.25 to 0.30 (at $x/D_0 = 6-8$. Van VAN VELDHOVEN [2002] found this value to be 0.18 in his tests.

Measurements from BLAAUW and VAN DE KAA [1978] show varying turbulence intensities for different radial distances from the propeller axis. Figure B-21 is an adapted figure from BLAAUW and VAN DE KAA [1978].

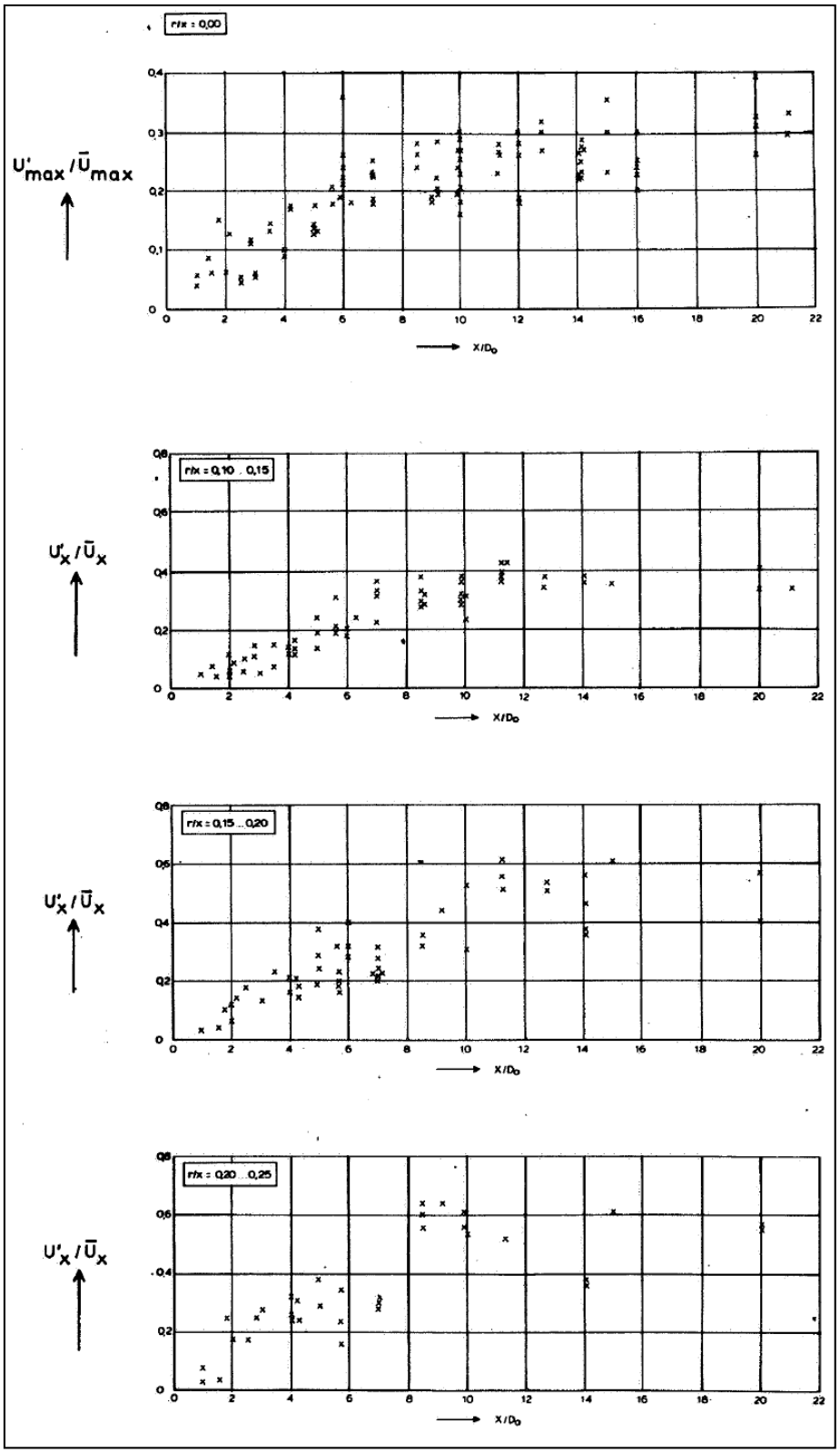

Figure B-21: Relative turbulence intensities in a propeller jet, from VERHEIJ [1985]

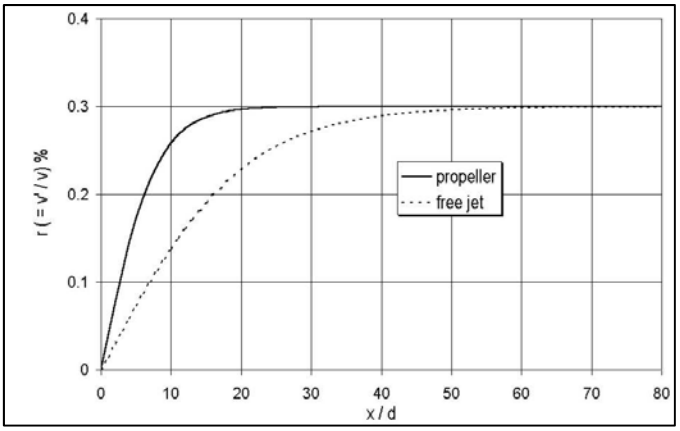

Figure B-22: Turbulence in propeller wash and free water jet by HINZE [1975]

SCHOKKING [2002] presented relative turbulences at the axis of a ducted propeller jet compared with a non-ducted propeller jet and a water jet as in Figure B-23. In fact, these jets were not free jets, because they were bounded by bed, water level and slope. Free should be replaced by non-ducted, in case of the propeller jet. In case of the water jet, free should be removed.

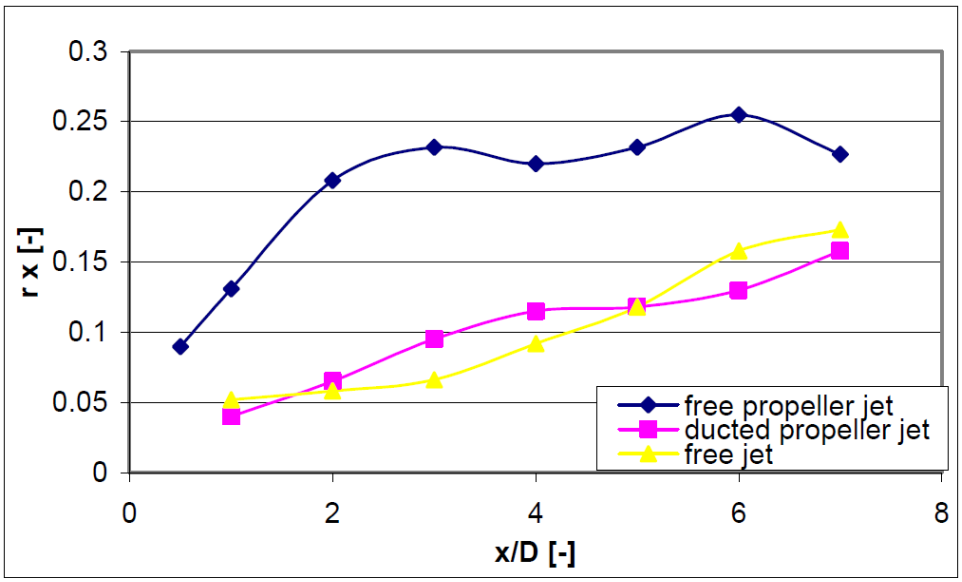

Figure B-23: Relative axial turbulence by SCHOKKING [2002]

This figure shows relative turbulence intensities for a ducted propeller jet comparable to a water jet.

LAM *et al.* [2010] measured velocities and turbulence intensity as in respectively Figure B-24 and Figure B-25.

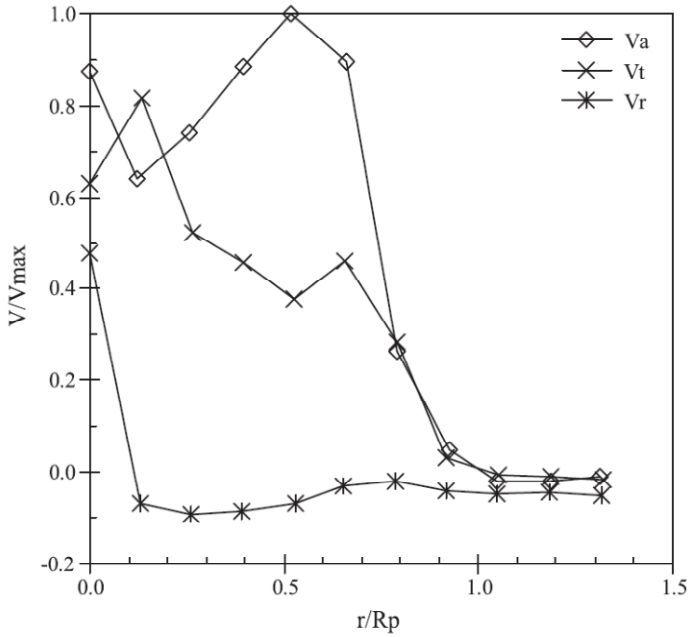

Figure B-24: Dimensionless time-averaged axial (Va), tangential (Vt) and radial (Vr) components of velocity at efflux plane by LAM *et al.* [2010]

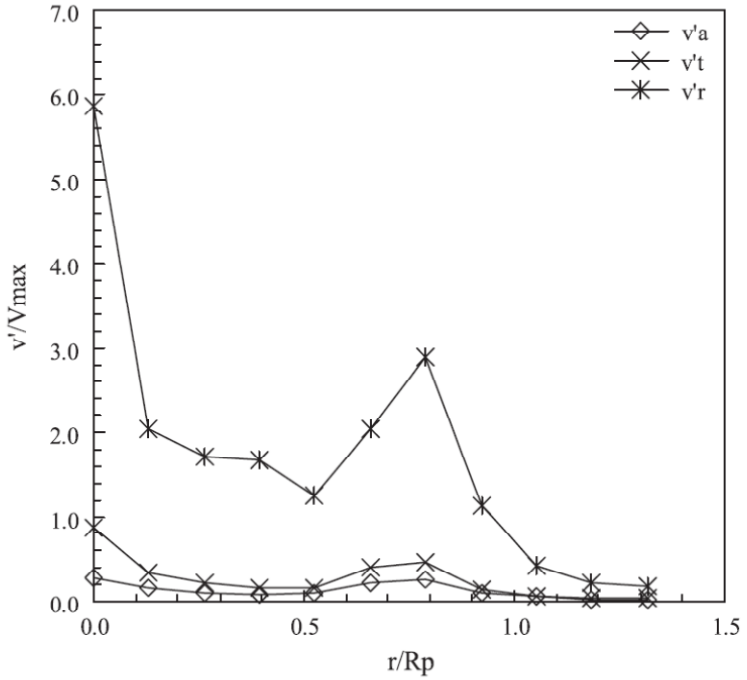

Figure B-25: Dimensionless axial (v'a), tangential (v't) and radial (v'r) components of turbulence intensity at efflux plane by LAM *et al.* [2010]

B.4 Overview

Efflux velocity

Source	Equation
Axial momentum theory, BLAAUW and VAN DE KAA [1978]	$U_0 = 1.60 \cdot n_p \cdot D_p \cdot \sqrt{K_T}$ or: $U_0 = C_3 \cdot \left(\frac{P}{\rho_w \cdot D_p^2} \right)^{1/3}$ with C_3 = 1.17 for ducted propellers, 1.48 for non-ducted propellers
Hamill (1987)	$U_0 = 1.33 \cdot n_p \cdot D_p \cdot \sqrt{K_T}$
STEWART *et al.* [1991]	$U_0 = C_1 \cdot n_p \cdot D_p \cdot \sqrt{K_T}$ $C_1 = D_p^{-0.0686} \cdot [P']^{1.519} \cdot [\beta]^{-0.323}$
HAMILL *et al.* [1996a]	$U_0 = C_1 \cdot n_p \cdot D_p \cdot \sqrt{K_T}$ $C_1 = \left[\frac{D_p}{D_h} \right]^{-0.403} \cdot [K_T]^{-0.179} \cdot [\beta]^{0.744}$
RÖMISCH [2001]	$U_0 = C_3 \cdot \left(\frac{P}{\rho_w \cdot D_p^2} \right)^{1/3}$ with C_3 = 1.19 – 1.37 depending on the thruster layout
CIRIA *et al.* [2007]	$U_0 = C_3 \cdot \left(\frac{P}{\rho_w D_0^2} \right)^{1/3}$ with C_3 = 1.17 for ducted propellers, 1.48 for non-ducted propellers
BAW [2011]	$U_0 \approx 1.1 \cdot \left(\frac{P}{\rho_w \cdot D_p^2} \right)^{1/3}$

Maximum axial flow velocity

	Establishing flow	Established flow
ALBERTSON *et al.* [1948] **0 - 6.2 - ...**	$U_{x,\max} = U_0$	$U_{x,\max} = U_0 \cdot \frac{1}{2 \cdot C_2} \cdot \left(\frac{x}{D_0}\right)^{-1.0}$
FUEHRER and RÖMISCH [1977] **0 – 2.6 - ...**	$U_{x,\max} = U_0$	$U_{x,\max} = 2.6 \cdot U_0 \cdot \left(\frac{x}{D_p}\right)^{-1.0}$
BLAAUW and VAN DE KAA [1978] **0 – 2.8 - ...**	$U_{x,\max} = U_0$	$U_{x,\max} = 2.78 \cdot U_0 \cdot \left(\frac{x}{D_p}\right)^{-1.0}$
Berger et al. (1981) **0 – 1.0 - ...**	$U_{x,\max} = U_0$	$U_{x,\max} = 1.025 \cdot U_0 \cdot \left(\frac{x}{D_p}\right)^{-0.6}$
VERHEIJ [1983] **0 – 1.5 - ...**	$U_{x,\max} = U_0$	$U_{x,\max} = 1.275 \cdot U_0 \cdot \left(\frac{x}{D_p}\right)^{-0.7}$
Hamill (1987) **0 – 2.0 - ...**	for $x/D_p < 0.35$: $U_{x,\max} = U_0$ and for $x/D_p > 0.35$: $U_{x,\max} = U_0 \cdot 0.87 \cdot \left(\frac{x}{D_p}\right)^{-\beta/4}$	$U_{x,\max} = U_0 \cdot A' \cdot \left(\frac{x}{D_p}\right)^{B'}$ $A' = -11.4 \cdot K_T + 6.65 \cdot \beta + 2.16 \cdot (P')$ $B' = -(1.0 \cdot K_T)^{-0.216} \cdot \beta^{1.024} \cdot (P')^{-1.0}$
Stewart (1992) **0 – 3.25 - 10**	$U_{x,\max} = U_0 \cdot \left[1.0172 - 0.1835\left(\frac{x}{D_p}\right)\right]$	$U_{x,\max} = U_0 \cdot \left[0.543 - 0.0281 \cdot \left(\frac{x}{D_p}\right)\right]$
Hashmi (1993) **0 – 3.25 - 16**	-	$U_{\max} = U_0 \cdot \left[0.638 \cdot \exp\left(-0.097 \cdot \left(\frac{x}{D_p}\right)\right)\right]$
Römisch (1993) **0 – 2.6 - ...**	$U_{x,\max} = U_0$	$U_{x,\max} = U_0 \cdot A_R \cdot \left(\frac{x}{D_p}\right)^{-C_4}$
HAMILL *et al.* [1996b] **0 – 3- ...**	$U_{x,\max} = U_0 \cdot \left(1.107 - 0.1835\left(\frac{x}{D_p}\right)\right)$	$U_{x,\max} = U_0 \cdot \left(0.543 - 0.0281 \cdot \left(\frac{x}{D_p}\right)\right)$
Schmidt (1998) **0 – 2- ...** **Bow thruster**	$U_{x,\max} = U_0$	$U_{x,\max} = U_0 \cdot 2.0 \cdot \left(\frac{x}{D_p}\right)^{-1.0}$
SCHOKKING [2002] **Bow thruster inclining slope**	-	$x/D > 6.0 : U_{x,\max} = 2.3 \cdot U_0 \cdot \left(\frac{x}{D_p}\right)^{-0.825}$
RÖMISCH [2006] **1 – 6.0 - ...**	$U_{x,\max} = U_0 \cdot 1.9 \cdot \left(\frac{x}{D_p}\right)^{-C_4}$	$U_{x,\max} = U_0 \cdot 2.3 \cdot \left(\frac{x}{D_p}\right)^{-0.825}$
LAM *et al.* [2011] **0 – 3.68 - ...**	$U_{x,\max} = U_0 \cdot \left[1 - 0.1592\left(\frac{x}{D_p}\right)\right]$	-
BAW [2011] **0 – 1.0 - ...** **Bow thruster inclining slope**	$U_{x,\max} = U_0$ $x/D > 1.0 : U_{x,\max} = U_0 \cdot \left(\frac{x}{D_p}\right)^{-1/3}$	-

Velocity distribution by propeller jet

	Establishing flow	Established flow
BLAAUW and VAN DE KAA [1978] 0 – 2.8 - ...	-	With C_2 = 0.18 this results in: $U_{x,r} = U_{x,\max} \cdot \exp\left[-15.43 \cdot \left(\frac{r}{x}\right)^2\right]$
Hamill (1987) 0 – 2.0 - ...	$U_{x,r} = U_0 \cdot \exp\left[\frac{-(r - R_{m0})^2}{2 \cdot (\sigma)^2}\right]$ up to 0.5 Dp: $U_{x,r} = U_{\max} \cdot \exp\left[\frac{-(r - R_{m0})^2}{2 \cdot (R_{m0}/2)^2}\right]$ beyond 0.5 D_p: $U_{x,r} = U_{\max} \cdot \exp\left[\frac{-(r - R_{m0})^2}{2 \cdot \left(\frac{R_{m0}}{2} + 0.075(x - R)\right)^2}\right]$	-

Velocity distribution for a free circular jet

	Establishing flow	Established flow
ALBERTSON *et al.* [1948] 0 - 6.2 - ...	$U_{x,r} = U_{x,\max} \cdot \exp\left[-\frac{r^2}{2 \cdot \sigma^2}\right]$ $U_{x,r} = U_0 \cdot \exp\left[-\frac{\left(r + C_2 \cdot x - \frac{D_0}{2}\right)^2}{2 \cdot (C_2 \cdot x)^2}\right]$	$U_{x,r} = U_{x,\max} \cdot \exp\left[-\frac{1}{2 \cdot C_2^2}\frac{r^2}{x^2}\right]$ With C_2 = 0.081 this results in: $U_{x,r} = 6.2 \cdot \left(\frac{D_0}{x}\right)^{1.0} \cdot U_0 \cdot \exp\left(-69 \cdot \left(\frac{r}{x}\right)^2\right)$

Velocity distribution for a water jet

	Establishing flow	Established flow
VERHEIJ [2010] High powered jets	-	$U_{x,r} = 12.4 \cdot \left(\frac{1}{x}\right)^{1.17} \cdot U_0 \cdot \exp\left(-92.8 \cdot \left(\frac{r}{x}\right)^2\right)$
Low powered jets	-	$U_{x,r} = 2.8 \cdot \frac{D_0}{(x)^{0.85}} \cdot U_0 \cdot \exp\left(-25 \cdot \left(\frac{r}{x}\right)^2\right)$

Maximum bed velocity for one propeller

	Establishing flow	With
BLOKLAND [1997]	$U_{b,\max} = f_p \cdot C_5 \cdot U_0 \cdot \frac{D_0}{h_{pb}}$	C_5 = 0.306 by Blokland [1997] f_p = 100% for bow thrusters
CIRIA *et al.* [2007]	$U_{b,\max} = C_5 \cdot U_0 \cdot \left(\frac{D_0}{h_{pb}}\right)^{\gamma}$	Two varying parameters: C_5 = 0.3 by Blaauw and Van de Kaa [1978] γ = 1.0

Velocity distribution influenced by a slope

	Establishing flow	Established flow
BLOKLAND [1997] 0 – 2.8 - …		$U_{b,\max} = a \cdot \frac{U_0 \cdot D_0}{L} \cdot \frac{\exp\left(-\frac{b}{\alpha_m^2} \cdot \left(\frac{L}{x_{\max}} - 1\right)^2\right)}{x_{\max}/L}$ $\frac{x_{\max}}{L} = \frac{b}{\alpha_m^2} \cdot \left(\sqrt{1 + 2 \cdot \frac{\alpha_m^2}{b}} - 1\right)$ $U_{b,\max} = 2.897 \cdot \frac{U_0 \cdot D_0}{L}$ if a = 2.8, b = 15.4 and α_m = 1.5
HAMILL *et al.* [1996b] 0 – 3.0 - …	$U_{x,\max} = U_0 \cdot \left(A - B \cdot \left(\frac{x}{D_p}\right)\right)$ $A = 1.107$ $B = 0.1835 \cdot (1 + \tan\alpha)^{-1.03} \cdot \left(1 + \frac{D_p}{x_R}\right)^{4.865}$	$U_{x,\max} = U_0 \cdot \left(A - B \cdot \left(\frac{x}{D_p}\right)\right)$ $A = 0.543(1 + \tan\alpha)^{1.968} \cdot \left(1 + \frac{D_p}{x_R}\right)^{-9.13}$ $B = 0.0281(1 + \tan\alpha)^{2.725} \cdot \left(1 + \frac{D_p}{x_R}\right)^{-6.3}$

Appendix C Scour around piles

At open quay structures, piles form obstacles for the flow. This results in a contraction of the flow between the piles and horseshoe vortices around the piles.
This jet scour consists of two basic mechanisms. The pile obstruction is dominated by the down flow and the horseshoe vortex. The jet diffusion is controlled by bed shear stress.
The scour process by the pile obstruction is initiated due to local flow acceleration and the formation of a down flow and horseshoe vortex around the pile.
The erosion process by the diffusion mechanism is caused by the action of the shear stress and turbulence

In case of a much smaller pile diameter than the water depth, which is the case for these kind of constructions HOFFMANS and VERHEIJ [1997] presented an equation to estimate the final scour depth:

$$S = 2.0 \cdot D \qquad \text{(C-1)}$$

Where:

S	final scour depth	[m]
D	pile diameter	[m]

When the spacing between the piles is larger than 5 D, the scour holes of the individual piles do not influence each other. For open quay constructions regularly have a spacing of about 10 D.
In case of a smaller distance between the piles than 5 D, the different effects should be included:

$$S = 2.0 \cdot K_i \cdot D \qquad \text{(C-2)}$$

In the Scour Manual by HOFFMANS and VERHEIJ [1997] the case of a single cylindrical pier has been used as a reference and deviations to this case are expressed in K-factors:

$$K_i = K_s \cdot K_\omega \cdot K_g \cdot K_{gr} \qquad \text{(C-3)}$$

Where:

K_g	factor for the influence of gradation of bed material	[-]
K_{gr}	factor for the influence of a group of piers	[-]
K_i	correction factor	[-]
K_s	pier shape factor	[-]
K_ω	factor for orientation of the pier to the flow	[-]

Since this investigation is focused on piers of quay constructions, only cylindrical and square piles will be included.
For rectangular piles, the shape factor K_s is 1.1. The factor K_ω is 1 for a single pile, because of the symmetrical shape of the piles.
The influence of gradation of bed material is dependent on the geometric standard deviation:

$$\sigma_g = \frac{D_{84}}{D_{50}} \qquad \text{(C-4)}$$

For a single grain size, this factor is 1.

Figure C-1 shows the vertical flow velocities measured by CHIN *et al.* [1996]. In this figure, flow velocities are given for the situation with a flat bed before any erosion has occurred and the velocities in a situation with a scour hole are presented. Remark here is that CHIN *et al.* [1996] investigated a situation with the pipe situated at the bottom, which is not the case for the tunnel of a bow thruster.

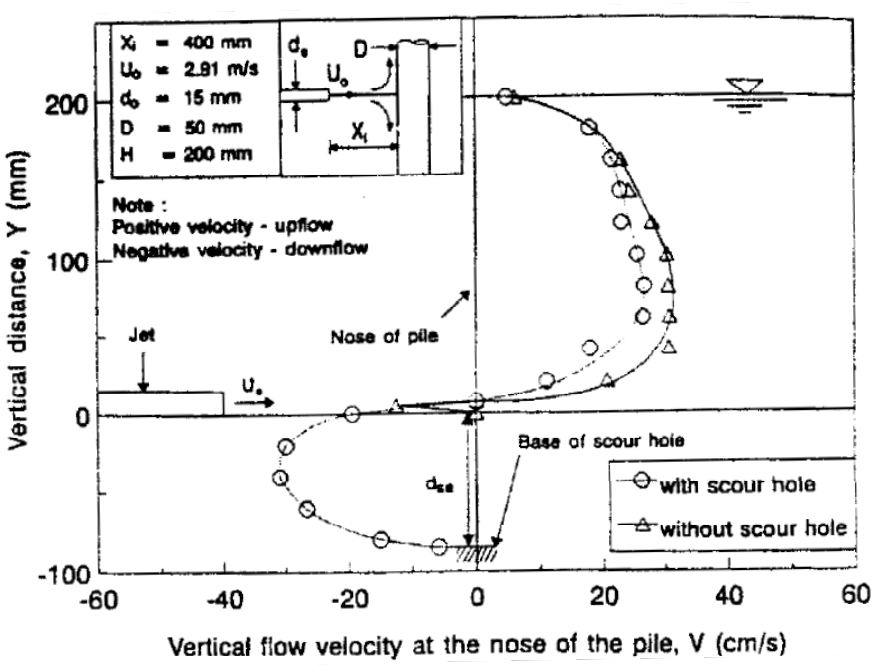

Figure C-1: Vertical flow velocity at nose of pile by CHIN *et al.* [1996]

CHIN *et al.* [1996] found that the densimetric Froude number has a large influence on the scour around vertical piles.

$$F_0 = \frac{U_0}{\sqrt{g \cdot D_{50} \cdot \left(\frac{\rho_s - \rho_w}{\rho_w}\right)}} \qquad \text{(C-5)}$$

Where:

F_0	densimetric Froude number	[-]
U_0	flow directly behind a propeller, located at the point of maximal contraction of the jet	[m/s]
g	acceleration due to gravity	[m/s^2]
D_{50}	sieve diameter, diameter of stone that exceeds the 50% value of sieve curve	[m]
ρ_s	density of stones	[kg/m^3]
ρ_w	density of water	[kg/m^3]

CHIN *et al.* [1996] found F_0 to be the predominant parameter affecting the maximum equilibrium scour depth. The relation for this was found:

$$\frac{d_{se}}{d_0} = 0.21 \cdot F_0 \qquad \text{(C-6)}$$

Where:

d_{se}	maximum equilibrium scour depth of scour hole	[m]
d_0	diameter of the jet	[m]

CHIN *et al.* [1996] found the effect of the pile diameter on the scour hole depth to be negligible.

C.1.1 Pile groups

The factor for influence of a group of piers has been investigated and for example the maximum scour depth around the front pier will increase will increase by a maximum of 15% if there is a second pier within 2 to 3 D behind the front pier. In Figure C-2 several values for the factor K_{gr} are given. 'b' in this figure is the diameter D of the pier or pile. The second scenario consists of two piers with an angle of attack of 45°.

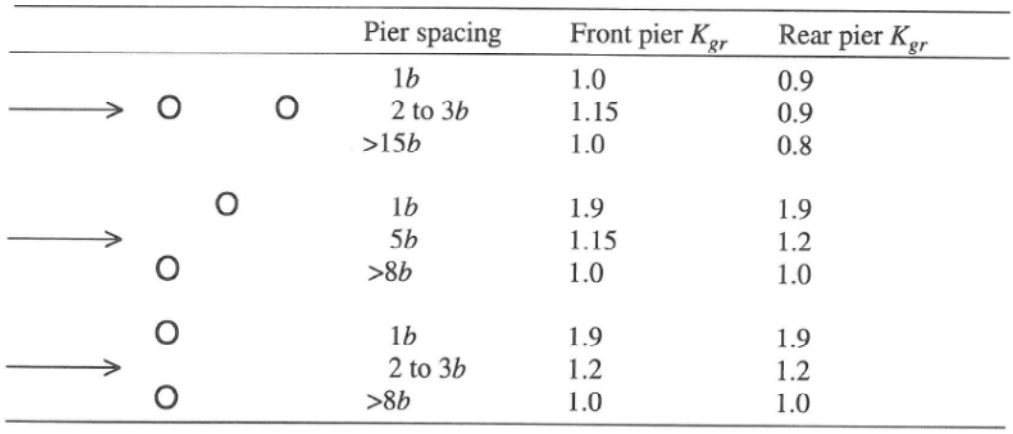

	Pier spacing	Front pier K_{gr}	Rear pier K_{gr}
→ O O	1*b*	1.0	0.9
	2 to 3*b*	1.15	0.9
	>15*b*	1.0	0.8
→ O	1*b*	1.9	1.9
	5*b*	1.15	1.2
O	>8*b*	1.0	1.0
O	1*b*	1.9	1.9
→	2 to 3*b*	1.2	1.2
O	>8*b*	1.0	1.0

Figure C-2: The factor Kgr for a group of 2 piles by HOFFMANS and VERHEIJ [1997]

By FWHA [2001] a group of piles has influence on the correction factor for the attack angle and the shape factor. The correction factor for the angle of attack reads:

$$K_{\omega} = \left(\cos\omega + L_p/D \cdot \sin\omega\right)^{0.65} \qquad \text{(C-7)}$$

By HOFFMANS and VERHEIJ [1997] Froehlich (1988) has given:

$$K_{\omega} = \left(\cos\omega + L_p/D \cdot \sin\omega\right)^{0.62} \qquad \text{(C-8)}$$

Where:

ω	angle of flow attack	[-]
L_p	length of the pier or pile	[-]

FWHA [2001] gives the following approach to determine L_p, where in Figure C-3 a = D.

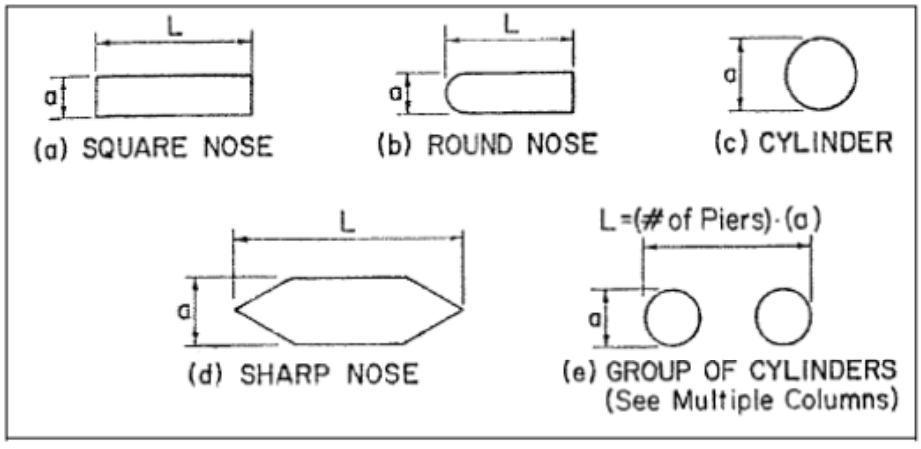

Figure C-3: Common pier shapes by FWHA [2001]

FWHA [2001] recommends for scour at a pile group:

$$K_{gr} = 0.57 \cdot \left(1 - \exp\left[\frac{-G}{D}\right]\right) + \exp\left[\frac{-0.5 \cdot G}{D}\right] \quad \text{(C-9)}$$

Where:

G	spacing between piles	[m]
D	pile diameter	[m]

C.1.2 Increase in flow velocity

By a strong simplified view at the flow velocity between piles, an increase in flow velocity occurs between the piles. Because of a decreased flow area because of obstruction by the piles, the flow velocity increases when the flow rate is assumed constant.

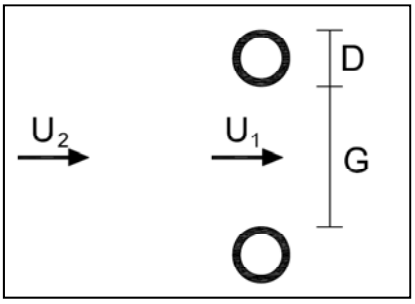

$$U_1 = \left(\frac{G + \alpha_P \cdot D}{G}\right) \cdot U_2 \quad \text{(C-10)}$$

Where:

U_2	undisturbed mean flow velocity	[m/s]
U_1	disturbed mean flow velocity	[m/s]
α_P	coefficient	[-]
G	spacing between piles	[m]
D	pile diameter	[m]

Piles in the scale model have a diameter of 0.03 m and a centre-to-centre distance of 0.20 m. For a situation with piles, the available 'flow area' thereby reduces to 75 % of the original area. If this approach would be valid, the flow velocity for the situation with piles would be 133 % of the original flow velocity without piles.
A local increase in flow velocity results in a decrease in a local turbulence intensity.

Appendix D Forces and stability

When a stone is exposed to a flow, several hydrodynamic forces may be considered as for example described in SCHIERECK [2004]. In Figure D-1 these forces are the forces acting on a stone schematically given.

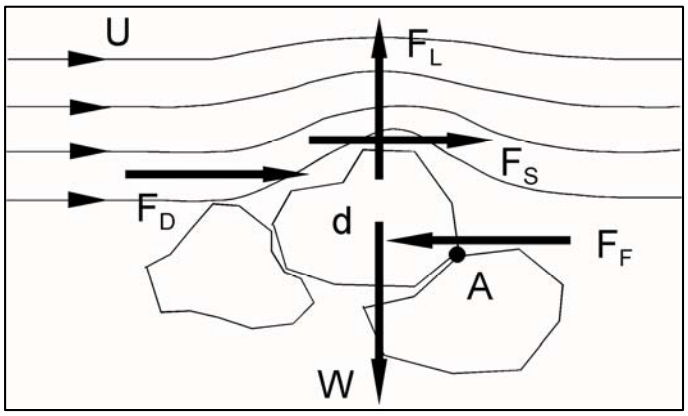

Figure D-1: Forces on a grain in flow SCHIERECK [2004]

A drag, shear and lift force have the forms:

$$F_D = \frac{1}{2} \cdot C_D \cdot A_D \cdot \rho_w \cdot u \cdot |u| \quad \text{(D-1)}$$

$$F_S = \frac{1}{2} \cdot C_S \cdot A_S \cdot \rho_w \cdot u \cdot |u| \quad \text{(D-2)}$$

$$F_L = \frac{1}{2} \cdot C_L \cdot A_L \cdot \rho_w \cdot u \cdot |u| \quad \text{(D-3)}$$

Where:

C_D	drag coefficient	[-]
C_S	shear coefficient	[-]
C_L	lift coefficient	[-]
A_D	exposed surface area to drag, proportional to $\sqrt{D_{50}}$	[m^2]
A_L	exposed surface area to lift, proportional to $\sqrt{D_{50}}$	[m^2]
u	velocity near the grain	[m/s]

As investigated by HOAN [2008], these forces can be considered as in Figure D-2. Further in this appendix, the investigation by Hoan is explained.

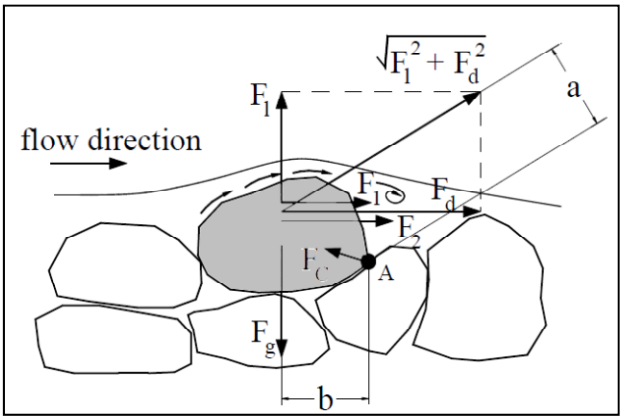

Figure D-2: Forces acting on particles resting on a bed surface by HOAN [2008]

A frictional force F_1 is presented on the rough surface of the stone. When the particle Reynolds number is less than 3.5, this surface friction is the main force acting on a stone. In the case that this Reynolds number is larger than 3.5, "separation of streamlines in the form of a small wake occurs behind the top of the particles and vortexes form there. This causes a pressure difference between the front and the back surface of the particle, forming the resistance F_2." As a resultant of F_1 and F_2 the drag force F_D remains. The frictional force F_1 can be neglected in case that the Reynolds number is larger than around 500.

D.1 Izbash

Izbash and Shields give values for stability of stones in flow conditions. With the original Izbash equation (with equivalent forms):

$$\Delta \cdot g \cdot D_{50} = \frac{\beta_{Iz}}{2} \cdot \bar{u}^{-2} \qquad \text{(D-4)}$$

In this original equation by Izbash, the squared time averaged velocity is used. Which is not the maximum bed velocity as used in the equation by BLOKLAND [1997]. For the original Izbash relation β_{iz} = 0.7 is valid.

IGWR uses the following method by BLOKLAND [1997] to dimension the bed protection by armour stone (Izbash method):

$$D_{50} \geq \beta_{is,cr} \cdot m_h \cdot \frac{U_{b,\max}^2}{2 \cdot g \cdot \Delta} \qquad \text{(D-5)}$$

With a slope coefficient to include the flow direction at the slope according to CIRIA *et al.* [2007]

$$m_h = \frac{\tan(\varphi_s)}{\cos(\theta_u) \cdot \sin(\alpha) + \sqrt{\cos^2(\alpha) \cdot \tan^2(\varphi_s) - \sin^2(\theta_u) \cdot \sin^2(\alpha)}} \qquad \text{(D-6)}$$

Hereby a factor $m_h = \left(1 - \frac{\sin^2 \alpha}{\sin^2 \varphi_s}\right)^{-0.5}$ follows for flow parallel to a slope.

For flow directed upwards to a slope: $m_h = \frac{\sin \varphi_s}{\sin(\varphi_s + \alpha)}$

Where:

$\beta_{Is,cr}$	critical stability coefficient	[-]
β_{Iz}	original stability coefficient for Izbash equation (= 0.7)	[-]
D_{50}	median rock diameter	[m]
Δ	relative density of rock	[-]
$U_{b,\max}$	maximum flow velocity along horizontal bed	[m/s]
m_h	slope coefficient	[-]
θ_u	angle of velocity component, where 0 = upwards slope	[°]
α	slope angle	[°]
φ_s	angle of repose (for armour stone 40° - 42°)	[°]

In the Izbash equation the location of the velocity in the water column is not clear, as a jet flow.

D.2 Shields

The Shields (1936) formula is widely used to determine the required stone size for a bed protection. This formula considers only the near bed shear stress as representing quantity for the flow forces. Research had shown that not only the near bed shear stress (mean velocity) but also turbulence affects the stability of the bed protection.

$$\psi_s = \frac{\tau_b \cdot D^2}{g \cdot (\rho_s - \rho_w) \cdot D^3} = \frac{\tau_b}{\rho_w \cdot \Delta \cdot g \cdot D} \qquad \text{(D-7)}$$

With the bed shear stress as $\tau_b = \rho \cdot u_*^2$, this results in:

$$\psi_s = \frac{u_*^2}{\Delta \cdot g \cdot D} \qquad \text{(D-8)}$$

D.3 Hoan

Research of HOAN [2008] resulted in new formulas for the stability parameter. This research is based on earlier research by Jongeling and Hofland. Jongeling, Hofland and Hoan extended the Shields relation for use in situations with turbulence.

Jongeling et al. (2004) found a criterion for non-uniform flow:

$$\Psi_{wl} = \frac{\left\langle \left(\bar{u} + \alpha_T \sqrt{k} \right)^2 \right\rangle_{hm}}{\Delta \cdot g \cdot D_{n50}} \tag{D-9}$$

$$with\ \alpha_T = 6\ and\ h_m = 2 \cdot D_{n50} + 0.2h \quad \Rightarrow \quad \psi_{WLcrit} = 8$$

$$k = \frac{1}{2}\left(\overline{u'^2} + \overline{v'^2} + \overline{w'^2} \right) \tag{D-10}$$

Hofland (2005) defined a large eddy near the bottom for the equation by Jongeling in order to determine the stability coefficient:

$$\Psi_{Lm} = \frac{\max\left[\left\langle \bar{u} + \alpha_T \sqrt{k} \right\rangle_{Lm} \frac{L_m}{2} \right]^2}{\Delta \cdot g \cdot D_{n50}} \tag{D-11}$$

$$L_m = \kappa z \sqrt{1 - \frac{z_b}{h}} \tag{D-12}$$

HOAN [2008] found:

$$\Psi_{u-\sigma[u]} = \frac{\left\langle \left[\bar{u} + \alpha_T \cdot \sigma(u) \right]^2 \sqrt{1 - \frac{z_b}{h}} \right\rangle_h}{\Delta \cdot g \cdot D_{n50}} \tag{D-13}$$

The mean velocity $\bar{U}$ is computed as:

$$\bar{U} = \frac{1}{N} \sum_{i=1}^{N} u(i) \tag{D-14}$$

The velocity fluctuation u'(i) is obtained as:

$$U'(i) = u(i) - \bar{U} \tag{D-15}$$

The turbulence intensity of u is defined as $\sqrt{\overline{u'^2}}$ and is therefore identical to the standard deviation of u:

$$\sigma(u) = \sqrt{\frac{1}{N}\left[\sum_{i=1}^{N} u(i) - \bar{u} \right]^2} = \sqrt{\overline{(u')^2}} \tag{D-16}$$

Where:

ψ_s	Shields number	[-]
D_{n50}	median nominal diameter	[m]
$\bar{u}$	velocity averaged	[m/s]
α_T	turbulence coefficient	[-]
k	kinetic turbulent energy	[m^2/s^2]
L_m	Bakmetev mixing length	[m]
κ	Von Kármán constant (≈0.38)	[-]
z_b	distance from bed	[m]
α	slope angle	[°]
φ_s	angle of repose (for armour stone 40° - 42°)	[°]

This results in the following equations for a practical purpose:

$$D_{n50} = \frac{\left(K_v \langle \bar{u} \rangle_h\right)^2}{K_s \Delta \Psi_{s,c} C^2} \text{ (based on original Shields equation, by Schiereck [2004])} \quad \text{(D-17)}$$

$$D_{n50} = \frac{\left\langle \left[u + \alpha\sigma(u)\right]^2 \sqrt{1 - \frac{z}{h}} \right\rangle_h}{\Delta g \Psi_{Hoan,c} C^2} \text{ (by Hoan)} \quad \text{(D-18)}$$

With:

$\psi_{Hoan} = 2.9$ $\alpha = 3$ and C = Chezy coeffcient $\left[m^{1/2}/s\right]$

HOAN [2008] compared the method of Shields and Hoan, as showed in Figure D-3 and Figure D-4.

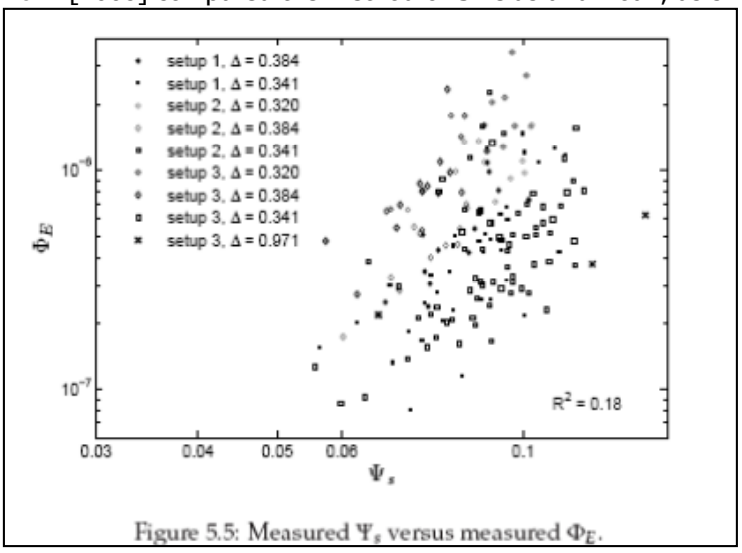

Figure D-3: Shields, by HOAN [2008]

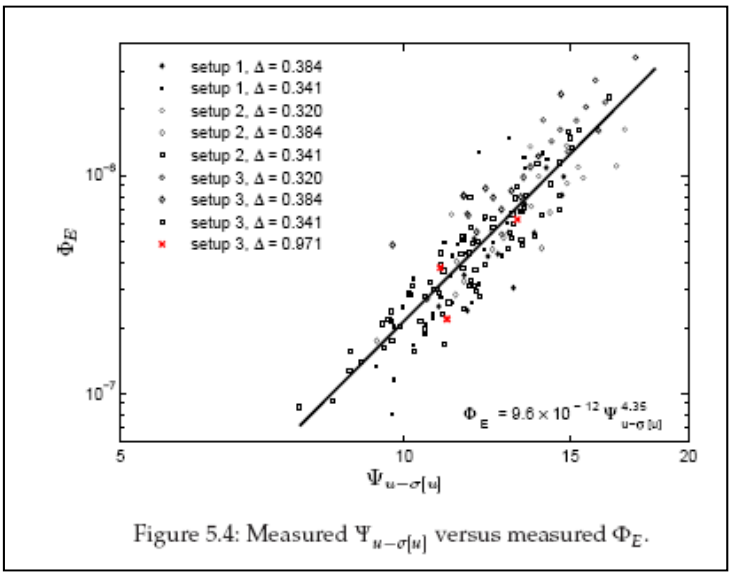

Figure D-4: Hoan, by HOAN [2008]

Hoan concluded that the Shields stability parameter is not sufficient in order to present the flow forces acting on a bed in non-uniform flow. Conventional turbulence correction does not physically explain the influence of turbulence. The method described by Hoan has physically explained and quantitatively better described the impact of flow on stone stability.

D.4 Stability for a propeller jet

In the first paragraphs of this chapter, 'standard' methods to determine the required bed protection are treated. For the stability of a bed protection loaded by a propeller jet, additional research is done in the past. In this paragraph is dealt with several methods focused on propeller jets.

WL [1988] equation II.91 gives for a propeller jet the following equation to determine the stability of bed material, based on performed investigation:

$$D_{50} \geq 3.0 \cdot m_h \cdot \frac{U_{b,\max}^2}{2 \cdot g \cdot \Delta} \qquad \text{(D-19)}$$

In other literature, also the following form is found:

$$D_{n50} \geq 2.5 \cdot m_h \cdot \frac{U_{b,\max}^2}{2 \cdot g \cdot \Delta} \qquad \text{(D-20)}$$

with $D_{n50} \approx 0.84 \cdot D_{50} \quad \Rightarrow (0.84 \cdot 3.0 = 2.5)$

This factor 3 translated to the Shields parameter results in:
$\psi_s \approx 0.045$ (which means that some transport is acceptable)
BLOKLAND [1997] also uses the factor 3.0 as given above for situations where almost no transport of stones is allowed and decreases this to 2.5 for situations where some movement of stones is allowed or the frequency of the design load is low.

In addition, for more detailed design the following (rewritten) equation from VERHEIJ [1985]:

$$D_{50} \geq \frac{2}{\beta_s^2} \cdot m_h \cdot \frac{U_{b,\max}^2}{2 \cdot g \cdot \Delta}$$

with $\beta_s = 0.55$ for hardly any transport (D-21)
and $\beta_s = 0.70$ for some transport time by time
the factor 3.0 follows when using $\beta_s = 0.81$

From WL [1988]: "Hereby the use of the factor 3.0 results in an increase of stone transport, but this is still considered acceptable".

WL [1988] equation II.93 gives also a method by using the acceptable amount of bed transport (rewritten):

$$\frac{U_{b,\max}^2}{(g \cdot \Delta \cdot D_{50})^{0.5}} \leq 2.4 \cdot \phi^{0.103} \quad \Rightarrow \quad D_{50} \geq \frac{1}{2.88 \cdot \phi^{0.206}} \cdot m_h \cdot \frac{U_{b,\max}^2}{2 \cdot g \cdot \Delta} \qquad \text{(D-22)}$$

This method is based on the Paintal (1971) formula. SCHIERECK [2004] gives for this:

$$\phi_s = 6.56 \cdot 10^{18} \cdot \psi^{16} \text{ for } \psi < 0.05 \qquad \text{(D-23)}$$

$$\phi_s = 13 \cdot \psi^{2.5} \text{ for } \psi > 0.05 \qquad \text{(D-24)}$$

$$\text{with } \phi_s = \frac{q_s}{\sqrt{\Delta \cdot g \cdot d^3}} \qquad \text{(D-25)}$$

One important remark is that the Paintal formula is derived for uniform flow. A propeller jet is clearly non-uniform. For the threshold of motion, a value of 0.03 for ψ_c is considered as a safe choice. This gives a value of $2.82*10^{-6}$ for the dimensionless entrainment rate.

For example with a dimensionless entrainment rate of respectively 10^{-5} and $2.82*10^{-6}$ this results in:
$\frac{1}{2.88 \cdot \phi^{0.206}} = 2.31$ and $\frac{1}{2.88 \cdot \phi^{0.206}} = 4.83$
In other words, the factor $\beta_{Is,cr}$ would be respectively 2.31 and 4.83 in this case. For the 'safe' 4.83 this would result in relatively large stones.

D.4.1 Entrainment rate

Hoan performed research for non-uniform flow situations. The dimensionless entrainment rate is defined by HOAN [2008] as:

$$\phi_E = \frac{E}{\sqrt{\Delta g d}} \qquad \text{(D-26)}$$

with

$$E = \frac{n_E d^3}{A_E T_E} \qquad \text{(D-27)}$$

Where:

ϕ_E	dimensionless entrainment rate	[-]
E	entrainment rate	[-]
Δ	relative density of rock	[-]
g	acceleration due to gravity	[m/s^2]
d	stone, particle diameter	[m]
n_E	number of stones picked up per unit of time and area	[-]
A_E	area	[m^2]
T_E	period	[s]

For ϕ_s (Paintal, uniform flow) the following values are given by WL [1988], figure 18:

Transport criterion		ϕ_s
1	occasional movement at some locations	10^{-5}
2	frequent movement at some locations	$5 \cdot 10^{-5}$
3	frequent movement at several locations	10^{-4}
4	frequent movement at many locations	$5 \cdot 10^{-4}$
5	frequent movement at all locations	10^{-3}
6	continuous movement at all locations	$5 \cdot 10^{-3}$
7	general transport of the grains	10^{-2}

Table D-1: Transport parameters

D.4.2 Turbulence in Izbash relation

When turbulent fluctuations are included in this equation, the velocity component has to be rewritten. VERHAGEN [2001] states that in reality turbulence should be included in the Izbash relation by using:

$$\overline{u^2} = \overline{\left(\overline{u} + u'\right)^2} = \overline{\overline{u}^2} + \overline{2\overline{u}u'} + \overline{u'^2} = \overline{\overline{u}^2} + 2\overline{u} \cdot \overline{u'} + \overline{u'^2} = \overline{\overline{u}^2} + 2\overline{u} \cdot 0 + \overline{u'^2} = \overline{u}^2 + \overline{u'^2} \qquad \text{(D-28)}$$

This results in:

$$\Delta \cdot g \cdot D_{50} = \frac{\beta_{Iz}}{2} \cdot \left(\overline{u}^2 + \overline{u'^2}\right) \qquad \text{(D-29)}$$

And with the relative turbulence intensity:

$$r = \frac{\sqrt{\overline{u'^2}}}{\overline{u}} \qquad \text{(D-30)}$$

$$\Rightarrow \Delta \cdot g \cdot D_{50} = \frac{\beta_{Iz}}{2} \cdot \left(1 + r^2\right)\overline{u}^2 \qquad \text{(D-31)}$$

Where:

β_{Iz}	original stability coefficient for Izbash equation (= 0.7)	[-]
$\overline{u}$	average value of u	[m/s]
u'	turbulent velocity fluctuation	[m/s]

When we assume that the stability is depending on the maximum flow velocity peaks instead of the squared time averaged velocity, the following can be stated:

$$u_{max} = \overline{u} + p \cdot \sigma_u \qquad \text{(D-32)}$$

with $\sigma_u = \sqrt{\overline{u'^2}}$, the standard deviation or also turbulence intensity

This results in:

$$\Delta \cdot g \cdot D_{50} = \frac{\beta_{Iz}}{2} \cdot \left(\overline{u} + p \cdot \sqrt{\overline{u'^2}}\right)^2 \qquad \text{(D-33)}$$

Or with the relative turbulence intensity included:

$$\Delta \cdot g \cdot D_{50} = \frac{\beta_{Iz}}{2} \cdot \left(1 + p \cdot r\right)^2 \cdot \overline{u}^2 \qquad \text{(D-34)}$$

VERHAGEN [2001] stated that for the original Izbash relation a relative turbulence intensity of 0.1 is reasonable to assume. Using equation (D-31) this results in a β coefficient without turbulence:

$$\beta_{Iz} = \left(1 + r^2\right) \cdot C \Leftrightarrow 0.7 = \left(1 + 0.1^2\right) \cdot 0.693 \qquad \text{(D-35)}$$

Here the result is a factor C, which is with 0.693 almost equal to 0.7.

However, this should be:

$$\beta_{Iz} = \left(1 + p \cdot r\right)^2 \cdot \beta_{Iz,0,p} \Leftrightarrow 0.7 = \left(1 + p \cdot 0.1\right)^2 \cdot \beta_{Iz,0,p} \qquad \text{(D-36)}$$

Because Izbash uses $D_{50} \propto \overline{u}^2$ and not $D_{50} \propto \overline{u^2}$.

Which results for example in a new β coefficient $\beta_{Iz,0,p}$ = 0.41 in case p = 3.
The value of $\beta_{Iz,0,p}$ depends on the assumed value of p.

Appendix E Scale model dimensions

This appendix contains drawings of the scale model. Dimensions can be derived from the drawings. Visual impression in 'Sketchup' is included in the digital files, which provides a clear overview with respect to the ten tested scenarios.

Appendix F Specification Chinese clay

Source: http://www.imerys-perfmins.com/kaolin/eu/kaolin.htm

Polwhite™ E

Polwhite E is a high quality medium particle size kaolin produced from deposits in the South West of England.

IMERYS PERFORMANCE & FILTRATION MINERALS
Par Moor Centre,
Par Moor Road, Par
Cornwall, PL24 2SQ - UK
Tel: +44 1726 818000
Fax: +44 1726 811200

SPECIFICATION

Brightness	(ISO R457)	78.5 ± 1.5
+ 300 mesh	(mass % max.)	0.05
+ 10 µm	(mass % max.)	35
- 2 µm	(mass % min.)	25
Moisture	(mass % max.)	1.5

TYPICAL VALUES

Yellowness		7
Specific gravity		2.6
pH		5.0
Surface area	(BET; m^2/g)	8
Oil absorption	(g/100g)	33
Water soluble salt content	(mass %)	0.15
Aerated powder density	(kg/m^3)	360
Tapped powder density	(kg/m^3)	810
Chemical analysis by X-ray fluorescence		
SiO_2	(mass %)	50
Al_2O_3	(mass %)	35

CAS No. 1332-58-7

ISO 9001
FM 14752

Kaolin does not appear in EINECS as an individual entry but is classified as "naturally Occurring Substance" with the EINECS No. 310-127-6.

TYPICAL PARTICLE SIZE DISTRIBUTION

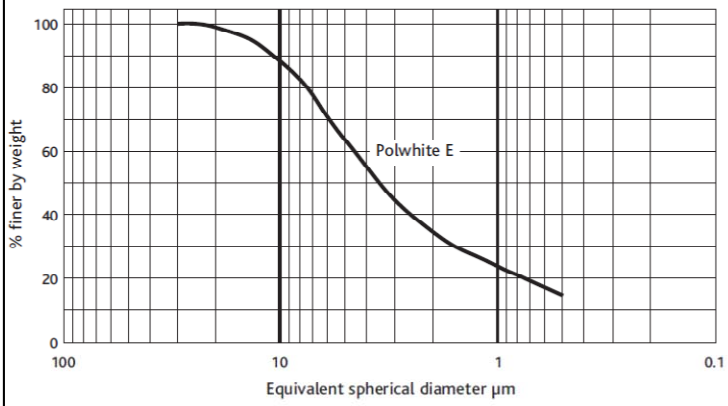

The data quoted are determined by the use of IMERYS Minerals Ltd Standard Test Methods, copies of which will be supplied on request. Every precaution is taken to ensure the products conform to our published data, but since the products are based on naturally occurring raw materials, we reserve the right to change these data should it become necessary. Sales are in accordance with our 'Conditions of Sale', copies of which will be supplied on request.

IMERYS Performance Minerals

DAT020K
March 2008 - Sixth Edition.
This data sheet supersedes the data sheet dated March 2004.

Appendix G Results of model tests

G.1 Outflow velocity

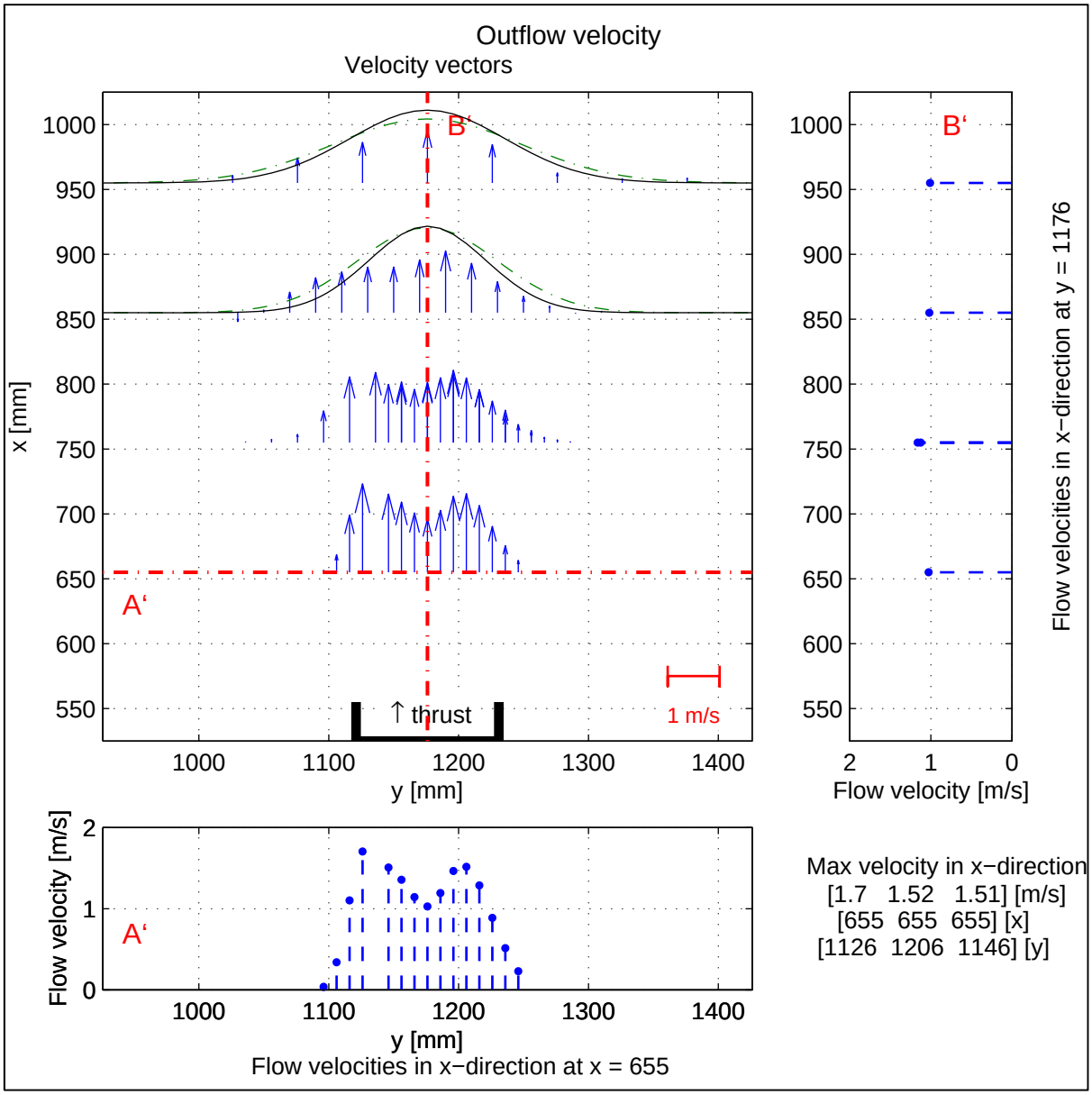

Figure G-1: Measured flow velocities in horizontal plane behind propeller

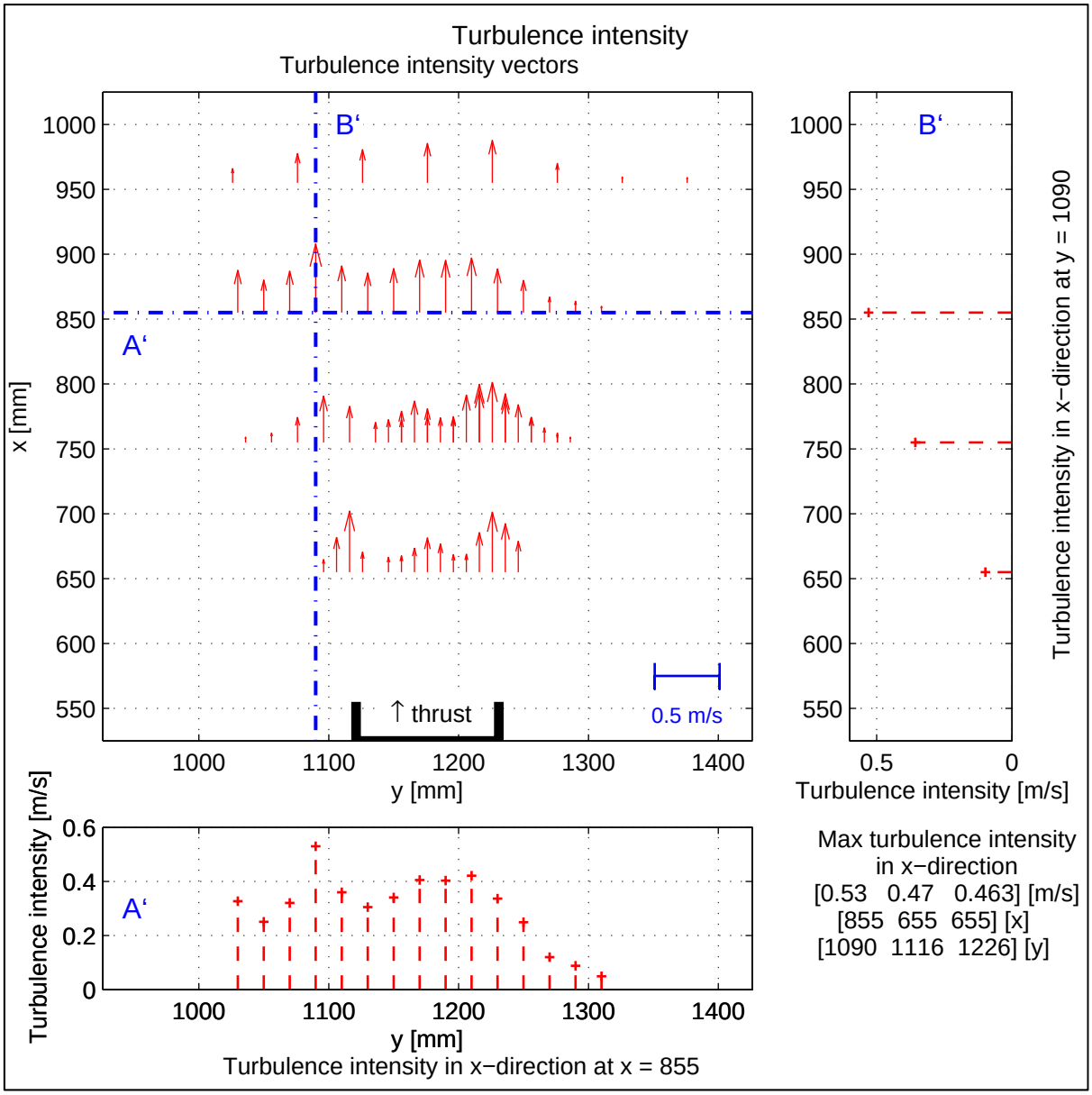

Figure G-2: Measured turbulence intensities in horizontal plane behind propeller

G.2 Vertical distribution of flow velocity

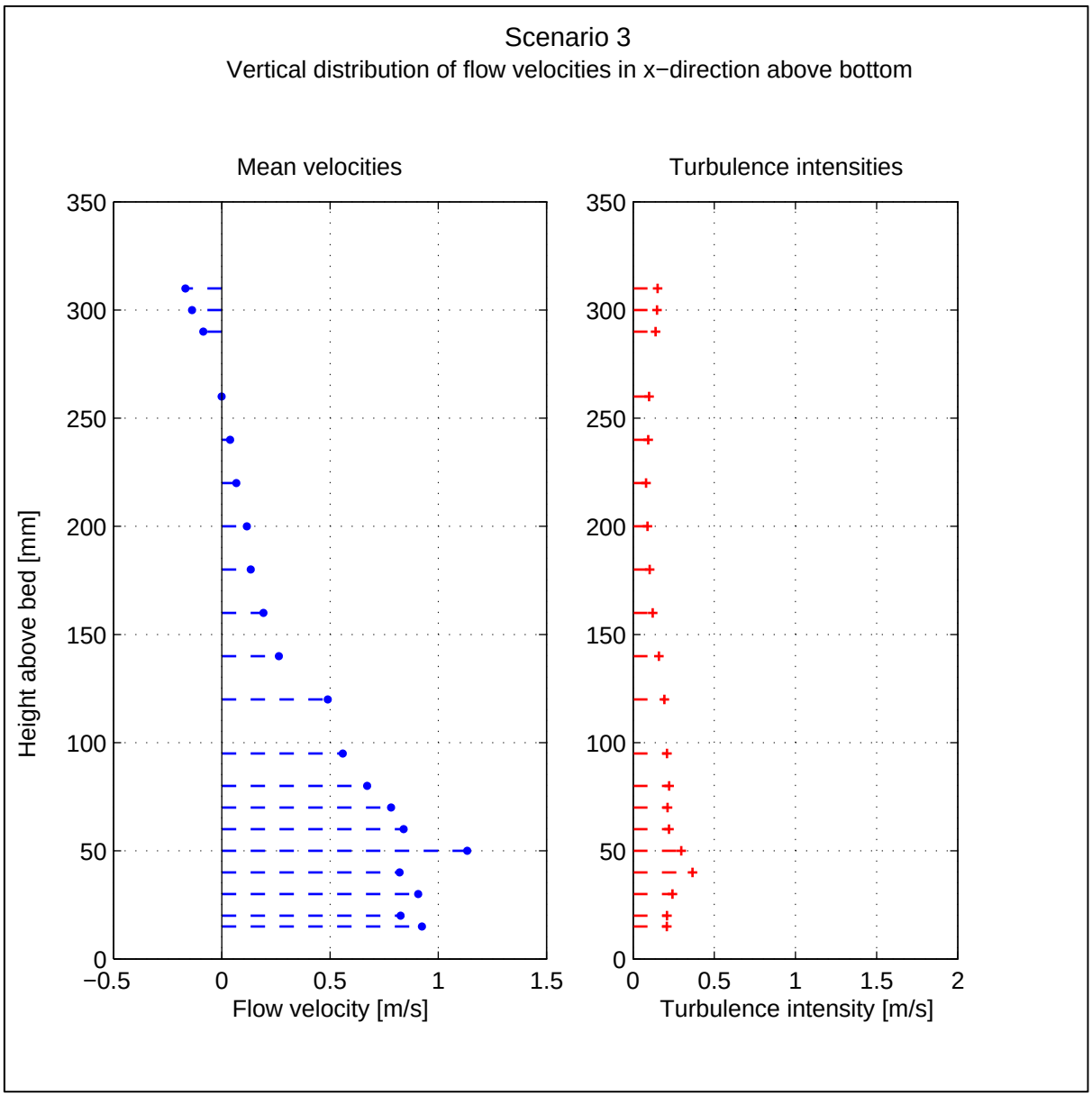

Figure G-3: Vertical distribution of flow velocities

Measured in scenario 3, at x = 1300 and y = 2300. This plot displays the measured flow velocities in x-direction.

G.3 Near-bed flow velocity

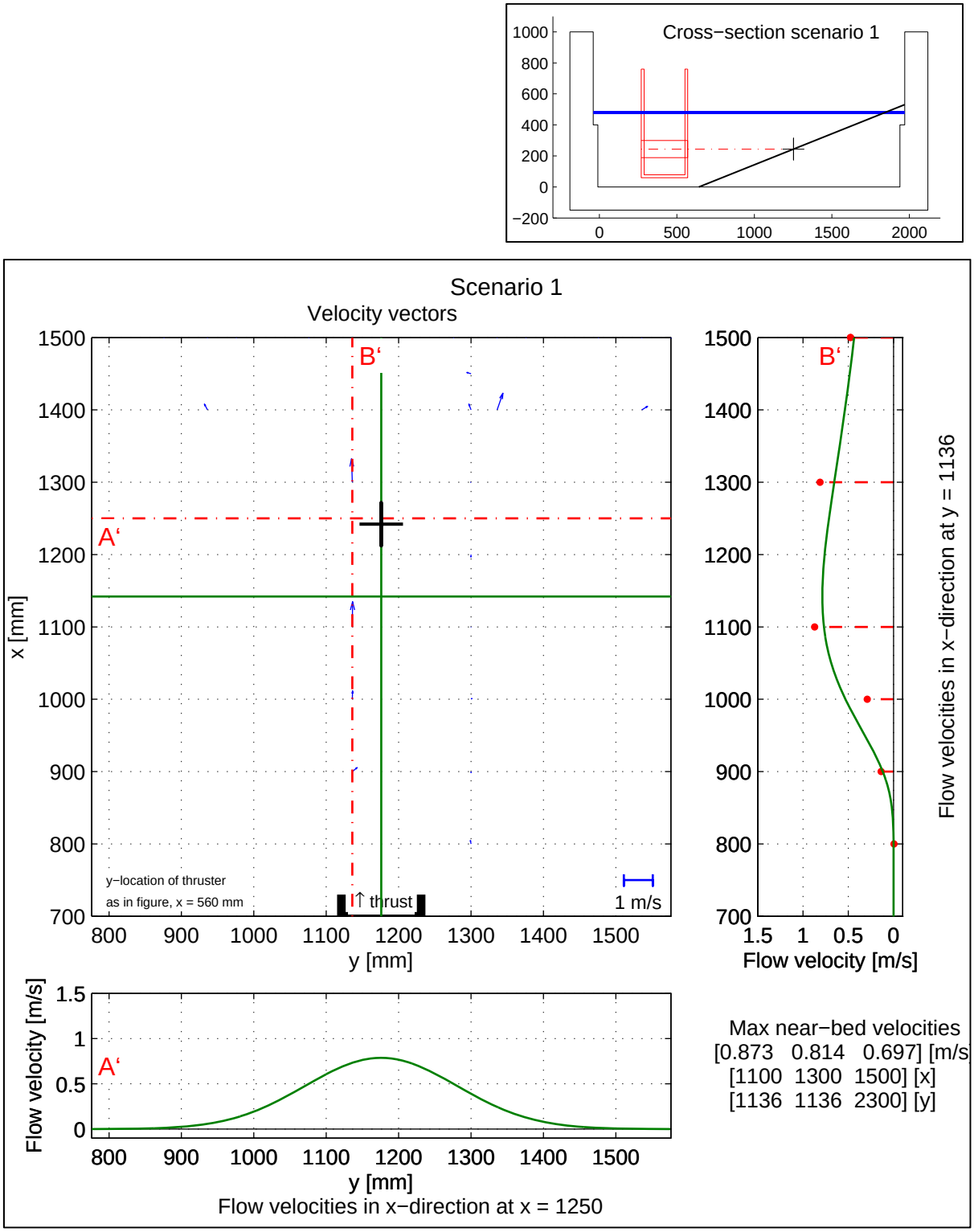

Figure G-4: Near-bed flow velocity, scenario 1

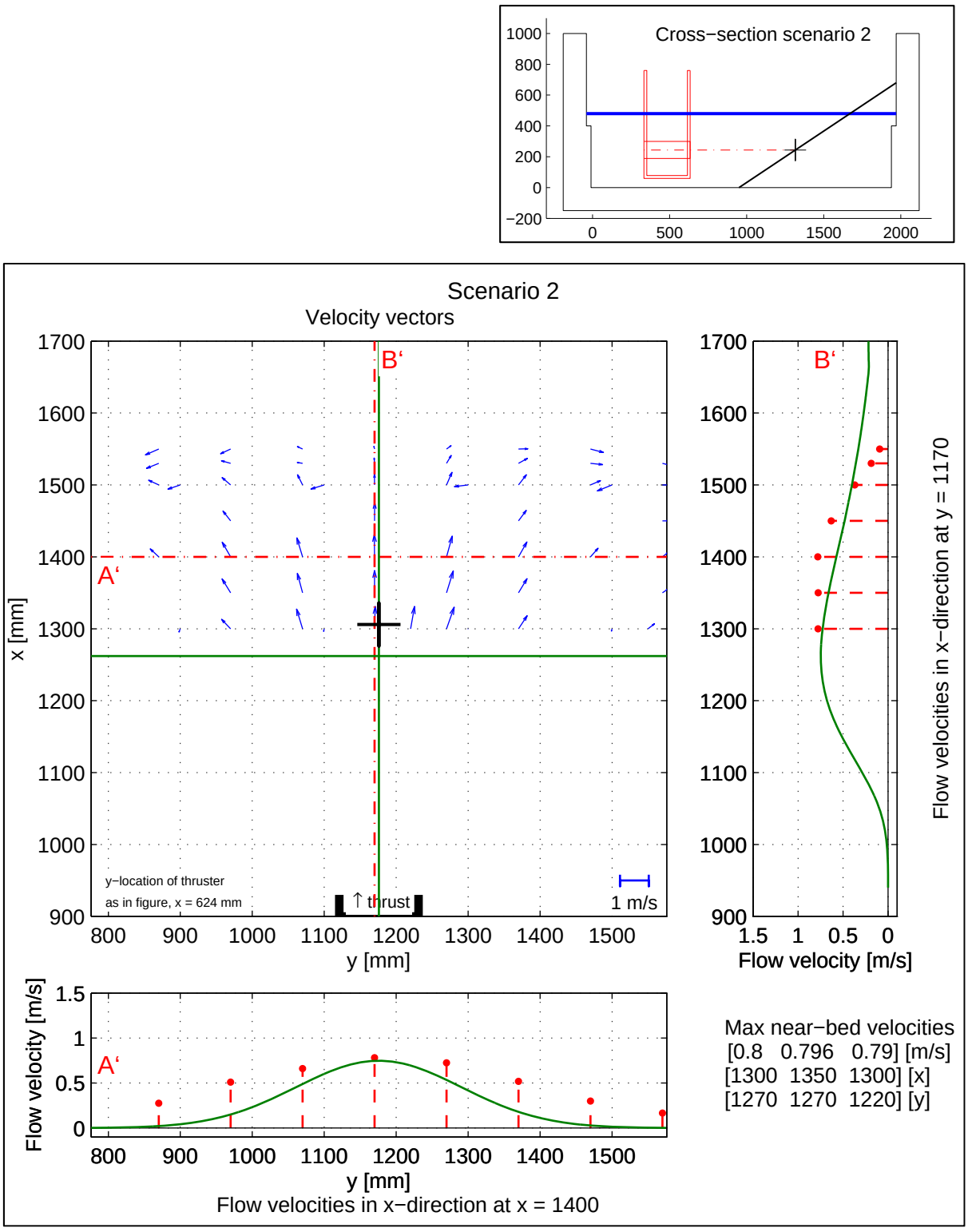

Figure G-5: Near-bed flow velocity, scenario 2

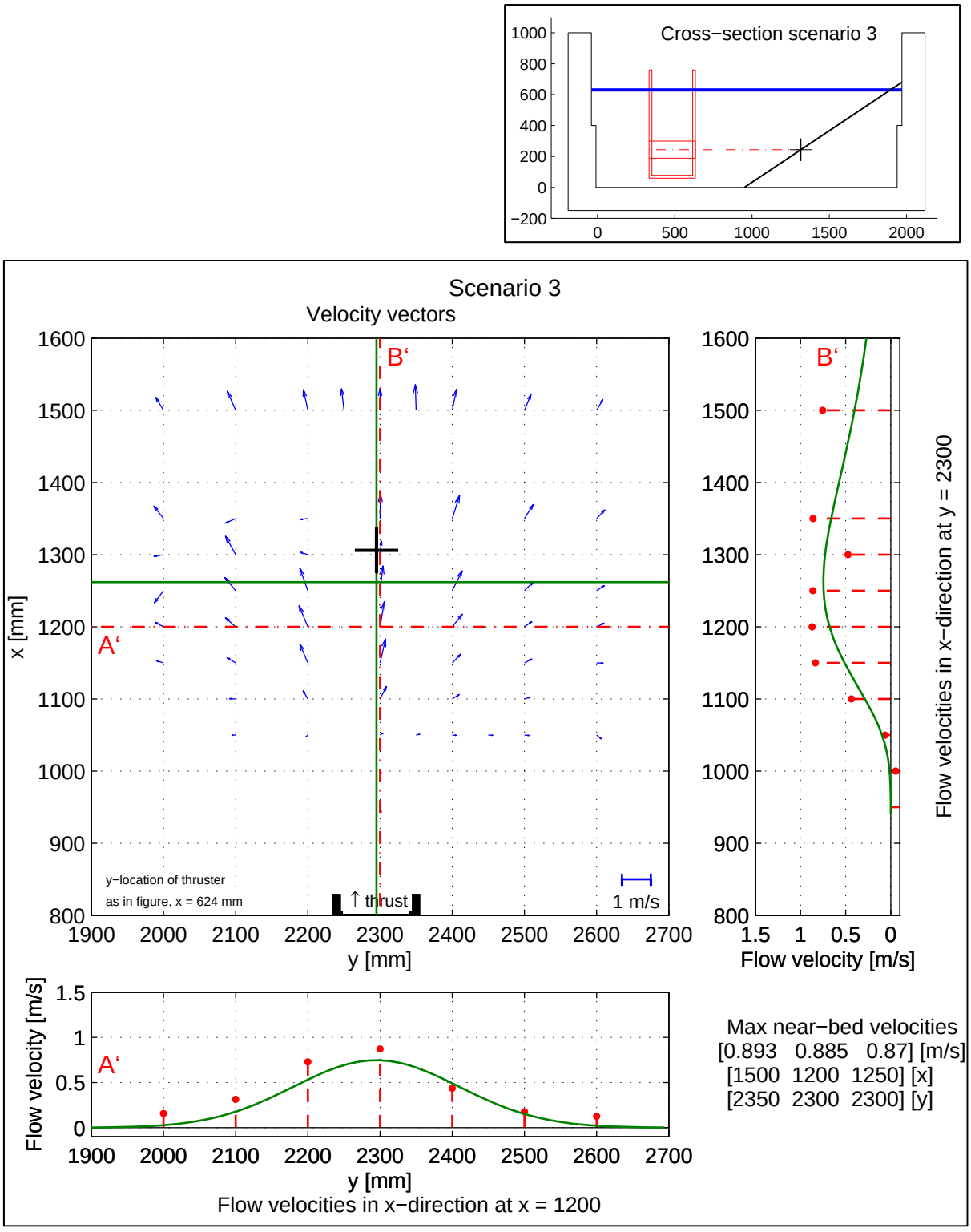

Figure G-6: Near-bed flow velocity, scenario 3

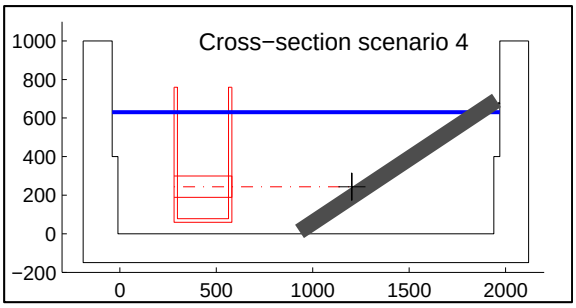

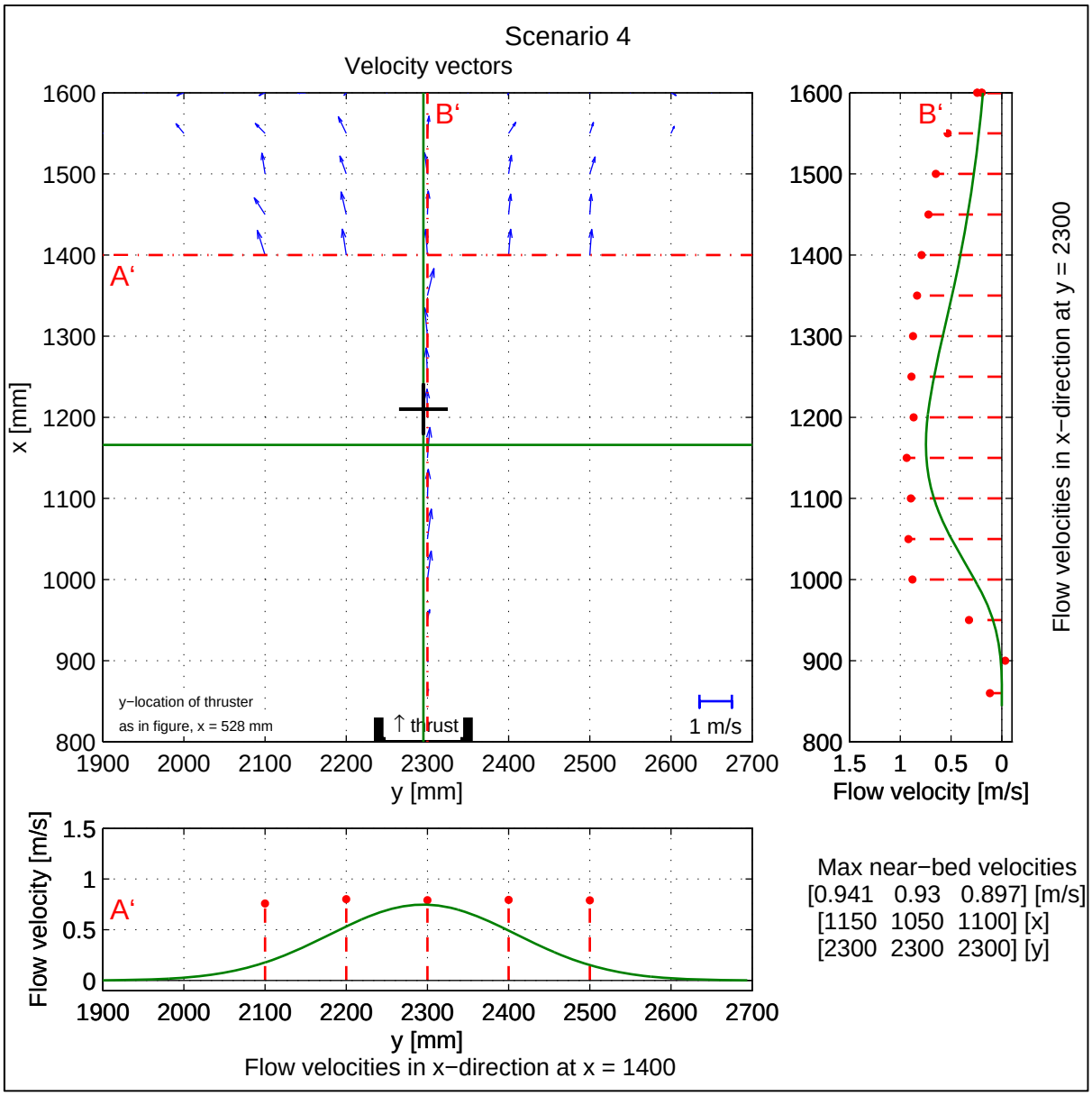

Figure G-7: Near-bed flow velocity, scenario 4

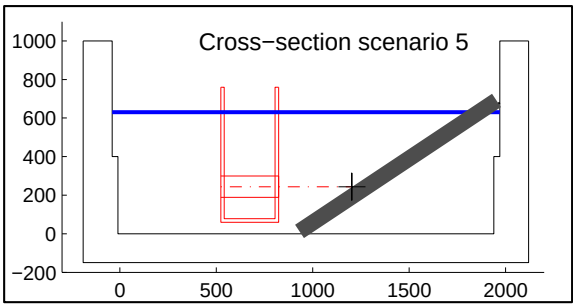

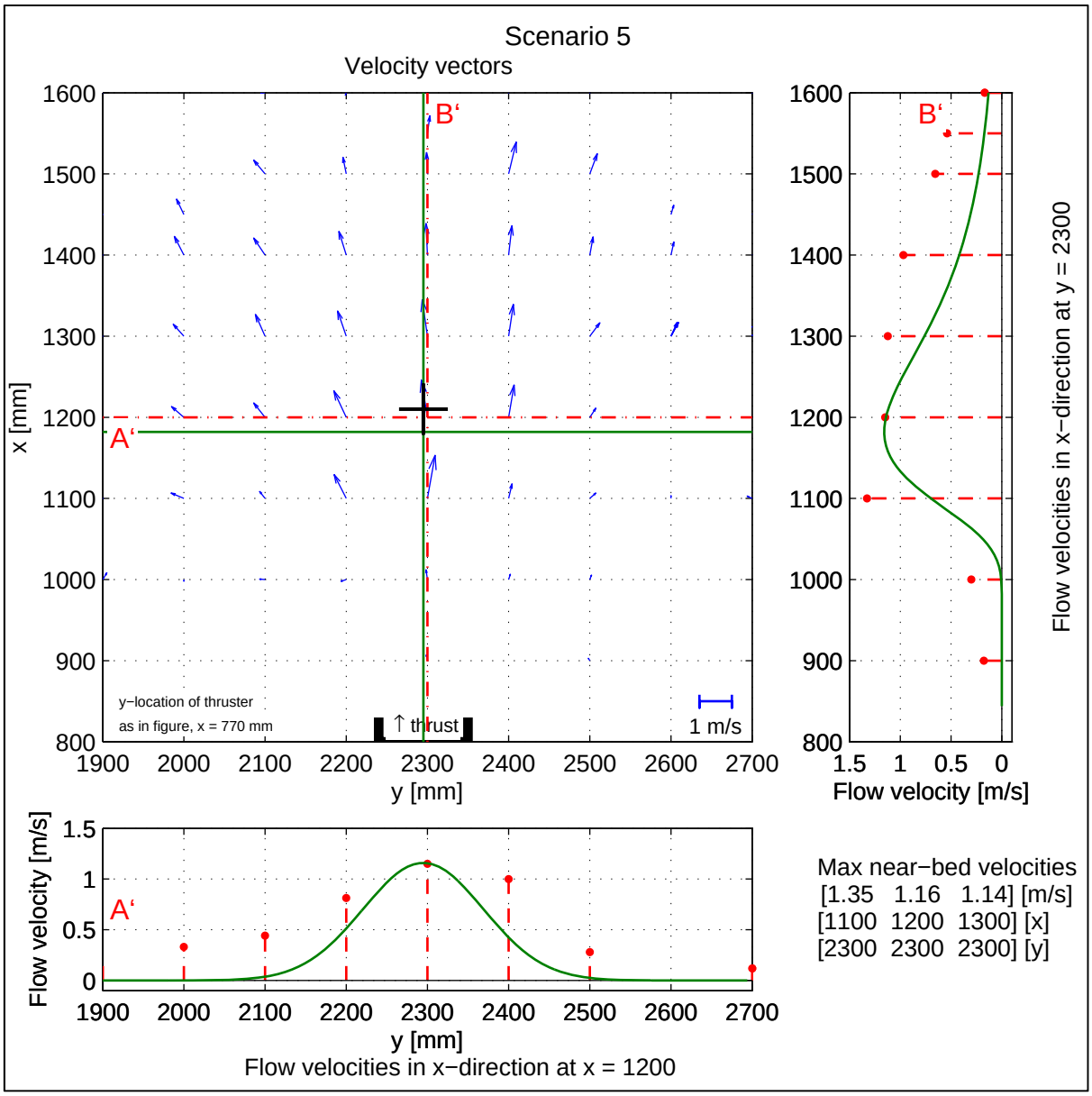

Figure G-8: Near-bed flow velocity, scenario 5

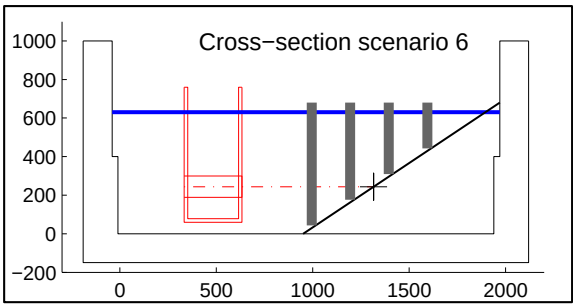

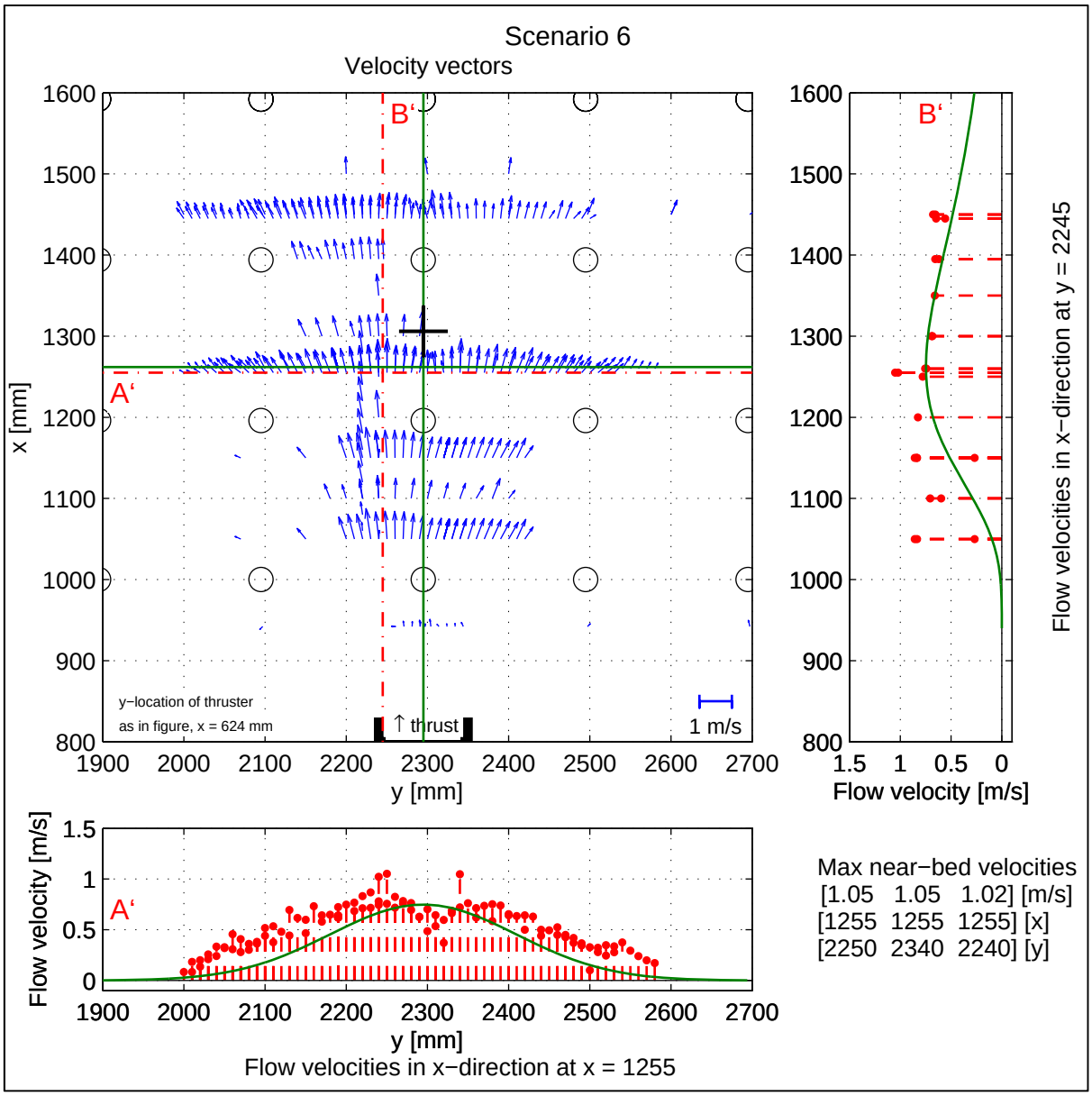

Figure G-9: Near-bed flow velocity, scenario 6

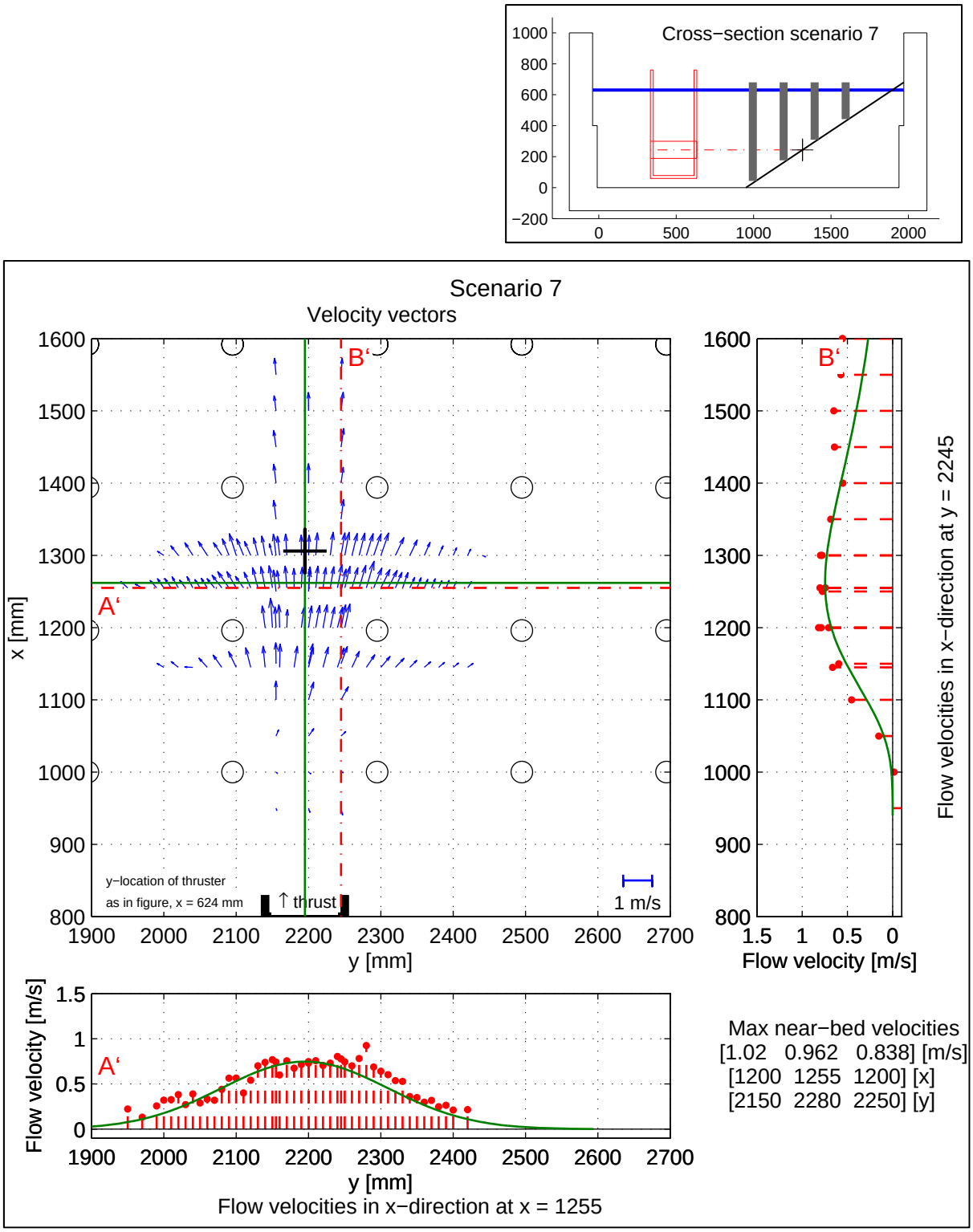

Figure G-10: Near-bed flow velocity, scenario 7

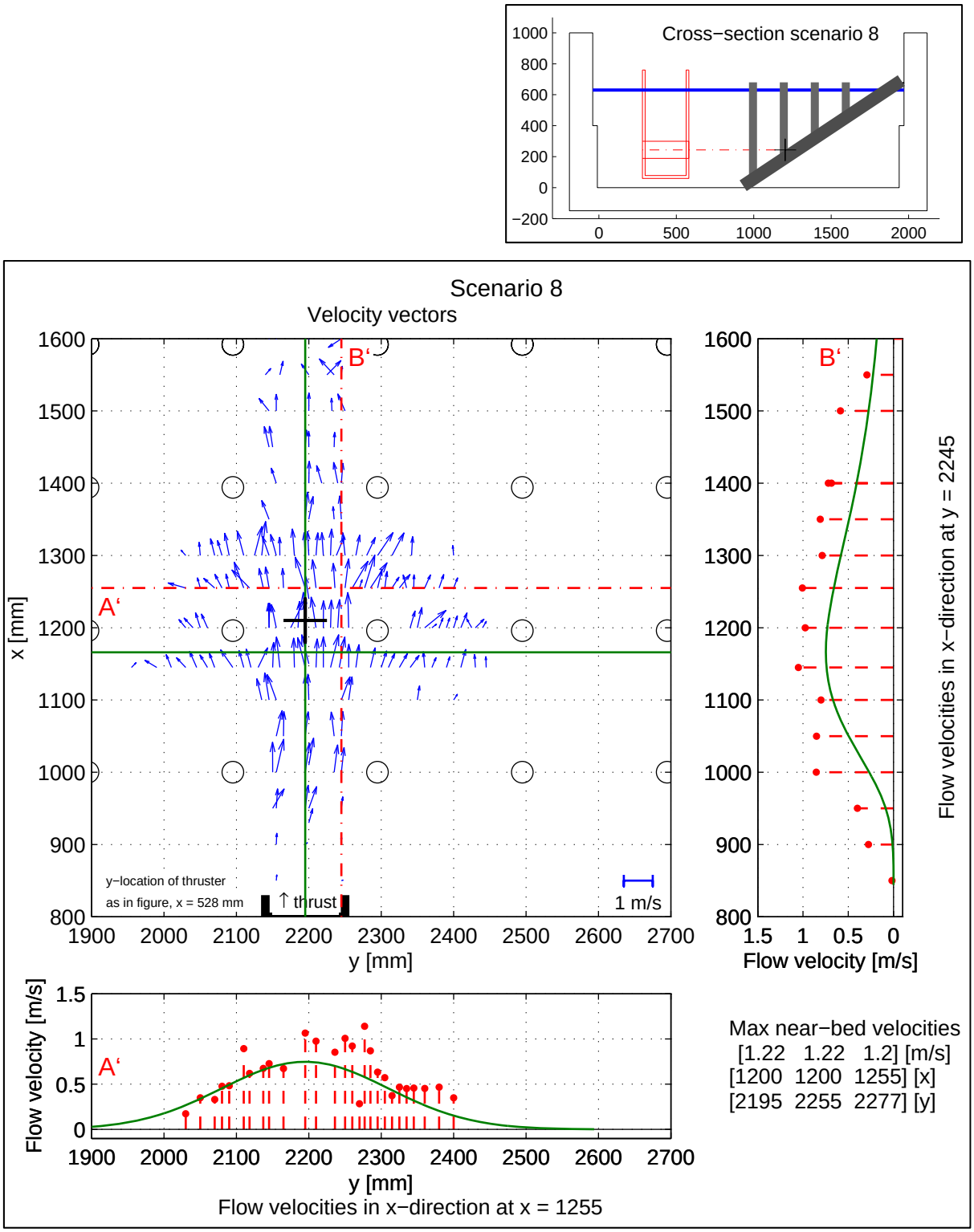

Figure G-11: Near-bed flow velocity, scenario 8

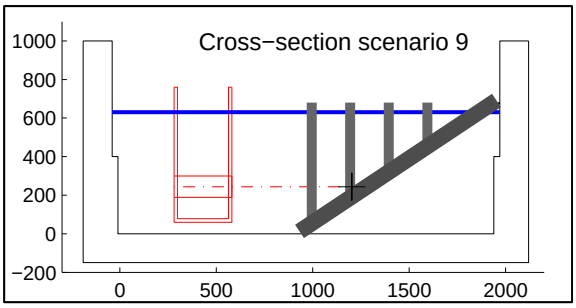

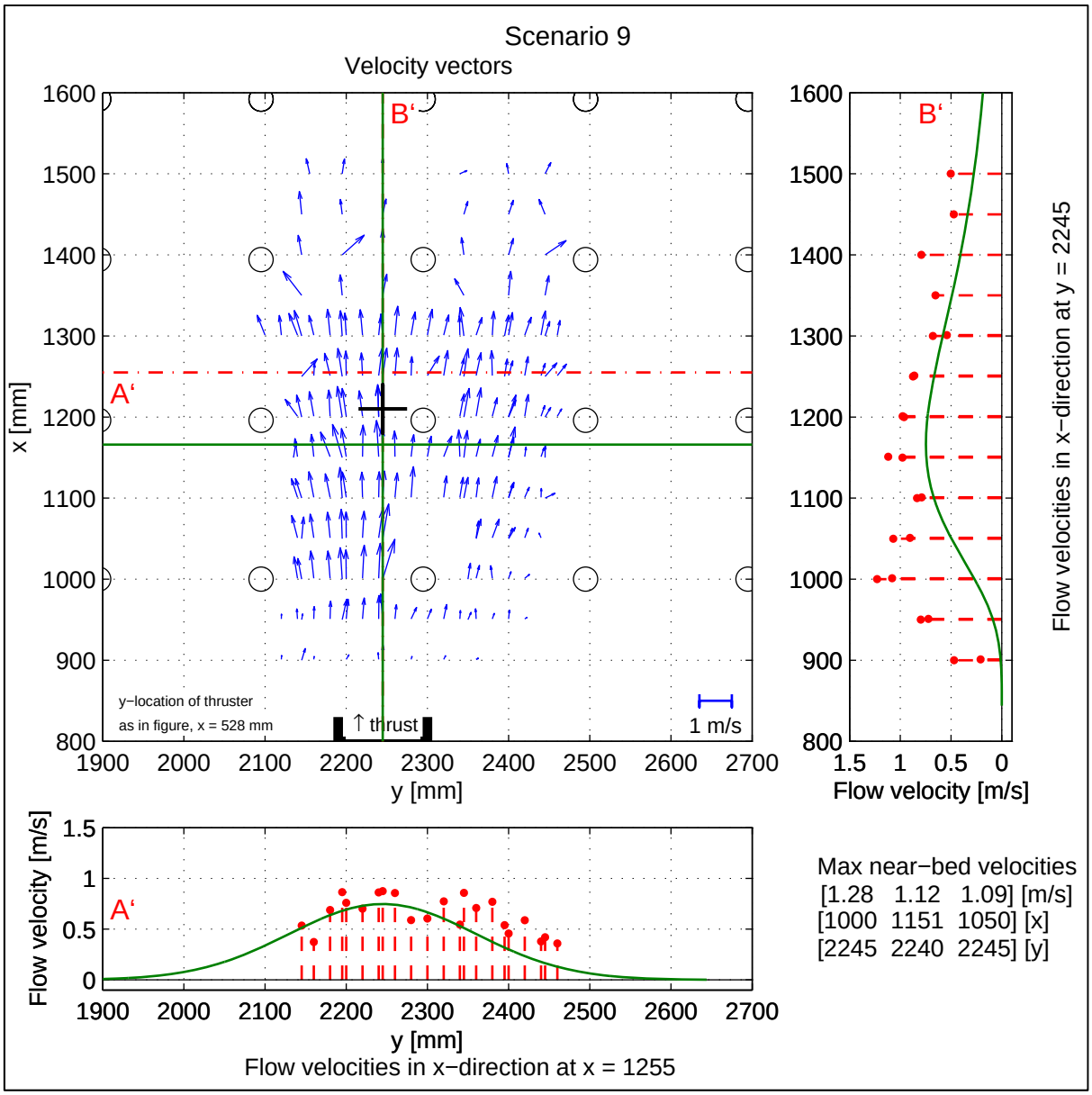

Figure G-12: Near-bed flow velocity, scenario 9

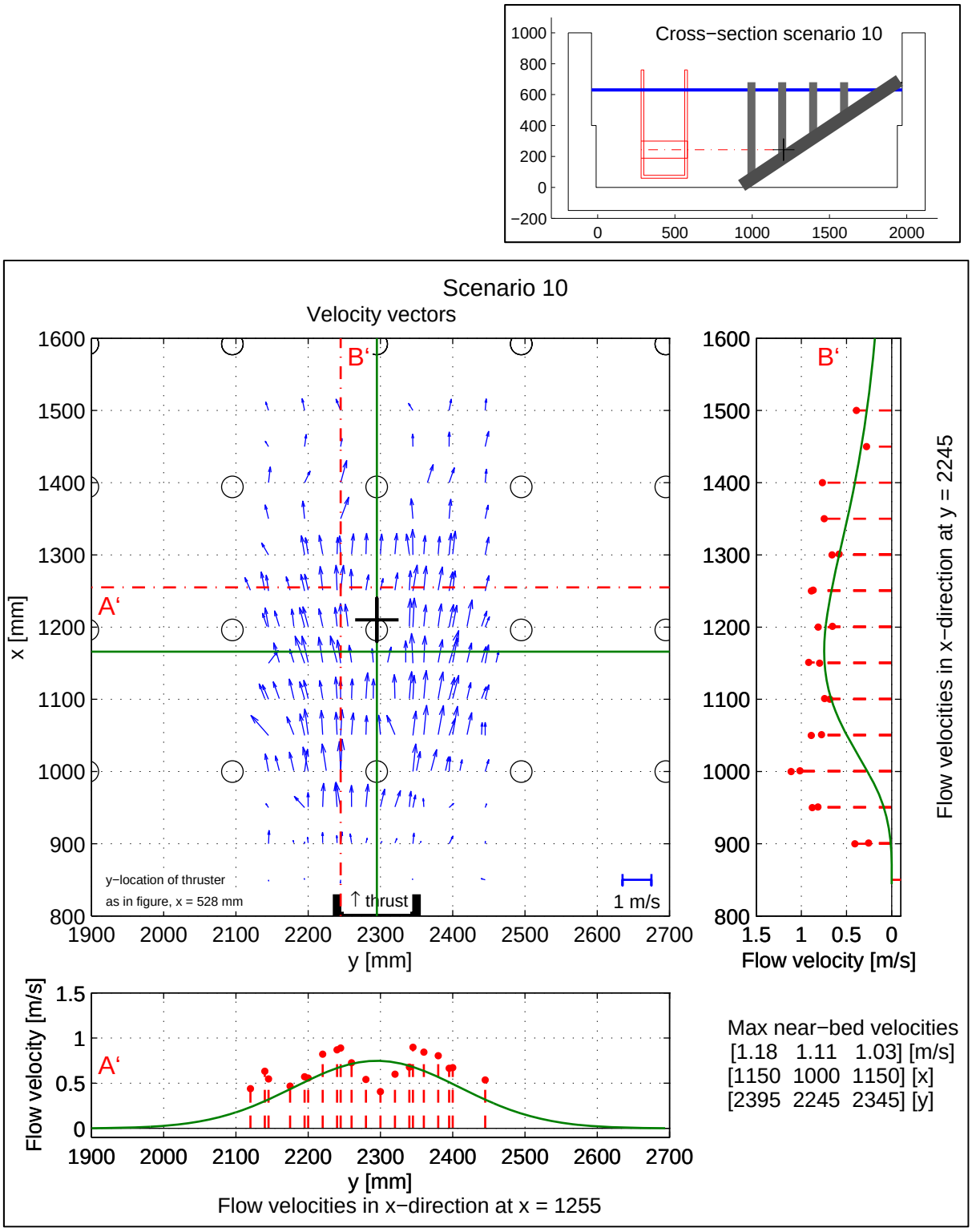

Figure G-13: Near-bed flow velocity, scenario 10

G.4 Near-bed turbulence intensity

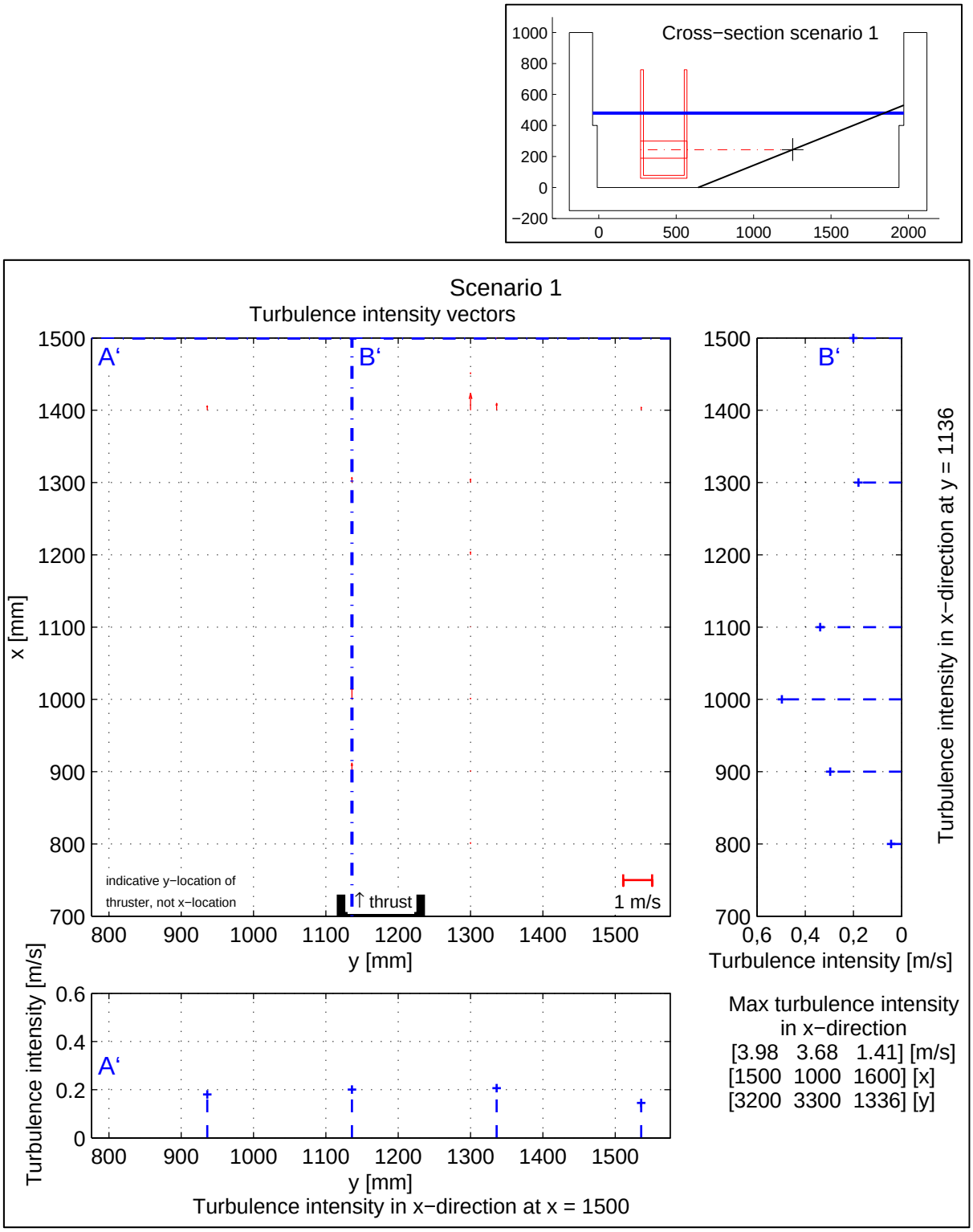

Figure G-14: Near-bed turbulence intensity, scenario 1

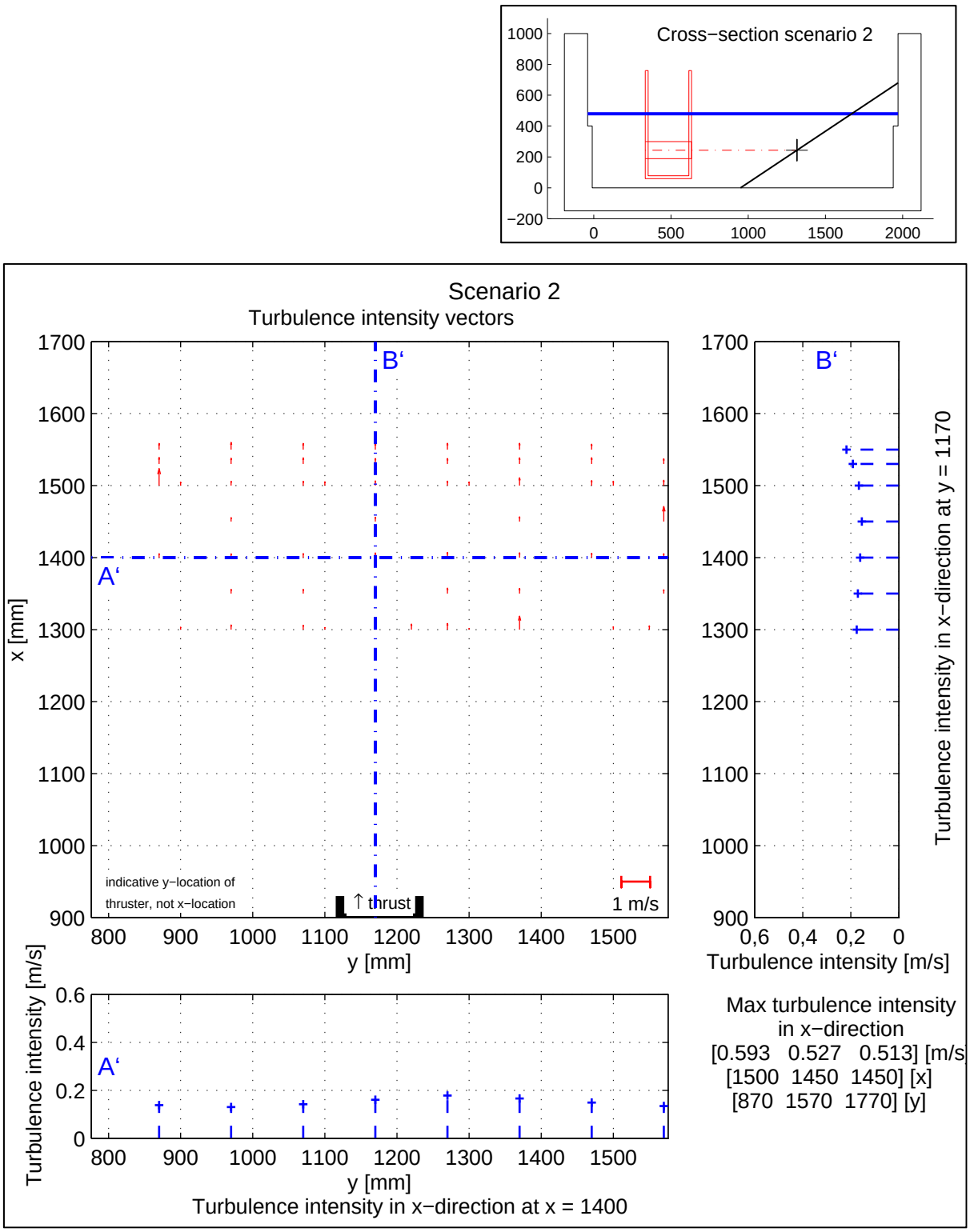

Figure G-15: Near-bed turbulence intensity, scenario 2

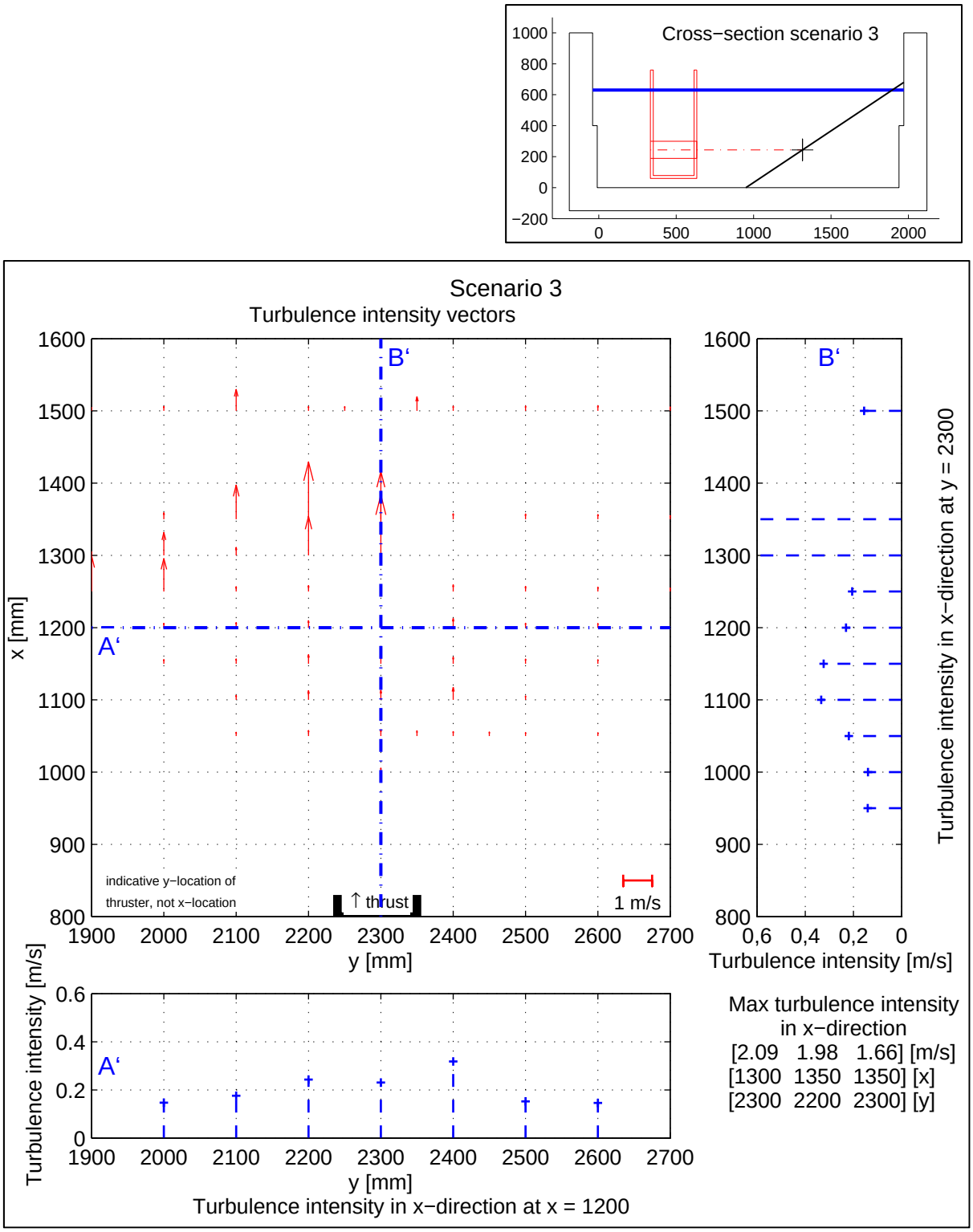

Figure G-16: Near-bed turbulence intensity, scenario 3

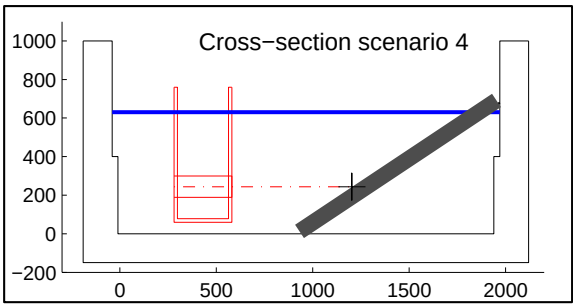

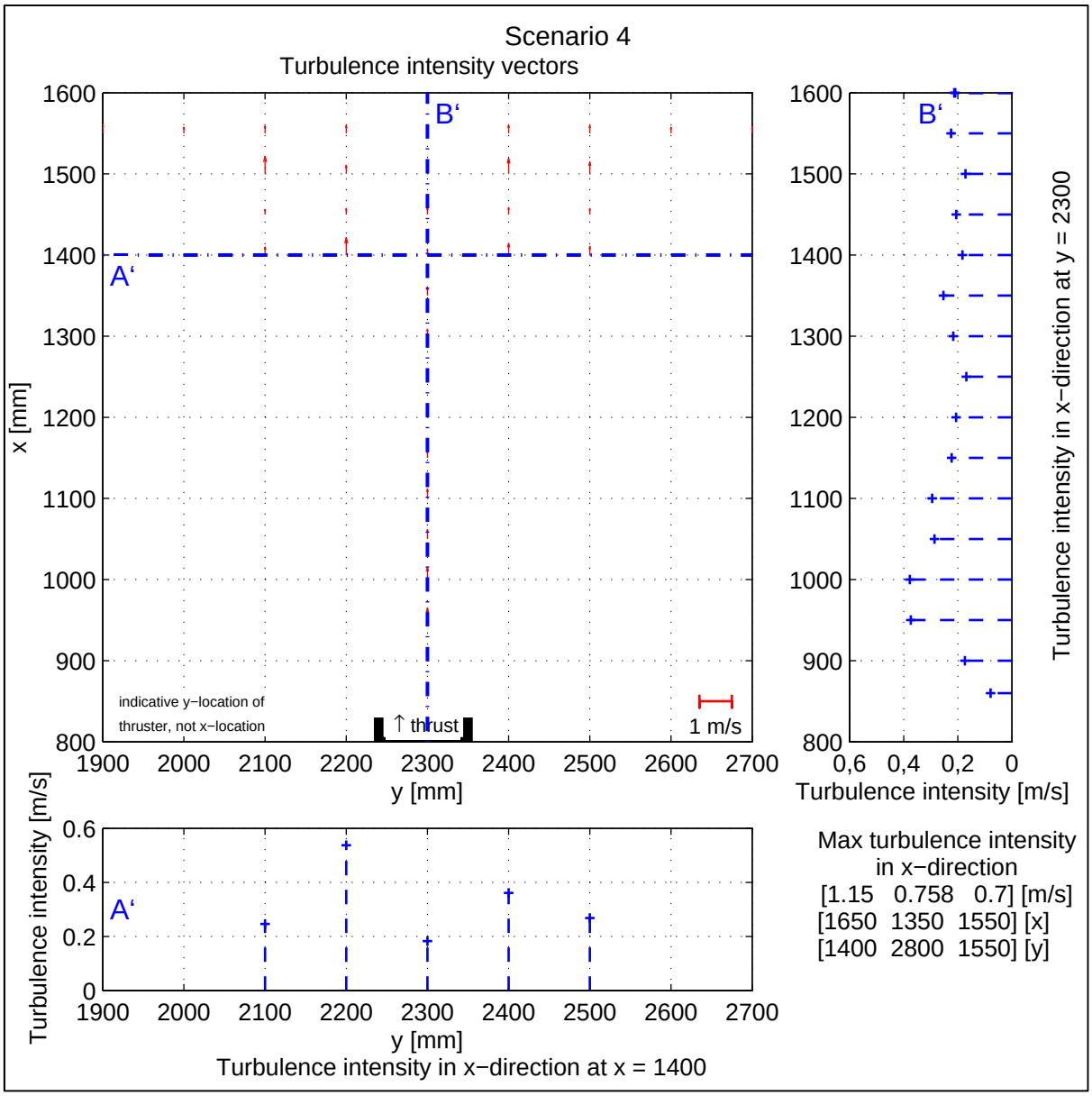

Figure G-17: Near-bed turbulence intensity, scenario 4

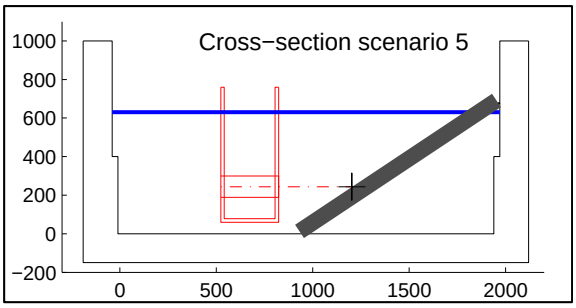

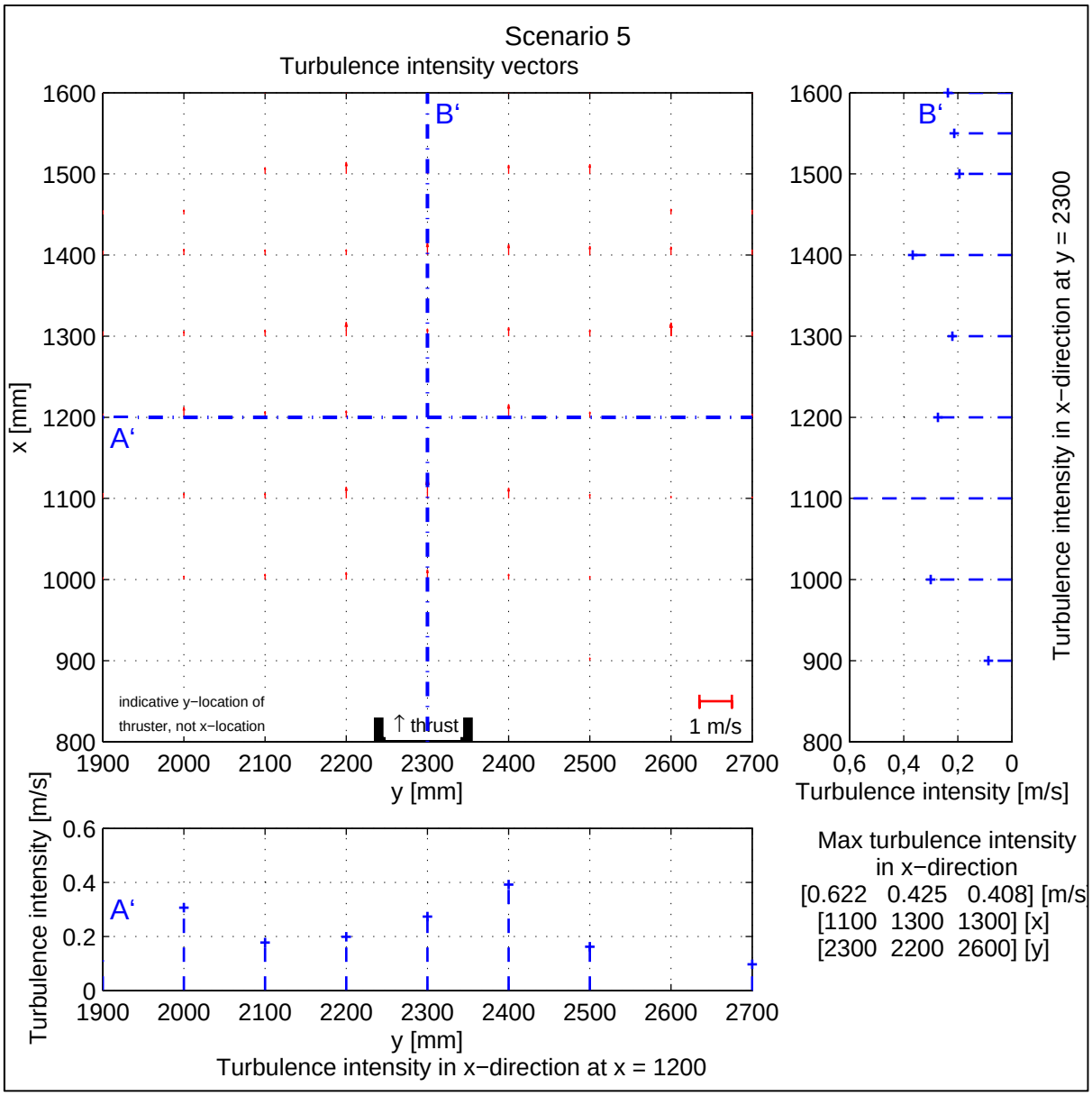

Figure G-18: Near-bed turbulence intensity, scenario 5

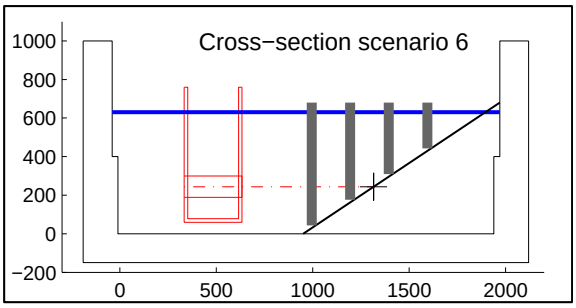

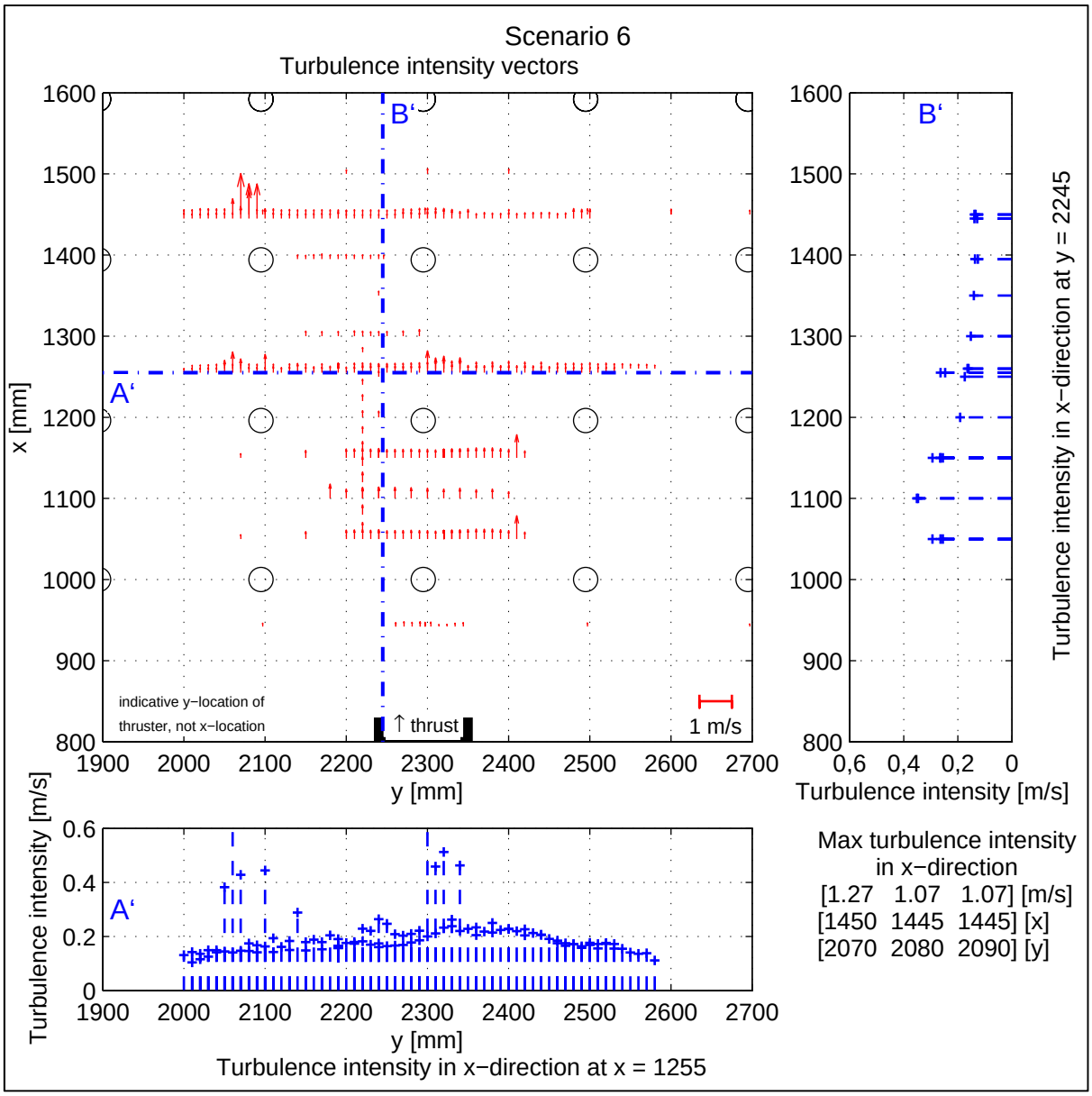

Figure G-19: Near-bed turbulence intensity, scenario 6

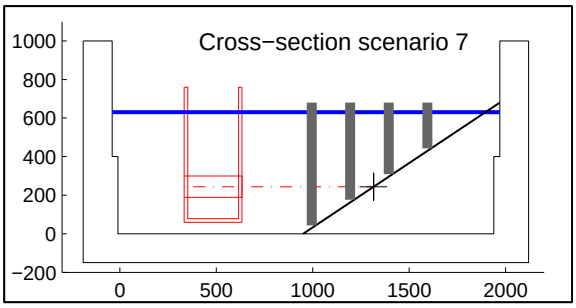

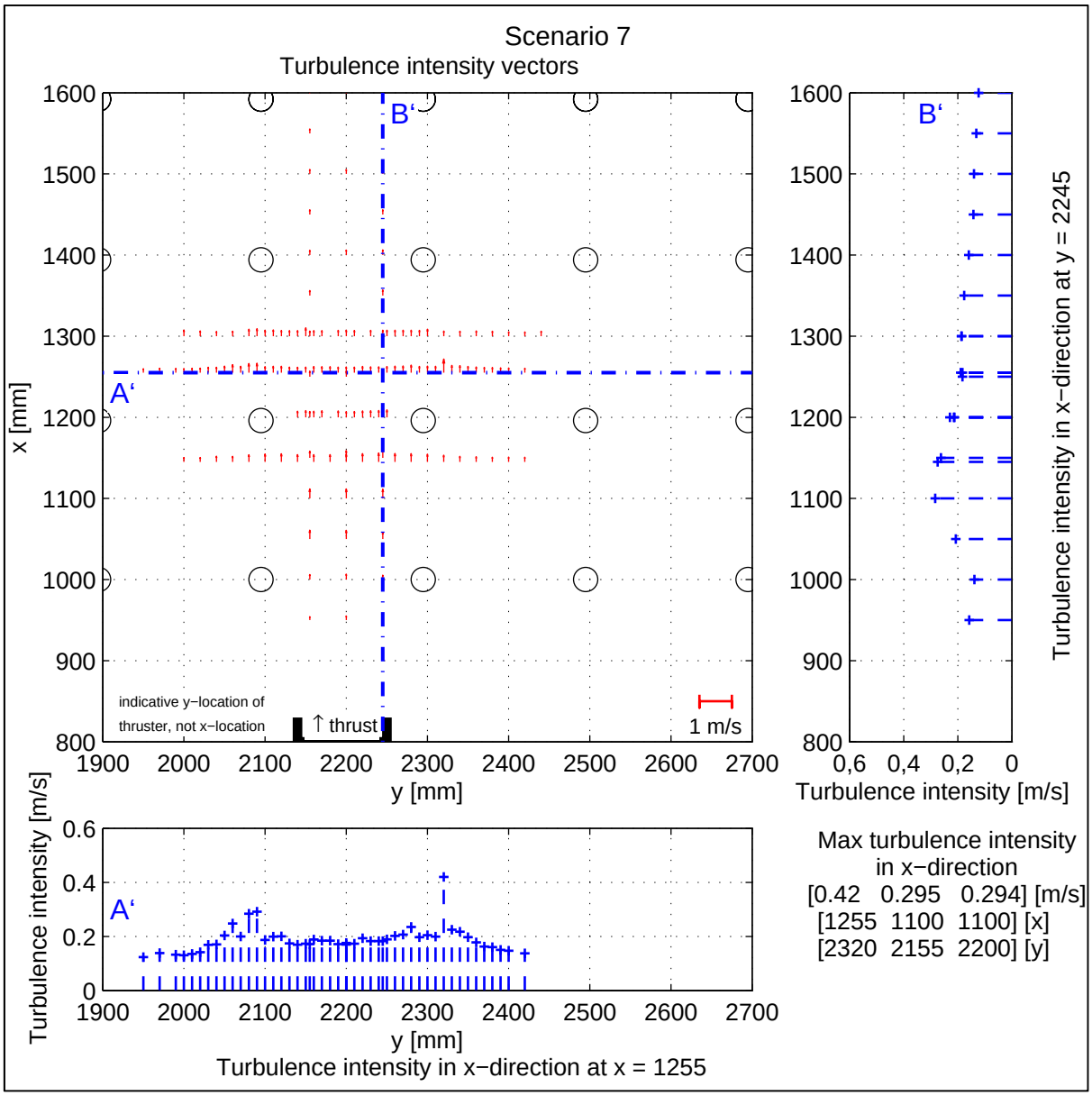

Figure G-20: Near-bed turbulence intensity, scenario 7

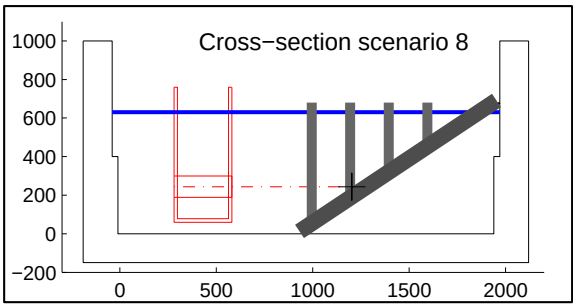

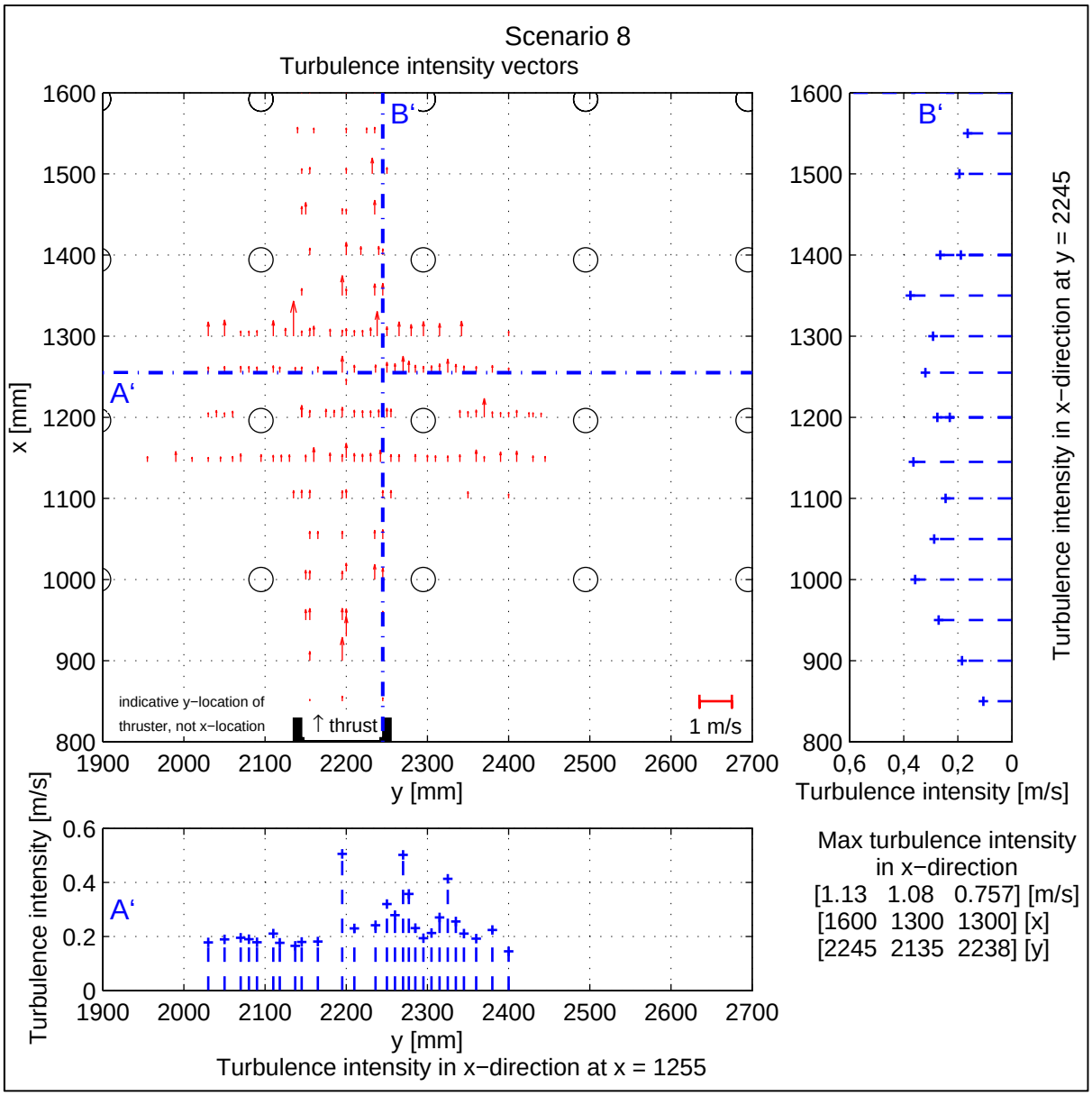

Figure G-21: Near-bed turbulence intensity, scenario 8

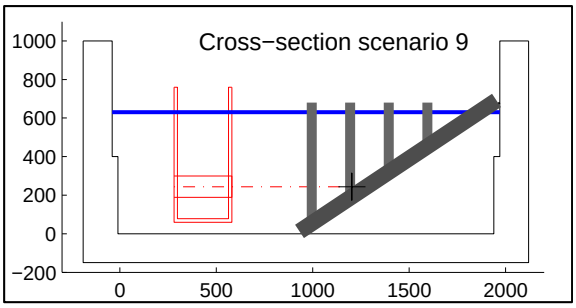

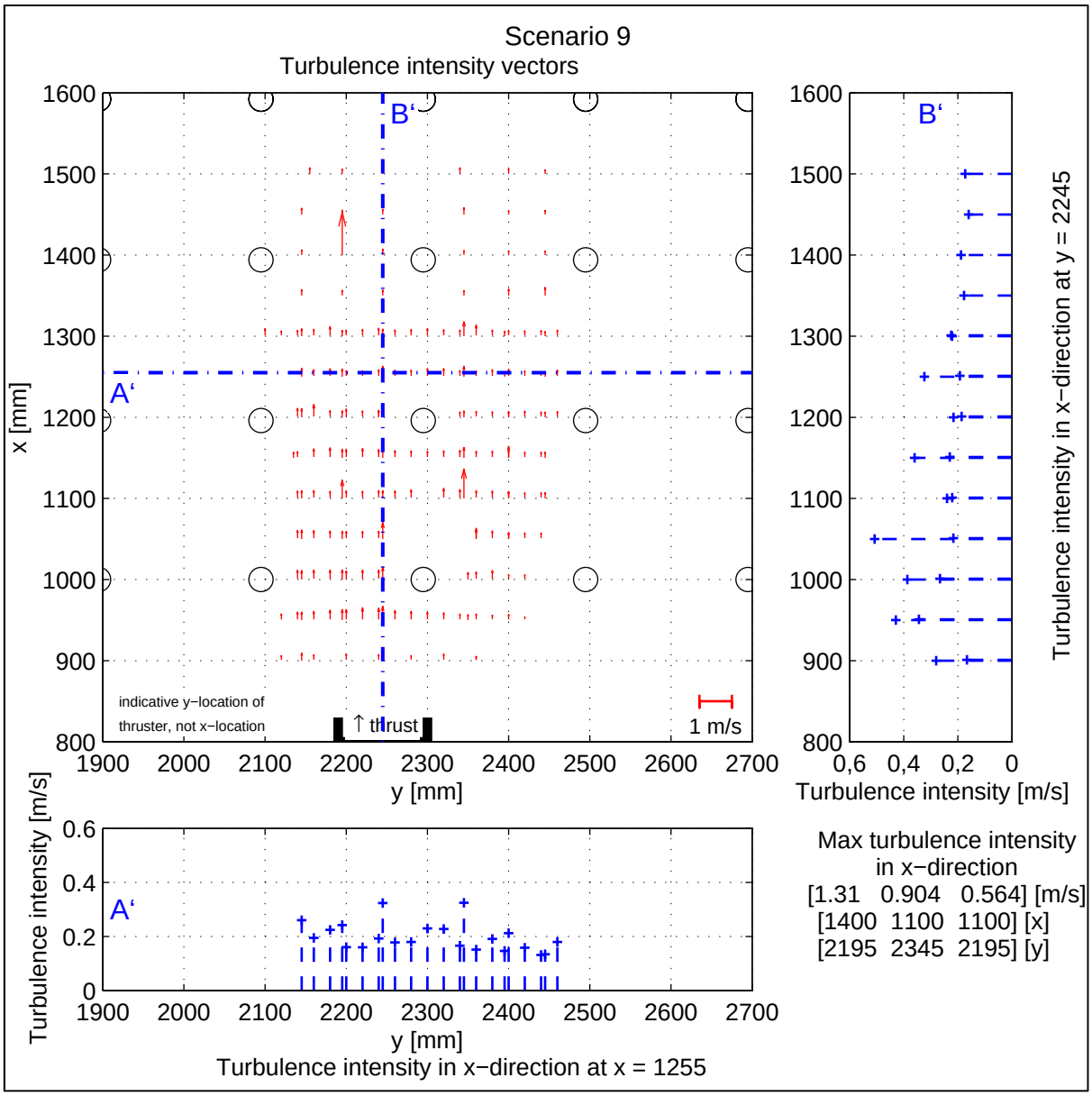

Figure G-22: Near-bed turbulence intensity, scenario 9

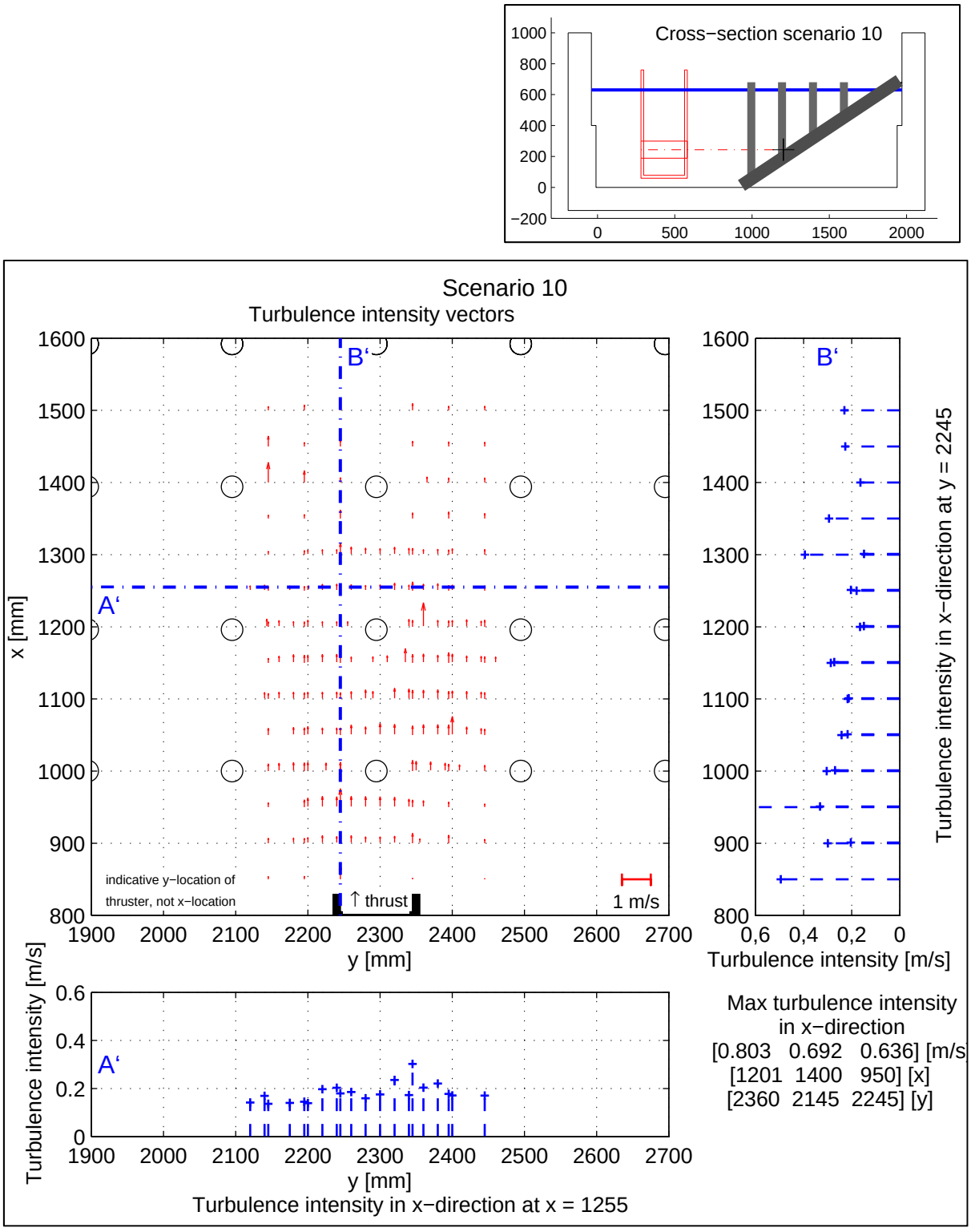

Figure G-23: Near-bed turbulence intensity, scenario 10

G.5 Checklist ADV

Below a checklist is given based on experience from the performed measurements. By taking into account this checklist, future ADV measurements can be performed more easily. In addition this results in more precise measurements and high quality results. This checklist includes the recommendations by VAN BLAADEREN [2006].

Before the measurements	
Is the instrument mounted properly? The instrument should be mounted properly. The flow should not be able to move the instrument to prevent that the vibrations will be measured as additional turbulence.	
Is the seeding apparatus rightly aligned and turned on? If a bubble frame is used for the seeding. The flow should transport the bubbles to the measurement location. When this is not the case, there will be no, or a very bad signal for measuring the velocities. This shows as an noisy signal. This is also produced when the instrument is out of the water. Seeding can also be performed by using small particles suspended in the water. As described in chapter 3, Chinese Clay performs well. This can be mixed with water and subsequently added into the flow. In a closed basin a continuous inflow of seeding particles may not be needed, as particles keep suspended by the flow in the basin.	
At the start of each measurement	
Orientation of the instrument Document how the instrument is positioned. This could be important for the analysis.	
Instrument configurations Nominal velocity (see chapter 3 for advise) Measurement volume (see chapter 3 for advise) Signal strength (see chapter 3 for advise)	
During the measurements	
To keep an eye on: Signal strength (minimum of 70 counts is advise by the manufacturer) Measurement restrictions (maximum velocity, close to the bed or surface)	
Data analysis	
Converting the data Acquired data is converted by using the 'Vectrino' software from Nortek. This is supplied with the ADV, or can be downloaded from the website of Nortek. A description of the acquired data-file and available data is included in the ADV manual.	
Data analysis One should keep in mind that a certain noise level is in the acquired data. This can be filtered by using for example the 'Despike' function as included with the data from the performed research in this thesis. Also the orientation of the instrument should be kept in mind. Flow velocities and directions may have to be converted into another coordinate system or direction.	

Appendix H Oscillating angles of flow velocity

For all measuring points, the mean angle and standard deviation of the angle of flow direction can be calculated. This results for all (> 2000) points in an average standard deviation of 45 degrees. One is interested in the locations with the maximum bed load, which occur in the line with the propeller axis. At these locations of maximum bed load, the flow direction is most important. When for example all locations with a y-coordinate at the propeller axis are taken, other average values may occur.
For these locations, the average standard deviation is 49 degrees.

A short zoom onto details reveals that more investigation can be done to the angles of flow velocity. The average values, - based on all scenarios - are quite high. The two figures below show that for one specific situation a large variation can be observed.

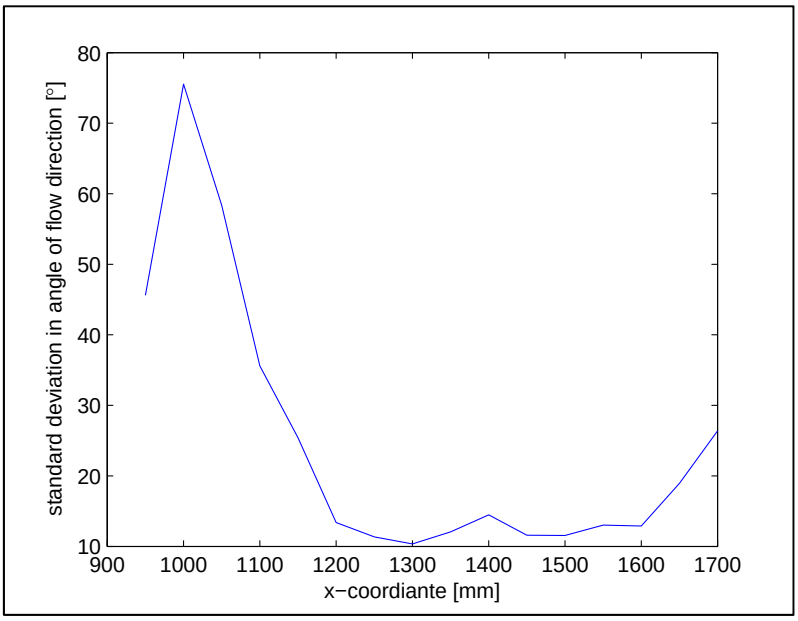

Figure H-1: Standard deviation of flow direction for S7

Figure H-1 and Figure H-2 are an illustration of the possible variation of the flow direction. Scenario 7 and 8 are respectively smooth and rough bed situations. Both including piles in the scale model. These figures show a peak at the location where the jet first hits the slope (around x = 900 to 1000). This location is also loaded by the largest flow velocities and turbulence intensities. Hereby one could imagine this standard deviation of the angle to be especially important to include in the calculations for this location.

Other peaks as observed in Figure H-2 can be caused by the fact that the plots are only based on one y-location. When one would include a set of y-locations, this would probably result in a more organized view with less sharp peaks. Because of the available time for this thesis, not an extensive analysis of this subject is done.

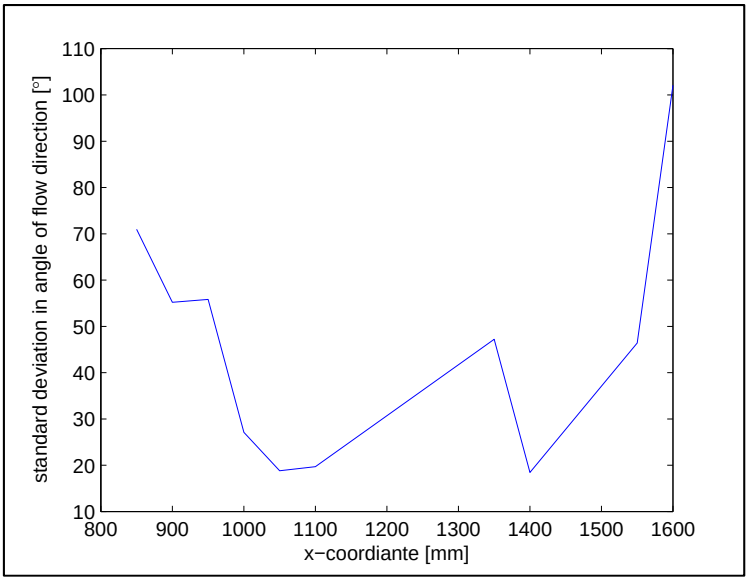

Figure H-2: Standard deviation of flow direction for S8

Further research is recommended with respect to this subject. As a start, here some possible parameters to include are given. For these parameters, their influence on the angles should be investigated:

- Location close to piles;
- Distance from propeller;
- Rough or smooth slope;
- Location where a propeller jet hits the slope;
- Bow thruster or main propeller.

Appendix I Spectral analysis

Here some aspects are presented with respect to the spectral analysis of the ADV samples. Using autocorrelation, the size of vortexes is estimated.

SCHOKKING [2002] used the following method to analyse the size of vortices.

The autocorrelation coefficient can be used to estimate the size of the average vortex in the water. A vortex is transported with the mean flow velocity. As long as the correlation between several lags 'k' is positive, the fluctuations in those steps have a similar direction. During the time of positive correlation, the vortex passes a certain point with a velocity equal to the mean flow velocity.

Hereby, the vortex size is defined as:

$$\lambda = \overline{u} \cdot t \qquad \text{(I-1)}$$

Where:

λ	average vortex size	[m]
$\overline{u}$	mean flow velocity	[m/s]
t	duration	[s]

The used autocorrelation coefficient is defined as:

$$r_k = c_k / c_0 = \frac{\frac{1}{N}\sum_{t=1}^{N-k}\left(x_t - \overline{x}\right)\left(x_{t+k} - \overline{x}\right)}{\frac{1}{N}\sum_{t=1}^{N}\left(x_t - \overline{x}\right)^2} \qquad \text{(I-2)}$$

Measurement 1833 from the dataset is used to visualise the autocorrelation coefficient. This measurement was done in scenario 10, at location (x,y) = (1300,2245).
Using the autocorrelation function as done in SCHOKKING [2002], the derivative is calculated for the first two points in Figure I-2. The time (lag) where this derivative is zero, is the time used in equation (I-1). In combination with the mean flow velocity, the average vortex size is calculated.

For example, a time of 0.12 s with a mean flow velocity of 0.5 m/s results in an average vortex size of 0.06 m.
This calculation is done for all measurements and Figure I-3 and Figure I-4 provide histograms of the estimated vortex sizes. Notable difference for these figures is the peak in average vortex size in Figure I-4. For the measurements in scenarios with piles, there is a peak in vortex sizes around 0.03 m, equal to the pile diameter. This confirms the validity of this method to estimate vortex sizes, because around structures vortex sizes equal to the structure size appear.

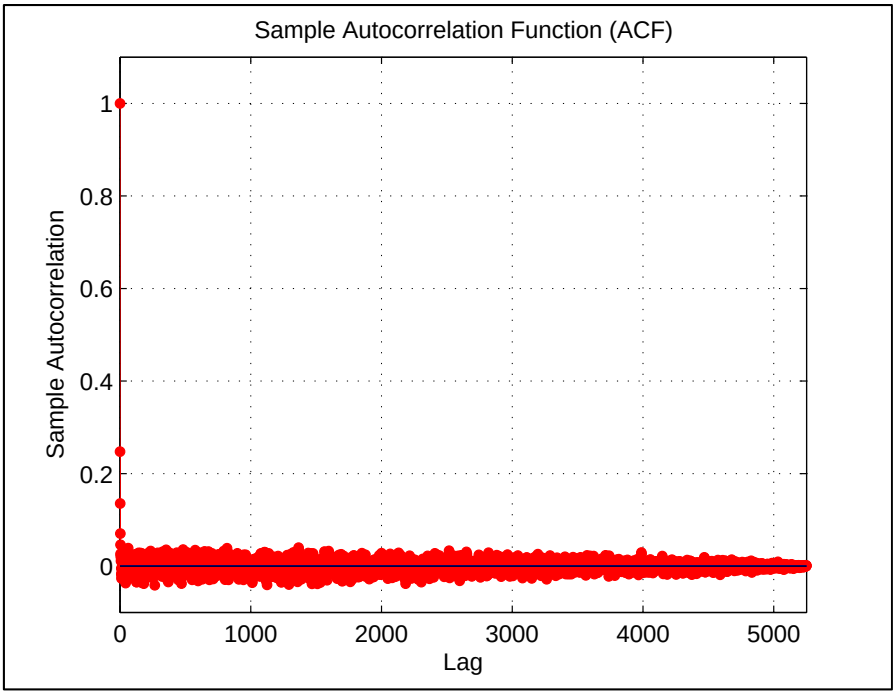

Figure I-1: Autocorrelation for 210 s

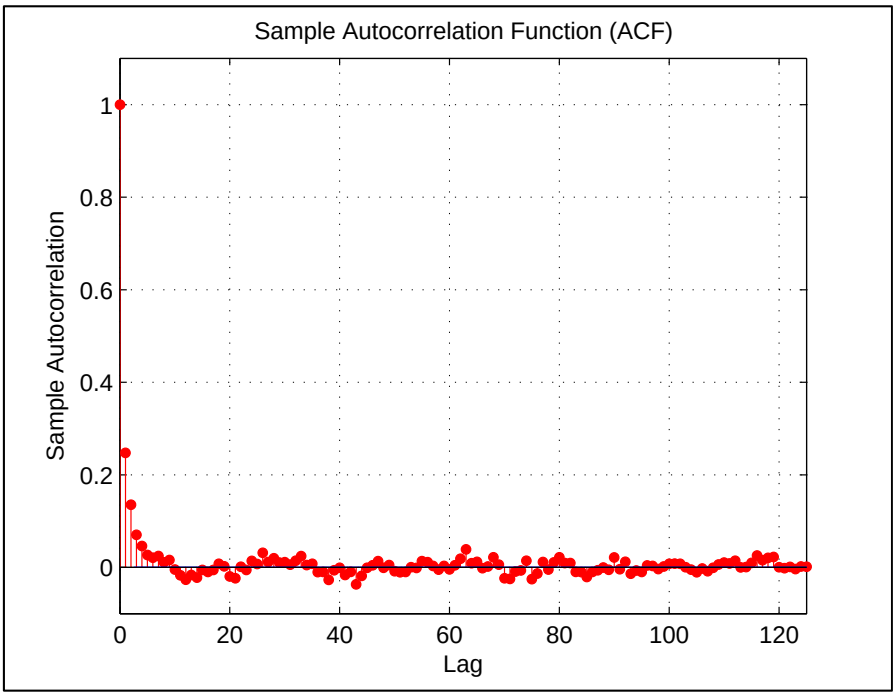

Figure I-2: Autocorrelation for 5 s

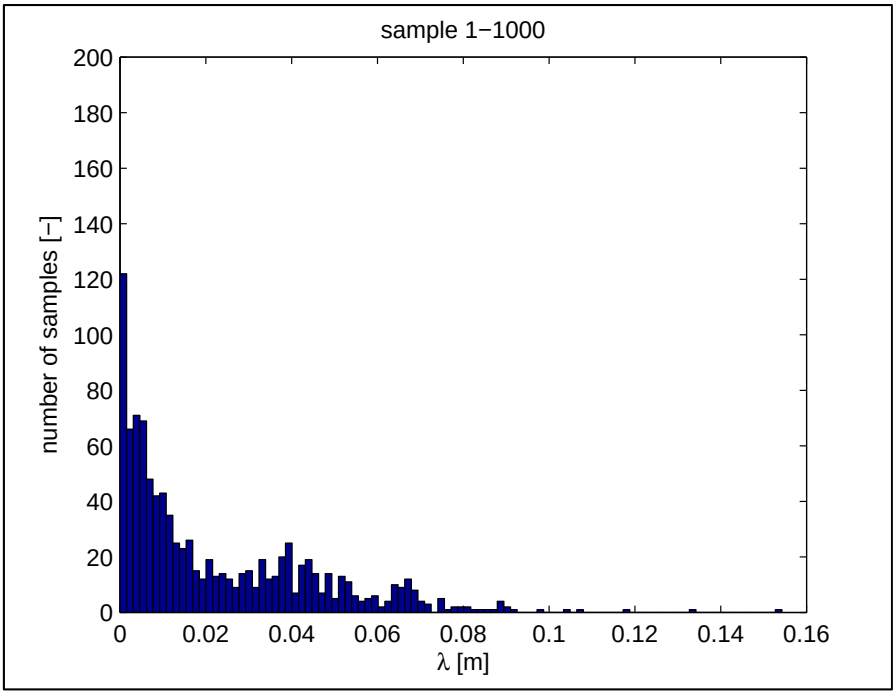

Figure I-3: Histogram of measurement 1-1000 (without piles)

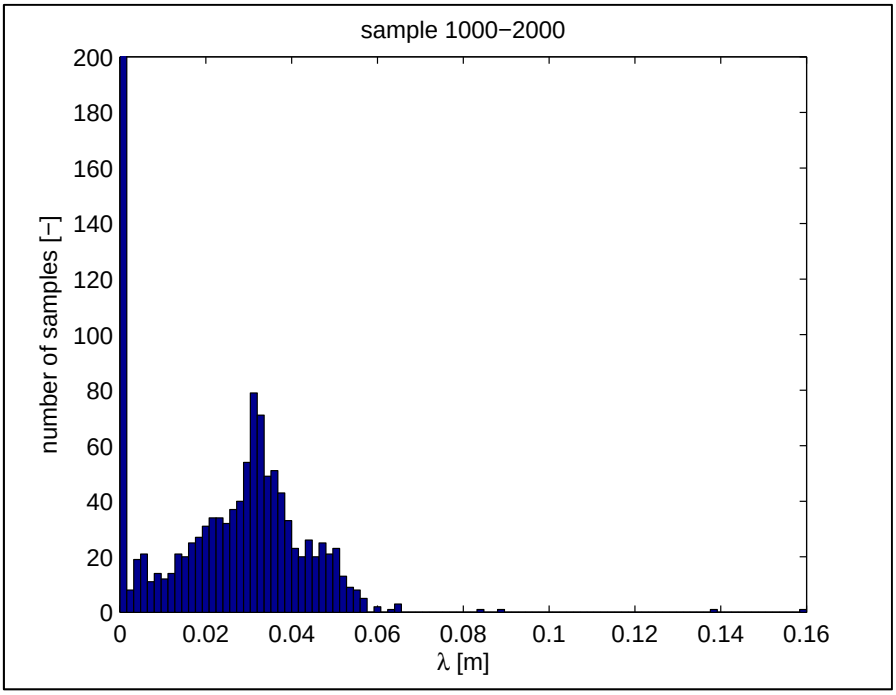

Figure I-4: Histogram of measurement 1000-2000 (with piles)

Appendix J Measurement data

The disk as supplied with this thesis contains all original data-files, filtered data-files and Matlab-scripts that were used to perform calculations and analysis. Here a list is included with all available files and their content.

Filename	Content
\Matlab	
Data_all.mat	despiked measurement data per location
Data_despiked.mat	despiked measurement data (375 MB)
..1_Despike_v6.m	Matlab: despike function for raw data
..2_Calc_from_despiked_011.m	Matlab: calculate values from raw data
..3_Plot_directional_turb_006.m	Matlab: plot turbulence intensities
..3_Plot_efflux_directional_mean_003.m	Matlab: plot Figure 4.3
..3_Plot_efflux_directional_mean_analysis_003.m	Matlab: plot Figure 5.1
..3_Plot_efflux_directional_turb_003.m	Matlab: plot Figure 4.3
..3_Plot_vert_mean_003.m	Matlab: plot Figure 4.4
..4_Plot_scen_sections_002.m	Matlab: plot Figure 4.2
..5_Plot_directional_mean_010_incl.m	Matlab: several plots in chapter 4 and 5
..6_Vector_angles_001.m	Matlab: plot Figure 5.4
..7_Autocorr_001.m	Matlab: plot Figure I-1
..9_x_profiles_001.m	Matlab: plot Figure 5.7
func_despike_phasespace3d.m	Matlab: function to despike data
func_excludeoutlier_ellipsoid3d.m	Matlab: function to despike data
suplabel.m	Matlab: function to plot extra labels
\Data	
all 2205 measurement files	raw Vectrino measurement data (190 MB)
\Model	
MSc_RvD_model_010.skp	Sketchup scale model drawings
MSc_RvD_Scalemodel_026.dwg	AutoCAD scale model drawings
MSc_RvD_Scalemodel_026.pdf	AutoCAD scale model drawings
yellowsun_11-16_gradation.xls	gradation of used stones at bed
\Photo	
several photos	indication of the scale model dimensions

Table J-1: Available data-files and scripts

J.1 Description of data files

Data_despiked.mat contains all organised and despiked measurement data from the ADV. This is one file with all 2205 measuring points included, which each consist of a few thousand samples. Each measuring point is organised as schematised below. Data_despiked.mat is extracted from the raw Vectrino (ADV) measurement data files. Scenario names and measurement coordinates were extracted from the filenames of these Vectrino (ADV) files.

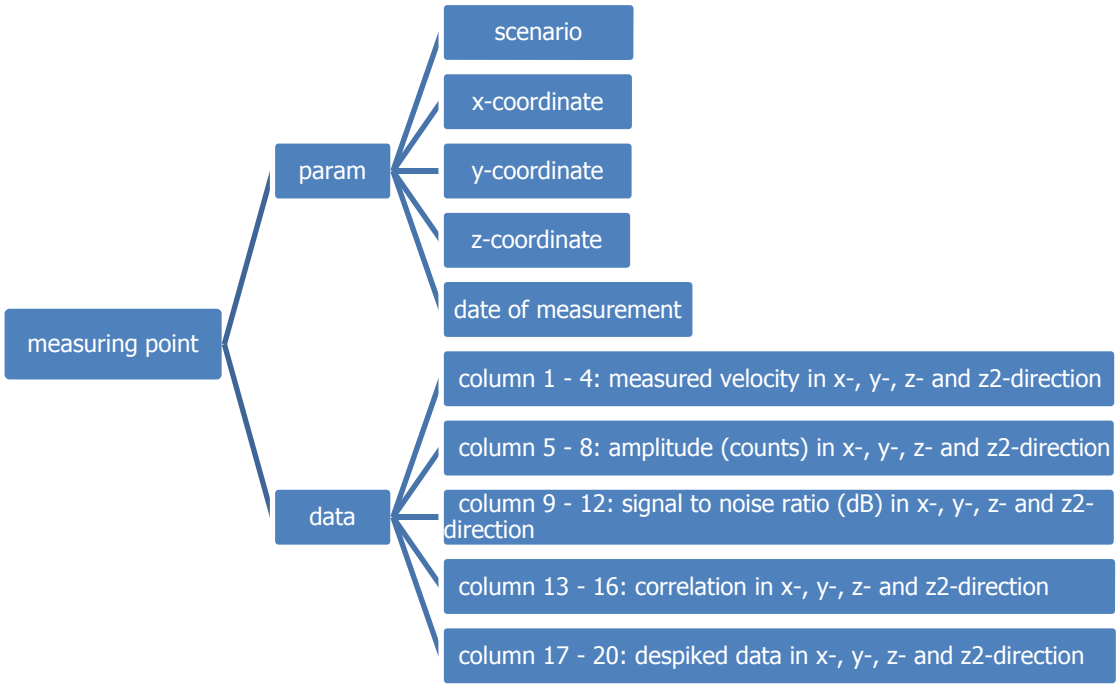

Table J-2 contains a description of available data in Data_all.mat, which is calculated using Data_despiked.mat.

Column	Content
1	scenario number (1-10)
2	x-coordinate [mm]
3	y-coordinate [mm]
4	z-coordinate [mm]
5	date and time of measurement
6	velocity component in x-direction [m/s]
7	velocity component in y-direction [m/s]
8	velocity component in z-direction [m/s] (first)
9	velocity component in z-direction [m/s] (second)
10	turbulence intensity in x-direction [m/s] (standard deviation)
11	turbulence intensity in y-direction [m/s] (standard deviation)
12	turbulence intensity in z-direction [m/s] (standard deviation)
13	turbulence intensity in z-direction [m/s] (standard deviation)
14	velocity component in x-direction parallel to slope [m/s]
15	velocity component in y-direction parallel to slope [m/s] (equal to column 7)
16	velocity component in z-direction parallel to slope [m/s] (first)
17	velocity component in z-direction parallel to slope [m/s] (second)
18	turbulence intensity in x-direction parallel to slope [m/s] (standard deviation)
19	turbulence intensity in y-direction parallel to slope [m/s] (standard deviation)
20	turbulence intensity in z-direction parallel to slope [m/s] (standard deviation)
21	turbulence intensity in z-direction parallel to slope [m/s] (standard deviation)
22	correlation of velocity components in x-direction
23	correlation of velocity components in y-direction
24	correlation of velocity components in z-direction (first)
25	correlation of velocity components in z-direction (second)

Table J-2: Description of data in Data_all.mat

J.2 Description of available data

Data_all.mat contains 2205 measurements, which are not all used or analysed in this research. Possibly these unused data can be used in further research and thereby a description of all data is included here.
Some of the data are filtered out of the analysis when it was clear that a measurement was inaccurate compared to the measurements around this location. This data is marked with a scenario number 11 for scenario 1, 22 for scenario 2 and so on until 1010 for scenario 10. In this way it was easy to exclude these data in the analysis. Most of these data are represented by low correlation values.

This thesis focuses on measurements in the zone close to the propeller axis. In addition, measurements were performed at larger distances sideways. Analysis of these measurements could provide details about the sideward flow parallel to the slope. A brief introduction into this is presented in paragraph 0.

Z-coordinates in the measurement files are not equal to the z-coordinates as presented in Figure 3.9. A traverse system was used to easily move the ADV parallel to the slope. The z-coordinates are values from the vertical measuring-tape as indicated in Figure J-1. Measurements at equal distance above the slope therefore have equal z-coordinates.

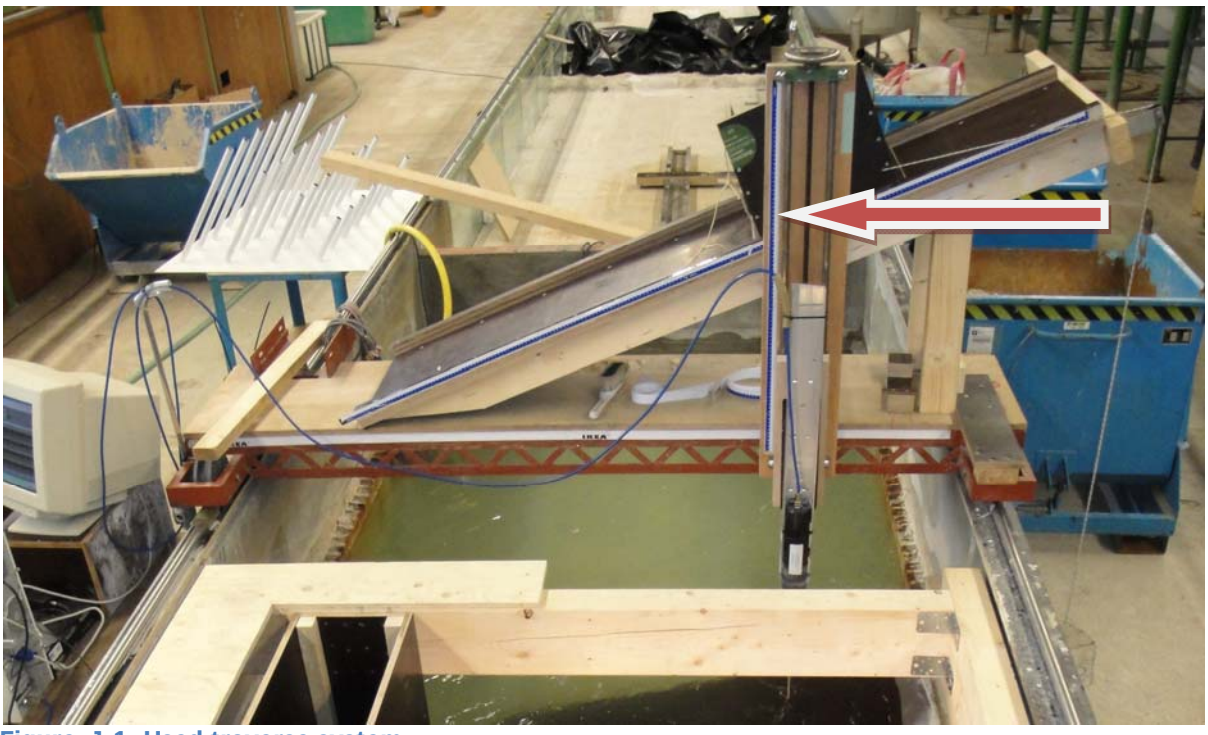

Figure J-1: Used traverse system

More photos are digitally attached with this thesis, as indicted in Table J-1.

J.2.1 Assessment of measurement signal and data

During the measurements the signal quality from the ADV was checked and improved when necessary. In addition, some data have been excluded from the analysis based on the quality of the data. This paragraph describes the way of assessing the signal and data to provide insight into the acquisition and processing of data.

During the scale model tests the measurement signal from the AVD could be checked real-time. A certain amount of seeding material in the basin was required in order to get a reasonable signal quality. Not enough particles were present in the used drinking water to reflect the sound pulses used by the ADV and Chinese clay was used as seeding material to provide enough particles in the water. During the measurements the clay particles slowly settle and from time to time particles were stirred up, using a broom in the basin. If measurement data were recorded, no broom was swiped through the basin to prevent disturbances, but clay particles were added to the basin just in front of the inflow opening of the thruster.

Another error source during the measurements was the ADV distance to the bed. In the first test series experiments were done to test the ideal position for the ADV with respect to the bed. At certain distances to the bed sound pulses emitted by the ADV seemed to reflect at the bed and disturbed the measurement signal. By changing the ADV distance to the bed with 1 to 10 mm, this disturbance was not present anymore. This 'problem' can be found at the website of the ADV manufacturer 'Nortek'. In the 'Forum' part on the website, troubles with ADV apparatus are discussed.

After performing the scale model tests data spikes were filtered out using a standard 'de-spike' function. After this edit, still some data were present with a high noise level. Based on the 'correlation' values from the measurements, data with a correlation below 40 were filtered out. In addition, at several locations more than one measurement was done. At these locations measurement data with the largest correlation value were used to analyse the measurements.